Flasher calibration of the T1 and T2 CANGAROO telescopes and TeV gamma ray observation of Markarian 421 and EXO 055625-3838.6 BL Lacertae blazars

David Swaby

This thesis is submitted as a Master of Science (Research) to the

School of Chemistry and Physics (High Energy Astrophysics),
University of Adelaide

Supervisor:
Prof. Roger Clay

Adelaide, December 2010

Chapter 1

Introduction

1.1 Strongly ionizing radiation from space

The discovery of strongly ionizing radiation (distinct from weakly ionizing radiation, such as ultraviolet (UV)), from astrophysical sources is a comparatively recent twentieth century phenomena, when the knowledge and technical means for the detection of strongly ionizing radiation emanating from outer space became a possibility. Until the 1900's, most discoveries in astronomy relied on telescopes using the non-ionizing visible light spectrum. In the last decade of the nineteenth century, the discoveries of strongly ionizing radiation in the form of X-rays by Röntgen, and in the radioactive decay of radionuclides by Becquerel, gave impetus to the idea that this form of high energy ionizing radiation may be arriving at Earth from beyond our atmosphere.

In testing the degree of ionizing radiation in the atmosphere, in 1912 the Austrian physicist Victor Hess, made a famous manned balloon flight and used a Wulf electrometer detector to measure the products of ionizing radiation at various altitudes. The result of this flight showed conclusively that the degree of ionizing radiation increased with altitude with "strange effects", namely that the degree of ionization dropped off initially from sea level then gradually increased with altitude, partly contrary to an expectation of a straightforward correlation of degree of ionizing with atmospheric density, (i.e. altitude). Much later this effect was discovered to be caused by ionizing particles, emitted from hadronic or cosmic ray atmospheric showers.

In the 1920s, experiments of a similar nature to Hess' at varying geophysical altitudes high in the atmosphere, and submerged in lakes, by the American physicist Robert Millikan, demonstrated the extraterrestrial nature of the ionizing radiation which Millikan named "cosmic rays", Clay & Dawson (1997) [48]. These experiments were carried out partly due to a concern that at least some of the ionizing radiation detected in the atmosphere was of geological origin. Millikan hypothesized that the cosmic rays were gamma rays, which was later found to be largely erroneous.

Experiments continuing into the 1920s and 1930s discovered the so called latitude effect with cosmic ray measurements. At sea level there is a 6% drop in intensity of cosmic rays from the poles to the equator, more pronounced at higher altitudes. This and the East-West effect, predicted by Georges Lemaître, Manuel Vallarta and Bruno Rossi, show that charged cosmic ray particles (such as free electrons) are deflected by the Earth's magnetic field. If the cosmic ray particles were made up of primarily one type of charged particle, then there should be more arriving in a Easterly direction than the Westerly direction for example. This was duly detected independently using Geiger Tube counters by Lemaître and Vallarta in Mexico and by Rossi in East Africa, [48]. Uncharged particles like gamma ray photons would arrive largely undeflected by the Earth's magnetic field. To the surprise of these experimenters, there were more particles arriving in the West than the East in equatorial regions, indicating that the majority of primary cosmic ray particles had positive charge.

In the 1930s many charged particles such as the positron were discovered via their ionization tracks made visible in Wilson cloud chambers situated between the dipoles of a magnetic field. The charge and mass of those charged particles can be derived in this way. When cosmic rays (and gamma rays) enter the Earth's atmosphere, they collide or scatter with a nucleus from an atom of the atmosphere's gas and initiate a cascade of many millions of secondary particles called an Extensive Air Shower (EAS). This phenomenon was first discovered by Pierre Auger and Dimitry Skobeltzyn in 1927-29 (the particles hitherto detected in the Wilson cloud chamber), [48]. The full properties of new uncharged particles with "mass" which made up an cosmic ray air shower, such as secondary nucleons, mesons, leptons and photons, were not discovered until some

time later.

In the late 1940s, experiments pioneered by Cecil Powell at the University of Bristol with very high altitude balloons and photographic emulsions were conducted, [48]. Photographic emulsion is able to record the track of cosmic ray particles. This technique was finally able to detect the primary (mainly positively charged) particles responsible for cosmic rays. These turned out mainly to be protons, but also heavier nuclei such as $\mathbf{He}^{++}$ **and** $\mathbf{O}^{8+}$ were detected. Despite these charged particles being affected by the Earth's magnetic field when entering the atmosphere, the great majority of cosmic rays arrive at the boundary of the Earth's magnetosphere isotropically as they are largely trapped within the Galactic magnetic field. This randomizes the source directions of cosmic ray particles from likely emission sources within our galaxy, such as supernova remnants and most cosmic ray particles arriving from extragalactic sources, whereas gamma rays arrive at the Earth undeflected by magnetic fields. This fact that gamma ray photons are not randomized by galactic magnetic fields can be used to discriminate cosmic rays from gamma rays in the imaging atmospheric Čerenkov (pronounced Cherenkov), detection technique as discussed in Section 2.1.

The species of high energy particles that emanate from astrophysical sources are now quite well known, although the physical process that produces the ionizing radiation at the source or in propagation to Earth, may not be well understood. Briefly, the species of strongly ionizing astrophysical radiation is generally classified as: Cosmic rays, including all hadronic baryon particles such as protons and larger mass number nuclei plus single neutrons. Although the half-life of this particle is about 15 minutes, relativistic time dilation at high Lorentz factors can include neutrons from galactic sources.

The strongly ionizing astrophysical photons are now not traditionally classified as cosmic rays, although they are strongly ionizing at X-ray and gamma ray energies and are usually closely associated with astrophysical sources also likely to be cosmic ray emitters. Gamma rays produced from meson decay processes are also counted in gamma ray astronomy, as well as gamma rays produced from electron/positron acceleration processes, such as by synchrotron emission. Cosmic rays and photons are

related through the entire propagation process, from the emission of the particles from the source (in the interactions in transit from the source to Earth), to the EAS made when particles collide with Earth's atmosphere.

1.2 A brief history of Gamma Ray Astronomy

1.2.1 X-ray and Gamma Ray satellite detectors

Astrophysical gamma rays are photons typically considered to be in the energy range 1MeV-1PeV (PeV is peta electron-volts; 1×10^{15}eV) and above. Electronic models of gamma ray emission indicate that gamma rays are most likely to be produced by Inverse Compton (IC) scattering of electrons accelerated in shocks to very high Lorentz factors, γ, with low energy photons. See Sections 2.2.1 to 2.2.3 for more discussion. The next energy band down from gamma rays, the astrophysical X-rays, are considered to be in the energy range 1-1000 keV, Illingworth (1994) [87]. Apart from Bremsstrahlung at low X-ray energies, electronic models indicate that X-rays are produced by synchrotron emission in shock regions or in large scale magnetic fields.

Despite the great advancement in cosmic ray astrophysics, by the mid-twentieth century, gamma rays and X-rays from cosmological sources remained largely undetected until the 1960s. Since then, numerous X-ray detectors aboard satellites have been flown and many upper atmospheric balloon borne X-ray detection experiments carried out. In the 1980s the EXOSAT X-ray satellite was launched, Reynolds *et al.* (1999) [147], which subsequently detected a number of synchrotron X-ray spectrum peaks of sources at energies indicating the likelihood of HBL Lac. blazars, such as EXO055625-4848 (see Section 7.2 for more details on this source). Recent X-ray satellites include *Beppo*-SAX; Boella *et al.* (1997) [33], *Chandra*; Weisskopf *et al.* (2000) [169], ROSAT; Aschenbach (1991) [20], RXTE; Levine *et al.* (1996) [110], ASCA; Tanaka, Inoue, & Holt (1994) [159] and XXM-*Newton*; Jansen *et. al* (2001) [90]. These X-ray detectors have been used in multi-wavelength campaigns with IACTs (Imaging Atmospheric Čerenkov Telescopes), to study the flaring activities of HBL Lac. blazars.

Gamma ray detectors aboard satellites were initially launched in 1961 when the

Explorer XI satellite was launched with a gamma ray detector aboard which counted up to about 100 gamma rays from cosmological sources, Kraushaar *et al.* (1995) [101]. No gamma ray sources were located because of the very low angular resolution of this experiment. Further gamma ray counters were launched on satellites in the 60s: OSO; Ulmer *et al.* (1974) [161], *Vela*; Conner, Evans & Belian (1969) [49], OGO; Jackson & Vette (1975) [89], and the Russian series of COSMOS satellites, Chupp (1976) [46].

The first dedicated gamma ray satellite with some angular pointing resolution was SAS-2 (Small Astronomy Satellite) launched in 1972, Fichtel *et al.* (1975) [59]. This satellite discovered the 20 MeV to 1 GeV diffuse gamma ray emission from the galactic plane. Launched in 1975 and operated to 1982 was the COS-B satellite which detected X-rays and gamma rays in the range 2 keV to 20 GeV, Swanenburg *et al.* (1994) [158]. This was the first satellite to be able to crudely resolve gamma ray point sources and discovered 25 gamma ray sources around the galactic plane, including the Crab plerion, Vela and Geminga pulsars, and the extragalactic quasar 3C 273. However, the limited angular resolution of this instrument made it difficult to resolve these sources from the diffuse gamma ray emission of the galactic plane.

Gamma ray satellite detection entered a new era of discovery when the EGRET (Energetic Gamma Ray Experiment Telescope) gamma ray observatory experiment was launched aboard the CGRO (Compton Gamma Ray Observer) satellite in 1991. The EGRET instrument consisted of two series of multi-layered spark chambers at two different gap widths, a plastic scintillator hodoscope, a NaI(TL) calorimeter known as TASC (Total Absorption Shower Counter), and a plastic scintillator anti-coincidence dome to reject charged particles, see Figure 1.1. A gamma ray will pass through the anti-coincidence dome and scatter with one of the thin Tantalum layers of the upper spark chamber. The secondary electrons (positrons) may trigger the hodoscope, consisting of 4x4 array of plastic scintillator tiles in the middle of the spark chamber volume, and in a similar array at the bottom. A coincidence signal from combinations of tiles selected from preset electronics or command, together with a time of flight signature indicating downward moving particles, initiates the spark chamber high voltage pulse and later the readout of the spark chamber and energy data from electronics

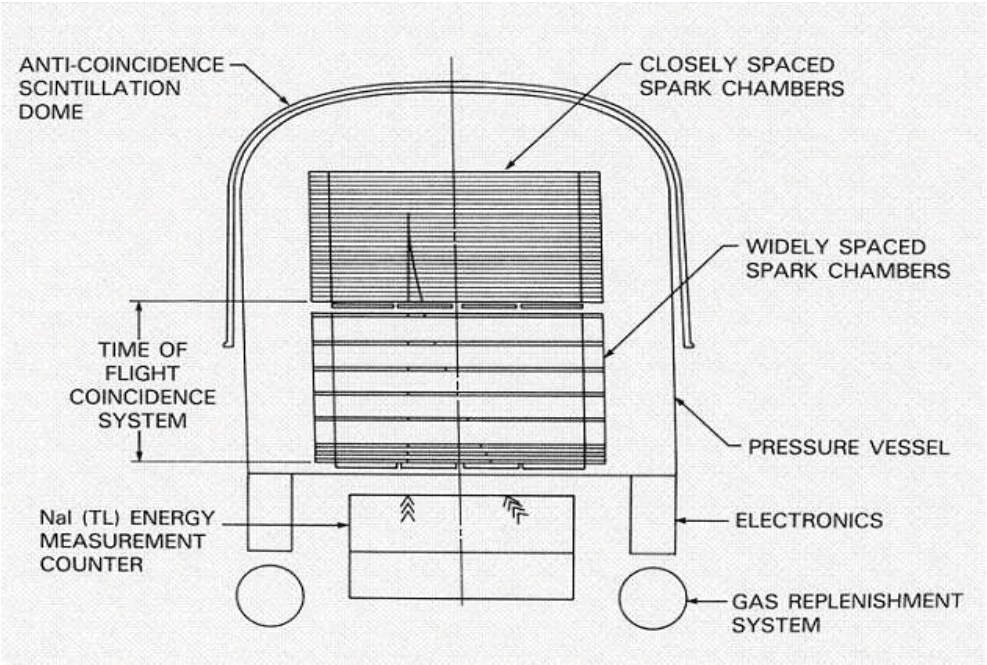

Figure 1.1: A sketch of the EGRET gamma ray observatory aboard the CGRO satellite.

modules at the bottom. The spark chamber record shows X and Y projected views, energy information, gamma ray arrival time and auxiliary information which are then transmitted to the ground as one event, Nolan *et al.* (1992) [128].

The EGRET instrument initially detected gamma rays in the energy range 20 MeV to 20 GeV. The lower energy threshold deteriorated over time due to gas depletion of the spark chamber gas replenishment system and the gradual deposition of charged particles on the spark chamber plates. The angular resolution of EGRET was estimated to be around 5 arc minutes, although this would be for bright sources with hard spectra, [128]. This instrument was responsible for detecting 271 gamma ray sources (Third EGRET Catalogue, 3EG, Hartman *et al.* (1999) [75]), during its operational lifetime, the largest number of gamma ray satellite detections at that time. Figure 1.2 indicates the positions of the sources of the third EGRET catalogue in Galactic coordinates. 3EG includes data from the second EGRET catalogue (2EG) and additional sources at energies greater than 100 MeV. The data were taken from April 22, 1991 to October 3, 1995 and 3EG uses completely reprocessed data (to correct a number of mostly

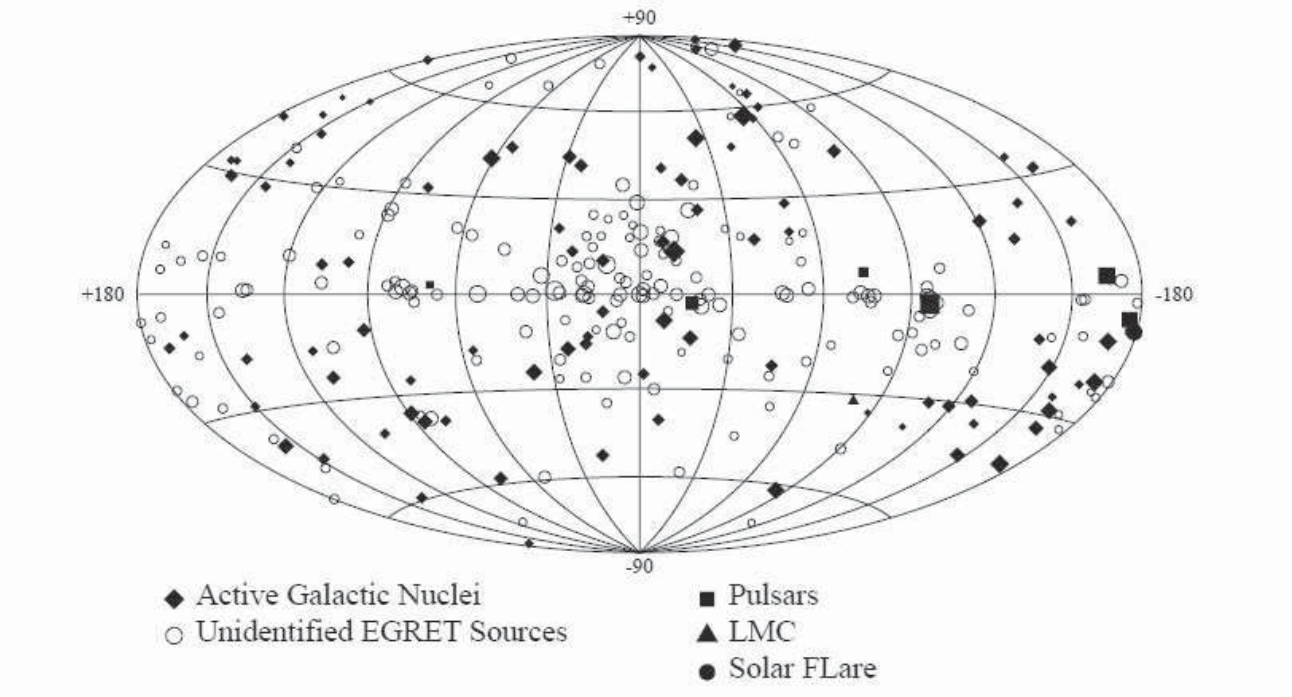

Figure 1.2: The third EGRET catalogue map in galactic coordinates. The size of the symbol on the map represents the intensity of the source as seen by EGRET, Hartman *et al.* (1999) [75].

minimal errors and problems). Within the 271 gamma ray sources of 3EG there have been identified; one bright solar flare in 1991; the Large Magellanic Cloud galaxy; five pulsars; one probable identification of the radio loud galaxy Cen. A; 66 high confidence identifications of blazars (BL Lac. objects, flat spectrum radio quasars and unidentified flat spectrum radio sources); 27 low confidence potential blazar sources and 170 sources not yet identified, [75].

A new generation of gamma ray satellite borne experiments has been launched in June 2008 aboard the *Fermi Gamma-ray Space Telescope* (*Fermi*) or GLAST. The primary gamma ray detector instrument aboard this satellite is LAT (Large Area Telescope). LAT searches for gamma ray emissions in the range from below 20 MeV to more than 300 GeV, Atwood *et al.* (2009) [24], which covers the range of gamma rays that have too low energies to be observed by ground based IACT telescopes and overlaps in energy well above the energy threshold for most of these instruments. "The LAT is a pair-conversion telescope with a precision tracker and calorimeter, each con-

sisting of a 4×4 array of 16 modules, a segmented anti-coincidence detector that covers the tracker array, and a programmable trigger and data acquisition system. Field-of-view of the detector is 2.4 Steradians. Data obtained with the LAT are intended to (i) permit rapid notification of high-energy gamma-ray bursts (GRBs) and transients and facilitate monitoring of variable sources, (ii) yield an extensive catalog of several thousand high-energy sources obtained from an all-sky survey, (iii) measure spectra from 20 MeV to more than 50 GeV for several hundred sources, (iv) localize point sources to 0.3 - 2 arc minutes, (v) map and obtain spectra of extended sources such as supernova remnants, molecular clouds, and nearby galaxies, (vi) measure the diffuse isotropic gamma-ray background up to TeV energies, and (vii) explore the discovery space for dark matter.", [24]. Another instrument aboard *Fermi* searching for gamma ray bursts (GRB) is the GLAST Burst Monitor (GBM). "The main goals of the GBM are to measure gamma rays at low energies within a larger FoV than that of LAT, to localize the GRBs occurring in this FoV, and to communicate this position to the LAT to allow for the re-pointing of this main instrument, and to perform time-resolved spectroscopy of the measured burst emission. These goals can be achieved by an arrangement of 12 thin Sodium Iodide (NaI) detectors which are inclined to each other to derive the position of the GRBs for the measured relative counting rates and to get the low-energy spectrum in the range ∼10 keV to ∼1 MeV.", Lichti *et al.* (2007) [112]. The FoV of GBM is ∼8-10 Steradians and the (expected performance) energy range of GRB is 8 keV to 30 MeV, [112].

Prior to the *Fermi* satellite, older gamma ray satellites such as EGRET left an energy gap in the gamma ray spectrum between its upper energy limit of 30 GeV and the lower threshold of ground based IACTs of around 500 GeV (energy threshold of single 10m IACT reflectors such as CANGAROO II and *Whipple*). *Fermi* is easily able to measure across this spectrum to beyond the lower energy threshold of IACT arrays (such as CANGAROO III), thus obtaining a continuous gamma ray spectrum from MeV to TeV energies.

1.2.2 A history of ground based gamma ray observatories

In 1952, one of the earliest atmospheric Čerenkov counting experiments was set up by Galbraith and Jelly, [66] for 3 nights of observations at the Atomic Energy Research Establishment in Berkshire, England. It consisted of a 26cm diameter parabolic mirror with a then (newly invented) photomultiplier tube at the focal point. This experiment showed the abundance of Čerenkov radiation in the atmosphere, mainly caused by cosmic rays. Ground based detection of astrophysical gamma rays began with work in the Crimea from 1960-64 with Chudakov *et al.* (1965) [45], in England in 1964 with Fruin *et al.* (1964) [63], in Ireland in 1968 with Fegan *et al.* (1968) [58], and the United States in 1968 with Fazio *et al.* (1968) [56].

Most of these detectors used a series of small primary parabolic mirrors with 1 to 3 photomultiplier tube detectors at each mirror focal point to count the Čerenkov induced signal pulses. These detectors were pointed at sources thought likely to be TeV gamma ray emitters, such as the Crab pulsar, the Cygnus X-3 micro-blazar, Weekes *et al.* (1972) [168], Grindlay *et al.* (1973) [72], [58], Gibson *et al.* (1982) [69], Centaurus A, and PSR 0532, [69]. One detection method using this technique was to rely on the timing difference of the arrival of the Čerenkov wavefront from a gamma ray shower, between the centre and the edges, of 1-3 nanoseconds. This would be attempted by using an array of small diameter mirrors placed strategically apart. Another way was to attempt to count gamma ray on-source trigger excesses over cosmic ray background triggers. This may work for a very high gamma ray flux source such as the Crab nebula, but, generally, the cosmic ray "noise" background rate swamps any gamma ray signal using this technique. This is so particularly for the energy threshold range of Atmospheric Čerenkov Telescopes, and is very difficult to statistically separate with high confidence.

Observations in the 1960s and 1970s found few significant results. Fazio *et al.* (1972) [57], reported a 3 sigma upper limit signal from 150 hours of observation of the Crab nebula from Mt. Hopkins Observatory (now confirmed). A delayed report from the Crimean and Tien Shan groups indicated a signal from Cygnus X-3 during a radio flare, Vladimirkski *et al.* (1973), [164].

The modern relatively successful era for TeV gamma ray astronomy began with the 9 sigma detection of the Crab nebula in 1989 by Vacanti *et al.* (1991) [162], with the newly established *Whipple* 10m Čerenkov telescope on Mt Hopkins, Arizona. This new type of Imaging Atmospheric Čerenkov Telescopes (IACT), utilizes a large mirror collection area and a "camera" of more than 100 densely packed photomultiplier tubes at the focal point, instead of multiple small mirrors each with a few photomultiplier tubes. The advantage of this new imaging technique over the old wavefront sampling or on/off source trigger counting was that, by image analysis of the gamma ray showers via a low resolution camera, the gamma ray shower event could more efficiently discriminate against cosmic ray showers thereby improving signal over noise (see Section 2.1). Also a large diameter mirror is able to gather more Čerenkov photons and so acquire lower energy showers.

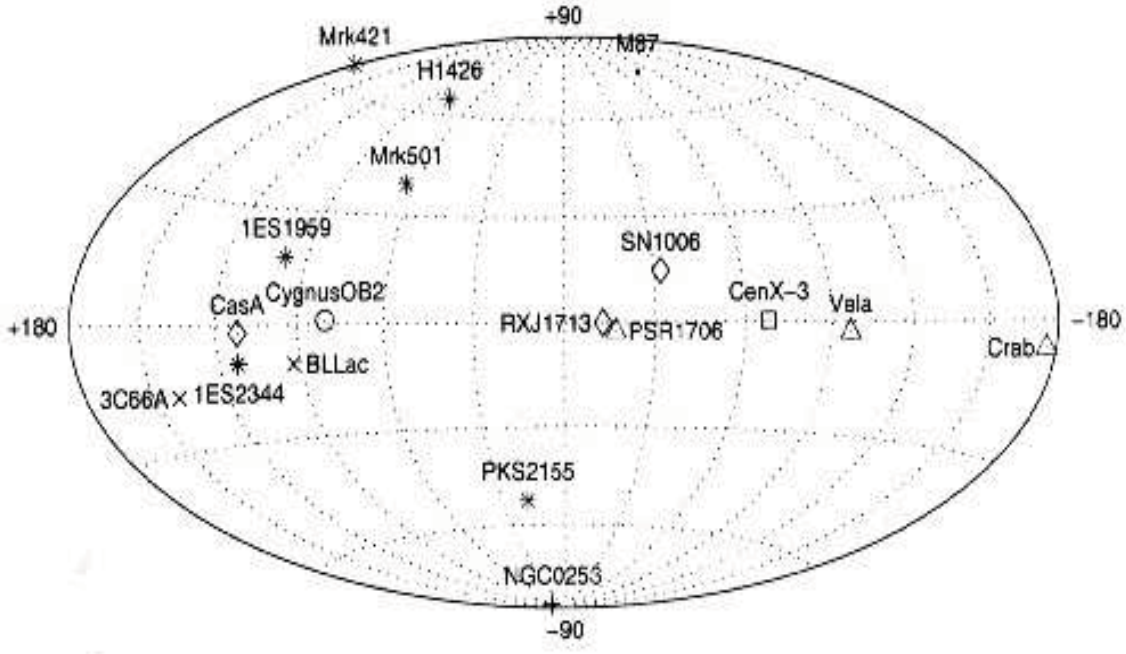

Figure 1.3: Distribution of high significance TeV gamma ray sources in galactic coordinates: HBL Lac.; *asterisks*, LBL Lac.; *cross*, radiogalaxy; *dot*, star-burst galaxy; *plus*, SNR; *diamonds*, plerions; *triangles*, binary system micro-blazar; *square*, OB star association; *circle*. These were the majority of TeV gamma ray sources at the time the observation of the two gamma ray sources in this thesis were taken.

In the 1990s and the first half decade of the twenty first century, IACT groups around the world have discovered close to 20 TeV gamma ray sources (at the time that the gamma ray sources were observed in this thesis, see Chapter 7), other than the Crab, with high confidence. Figure 1.3 shows the 1993 distribution of TeV gamma ray sources, which includes a large number of different types of galactic and extragalactic objects. For the large amount of time invested in IACTs, this may not seem very impressive when compared to the rate of discoveries of ground telescopes of lower energy spectra. However, in astronomy there is an extremely large energy gap between the UV spectrum and the GeV-TeV gamma ray spectrum, where the photon detection of this enormous gap can only be filled by satellites. Factors influencing the low numbers of sub-TeV to TeV gamma ray source count are:

1. Gamma ray attenuation in intergalactic space by the intergalactic infra red photon field (IIRF) and the cosmic microwave background (CMB), limiting their detection to $z < 0.3$ redshift (Section 2.4).

2. The power law index of the TeV energy spectrum is typically steep ($\alpha > 2$), so the flux of gamma rays are low. For instance the Crab nebula, which is one of the most intense gamma ray sources in the sky, has been reported by the *Whipple* observatory 10m IACT, to have a detection rate of about 6 gamma rays per minute, Punch (1993) [143].

3. The very high noise to signal ratio means that long exposures of the source over at least several hours are required, matched with the similar length exposure off source as well.

4. IACTs have a low duty cycle, where low skylight noise observations are only really possible on clear moonless nights.

IACTs have an advantage over zenith mode only gamma ray counting arrays, such as MILAGRO; Atkins *et al.* (2000) [21], and *Tibet* III; Amenomori *et al.* (2003) [16], in that the position of the gamma ray source can be resolved down to a few arc seconds in some cases.

Despite some limitations in the rate of detection of gamma ray sources, a generation of IACT observatories have made new inroads into the field of VHE gamma ray Astrophysics: CANGAROO III; Asahara (2003) [18], HESS; Bernlöhr (2003) [30], Hofmann (2003) [83], Hinton (2004) [82], VERITAS; Weeks (2002) [165], and MAGIC; Martinez (2003) [117]. With the exception of the single large IACT of MAGIC, the IACTs of these groups consists of an array of four or more telescopes, with dishes at least 10m in diameter and imaging cameras > 400 photomultiplier tube pixels. The arrays of IACTs are able to view showers in stereo mode. This application gives a more powerful algorithm for the image discrimination between gamma ray and cosmic ray showers, compared with a single telescope in mono mode, by reducing the uncertainty in the angular resolution direction of the gamma ray shower. Most of the above IACT systems operate in stereo mode using a common shower trigger configuration, and are able to trigger independently, possibly observing more than one source at a time.

Chapter 2

TeV gamma ray blazar emission and imaging of Čerenkov events

2.1 Čerenkov imaging of atmospheric showers

Cosmic rays at GeV-TeV energies arrive at Earth isotropically due to their diffusion in the galactic magnetic field (see Section 1.1). On the other hand, primary GeV-TeV gamma rays (produced at specific astrophysical sources), arrive from their source without magnetic field deflection from the source production area. This useful fact, enables the primary gamma rays to be distinguished from primary cosmic ray species, in that gamma rays can be vectored directly to the astrophysical object of emission. Note that the usage; "primary", refers to the particle from the astrophysical source rather than "secondary" particles produced as a result of an Extensive Air Shower (EAS) in the atmosphere.

Upon arrival at Earth, both primary cosmic rays and gamma rays initiate EAS in the atmosphere, where the initial interactions of a cosmic particle with nuclei of atmospheric gases, leads to a cascade of electromagnetic leptons, hadrons, mesons and electroweak muons (the secondary particles). The second useful fact in distinguishing cosmic rays from gamma rays is the profile of the shower development in the atmosphere which differs between these two types of primary particles. Figure 2.1 shows a comparison between the shower profile with atmospheric 250 GeV primary cosmic

ray particle on the left and a primary gamma ray (of the same energy) on the right. In this figure, the cascade composition of secondary particles of the cosmic ray shower leads to a considerably greater lateral extent than the gamma ray shower, and the primary gamma ray begins cascade interactions at a higher atmospheric altitude than the primary cosmic ray.

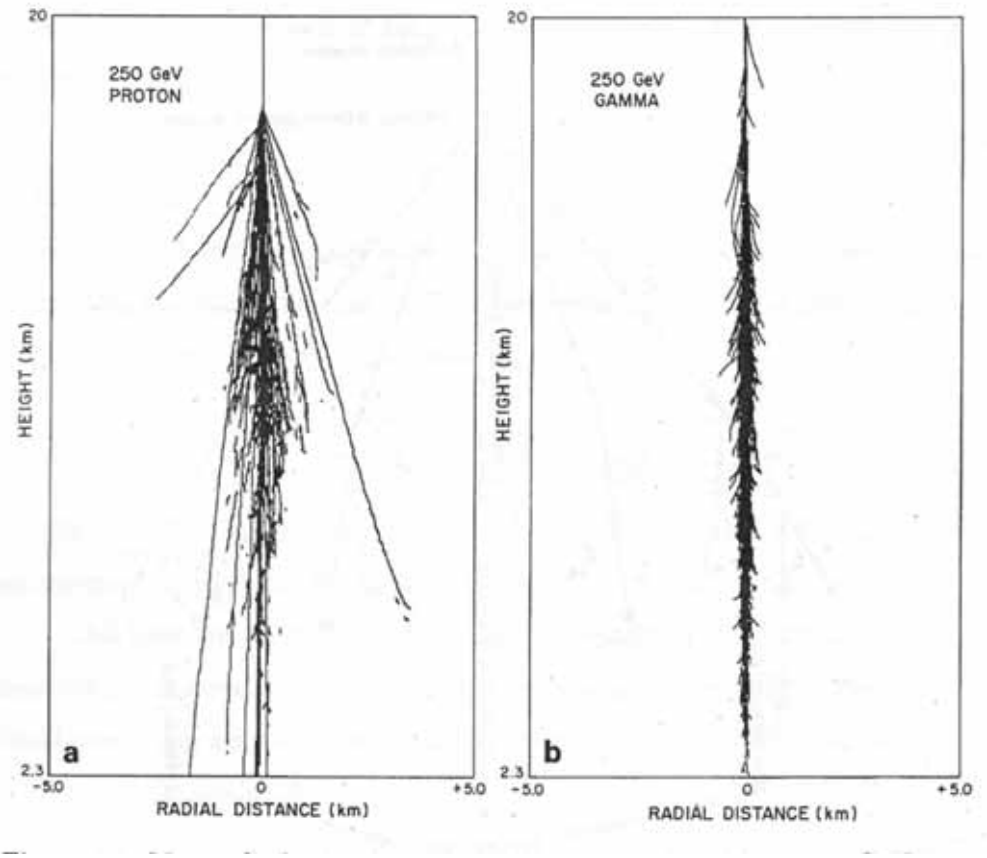

Figure 2.1: From Weekes (1988) [167]. A Monte-Carlo simulation showing the vertical and horizontal EAS profile (to an altitude of 20 km above sea level), of a 250 GeV cosmic ray proton (left) and 250 GeV primary gamma ray (right).

Furthermore, the complex secondary interactions of the primary cosmic ray particles include the decay of neutral and charged pions. The neutral pion (π^0) decay leads to a pair of secondary gamma rays and the charged pions ($\pi^{\pm}$) lead to the muonic component of an EAS. On the other hand, the EAS of a primary gamma ray is dominated by electronic cascade interactions (electron/positron pairs). Thus, the muon

yield from a primary cosmic ray (at the same energy) is at least a factor 100 times that of a primary gamma ray, Rowell (1995) [151]. This fact, although salient to distinguish primary gamma rays from cosmic rays, is seldom used in Imaging Atmospheric Čenenkov Telescope (IACT) experiments. A muon counter was deployed for a short time in tandem with CANGAROO-II data gathered with the T1 telescope in the early use of this instrument. However, the acceptance angle for many muon counters is too coarse to apply to IACTs operating in stereoscopic mode (see Section 3.2.7) as deployed by all current IACT experiments (with the exception of MAGIC operating in mono-mode), making muon counters less practical in IACT array experiments. Furthermore, with a commonly used off-axis imaging observation technique deploying half the camera (known as *wobble mode*, Albert *et al.* (2006) [12]), muon counting between cosmic ray and gamma ray showers becomes even more problematic because of the proximity of the on- and off-source shower images in the camera. It is beyond the scope of this thesis to further examine the secondary interactions of cosmic ray cascades.

2.1.1 Čerenkov radiation

"Any charged particle traveling though a dielectric medium will polarize atoms that lie along its path, including individual dipoles, localized and stationary in the observers frame", [151]. If a particle is passing through a dielectric medium at velocity (v), where $v > c/n$, n is the refractive index of the medium and, c is light velocity, an optical shock front results, as shown in Figure 2.2; "the time taken for the particle to traverse distance AB is equal to that of light to traverse AC (Huygens's principle), leading to the definition of the Čerenkov cone angle (θ_c) as", [151];

$$\cos\theta_c = \frac{1}{\beta n} \tag{2.1}$$

where, $\beta = v/c$, [151].

Features of Čerenkov radiation are that it is emitted from the dielectric medium and not from the particle itself, and that the Čerenkov radiation energy is much less than that of the traversing particle, [151]. A small angle cone (in air) of Čerenkov light is emitted in the same direction of the particle's travel. The cone is not solid;

Figure 2.2: From Rowell (1995) [151]. A sketch of a particle traveling at high velocity ($v > c/n$) through a dielectric medium of refractive index (n), will form an optical shock front with constructive interference at CB

an observer viewing down the velocity direction of a single particle would see a ring of Čerenkov radiation, [151]. Thus, the minimum speed that Čerenkov radiation can be emitted is ($\beta_{\min} = 1/n$) [151], and for the ultra-relativistic limit ($\beta \approx 1$), the maximum angle attainable for Čerenkov radiation is, [151]

$$\theta_{c\,(\max)} = \arccos\left(\frac{1}{n}\right) \tag{2.2}$$

Using equation 2.2 above, "For air at sea level where $n = 1.00029$, $\theta_{c\,(\max)} \sim 1.4°$", [151]. Most atmospheric Čerenkov photons will not extend beyond this angle.

Finally, Čerenkov radiation "in terms of photon emission ($E = h\nu$), per unit length", [151], is

$$\frac{dN}{dl} = \frac{2\pi Z^2}{137c} \int\limits_{\beta n > 1} \left(1 - \frac{1}{n^2\beta^2}\right)\, d\nu \tag{2.3}$$

for N photons emitted per path length, and a traversing particle with amount of charge

Ze ($e/hc \sim 1/137$), [151]. Čerenkov radiation will peak in the UV ($dN/dl \sim 1/\lambda^2$), [151]. The number of photons (Čerenkov intensity), emitted in the wavelength range ($\lambda_1 - \lambda_2$), over track length, l is, [151]

$$N = \frac{2\pi l}{137}\left(\frac{1}{\lambda_2} - \frac{1}{\lambda_1}\right)\left(1 - \frac{1}{\beta^2 n^2}\right) \tag{2.4}$$

Secondary cascade particles from EAS generate Čerenkov radiation at near UV wavelengths that can be detected by IACTs. However, EAS from gamma rays typically develop high in the atmosphere ($\sim$ 30 km ASL), thus their Čerenkov rays are subject to considerable intensity attenuation in transmission to ground via Rayleigh (molecular) scattering on its entire traverse length and Mie (aerosol) scattering in the lower atmosphere.

If Čerenkov photons from an EAS of reasonable intensity (to trigger the IACT for instance) reach the ground, the Čerenkov photons from the initial EAS development will reach the ground first (and is the part of the the EAS image furtherest away from the camera centre). If the camera centre is tracking on a gamma ray astronomical point source, the distance the EAS image is seen from the camera centre is a function of the distance the EAS developed away from the camera and the energy of the primary particle. The IACT technique captures the images of EAS on the ground two-dimensionally, thus the size of the "light pool" (or the area on the ground that is able to detect the EAS), is a function of altitude of the observatory. CANGAROO is 160 metres ASL, so the extent of its light pool (approximately at sea level) is about 100 metres across for a 1 TeV primary) particle. The size of the light pool decreases with altitude. The EAS image Čerenkov photons are "collected" by the primary parabolic mirror (although the CANGAROO-III primary mirror is compound with considerable gaps making a loss of $\sim$ 44% for non-reflective surface on the main dish (see Section 3.1.1)). The image is then focused onto the $\sim$ 1 metre diameter camera held at the focal plane of the telescope with the direction of the image inverted by reflection through the mirror (e.g. an EAS image at the top half of the camera is inverted to the bottom half). Because of the CANGAROO telescope's compound primary mirror system, the 114 individual mirrors are positioned with stepper motors to minimize the point-spread function of the image (Section 3.1.1).

The results of Čerenkov emission from the EAS of secondary particles initiated by primary gamma rays will been seen on the ground (two-dimensionally) as an elliptical shower image, with the semi-major axis of the ellipse pointing towards the astrophysical emission point. This is in contrast to Čerenkov images of cosmic rays, which have isotropic arrival directions (from the astrophysical emission point of these cosmological particles), and more complex shower development (including secondary shower images away from the primary shower image), in contrast to gamma ray showers.

2.1.2 Hillas parameters for gamma ray showers

Hillas defined a number of image parameters of the gamma ray ellipsoid (simulating the shape of the gamma ray shower), Hillas (1985) [81]. These results went on to become the shape parameters that enabled the Whipple telescope to first definitively detect the Crab Nebula in TeV gamma ray energies, Weekes *et al.* (1989) [166].

The moment of the ellipsoid from the two-dimensional shape of Čerenkov images of gamma ray showers on the ground (or in the telescope camera), can be transformed into the *Hillas Parameters*. There are Hillas Parameters other than shape parameters (for example, *concentration*), however this thesis only uses shape parameters. These Hillas (shape) Parameters are calculated using a weighted *moment* based fit analysis from the pixels in the camera registering Čerenkov signal. The Hillas (shape) Parameters based on the ellipsoid (shown in Figure 2.3), (all shown in unit of degrees) are:

- *Width:* RMS spread along the minor axis.
- *Length:* RMS spread along the major axis.
- *Distance:* The distance from the image centroid and the centre of the field of view
- *Miss:* Minimum distance between the major axis and centre of field of view.
- *Alpha:* The angle subtended by the major axis and a line joining the image centroid and centre of field of view.

- *Azwidth:* (Azimuthal-width): RMS width relative to axis from centre of field of view and image centroid, [151].

All Hillas (shape) Parameters except *azwidth* are used in the analysis of gamma ray detection in this thesis (see Sections 7.1.3 and 7.1.4).

Figure 2.3: From Dazeley (1999) [52]. A schematic diagram showing representations of the shape Hillas Parameters from the ellipsoid.

The calculation of the weighted moment from the Čerenkov signal pixel camera coordinates is indicated in Table 2.1 (below) (from Weekes *et al.* (1989) [166], and Reynolds *et al.* (1993) [148]). Using the results from Table 2.1, an axis is fitted to the image with (linear) equation; $y = ax + b$. Using the moment formulae from Table 2.1 and fitting to this line with ($d = \sigma_y^2 - \sigma_x^2$), we find that, [166], [148];

$$a = \frac{d + \sqrt{d^2 + 4(\sigma_{xy})^2}}{2\sigma_{xy}}, \qquad b =< y > -a < x > \tag{2.5}$$

Finally, in terms of the fitted line ($y = ax + b$) with components, a and b shown in equation 2.5 above, we can define the shape Hillas Parameters in Table 2.2 below, [166], [148];

ellipsoid moment	formula	formula squared	standard deviation
$< x >$	$\sum_i s_i x_i / \sum_i s_i$	$< x^2 >= \sum_i s_i {x_i}^2 / \sum_i s_i$	$\sigma_{x^2} =< x^2 > - < x >^2$
$< y >$	$\sum_i s_i y_i / \sum_i s_i$	$< y^2 >= \sum_i s_i {y_i}^2 / \sum_i s_i$	$\sigma_{y^2} =< y^2 > - < y >^2$
$< xy >$	$\sum_i s_i x_i y_i / \sum_i s_i$		$\sigma_{xy} =< xy > - < x >< y >$

Table 2.1: The weighted moment of the ellipse formulae, calculated from camera pixel coordinates (x_i, y_i), containing a signal, s_i.

Hillas Parameter	formula
$(length)^2$	$(\sigma_{x^2} + a^2\sigma_{y^2} + 2a\sigma_{xy})/(1 + a^2)$
$(width)^2$	$(\sigma_{y^2} + a^2\sigma_{x^2} - 2a\sigma_{xy})/(1 + a^2)$
$distance$	$\sqrt{< x >^2 + < y >^2}$
$miss$	$\mid b\sqrt{1 + a^2} \mid$
$alpha$	$\arcsin(miss/distance)$

Table 2.2: Hillas Parameters of the ellipsoid, based on the shape of a gamma ray shower on the ground (shown in units of degrees); see Figure 2.3. The Hillas Parameters are defined two pages back.

2.2 Blazar electronic emission models

Active Galactic Nuclei (AGN) are a broad class of extragalactic objects that emit in a semi-steady state (however, a high degree of variability can occur on timescales as short as minutes), where non-thermal radiation is emitted. AGNs are distinct from the Gamma Ray Bursts (GRB) that emit only once for a duration of milliseconds to several minutes, from a catastrophic event in distant galaxies (for example, a merger of two neutron stars). "An AGN consists of a super-massive black hole (10^7-10^{10} solar masses) surrounded in the inner regions by an accretion disc, and in the outer regions by a thick torus of gas and dust. In some AGN (the radio loud population of about 10%), a highly relativistic outflow of energetic particles exists approximately perpendicular to the accretion disc and torus plane (in collimated radio emitting jets), which generate non-thermal emission from radio to gamma rays. It is believed that

some of the numerous AGN classifications result from viewing these objects at various orientation angles with respect to the torus plane. For example, some are radio-loud objects of the BL Lacertae (BL Lac.) type, that have their jet pointed close to the observers line of sight", Aharonian *et al.* (2005) [4].

"The distinction between the BL Lac. type and other blazars is primarily based on their optical spectra which are characterized by weak or absent emission lines. These (BL Lac. type) AGN are characterized by a 'double hump' Spectral Energy Distribution (SED) (see Figure 2.8), where the low energy component is widely accepted as originating from synchrotron radiation of relativistic electrons in the magnetic field around the object. However, the origin of the high energy component is the subject of much debate. Various models involving either leptonic (electronic) or hadronic processes have been proposed.", [4]. " Blazars are known to be highly variable at all wavelengths, typically characterized by a low-emission quiescent states interrupted by periods of flaring behaviour where the flux increases dramatically. In some cases, this is [by] several orders of magnitude.", [4]. For a discussion on the various emission processes of blazars see this section (2.2) and Section 2.3.

Blazar electronic emission models are many and various, and tend to rely on providing a theoretical framework for observed blazar emission from radio to gamma rays. This paradigm itself is subject to considerable uncertainties because of our understanding of the cosmological Extra-Galactic Background (EBL) light is not complete and the very high energy (gamma ray) photons from these blazer sources are subject to considerable intergalactic absorption by the EBL (see Section 2.4 further in this chapter). Since the majority of theoretical publications on electronic blazar emission tend to be model specific or specific to a particular blazar source, the author has avoided using a particular one. However, we will briefly discuss a straightforward explanation of the main processes in blazar GeV-TeV gamma ray emission; Inverse Compton scattering, synchrotron emission and the process that follows this for GeV-TeV energies; Synchrotron Self-Compton (SSC) emission. Recommended electronic emission models references for blazers are; Graff *et al.* (2008) [71], Röken & Schlickeiser (2009) [149], Arbeiter, Pohl & Schlickeiser (2005) [17].

2.2.1 Inverse-Compton scattering emission

Normal Compton scattering is a knock-on interaction between a photon and an electron. For brevity, the text reference in the following sections to *electrons* will also include positrons. In Normal Compton scattering, the electron gains energy from the scattering collision and the photon loses energy; ($E_{\rm ph} = hc/\lambda$, h is the Planck constant), and hence decreases frequency and increases wavelength. The change in scattered photon wavelength (λ_s) from the incoming wavelength (λ) is; $\lambda - \lambda_s = h(1 - \cos\theta)/mc$, where the scattering angle between the electron and photon is θ, and h/mc is known as the *Compton wavelength* (0.511 MeV), Bradt (2008) [38]. Normal Compton scattering (in the observer's frame), occurs for non-relativistic electrons and is not applicable to shock accelerated particles which are relativistic in most astrophysical sources exhibiting high energy emission. The final expression to describe the (Normal) Compton scattering is, [38]

$$h\nu_s = \frac{h\nu}{1 + \frac{h\nu}{mc^2}(1 - \cos\theta)} \tag{2.6}$$

where ν and ν_s are the incident and Compton scattered frequencies respectively, θ is the scattering angle, m is the rest mass of the electron and c is the speed of light.

When the electrons have energies substantially larger than the photons, this leads to the condition of Inverse Compton (IC) scattering. In equation 2.6 (above), the frame of frame of reference condition is that "the electrons are at rest, the collision can be viewed in this rest frame and the photon energy determined. Transformation back to the observer's frame yields the frequency of the [Compton] scattered photon", [38]. For IC scattering, "the photon is backscattered in the electron's frame of reference; doing so gives the maximum possible energy to the scattered photon.", [38].

The electron in the observer's frame (S) is moving (left to right) relativistically. Figure 2.4 shows the IC scattering frames of reference. The scattered photon is in the electron's rest frame (S'). The photon in Figure 2.4 (parts (b) and (c)) undergoes a head-on (backscatter) collision with the electron. From the (normal) Compton scatter in S', the energy of the backscattered photon ($h\nu'_s$) is (see equation 2.6), [38]

$$h\nu'_s = \frac{h\nu'}{1 + \frac{2h\nu'}{mc^2}} \tag{2.7}$$

NOTE:
This figure is included on page 24
of the print copy of the thesis held in
the University of Adelaide Library.

Figure 2.4: From Bradt (2008) [38]. Head-on IC scattering frames of reference: (b) Before collision in the relativistic electron rest frame, becoming a normal Compton scattering event. "The incident photon in S', has been Doppler shifted to higher energy ($h\nu'$), because of the motion of this frame relative to an observer at S.", [38]. (c) After scattering in S' frame. "The photon having been backscattered with energy ($h{\nu_s}'$), moves to the right with slightly less energy.", [38]. (d) The scattered photon has a much higher energy ($h\nu_s \gg h{\nu_s}'$), having been transformed back into the observer's rest frame, S. Diagram (a) is not shown due to its superfluity in our case.

Meanwhile the backscattered photon undergoes a double Doppler shift, i.e. an observer in S' (Figure 2.4 (c)), and with the reverse transformation back to the S frame (Figure 2.4 (d)), [38]

$$h\nu' = \sqrt{\frac{1+\beta}{1-\beta}}\, h\nu \ (S' \text{ frame}), \quad h\nu_s = \sqrt{\frac{1+\beta}{1-\beta}}\, h\nu_s' \ (S \text{ frame}); \quad \sqrt{\frac{1+\beta}{1-\beta}} \xrightarrow[\beta\approx 1]{} 2\gamma \tag{2.8}$$

where $\beta \approx v/c$ is the speed parameter related to Doppler-shift (Section 2.2.4), γ is the Lorentz factor and in this particular case for equation 2.8 ($\gamma \gg 1$).

Given that ($2\gamma h\nu$) is the photon's incident energy in the moving frame S' (Figure 2.4 (b)), and mc^2 is the rest energy of the electron, substituting the result of equation 2.8 into equation 2.7 yields, [38]

$$h\nu_s \approx 4\gamma^2 h\nu = 4\left(\frac{U}{mc^2}\right)^2 h\nu \tag{2.9}$$

where U is the total (rest plus kinetic) energy of the electron and also where, $4\gamma h\nu \ll$

mc^2 ($\gamma \gg 1$), [38]. "In a real source, the electron will collide with many photons with various directions of travel and 'impact parameters'. Not all collisions will be head-on backscatters; many other scattering angles in S' must be accounted for.", [38]. "A proper calculation for an isotropic distribution of incident photon directions in the observer frame, yields an *average* scattered energy that is one-third of that given in equation 2.9 (above)", [38]; that is, [38]

$$h\nu_{s,\mathrm{iso}} = \frac{4}{3}\,\gamma^2 h\nu \quad \text{where, } 4\gamma h\nu \ll mc^2\ (\gamma \gg 1) \tag{2.10}$$

Finally, the rate of energy loss by the electron due to IC emission is given as, [38]

$$\left(\frac{dU}{dt}\right)_{IC} = -\frac{4}{3}\sigma_T c\beta^2\gamma^2 U_{\mathrm{ph}} = -2.66\times 10^{-20}\beta^2\gamma^2 U_{\mathrm{ph}} \tag{2.11}$$

where σ_T is the Thomson cross-section (see Section 2.2.3 for definition). In equation 2.11 above; U_{ph} is the photon energy density, where $U_{\mathrm{ph}} \equiv n_{\mathrm{ph}} h\nu_{\mathrm{av}}$, is a product of the average frequency (ν_{av}) (equation 2.10 above), and the photon density (n_{ph}).

Inverse Compton scattering can occur between ultra-relativistic electrons in the blazar jet with (thermal) infrared photons (External Inverse Compton; EIC), and also with the synchrotron emitted photons with the same population of ultra-relativistic electrons (Synchrotron Self-Compton; SSC (Section 2.2.3)), to energize the photons to X-ray and gamma ray frequencies. An explanation of the synchrotron process is in the next section.

2.2.2 Synchrotron radiation

Electronic particles (electrons and positrons) moving in a magnetic field (**B**-field) will spiral about the **B**-field lines and radiate. In the blazar case for relativistic electrons being accelerated along AGN jets; "for extremely relativistic particles, the frequency spectrum is much more complicated (than cyclotron radiation) and can extend to many times the gyration frequency. This radiation is known as *synchrotron radiation*.", Rybicki & Lightman (1979) [152].

Figure 2.5 (below) shows the helical motion of the electron as it gyrates about the

B-field. The frequency (ω_B) of gyration (or rotation) is [152],

$$\omega_B = \frac{eB}{\gamma m_e c} \tag{2.12}$$

where e is the electron charge, B is the magnetic field strength (in tesla), γ is the relativistic Lorentz factor (of a single particle), m_e is the electron's rest mass and, c is the speed of light.

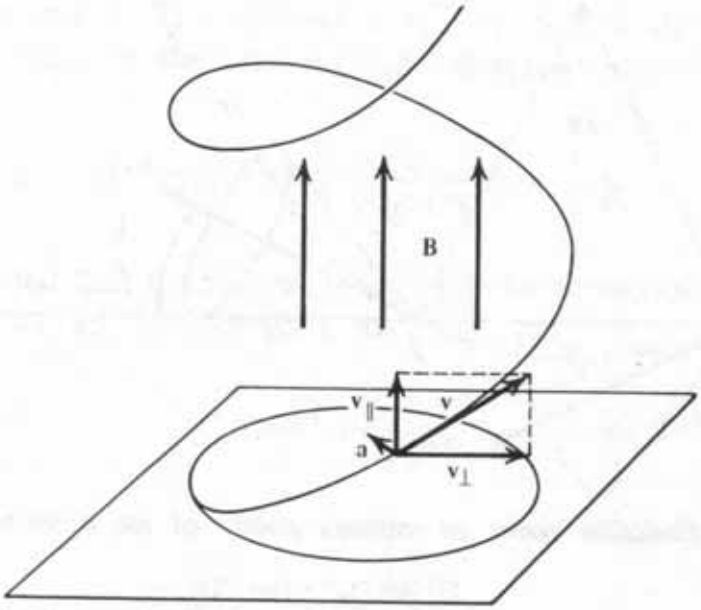

Figure 2.5: From Rybicki & Lightman (1979) [152]. Sketch showing helical gyro-rotation of a particle in an uniform **B**-field. Particle velocities and acceleration is shown.

"Because of the *beaming effect*, the emitted [synchrotron] radiation fields appears to be concentrated in a narrow set of directions about the particle's velocity (i.e. near the forward direction of the particle's propagation. The observer will see a pulse of radiation confined to a time interval much shorter than $\omega_B/2\pi$. This is an essential feature of synchrotron radiation.", [152]. Figure 2.6 shows the emission cones from various points of the accelerated particle's trajectory. From this figure, "the observer will see a pulse from points 1 and 2 (shown) along the particle's path, where these points are such that the cone of emission of angular width $\sim 1/\gamma$ includes the direction of observation.", [152].

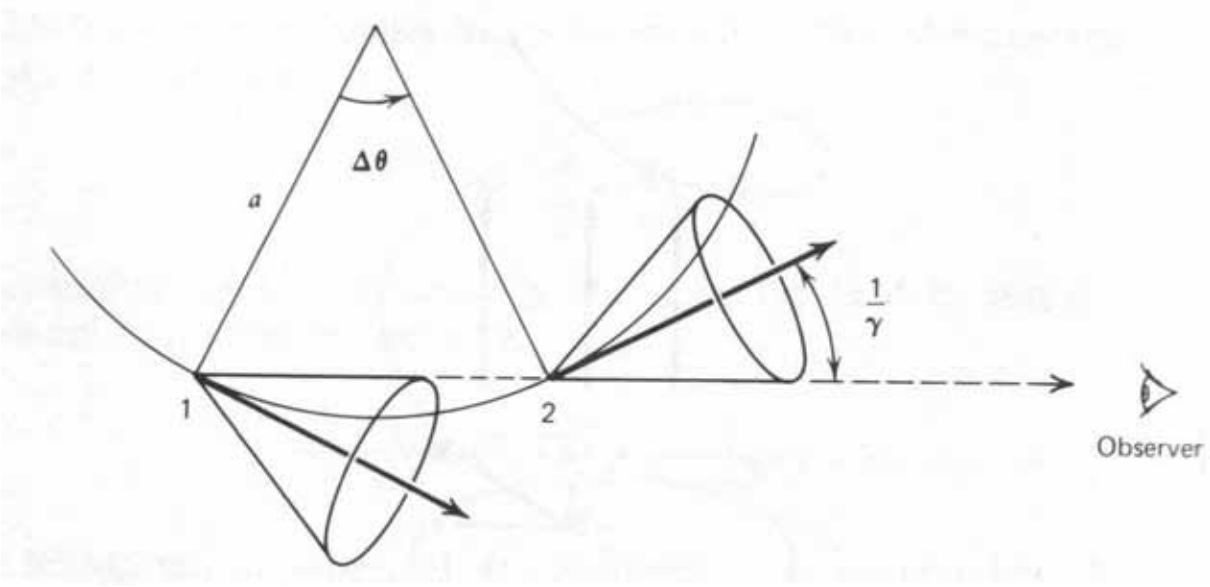

Figure 2.6: From Rybicki & Lightman (1979) [152]. Sketch showing emission cones at various points of the particles trajectory, emitting synchrotron radiation.

"The width of the observed pulses (discussed above) is smaller than the gyration period by a factor γ^3. From spectra associated with particular pulses, we would expect that the spectrum is fairly broad, cutting off at frequencies like $1/\Delta t^A$, where t^A is the *arrival times* of radiation at the point of observation from points 1 and 2 (Figure 2.6).", [152]. The critical frequency (ν_c) is given as, Longair (1997) [114]

$$\nu_c = \frac{3}{2}\gamma^2 \frac{eB}{2\pi m_e} = 4.199 \times 10^{10}\, \gamma^2 B \quad \text{Hz} \tag{2.13}$$

"then we would expect the [synchrotron] spectrum to extend to something of the order, ν_c before falling away", [152]. Applying the manifestation of the *beaming effect* (discussed above), the emission spectrum (frequency=ν) of the single electron is, [114]

$$j(\nu) = \frac{\sqrt{3} e^3 B \sin\alpha}{4\pi\epsilon_0 c m_e}\, F\left(\frac{\nu}{\nu_c}\right) \tag{2.14}$$

which becomes, [114]

$$j(\nu) = 2.344 \times 10^{-25} B \sin\alpha\, F\left(\frac{\nu}{\nu_c}\right) \quad \text{watts Hz}^{-1} \tag{2.15}$$

The function ($F(\nu/\nu_c)$) is has values shown in Table 18.1 of [114], describing the synchrotron radiation spectrum of a single ultra-relativistic electron. "The [synchrotron]

radiation spectrum of a power-law electron energy distribution ($N(E) = \kappa E^{-p}$) in the case of a random magnetic field is", [114]

$$J(\nu) = \frac{\sqrt{3}e^3 B\kappa}{4\pi\epsilon_0 c m_e}\left(\frac{3eB}{2\pi\nu {m_e}^3 c^4}\right)^{(p-1)/2} a(p) \tag{2.16}$$

and, [114]

$$a(p) = \frac{\sqrt{\pi}}{2}\frac{\Gamma\left(\frac{p}{4}+\frac{19}{12}\right)\Gamma\left(\frac{p}{4}-\frac{1}{12}\right)\Gamma\left(\frac{p}{4}+\frac{5}{4}\right)}{(p+1)\Gamma\left(\frac{p}{4}+\frac{7}{4}\right)} \tag{2.17}$$

where the Gamma function is determined by the electron momentum ($p = E/c$) and the values of $a(p)$ is given in Table 18.2 of [114]. Re-writing equation 2.16 (above) in terms of GeV energies and where the units of $N(E)$, are particles per cubic metre per GeV, [114]

$$J(\nu) = 2.344{\times}10^{-25} a(p) B^{(p+1)/2} \kappa' \left(\frac{3.217\times10^{17}}{\nu}\right)^{(p-1)/2} \text{ watts m}^{-3}\text{ Hz}^{-1} \tag{2.18}$$

‘

2.2.3 Synchrotron Self Compton (SSC) emission

"If the radiation energy density of synchrotron photons within a source region are

Figure 2.7: From Bradt (2008) [38]. Sketch showing a simplistic model of the Synchrotron Self-Compton emission process.

sufficiently intense, the photons will undergo IC scattering by the very same electrons

that emitted them in the first place. Any such scattering process will occur before the synchrotron photon will have left the source region. This [emission] is *Synchrotron Self-Compton* (SSC)", Bradt (2008) [38]. Figure 2.7 shows a simplistic model of the SSC process.

"The Inverse Compton scenario can provide an approximate rate of energy loss (dU/dt) for an electron undergoing multiple IC scattering", [38], then the rate of energy loss by the electron due to inverse Compton scattering (provided $\gamma h\nu \ll mc^2$) [38] is contained in equation 2.11 in Section 2.2.1, from where the Thomson cross section is $\sigma_{\mathrm{T}} = 6.65 \times 10^{-25}$ cm^2, Rosswog & Brüggen (2007) [150]. Inserted into equation 2.11 is $\beta = v^2/c^2$ (the electron speed factor) "to obtain a more general expression that includes the non-relativistic case", [38]. The general expression referring to "an energy loss of a single electron immersed in a sea of photons of energy density U_{ph}", [38] (after substitution of physical constants σ_{T} and c) is

$$\left(\frac{dU}{dt}\right)_{\mathrm{IC}} = -2.66 \times 10^{-20}\beta^2\gamma^2 U_{\mathrm{ph}} \tag{2.19}$$

Consider the case of volume emissivity. "If a population of relativistic electrons of density n_e (each of energy $U = \gamma mc^2$ with $\gamma \gg 1$) is immersed in a sea of photons (energy density, U_{ph}) and the photon energies are negligible compared with the IC up-scattered energies ($h\nu_{\mathrm{av}} \ll h\nu_{\mathrm{s,iso}}$) then, in this case, the rate of scattered energy emerging from a single electron approximates the electron energy loss rate (equation 2.11). The radiation emerging from unit volume is thus the negative of equation 2.11, multiplied by the electron number density (n_e)", [38], so that the spectral volume emissivity, j (Wm^{-3}) is expressed as: [38]

$$j = \frac{4}{3}\sigma_{\mathrm{T}} c\beta^2\gamma^2 n_e U_{\mathrm{ph}} \tag{2.20}$$

This is expressed as the spectral volume emissivity j, integrated over all emitted frequencies, $j = \int j_\nu d\nu$, [38]. "For a realistic system, one would also integrate over the spread of electron energies (γmc^2)", [38].

An electron in SSC emission is subject to radiative energy losses from both synchrotron and IC scattering. The rates of energy losses of both processes (synchrotron

and IC scattering) are easily compared, [38]. "One can thus state, independent of electron energy, but still with the requirement that the photon energy in the electron frame be substantially less than mc^2 ($\gamma h\nu \ll mc^2$) that", [38]

$$\frac{(dU/dt)_{\rm IC}}{(dU/dt)_{\rm synch}} = \frac{U_{\rm ph}}{U_B} \tag{2.21}$$

where the IC energy density ($U_{\rm ph}$) is explained in equation 2.19 (above) and the magnetic field energy density is, $U_B = B^2/8\pi$, [150]. "The radiative energy loss by electrons through the two processes (in equation 2.21) depends solely on the relative energy densities of the photons and magnetic fields - the target material in each case. Inverse Compton losses are important if the ratio $U_{\rm ph}/U_B$ approaches order unity (e.g. $U_{\rm ph}/U_B \gtrsim 0.1$)", [38].

The electron energy loss rate from synchrotron and IC radiation (i.e. SSC) was originally thought to be subject to the *Compton limit*, [38]. In a compact source (such as Mkn 421 because of its short timescale flaring variability, Section 8.2.2), "radiation energy densities become comparable to magnetic energy densities", where second order Compton scattering (i.e. two IC scatterings) is likely to occur before the electrons leave the nebula, [38]. "Under these conditions, if more energy is pumped into the electrons in the nebula, it will be immediately radiated away, i.e. one cannot make the nebula 'hotter'. This is known as the Compton limit (*Compton Catastrophe*) and is likely to occur when the nebula exhibits a [radio] *antenna temperature* of $\sim 10^{12}$ kelvin (antenna temperature by radio astronomers is meant to be a measured specific intensity at some frequency under the assumption of a black-body spectrum in the Rayleigh-Jeans approximation). The Compton limit became important with the discovery of rapid variation of radio flux from AGN on the timescale of hours or days. Temporal variability implies a size (D) for the emission region that is smaller than the light crossing time; $D \lesssim c\Delta t$. The associated small angular size yields a high specific intensity (energy flux per steradian-Hz) and therefore high antenna temperature.", [38]. It was inferred that some AGN sources having antenna temperatures $\sim 10^{13-14}$ K (kelvin) were well above the 10^{12} K Compton limit, [38]. However, the Compton limit dilemma was resolved when it became apparent that jets of material were being ejected from AGN, and this was subject to relativistic Doppler beaming (Section 2.2.4), [38].

Figure 2.8: From Bradt (2008) [38]. Theoretical Spectral Energy Distributions (SED) from SSC emission, for blazars across a broad frequency range showing observational wavelengths (grey shaded areas). The SED of blazars though SSC emission shows a classic "double hump". The LBL (Low energy peaked BL Lac.) blazars SED is shown as a solid line where synchrotron emission occurs in radio to optical energies and X-ray though IC emission from the same synchrotron electrons (higher energy peak). The HBL (High energy peaked BL Lac.) blazars (shown as a dotted line) are emitting synchrotron X-rays (low energy peak) and IC scattering though to GeV-TeV gamma rays (higher energy peak). The SEDs of LBL versus HBL blazars may be compounded by Doppler shift.

Additionally, the Compton limit dilemma no longer applies on its own where X-ray and gamma ray luminosities dominate the spectra of certain classes of AGN (HBL Lacertae objects for instance), [38].

For blazars, synchrotron source photons typically emit (non-thermally) from radio to optical wavelengths with a cutoff in the synchrotron spectrum above visible radiation energies (see Figure 2.8 spectrum solid line). In the case of Synchrotron-Self Compton (SSC) emission, the same relativistic electrons producing synchrotron emission in the first place, may up-scatter their synchrotron photons via IC processes to higher

energies (in X-ray). In cases where the electrons are traveling ultra-relativistically in the jet (such as in certain classes of blazars, such as High energy BL Lacertae (HBL Lac.)) sources, the synchrotron emission is in X-ray energy and the X-ray synchrotron photons are up-scattered via IC (by the same electrons responsible for the synchrotron radiation), to GeV-TeV gamma ray energies. This is shown as a dotted line in Figure 2.8 spectrum.

The SSC emission from blazars at GeV-TeV energies tends to be "highly variable and polarized", [38], where the jet beam is pointing towards the observer. Blazars have a Spectral Energy Distribution (SED), that is doubled-peaked, similar to the Crab Nebula (Figure 2.8), [38]. This figure shows a theoretical model of SSC emission in Low peaked BL Lacs. (LBL) and HBL Lacs (indicated). "In the observer's frame, the SSC photons are beamed and Doppler [blue]-shifted (boosted), the resulting SED will depend upon the exact parameters chosen (i.e. LBL or HBL Lac.). Note that the HBL Lac. blazar is radio-quiet.", [38].

There is strong correlation between X-ray flaring and GeV-TeV gamma ray flaring from HBL Lac. sources (e.g. Markarian 421 (Section 8.2.2), Holder (2001) [85], Horns, Kohnle & Aharonian (2001) [86]), indicating that the most likely emission for these class of blazars is SSC.

2.2.4 Doppler boosting

The AGN jets may be oriented towards the observer's line of sight. In this case the (IC and SSC emission processes) photons are likely to be subject to *Doppler boosting* (or Doppler blue-shifting). Conversely, as this section indicates, AGN jets that become more orthogonal to the observers line of sight (above a critical angle), emission photons are subject to Doppler de-boosting (or Doppler red-shifting).

"The beam angle θ_b is the half-angle of the cone (of beamed radiation; $v \approx c$), that includes one-half of the rays (see Figure 7.9(b), Bradt (2008) [38])", [38]. This is analogous to a headlight beam, thus from [38];

$$\cos\theta_b = \beta = \sqrt{1 - \frac{1}{\gamma^2}} \tag{2.22}$$

where γ is the Lorentz factor. For speeds close to light velocity, $\theta_b \approx 0$, thus we obtain from equation 2.22 (above) that $\theta_b \approx 1/\gamma$ ($\gamma \gg 1$), [38]. That is, "the opening half-angle of the headlight beam, according to an observer at S, is the reciprocal of the Lorentz factor for a highly relativistic source.", [38].

Figure 2.9: From Bradt (2008) [38]. Beamed radiation from a fast moving ($\gamma = 10$) source, emitting isotropically in the rest frame. The beam includes half the rays lying within the inner cone of the half-angle ($\sim 1/\gamma = 5.7°$, equation 2.22) at this Lorentz factor. The outer cone half-angle is situated at $\delta = 1$ ($\nu = \nu_0$, equation 2.23), at 25.2° representing a null Doppler shift at this location. Angles greater than this will be observed to be Doppler red-shifted.

"The observer of radiation produced from a relativistically moving source may or may not be within the beam opening angle θ_b (explained above), which can be quite narrow. The intensity of within the beam can be greatly enhanced (boosted) owing to both the beaming and Doppler shifting of the frequency.", [38]. Consider the Doppler factor (δ) by which the (emitted) frequency is Doppler shifted, [38]

$$\delta \equiv \frac{\nu_{\text{observed}}}{\nu_{\text{emitted}}} = \frac{\sqrt{1-\beta^2}}{1-\beta\cos\theta} \xrightarrow[\theta=0]{} \sqrt{\frac{1+\beta}{1-\beta}} = \frac{1+\beta}{\sqrt{1-\beta^2}} \xrightarrow[\beta\approx 1]{} 2\gamma \tag{2.23}$$

where $\beta \equiv v/c$, (the speed parameter of the frame S', as well as the radiating source measured in frame S, [38]), $\beta \approx 1$, and $\theta \approx 0$. Thus the relation in equation 2.23, where ($\delta \sim 2\gamma$), "is a useful approximation for highly relativistic jets viewed nearly head-on", [38].

Figure 2.9 (above) shows how the isotropically emitted radiation (in the rest frame, where $\gamma = 10$) in the blazar jet moving right, is highly Doppler blue-shifted through viewing a jet source from nearly head on ($< 6°$) at O_1, or lesser Doppler blue-shifted from viewing at a small inclination angle from the jet ($< 25°$), at O_2. Observers O_4, and O_5, will view strongly Doppler de-boosted (red-shifted) radiation and would fail (in this case) to see GeV-TeV gamma ray emission. Observer O_3 ,"sees a red-shifted and de-boosted signal, even though at the time of emission, the [jet] source was approaching the observer. However, all detected photons outside the 6° beam are emitted in the rearward direction in the source rest frame.", [38]. Observer O_3 would also be unlikely to see GeV-TeV gamma ray emission from a blazar jet. There is considerable evidence that the classification of blazars into LBL and HBL (Figure 2.8) is strongly dependent on Doppler boosting (de-boosting) due to jet source orientation to the viewer ("the observer is deemed to lie within the jet beam"), [38].

2.3 Blazar hadronic emission models

As with electronic modeling of blazar emission (Section 2.2), hadronic emission models also suffer from the EBL being not completely de-convolved from uncertainties in TeV observation of extragalactic sources and from incomplete satellite data to describe infrared and other low energy radiation fields permeating space. As with electronic emission processes, hadronic modeling of blazars are often source-specific. For necessity, we have provided a source-specific model; Protheroe & Mücke (2001a) [140], Protheroe & Mücke (2001b) [141].

Hadronic collision/decay processes that produce gamma rays are of interest in modeling blazar jets. Meson particles are often the result of baryonic collisions. There are several species of meson particles, whose decay pathways often lead to gamma ray emission. Proton-proton collisions occur in blazar jets. "These collisions produce π^0 mesons (rest energy 135 MeV) that immediately decay into two gamma rays, each 67.5 MeV in the π^0 rest frame.", [38]. It is conceivable that these gamma rays from π^0 decay, could be Doppler boosted to higher energies that are detectable by an IACT

array, but this would require the jets to be viewed nearly head-on and ultra-relativistic Lorentz factors of at least $\gamma \gtrsim 70$ for each particle in the observer's frame (see equation 2.23).

"In proton blazar models, the high energy [gamma ray] part of the SED (Figure 2.8), is due to the interaction of protons accelerated along with electrons in the AGN jet, on direct or scattered 'UV bump' radiation from an accretion disc, or direct synchrotron emission by protons, muons and charged pions. To accelerate protons to energies sufficiently high that they can produce the high energy part of the SED, a large magnetic field [strength] is required. Proton blazars would contain relativistic plasma of electrons and protons and a non-negligible magnetic field", Protheroe & Mücke (2001a) [140].

Assuming that the lower energy 'double spectrum hump' SED (Figure 2.8) is due to synchrotron emission from electrons (co-accelerated with protons) and the higher energy hump in the SED is mainly due to proton processes, Protheroe & Mücke (2001b) [141], have considered the "case where the maximum energy of the accelerated protons is above the threshold for pion photo-production interactions on the synchrotron photons of the low energy part of the SED."

Protheroe & Mücke (2001b) [141], have used the proton blazar model to simulate the Markarian 501 (a HBL Lac. object) flare from April 1997 (12 hour variability time-scale). The parameters used for this modeling are; $D = 12$ (Doppler factor; $[\Gamma(1-\beta\cos\theta)]^{-1}$, [140]), $B \approx 20$ gauss, $R_{\rm blob} = 8 \times 10^{15}$ cm (the radius of the emission region), giving a (target) photon energy density of this radiation field as $U_{\rm target} = 60$ GeV/cm^3. The relevant radiation loss time scales were taken into account; photo-meson production, Bethe-Heitler pair-production, proton synchrotron emission and adiabatic losses due to jet expansion, [141].

Monte-Carlo algorithms were applied ([141]) to simulate particle production and cascade development of the aforementioned processes; this allows us to use exact cross sections, [141]. Figure 2.10 shows the results of these simulations applied to Markarian 501: "We find that the emerging cascade spectra initiated from gamma rays from π^0 decay (and also by electrons-positrons from $\mu^{\pm}$ decay), turn out to be relatively

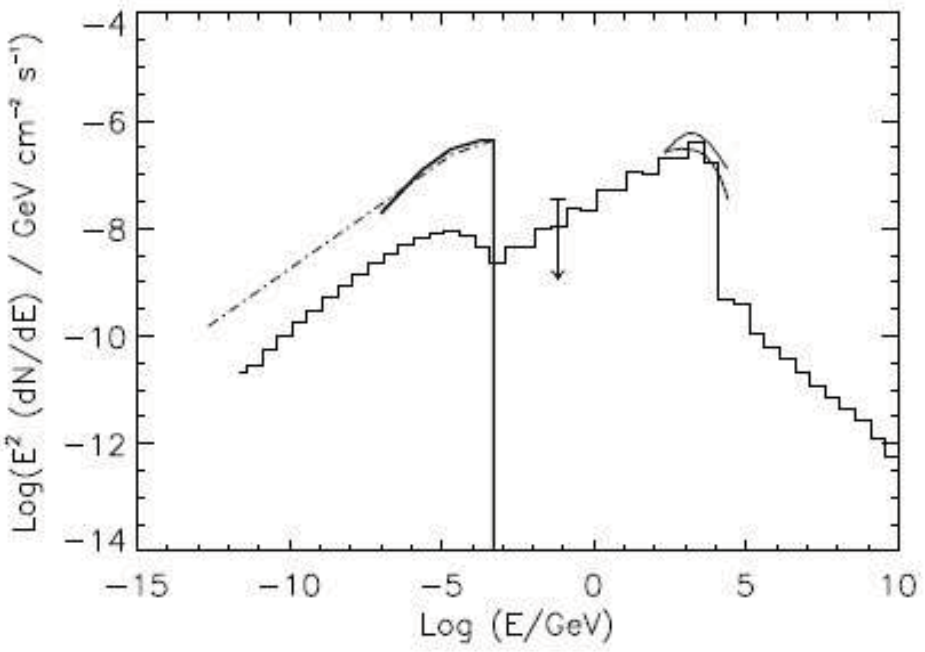

Figure 2.10: From Protheroe & Mücke (2001b) [141]. Showing best-fit model in comparison to the flaring data from Markarian 501 in 1997 from Catanese *et al.* (1997) [43]. Dot-dashed line is the input target spectrum (Mücke & Protheroe (2001) [125]). Straight-solid lines: Parameterization from the synchrotron spectrum observations (from Beppo-Sax & Oriented Scintillation Spectrometer Experiment on the CGRO), and TeV emission corrected for EBL on two different infrared models (Bednarek & Protheroe (1997) [28]). The 100 MeV upper limit shown is from [43].

featureless. Synchrotron radiation produced by $\mu^{\pm}$ from $\pi^{\pm}$ decay, and even more importantly by protons and subsequent synchrotron-pair cascading, is able to reproduce well the high energy part of the SED. For this fit (Figure 2.10), we find that synchrotron radiation by protons dominates the TeV emission. Pion photo-production is important, with the consequence that we predict a significantly lower neutrino flux than in other proton blazar models.", [141].

A comprehensive study of the hadronic emission processes in blazar jets is beyond the scope of this thesis.

2.4 Extragalactic Background Light (EBL) absorption

The Extragalactic Background Light (EBL), extends over a large range of the non-ionizing electromagnetic spectrum (except for ultraviolet, UV), from diffuse ultraviolet starlight to the far infrared (IR). The Cosmological Microwave Background (CMB), which is the red-shifted remnant of the Big Bang, is traditionally not counted as part of the EBL, Hauser & Dwek (2001) [76]. A large proportion of the EBL in flux is the Cosmic infrared Background (CIB). The CIB, is responsible for attenuation of gamma rays principally above 10 GeV energies, as they propagate from the source to the Earth. A primary gamma ray photon scatters with a CIB soft photon to produce a positron-electron pair, e^+e^-. The electronic particles, in turn, Inverse Compton (IC) scatter with the CIB photons to re-emit gamma rays at a similar energy to the original gamma ray primary and so on, resulting in radiative losses from the e^+e^-, especially if substantial **B**-fields are present. The electron-positron pair production equation can be expressed as

$$\gamma_{\rm TeV} + \gamma_{\rm IR} \rightarrow e^+ + e^- \tag{2.24}$$

During this process over distances of more than a few mega-parsecs, such as for the sources studied in this thesis, the flux of the primary gamma rays emitted from the source is attenuated by CIB interactions. The attenuation of the primary gamma ray flux increases with increasing redshift of the source, z.

The CIB as seen from Earth is a mixture of local fields, i.e. the solar system zodiacal light, galactic cirrus of the Milky Way, and extragalactic fields produced principally by galactic clusters and super-clusters which may extend as far back as the earliest formation epoch of galaxies in the universe, Kashlinsky (2005) [93]. It is this mixture of the CIB which makes it so difficult to resolve contributing parts from one another. The CIB spectrum is postulated therefore, principally via a combination a direct satellite measurements and CIB model dependencies; [93], in Salamon and Stecker (1998) [153], in Primack (2001) [139], in Dwek and Krennrich (2005) [54], in Schroedter (2005) [155], in Kneiske (2002) [96], and Kneiske *et al.* (2004) [97]. Furthermore, in modeling the

CIB for the early epoch of the Universe in early galaxy formation is affected strongly by the uncertainties in cosmological constants at very large cosmological distances, such as the Hubble constant (H_0). Another constraint in directly measuring the CIB in the range suitable for Imaging Atmospheric Čerenkov telescopes is uncertainty in the GeV-TeV gamma ray measurements themselves (e.g. through the observation of extragalactic objects such as such as HBL Lacs., [155], [54]) from ground based gamma-ray observatories such as CANGAROO.

Previously it was considered by many authors such as Schroedter (2005) [155], that the local Milky Way IR field hardly contributes to the attenuation of gamma rays arriving from intergalactic sources, let alone TeV sources within the Milky Way. However modeling by Moskalenko, Porter and Strong (2005) [124], indicates that for gamma rays above 10 TeV, the Milky Way IR field attenuation of these primary photons is at least 10%. This has important implications for the spectrum of TeV gamma ray blazar sources which are located a few degrees above and below the Galactic Plane.

The flux of the CIB spectrum has been measured by satellites such as *COBE*, Boggess *et al.* (1992) [34], with the *DIRBE* experiment, Hauser *et al.* (1998) [77], and by direct measurement by ground observatories at wavelengths where atmospheric opacity does not interfere, and estimated by cosmological modeling such as galaxy formation and morphology in the universe. All of the CIB spectrum does not concern us here, but only the CIB which effects GeV to TeV primary photons.

2.4.1 TeV gamma ray attenuation due to pair production

A TeV photon collides inelastically with a soft CIB photon though pair production previously discussed. Pair production is the most likely type of inelastic collision in intergalactic space as the photon density is much higher than the matter density. For pair production to occur, the total energy available must be greater than $2m_e$ ($\sim$ 1MeV). For gamma rays between the energies of 100 GeV to 20 TeV, the scattering target soft CIB photon must be in the range from 10 eV to 0.05 eV, [155]. The cross section of the Pair Production is as follows (from Jauch & Rohrlich (1955) [91], and

[54])

$$\sigma_{\gamma\gamma}(E_\gamma, \epsilon, \mu) = \frac{3\sigma_T}{16}(1-\beta^2)\left[2\beta(\beta^2-2) + (3-\beta^4)\ln\left(\frac{1+\beta}{1-\beta}\right)\right] \tag{2.25}$$

where $\beta \equiv \sqrt{1-\frac{\epsilon_{\rm th}}{\epsilon}}$ (ϵ is the EBL photon energy) and the Thomson Cross Section is $\sigma_T = 6.65 \times 10^{-25}\,{\rm cm}^2$. The threshold energy, $\epsilon_{\rm th}$ of the interaction is

$$\epsilon_{\rm th}(E_\gamma, \mu) = \frac{2(m_e c^2)^2}{E_\gamma(1-\mu)} \tag{2.26}$$

and $\mu \equiv \cos\theta$, where θ is the angle between the incident photons. The γ-γ cross section for an interaction with an anisotropic distribution of background photons has a peak value of $1.70 \times 10^{-25}\,{\rm cm}^2$ for $\beta = 0.70$, which corresponds to energies for which the product; $E_\gamma \epsilon \approx 4(m_e c^2)^2 \approx 1$ MeV^2, or $\lambda_\epsilon(\mu{\rm m}) \approx 1.24 E_\gamma$ (TeV), where λ_ϵ is the wavelength of the CIB photon, [54].

The optical depth traversed by a photon at energy, E_γ that was emitted from the source at redshift, z is given by

$$\tau_\gamma(E_\gamma, z) = \int_0^z \left(\frac{dl}{dz'}\right) dz' \int_{-1}^{+1} d\mu \frac{1-\mu}{2} \int_{\epsilon'_{\rm th}}^{\infty} d\epsilon' n_\epsilon(\epsilon', z') \sigma_{\gamma\gamma}(E'_\gamma, \epsilon', \mu) \tag{2.27}$$

where $n_\epsilon(\epsilon', z')d\epsilon'$ is the co-moving number density of the EBL photons with energies between ϵ' and $\epsilon' + d\epsilon'$ at redshift z' and $\epsilon'_{\rm th} = \epsilon_{\rm th}(E'_\gamma, \mu)$, $E'_\gamma = E_\gamma(1+z')$, and where dl/dz is given by, e.g. Peacock (1999) [137]

$$\left(\frac{dl}{dz'}\right) = c\left(\frac{dt}{dz}\right) = \frac{R_H}{(1+z)E(z)} \tag{2.28}$$

$$\text{where, } E(z) \equiv \left\{(1+z)^2(\Omega_m z + 1) + z(2+z)[(1+z)^2\Omega_r - \Omega_\Lambda]\right\}^{1/2} \tag{2.29}$$

Here Ω_m and Ω_r are the cosmological constants for matter and radiation energy density respectively, normalized to the critical density; $\Omega_\Lambda = \Lambda/3H_0$, which is the dimensionless cosmological constant ($\Omega_m + \Omega_r + \Omega_\Lambda = 1$ in a flat universe). The Hubble radius is $R_H \equiv c/H_0$, [54].

2.4.2 Extragalactic background light prediction models

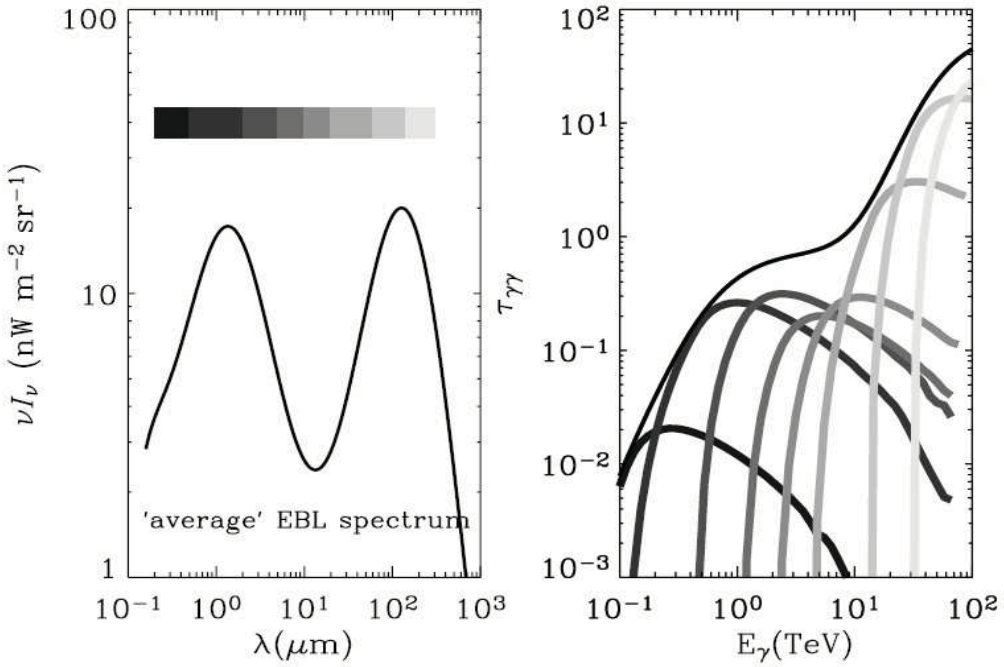

Figure 2.11: The *Left* figure is the "average" EBL spectrum as shown by Dwek & Krennrich (2005) [54], and where the shaded bar at the top indicates the different wavelength regions depicted in the *Right* panel figure. The *Right* figure is the γ-ray opacity (equation 2.27), located at redshift $z = 0.03$, shown as a thin black line. The shaded curves under this thin line represent the contributions to the different wavelength regions (depicted in the *Left* panel), to the total opacity, [54].

Figure 2.11 *right*, taken from Figure 3 of [54], compares the TeV opacity of a source located at redshift $z = 0.03$, i.e. approximately the distance of Markarian 421 (Mkn 421) and Markarian 501 blazars, to background photons with an EBL spectrum given by the average spectrum depicted in the *left* panel of Figure 2.11. This figure indicates the relationship between the rate of increase of TeV absorption opacity (equation 2.27) with gamma-ray energy and the spectral behaviour of the EBL at this particular redshift. The flattening in the centre of Figure 2.11 *right*, shows the rise in opacity between gamma-ray energies of $\sim$1 to 5 TeV, resulting from the dip in the EBL intensity between the stellar and dust emission peaks, clearly visible in Figure 2.12.

Figure 2.12 is taken from Figure 2 of Dwek & Krennrich (2005) [54]. This figure shows the different realizations of the EBL, with a series of different data points ob-

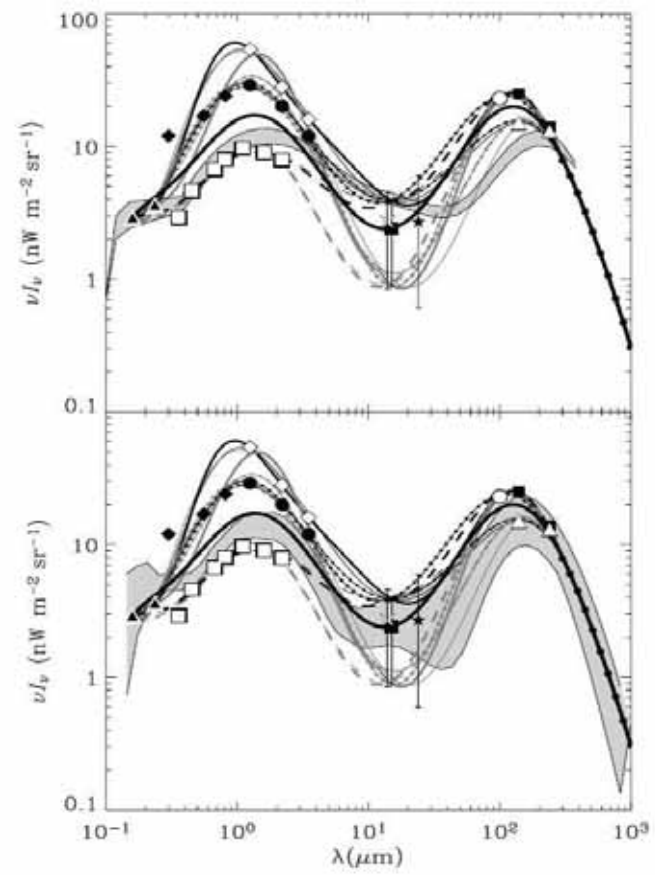

Figure 2.12: Template spectra representing different realizations of the EBL, from Fig. 2 of Dwek & Krennrich (2005) [54], where the realization templates are also discussed. This figure shows data points from a large number of authors showing theoretical EBL modeling and from experimental results (see Dwek & Krennrich (2005) [54], to ascertain data reference).

tained mainly through modeling of the EBL via different authors, used in the derivation of the fits (see [54] for details in Figure 2.12). The two EBL spectra representations shown in Figure 2.12 are identical, except that the shaded area in the *top* panel is bounded by two EBL model spectra presented in de Jager & Stecker (2002) [53], and the shaded area in the *bottom* panel represents a range of EBL intensities presented by Kneiske (2004) [97]. These models; [53], [99], [97], do not reproduce the high EBL intensities at UV to mid-IR wavelengths, a common problem in all EBL models.

Extragalactic EBL modeling is based on two processes; forward and backward evolution. Forward evolution relies on estimating the metallicity of stars at large redshift

and integrating through to redshift zero, i.e. the local cluster group. Although forward evolution models work well for the visible spectrum, the forward evolution data extrapolated to far infrared, does not fit particularly well the far infrared peak, thought to be caused mainly by thermal re-emission of starlight due to dust.

Backward evolution models consider the spectral characteristics of the EBL in the local extragalactic field and extrapolate it to high redshift through cosmological modeling. Although more recently backward evolution models have shown more success in modeling the extragalactic EBL, such as in Dwek & Krennrich (2005) [54], discussed here at length, and in deJaeger & Stecker (2002) [53], Konopelko *et al.* (2003) [99], and Kneiske (2002) & (2004) [96], [97], the weakness of backwards evolution is that galactic morphology (including the stars in them), is likely to change with redshift, compared to the local group which we are normalizing by. Here, we are chiefly concerned with the empirical effects in gamma-ray attenuation for blazars. While cosmological evolution modeling can assist us, its uncertainties remain significant while infrared data at $z > 0.001$ distances are not wholly de-convolved.

More recent work by Aharonian *et al.* (2006) [3], used the results of gamma ray emission, observed by HESS, from blazars at large (cosmological) distances; H 2356-309 (redshift, $z = 0.165$) and 1ES 1101-232 ($z = 0.186$) to empirically model the extragalactic background light at optical/near-infrared wavelengths. An upper limit was placed on the extragalactic background light from this work that appears close to the lower limit given by the integrated light of resolved galaxies, [3]. The background flux at these wavelengths has indicated that the EBL is dominated by direct starlight from galaxies, excluding contribution from other sources (such as first stars formed), and indicates that intergalactic space may be more transparent to gamma rays than previously thought, [3].

2.4.3 The effect of the EBL on the spectrum of Markarian 421

The emission modeling features of the HBL Lac. type blazar has been discussed in detail in Sections 2.2 and 2.3, previously. We will examine the spectrum of Mkn 421 in the TeV range, where absorption of the TeV Mkn 421 spectra from EBL has been

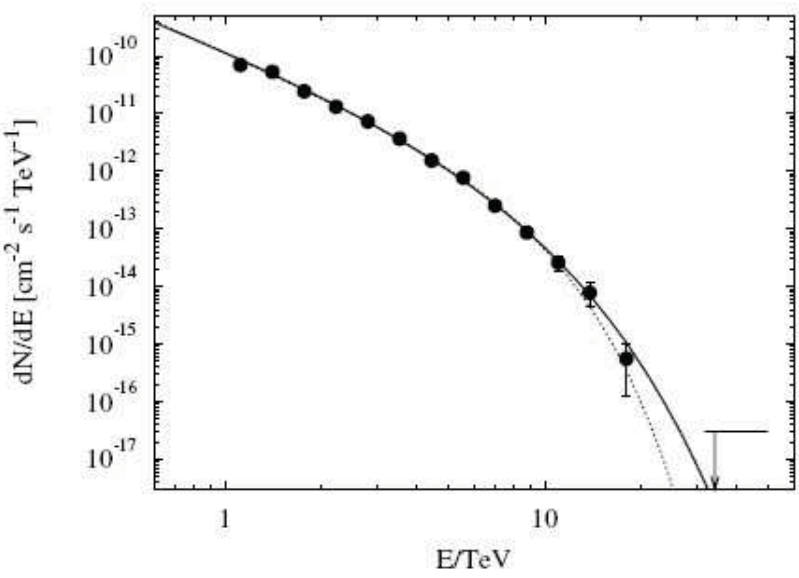

Figure 2.13: From Figure 1 of Aharonian *et al.* (2005), [5]. Differential energy spectrum of Mkn 421 taken by HESS in April-May 2004. The curve can be described by a power law, $\Gamma = 2.1 \pm 0.1_{\rm stat} \pm 0.3_{\rm sys}$, with an exponential cutoff at, $E_{\rm c} = 3.1(+0.5 - 0,4)_{\rm stat} \pm 0.9_{\rm sys}$ TeV shown by the solid line, or alternatively by a "super exponential" cutoff ($\exp(-(E/E_{\rm c})^{1.6\pm0.3})$, at $E_{\rm c} = (6.25 \pm 0.4_{\rm stat} \pm 0.9_{\rm sys})$ TeV (dashed line). The lower right hand line shows an upper limit at 30-50 TeV with 99% confidence level.

extensively modeled.

The intrinsic photon spectrum, $(dN/dE)_i$ of a blazer located at redshift, z, can be expressed as, [54];

$$\left(\frac{dN}{dE}\right)_i = \exp\left[\tau_{\alpha\alpha}(E,z)\right]\left(\frac{dN}{dE}\right)_{\rm obs}, \tag{2.30}$$

where the observed spectrum, $(dN/dE)_{\rm obs}$, can be fitted with a function, $f_{\rm obs}$ consisting of a power law with an exponential cutoff of the form

$$f_{\rm obs} = \Phi E^{-\alpha}\exp[-E/E_c]. \tag{2.31}$$

for energies, E above the cutoff energy, E_c and where the power law spectrum index of source is, α. The exponential cutoff is most likely showing the effect of increasing EBL absorption on the spectrum of Mkn 421 above the exponential cutoff energy, E_c, threshold at the distance of Mkn 421.

Figure 2.14: Differential energy spectrum of Mkn 421 from MAGIC, Fig. 10 of Albert *et al.* (2006) [12]. The observed (grey points) of the spectrum, and de-absorbed (black) points are multiplied by E^2. Solid line shows power law fit, and dot-dashed line the curved power law fit both to the intrinsic spectrum (without absorption), the results shown in inlays to this figure. Dotted line shows absorbed (observed) power law with cutoff.

The Mkn 421 spectra as seen by IACTs is shown by recent results from stereo observation from a high zenith angle of Mkn 421 in April 2004 by the HESS system of four 13m IACTs in the Khomas Highland, (23°16′S, 16°30′E) of Namibia (see Figure 2.13, Aharonian *et al.* (2005) [5]). These results were taken above 1 TeV (due to the high zenith angle) in which a total of 14.7 hours good observation data were selected for analysis, with over 100σ gamma ray signal significance over background. The Mkn 421 spectrum (Figure 2.13) clearly shows an exponential cutoff, E_c (see equation 2.31 above), [54]), at $E_c = 3.1(+0.5 - 0.4)_{\rm stat} \pm 0.9_{\rm sys}$ TeV. Similar cutoff threshold energies are reported for other IACT groups; HEGRA, Aharonian *et al.* (2002) [8], Whipple, Krennrich *et al.* (2002) [102].

Additionally, TeV spectra at lower energies than HESS have been measured with smaller zenith angle observations of Mkn 421 in April 2005 from the single MAGIC 18m IACT dish at La Palma in the Canary Islands, ($28^o45'$N, $17^o54'$W) shown in Figure

2.14, Albert *et al.* (2006) [12]. Unlike HESS, the observed spectra of Mkn 421 with MAGIC does not extend to high enough energies to infer a high energy exponential cutoff threshold.

Dwek and Krennrich (2005), [54], calculated the $\gamma\gamma$ opacity towards Mkn 421, deriving both intrinsic gamma ray spectra and spectra after EBL absorption. Similar work was done by Kneiske *et. al* (2004) [97], Konopelko *et al.* (2003) [99], and deJaeger & Stecker (2002) [53].

From data and modeling of the EBL by Dwek and Krennrich (2005) [54], Kneiske *et al.* (2004) [97], and other authors in the field of EBL research, quantified the effects of EBL on TeV blazars at redshift up to z $\approx$ 0.3. The EBL still remains uncertain, however, this EBL uncertainty limitation is a combination of large wavelength gaps between different IR satellite experiments and the implicit uncertainty in their IR data. Uncertainties in cosmological modeling of earlier epochs compounded by a mixture of IR fields at different distances, adds to the uncertainties in the EBL. Most importantly for TeV gamma rays, the high uncertainties (up to $\sim$10%) in the gamma-ray energies measured by the IACT technique makes it difficult to tightly constrain and select for few EBL models to the observed TeV data points. Considerable reduction in the uncertainties of measuring TeV blazars (such as Mkn 421), will have to be reached before the observed TeV spectrum of these sources can be used to quantify the CIB between $\sim$0.12 μm to $\sim$66 μm (IR target photons for pair production in the approximate IACT operating range). Conversely, accurate measurement of the CIB spectrum in this range will be needed to be carried out by future satellite experiments in order to tightly constrain the effects of EBL absorption upon the gamma-ray emission spectra of TeV blazars, at a range of redshifts.

For (BL Lacertae) blazar SED (Spectral Energy Distribution) modeling in particular; "Parameterizations of the EBL are poorly constrained leading to models with dramatically different behaviours, adding another significant uncertainty when using VHE (Very High Energy, i.e. GeV-TeV) upper limits to help model blazar emission. Due to [their] extreme variability, it has been shown that fitting the SED of of blazars has very large uncertainties when non-simultaneous multi-wavelength data are used.",

Aharonian *et al.* (2005) [4].

Chapter 3

The CANGAROO Imaging Atmospheric Čerenkov Telescopes

3.1 The CANGAROO-II 10 metre Imaging Atmospheric Čerenkov Telescope

This chapter describes the CANGAROO-II and CANGAROO-III Imaging Atmospheric Čerenkov Telescopes in some detail. Kawachi *et al.* (2001) [94], Ohishi *et al.* (2003) [129] describe the optical reflector of CANGAROO-II and CANGAROO-III and a report by Ohishi *et al.* (2003) [130] describes a CCD monitored optics alignment test for CANGAROO-III. Kabuki *et al.* (2003) [92] describe the CANGAROO-III camera design and operational parameters. Kubo *et al.* (2003) [104], and Kubo *et al.* (2001), [105], describes the electronic data acquisition systems of CANGAROO II and III.

3.1.1 The CANGAROO-II dish and mirrors

The CANGAROO-II 10 metre Imaging Atmospheric Čerenkov Telescope (IACT, referred to as T1) is located in South Australia 13 km NNW of the Woomera township in the G-Range area of the Woomera Rocket Range (136°47′ E 31°06′ S), on a low desert plateau 160 metres Above Sea Level (ASL). Its primary 10 metre parabolic reflector consists of 114 individual 80 cm diameter circular mirrors set close together, covering

56% of the area of the 10 metre dish, after excluding non-reflective gaps between the mirrors. Figure 3.1 (below), shows the T1 telescope and dish.

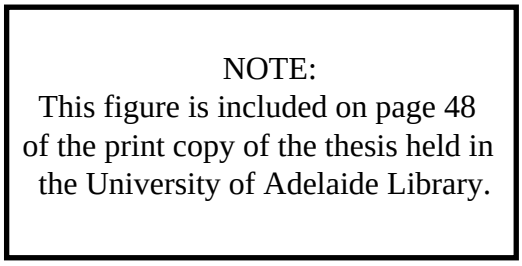

Figure 3.1: Photograph of the CANGAROO-II IACT, 10 metre diameter T1 telescope, from Mori (2000) [120]. The camera access tower in front of T1 is approximately 9 metres high. The hut at the ground level is the electronics, T1 data acquisition control, and telescope array control (observer's) hut.

The four camera struts shown in this picture support the ∼1 metre diameter camera cylinder out at the focal distance of 8.0 metres from the dish centre. The field of view of CANGAROO-II is 3 degrees. There are six mirror clusters, each sitting on a heavy steel plate section, see Figure 3.2 where the mirror numbers are also shown. The steel plates act as a counterweight to the camera. The 10 metre dish sits on an alt-azimuth mounting with the counterweights on the dish set for precision balance of the whole dish assembly on the mounts. The dish has a fast slew rate of about 0.5 degrees per second. Star rotation through the field of view whilst tracking has been tested to determine the precision of the tracking centre. This has been designated as being "better than 1 arc-minute", [94]. However, tests by the HEGRA collaboration on their IAC telescopes with Sevilla *et al.* (2003) [156], indicate that mast bending due to the torque-weight

of the camera at high zenith angles may make a significant contribution to systematic errors in the precision of the camera centre tracking. In a test of this type, applied to the CANGAROO telescopes, Kawachi (2001) [94] and work by Ohishi *et al.* (2003) [130], report that the gravitational distortion of the CANGAROO-II dish of various star images via CCD camera imaging is within 0.01°, well within optical specifications.

Figure 3.2: A diagram of the CANGAROO-III telescope mirror array, from Gunji (2006) [73]. There are six equally sized steel plate radial sections which each hold 19×80 cm, diameter mirrors. The black numbering of each 114 mirrors is indicated, as seen by the camera's point-of-view. The red numbering, e.g. D1, is a radially positioned mirror clustering indicator, and is extraneous.

Each 80 cm diameter component parabolic (secondary) mirror, consists of a laminar carbon fibre polymer silvered by an aluminium coating. The mean focal length of these 114 mirrors is 16.4 metres, [94]. The 80 cm mirrors have focal lengths, which are set according to the radial distance that the mirror is positioned on the 10 metre dish, so that the 114 component mirror surface of the 10 metre dish has its focus at the front plane of the camera cylinder. Despite a higher unit price, the carbon fibre polymer was

chosen over glass to reduce weight to the dish, and hence optical geometry inaccuracies caused by slumping of the dish, and in stresses caused by strong wind loading to the dish. Rough pointing adjustment of each individual mirror pointing was carried out in Japan before assembly of the T1 dish on the G-range site. At G-range, fine adjustment of the T1 mirrors were carried out using a bright artificial light source, 6.5 km distant from the telescope on a 30 metre high air traffic control tower at the Woomera airport. This illuminated the centre of the field of view (FoV) of the dish at the rest or park position.

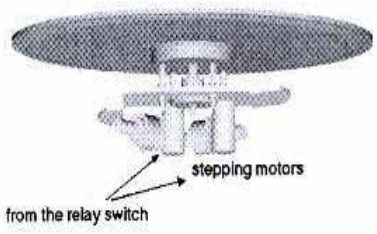

Figure 3.3: A sketch of the CANGAROO-II individual 80 cm mirror stepper motor adjustment, from Kawachi *et al.* (2001) [94].

The FWHM (Full Width at Half Maximum) is an expression of "the extent of a function given by the difference between two extreme values of the independent variable (on the abscissa), in which the dependent variable (on the ordinate), is equal to half of its maximum value. Clearly, for a Gaussian point spread function with a standard deviation of σ", Bevington (1992) [32],

$$\mathrm{FWHM} = 2\sqrt{2\ln(2)}\,\sigma \approx 2.354\,\sigma \tag{3.1}$$

From measurements after tuning, the point spread function of a bright star was found to be 0.21° FWHM through the optical axis at the focal plane by Ohishi *et al.* [129]. Optical precision of this type of system is affected by optical aberration of the overall primary dish reflector or of the 80 cm mirror parts. Optical aberration of the 80 cm mirror is possibly attributed to errors in the casting shape of the mirror or to evolving distortions in the polymer material, for example, due to gradual tightening or relaxation of the polymer bonds long after casting. With the large dish reflector,

optical aberration is a feature of the point spread function of the combined mirrors, the degree of which is due to the alignment of some of the 80 cm mirrors using the stepper motor shown in Figure 3.3, or to missing mirrors (a few which may have fallen off the dish). It is likely that the degree of optical aberration for any 80 cm mirror is much less than that of the misalignment of mirrors of the primary reflector, contributing to the point spread function. With atmospheric Čerenkov showers, the degree of optical precision achieved is sufficient for imaging of gamma ray EAS, with good combined individual mirror alignments, and the imaging inaccuracies of the T1 and T2 mirrors are at a higher resolution than the pixelated camera resolution.

3.1.2 The CANGAROO-II camera

Figure 3.4: The *Hamamatsu* R4124 spectral efficiency characteristics, from Hamamatsu (1998) [74], showing both quantum efficiency and cathode radiant sensitivity curves. The cathode radiant sensitivity is defined as the ratio of the cathode current, I_k, (less the dark current) to the incident photon flux, Φ, i.e. $S_k(A/W) = \frac{I_k(A)}{\Phi_e}$, where I_k is in milliamperes (mA), and Φ_e is in Watts", Flyckt & Marmonier (2002) [61]. The cathode radiant sensitivity is expressed in radiometric units; mA per Watt.

Figure 3.5: Sketch of the dimensional outline of the R4124 PMT (*left*) in millimetres, from Hamamatsu (1998) [74], and the positions of the cathode, anode and 10 dynodes pins in the socket, where **K** shown in the *middle* diagram is the cathode, **P** is the anode, **DY1** and **DY10** is the first and tenth dynodes respectively, and **IC** is the internal circuit. These PMT elements map to the *right* diagram positions, showing the 13 pins of each element and the short pin in the E678-13A socket of the R4124 PMT. The short pin, which is used to guide the PMT into the socket insertion, is shown in the *right* diagram as; ⊙

The CANGAROO-II telescope camera consists of sockets for up to 576 $\frac{1}{2}$ inch ($\sim$ 12.7 mm) photomultiplier tubes (PMT), type *Hamamatsu* R4124 UV, in a square array as shown in Figure 3.6, and Figure 3.7. A photomultiplier tube converts visible or near ultraviolet light into an electrical signal using the photoelectric effect from the photocathode (usually a photo-emissive semiconductor) at the front end of the tube, where the light photons pass through a glass window and then hit the photocathode. The special glass window usually has spectral sensitivity transmission characteristics, such as shown in Figure 3.4, for the *Hamamatsu* R4124 PMT. "The electrons released from the photocathode are initially focused via an electron-optical input system which accelerates and focuses the electron flux, then the electrons go through a series of cascade amplifications via a series of electron multiplier electrode plates known as dynodes, using similar photo-emissive semiconductor materials as the photocathode. At the back end of the tube, or at the end of the dynode chain, an anode grid collects the electrons from the last dynode", Flyckt & Marmonier (2002) [61]. A photomultiplier

tube is able to amplify the signal produced by incident light by a gain factor as much as 10^8 ([61]), where single photons can be resolved. Additionally, fast response PMTs have short time spreads in the order of 0.2 ns (nanosecond) FWHM. Hence, the PMT is useful in detecting the Čerenkov radiation from a EAS shower front which arrives at the telescope in the order of 10 to 50 nanoseconds duration.

The head-on 1/2 inch *Hamamatsu* R4124 UV phototube, used in the CANGAROO-II camera, consists of 10 linear focused dynodes, and a bialkali photocathode with a borosilicate glass window, shown in Figure 3.5. The wavelength of peak quantum efficiency of this tube is 420 nanometres and the quantum efficiency at this wavelength is 25%, see Figure 3.4. The PMT quantum efficiency (expressed as a percentage) is; the ratio of the number of emitted electrons to the number of incident photons, [61]. Typical gains for the *Hamamatsu* R4124 UV tube are 1.1x10^6. This tube was selected particularly for the fast pulse rise time at the anode (1.1 ns).

For photomultiplier tubes, the PMT gain is mainly a feature of the electron multipliers (or dynodes) and the applied voltage, and can be expressed as, [61]

$$M = \prod_{i=1}^{N} g_i \tag{3.2}$$

The total photomultiplier gain, M, is the product of the gain, g_i of an individual dynode, i, with a total number of dynode stages, N. The individual dynode gain, g_i, can be expressed as, [61]

$$g_i = \delta_i \, n_i \tag{3.3}$$

where the "individual dynode gain is the product of the secondary emission coefficient, δ_i of dynode i, and the collection efficiency, n_i, of the inter-dynode space that immediately follows it", [61]. The secondary emission coefficient is explained in Section 3.2.3. "The collection efficiency is the ratio between the number of electrons reaching the useful area of the first dynode and the total number of electrons emitted by the cathode, it varies with wavelength, but it is usually higher than 80%", [61]. The secondary emission coefficient, δ_i of dynode, i, and the collection efficiency (n_{i-1}) of the space that precedes it, are both increasing functions of the voltage V_i, between dynodes d_i and d_{i-1} (the rate of increase being faster for δ_i than for n_{i-1}). The product of n_{i-1}

and δ_i varies as the power of the applied voltage V_i (or through the High Voltage (HV) amplitude supplied to the PMT) as

$$n_{i-1}\ \delta_i = k_i\ V_i^{\alpha} \tag{3.4}$$

where k_i, is a constant and the exponent α, is usually between 0.65 and 0.75", [61]. Thus PMT gain directly increases with the applied HV level.

The CANGAROO-II camera consists of 36 "boxes" in a 6x6 configuration, see Figure 3.7. Each "box" is a square array of 4x4 (total 16) *Hamamatsu* R4124 UV PMTs. Each PMT in the camera sees 0.13 degrees of the field of view. As it is practicable to half fill the corner boxes, there are a total of 552 PMTs. In front of the PMT array are Winston cone type light gatherers (Figure 3.6), see Section 3.2.4. This improves the photon gathering capability of each PMT, over PMTs without a light cone, thus lowering the energy threshold of the telescope. The weight of the camera cylinder with PMTs, light guides and accompanying cables, sockets and racks is about 100 kg.

High voltage cables for the PMTs are supplied to each box and the voltage supply is common for the 16 PMTs in any box. The signals from the PMTs are transferred to an electronics rack in the control hut, via 36 twisted pair cables, carried on the exterior of the camera struts, along with the HV cables. There are some concerns that the twisted pair cables may induce crosstalk effects (see Section 3.2.5).

Calibrations taken during source observations to determine flat fielding are carried out using a semi-transparent diffuser in front of a plastic ultra-bright blue Light Emitting Diode (LED), (*Nichia* NSPB 510S, peak emission $\lambda\sim$470 nanometres) located in the centre of the dish. Between PMTs of the exact same type, gain does vary by a few percent. Flat fielding is the process whereby the varying gains in individual PMTs of the camera are normalized by a signal input of the same amplitude across the camera, in this case using a LED calibrator. Two different LED input voltages (hence two light output intensities) are manually switched to determine the gain immediately prior to shower data acquisition, then again after shower data acquisition is complete. These two LED calibration runs are denoted 0 Decibel (dB) and 1 dB and are fitted to a

Figure 3.6: A photograph of the front end of the CANGAROO-II camera, receiving light from the primary mirror, from Mori (2000) [121]. There are spaces for 576 $\frac{1}{2}$ inch PMTs, behind the Winston cone light guides shown. See Section 3.2.4 for a discussion on Winston cones.

calibration curve for each PMT to determine the gain of each PMT, during the raw to "format10" (or calibrated) data conversion using the *FULL* offline analysis software, originally developed by R. Enomoto, University of Tokyo. More detail about the LED calibration process is covered in Section 5.1.5.

The CANGAROO-II and CANGAROO-III data acquisition systems use ADC (Analogue to Digital Conversion), see Section 3.2.6. The ADC pedestal removal is determined by a monthly ADC pedestal data file taken with the camera lid fastened. This procedure is to exclude background sky noise (bright diffuse light in the sky due to terrestrial lights or astrophysical sources such as the Milky Way) added to the ADC pedestal. More detail about the ADC pedestal removal procedure and effects is presented in Section 5.1.6.

Figure 3.7: Sketch of the CANGAROO-II camera 36 boxes array with numbers shown, from Mori (2000) [122]. Each box holds 16 (4×4) $\frac{1}{2}$ inch PMTs. The corner boxes 33 to 36, hold only 10 PMTs.

3.1.3 The CANGAROO-II electronics modules

After signal splitting, the pulse delay in the signal cables from the PMTs to the electronics rack is compensated by a 40m long delay (about 200ns delay) cable, to enable the hardware trigger gate and PMT pulse to coincide. Monte-Carlo (MC) simulations and experimental data indicate that essentially all the Čerenkov photons from a GeV-TeV gamma ray atmospheric shower arrive within a 40ns time period, so the hardware trigger gate on CANGAROO-II has been made 50ns wide, to encompass the gamma ray shower Čerenkov photon arrival times. A detailed description of the CANGAROO-II and CANGAROO-III data acquisition system is contained in Section 3.2.6.

3.2 The CANGAROO-III 10 metre Imaging Atmospheric Čerenkov Telescopes

3.2.1 The CANGAROO-III project

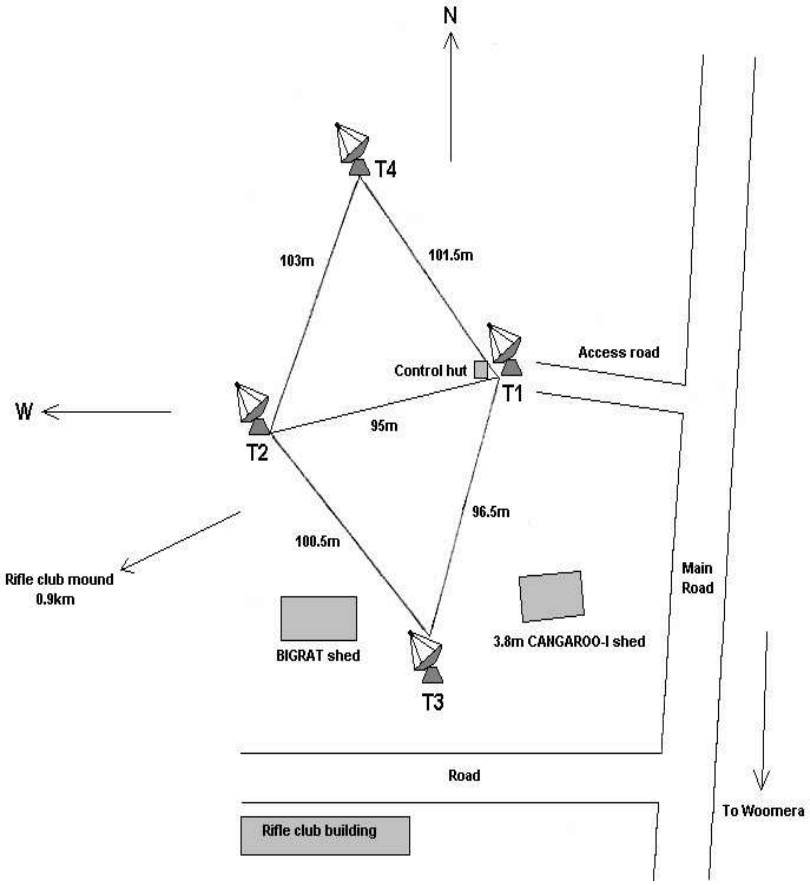

Figure 3.8: An overview sketch of the CANGAROO-III telescope array site at G-range, Woomera. Distances between telescopes are included in metres. Also shown are access roads, the direction of the rifle club mound where the flasher experiment was conducted, and nearby buildings; CANGAROO-I and BIGRAT (from previous IACT experiments), and the rifle club sheds.

In addition to the CANGAROO-II telescope which was constructed in 1999-2000, three other telescopes have been added to complete an array of four IACTs at the same observatory site. This is the CANGAROO-III project. Each new telescope consists of essentially the same dish and mirror geometry as CANGAROO-II but with an entirely

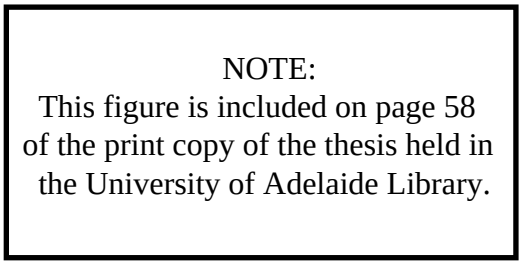

Figure 3.9: A photograph of the CANGAROO-III T2 telescope, from Mori (2002) [123]. This telescope has a 10m dish with the same compound mirror system as T1, but uses a different camera. The scale of T2 is very similar to T1, see Figure 3.1. The hut at ground level is the dish steering control hut, with the data acquisition hut sited on the left of the dish platform, above the dish pedestal.

new camera design. The fourth and final telescope, (T4), came on line in the middle of 2004. The CANGAROO-II dish is designated T1 with the new CANGAROO-III telescopes in the array designated T2, T3 and T4. Figure 3.8 shows the alignment and dimensions on the ground of the telescope array. The designs of telescopes T3 and T4 are not discussed in this chapter, however they are nearly identical to T2. The distance between each telescope in the four telescope array is approximately 100m. They were positioned this way following Monte Carlo simulations which is consistent with the Čerenkov light pool on the ground at near sea level altitudes, generated by a 1 TeV primary photon EAS, being about 100m in diameter.

The initial plan for the four telescope array was to position the telescopes on the vertices of a square of sides 100m. Considering that the telescope array could be upgraded with more telescopes, the four telescopes were geometrically positioned in a parallelepiped as a part of a overall hexagonal array plan of seven telescopes. For

instance, the ground layout of the four telescope CANGAROO-III array shown in Figure 3.8, has a geometrical symmetry which could enable an expansion of the existing four telescope array to a seven telescope hexagonal array. T2 would be the telescope in the centre of the hexagon, with the other IACTs being on the vertices of the hexagon, resulting in each telescope being equidistant by about 100 metres from each other. A square array does not have this capability to expand to an equidistant array using a minimum of seven telescopes, achievable by the hexagonal array geometry.

The array is designed for stereoscopic viewing of gamma ray showers. It allows an improvement in the measurement of the arrival direction of the gamma ray, plus an improvement in the discrimination between gamma ray and cosmic ray showers (see Section 2.1). The T2 telescope was completed by December 2002 (see Figure 3.9 photograph). The observer's control hut is sited within the ground level buildings used at T1 (see Figure 3.1). The observer's hut is used for controlling the overall four telescope array dish steering and data acquisition. Each telescope can be individually controlled in tracking and data acquisition time, or together as a group on the same source for stereoscopic viewing. In addition to T1, the T2 telescope has contributed to the overall data set of the flasher calibration studied in this thesis. T3 and T4 are not included because these telescopes started operating later than the results discussed in this thesis.

3.2.2 The CANGAROO-III camera

The CANGAROO-III camera of telescope T2, consists of 427, $\frac{3}{4}$ inch ($\sim$ 19.1 mm) PMTs in a hexagonal array (Figure 3.10). This camera geometry is more akin to the IACT telescopes used by the VERITAS and HEGRA collaborations, Pühlhofer *et al.* (2003) [142], and this design wastes less PMTs outside the FoV. This is in comparison to the square array T1 camera where more space is wasted outside the circular FoV, with PMTs not receiving an image from the primary mirror on the edge of the camera, particularly in the corners. The field of view of CANGAROO-III is 3 degrees. The PMTs are $\frac{3}{4}$ inch *Hamamatsu* head-on type R3479 consisting of 10 linear focused dynodes, bialkali photocathode with a UV transparent borosilicate glass

window. The wavelength of peak quantum efficiency of this tube is 400 nanometres and the quantum efficiency at this wavelength is 25%. The characteristics of this tube were taken from *Hamamatsu* R1450 which is very similar to the R3479, but the rise time of R3479, (1.3 ns) is faster than R1450, (1.8 ns). An introductory discussion of PMTs in general is found in Section 3.1.2.

Figure 3.10: A schematic view of the CANGAROO-III camera, taken from Ito (2000) [88].

The T2 camera is housed in a lightweight lightproof aluminium cylinder 800mm x 1000mm, together weighing about 100 kg. Twisted pair cables transmit data and supply high voltage for each tube. Each PMT module consists of a PMT and a preamplifier. Together they are 20.5 mm in diameter and 173.5 mm in length, and are held by two aluminium templates positioning the PMTs. The preamplifier *Maxim* MAX 4107, amplifies the PMT output by a factor of 60. Each module is shielded by mu-metal (μ-metal) to prevent geomagnetic gain variations, and to prevent crosstalk between modules taking place (see Section 3.2.5). Prior to telescope assembly, individual PMT gains were adjusted to $2\text{x}10^5$, determined from the single photo-electron peak (see Section 3.2.3). A HV bleeder circuit, [92], was installed and an active base, which

stabilizes the potential difference between the 6th and 8th dynodes of the R3479 PMT, was introduced to prevent deterioration when the bleeder suffers from large constant current flow, e.g. from bright stars impinging on the PMT. It was shown that the PMT's gain remains stable, even under bright background sky conditions, as when the FoV includes the Milky Way where many gamma ray sources are found.

Before the T2 camera was constructed, the characteristics of all 450 PMT modules (including reserves) were calibrated and recorded. The features tested were:

- High voltage dependence of the gain.
- Linearity from 1 to 1000 p.e.
- Timing resolution.
- Quantum Efficiency.

The above itemized features were determined in the laboratory. The PMT modules were calibrated using the following procedure:

1. "The HV was adjusted to give a gain of 1.2x10^7 (including the preamplifier gain), to measure the single electron spectrum.
2. The amount of light per pulse was changed sequentially to; 1,10,50,100,210,280,350,500,700, and 1000 p.e.
3. The HV dependence of the gain was measured with an input equivalent to 10 p.e.", [92].

"After this testing the whole T2 camera was assembled and the following features measured. The HV were arranged so that a pre-amplification gain of 1.2x10^7 was obtained according to the recorded gain, measured as per point (1.) above:

- The uniformity, over the photocathode, measurement of the gain.
- The incident-angle dependence of the acceptance efficiency (Section 3.2.4) and,
- Crosstalk effects (see Section 3.2.5)", [92].

CANGAROO-III calibrations taken during source observations for flat fielding and to determine the ADC pedestal, were carried out using a diffused ultra-bright blue LED (*Nichia* NSPB 510S) in the camera vessel and in the centre of the dish. For the camera LED, as well as opaque white plastic as a diffuser, a variegated shaded blank (based on a Monte Carlo simulation) on the camera lid is used to illuminate across the camera uniformly.

The CANGAROO-III camera is a significant improvement in design over the CANGAROO-II camera. The use of individual HV supply cables for each tube enable better gain and flat fielding control over the camera and the hexagonal geometry ensures improved coverage of the FoV, over the square array design of the T1 camera. This design also enables individual, or groups of tubes, to be switched off in response to a bright star moving through the FoV, maintaining a relatively constant trigger rate over the run exposure. The T1 camera uses a slightly higher density of pixels (and hence better image resolution) compared to the CANGAROO-III camera. However, the T1 camera used a negative polarity cathode voltage in the PMTs and, coupled with the common supply voltage to 16 PMTs per box and the semi-metallic light guides touching the bialkali windows of the PMTs, leads to discharge problems on humid nights and possibly increased noise level per PMT. The negative voltage cathode was originally used as it was thought that this configuration produced a more rapid response, i.e. better for photon arrival timing characteristics. However the very fast pulse analysis electronics now available (Time to Digital Count (TDC) and ADC modules) reduced the photon pulse arrival timing concerns. The CANGAROO-III camera uses the more conventional positive voltage cathode, producing an improvement to PMT stability. Tests with the Flasher Calibration experiment, (Chapter 5), indicate that the T2 camera pixels show a clearer signal with less noise than the T1 camera pixels.

3.2.3 CANGAROO-III photomultiplier tube specifications

The pixel size of the T2 camera is 0.17° across. The R3479 PMT was chosen because, [92]:

Figure 3.11: The *left* figure (figure(a)), shows the single electron peak from Flyckt & Marmonier (2002) [61], as it may appear when measured by a multi-channel analyzer. The relative scale of the horizontal axis represents increasing energy and the vertical axis represents the frequency count of each channel. Each dot in figure(a) represents a single channel. The *right* figure (figure (b)), represents the relative variation of the secondary emission coefficient, δ (vertical axis), as a function of primary electron energy, E_p (horizontal axis), [61]. The secondary emission coefficient ratio first increases to a maximum (when the initial energy of the primary electrons is, E'_p), then gradually decreases with primary electron energy, as the proportion of the electrons excited at greater depth in the material increases.

- Low transit time spread.
- Good response to near Ultraviolet wavelengths, i.e. Atmospheric Čerenkov wavelengths.
- Pre-Amplification gain of 10^5.
- A wide range of linear response of 1-300 photoelectrons (p.e.) with less than 20% deviation from linearity.
- Good signal to noise separation and a possible identification of the single photoelectron peak.
- Light weight and compact size.

For a PMT, the single electron spectrum peak, [61], or single photo-electron peak is generated when a PMT is used to detect very weak signals, such that the pulses from single photoelectrons are well separated in time. It can be advantageous to count those pulses using a multi-channel analyzer. An example of such a single electron peak is shown in Figure 3.11*a*. Because of the nature of the secondary-emission process (to take account of the noise contributions from fluctuations in the secondary emissions of the dynodes, [61]), the single electron pulses show very large amplitude fluctuations. The corresponding p.e. amplitude distribution, or single electron spectrum is characterized by:

- "The mean amplitude corresponding to the *centroid of the pulse height spectrum*" [61], i.e. the weighted mean of the frequencies present in the signal. If the secondary emission were free from any fluctuation then all pulses would have that amplitude.

- "The peak-to-valley (P/V) ratio. With a secondary emission coefficient (the ratio of the number of secondary electrons emitted to the number of primary electrons, see Figure 3.11*b* [61]), for the first dynode being at least 6 to 8, the single electron spectrum will show a peak and a P/V ratio can be estimated", [61]. The P/V ratio can then be used to monitor the performance of the photomultiplier.

- "Single electron resolution. If the first dynode has a high secondary emission coefficient (usually above 12), the P/V ratio may exceed two", [61]. Hence, it is possible to estimate a single electron resolution, defined as the FWHM of the single electron peak (Figure 3.11*a*), divided by the position of the peak maximum on the multi-channel analyzer (expressed as a percentage).

- "Relative variance for the distribution", [61].

Note that signal pulses caused by photoelectrons being inelastically backscattered by the first dynode, produce a large proportion (10-20%) of very small pulses, usually below one third of the single electron peak maximum position.

3.2.4 Winston light guides

Figure 3.12: Schematic side view of a Winston cone light guide, from Winston (1970) [170]. The *left* figure shows that the entrance and exit apertures are of radii, a, and a', respectively. F, is the focus of the upper parabola section and, f, its focal length. The *right* figure shows the origins and orientations of the focus-centred and symmetry axis-centred coordinate systems.

"Winston cones light guides are non-imaging light concentrators designed to funnel all wavelengths passing through an entrance aperture out through the exit aperture, using an off-axis parabola of revolution designed to maximize collection of incoming light rays within some field of view", Winston (1970) [170]. Figure 3.12 shows a schematic side view of a Winston cone. Winston cones "maximize the collection of incoming rays by allowing off-axis rays to make multiple reflection bounces before passing out the exit aperture, although there are certain families of off-axis rays that are ejected back out through the entrance aperture", [170].

Winston cone light guides in front of the PMTs of all CANGAROO telescope cameras, shown in the photograph of Figure 3.6, increase the light gathering capability of the T2 camera by up to 69% (including the gap) for rays arriving normally, when compared to PMTs without light guides. For T2, there is a 2mm gap between the

Figure 3.13: "The angular acceptance as a function of the angle of incidence light rays at the entrance aperture for an ideal three-dimensional Winston cone", from Winston (1970) [170]. The angular acceptance measures the degree of transmission from the exit aperture for rays entering the Winston cone at angles, where 1.0 is 100% and 0.5 is 50% transmission. Note that "the angular acceptance cuts off over a narrow region, $\Delta\theta$ (approximately 1° centred about $\theta_{\max}$). In this example, $\theta_{\max} = 16°$", [170].

light guides and the UV window of the PMTs to prevent electrical discharge, [92], this discharge prevention gap is missing in T1.

Acceptance efficiency is a definition which is not universal throughout physics, but is specific to the experimental approach or apparatus where a beam of particles or photons are usually involved, and is sometimes expressed as a percentage. According to an experiment by Beddar *et al.* (2003) [27], where a plastic scintillator detector was coupled by an optical fibre to a PMT, "the acceptance efficiency is estimated by calculating the approximate solid angle of the isotropic light emission from the centre of the scintillator that falls within the acceptance cone of a single fibre for total internal reflection", [27]. This example could reasonably be used to clarify our definition of acceptance efficiency of the T2 camera, in which, instead of a scintillator and optical fibre coupled to a PMT, we have a Winston cone and air gap coupled to a PMT. Using this definition by Beddar *et al.* (2003) [27], the acceptance efficiency of the T2 camera refers to the calculation of the approximate solid angle accepted from isotropically arriving light rays at the entrance aperture of the Winston cone, where the acceptance efficiency closely follows the angular acceptance function shown in Figure 3.13, from

Winston (1970) [170]. "The angle, $\theta_{\max}$, is the maximum angle an entering light ray can make with the Winston cone axis of symmetry", [170] (shown as three parallel dashed lines in the left figure of Figure 3.12). The ray showing $\theta_{\max}$ in Figure 3.12, is the dashed line joining the edge of the entrance aperture to the point F on the opposite edge of exit aperture, where the maximum acceptance angle, $\theta_{\max}$, is shown as θ in Figure 3.12. Note that there will be a slight modification to the angular acceptance function shown in Figure 3.13, due to the fact noted above that the light rays coming from the Winston cone exit aperture must pass between the cone and the photomultiplier face.

3.2.5 Crosstalk effects

Crosstalk effects may occur when two unshielded current carrying wires (called traces) are closely parallel. "When alternating current flows down one of the traces (called the aggressor or driven line), that current can inductively or capacitively couple onto the adjacent trace (called the victim line), and create two different noise signals", Brooks (2003) [40]. As shown in Figure 3.14, "one of these noise signals will flow in the victim line in the same (forward) direction of the aggressor current (shown as right pointing arrow (3)). The other noise signal will flow in the victim line in the opposite (backwards) direction, (shown as arrow (2)). These are called *forward* (or capacitance coupled), and *backward* (or inductive coupled) crosstalk, and cause different effects", which are explained in detail in [40]. The strength of the crosstalk effects are proportional to the amplitude of the aggressor current and the AC frequency, i.e. the higher the frequency the greater the crosstalk. The forward and backward crosstalk effects may cancel each other out. If they do not, the usual way in which crosstalk effects can be minimized in digital circuits is to either reduce the signal frequency, decrease the signal current amplitude (if possible), apply a high impedance terminator to the victim line, shorten the wire length, or to have multiple parallel wires traveling in strip-line environments.

Figure 3.14: Sketch of how forward and backward crosstalk effects can occur in parallel wires, from Brooks (2003) [40]. The lower wire carries the AC aggressor current, which has stepped down at point X and is moving to the right. The arrows indicate the flow directions of the crosstalk currents from point X, in the top victim line.

3.2.6 The T1 and T2 electronic data acquisition system

Čerenkov photons generated from EAS arrive at the ground within a very short time frame of less than 40 nanoseconds. While PMTs are able to respond rapidly enough to be able to detect these Čerenkov photons, very fast digitizing electronics have to be incorporated with the data acquisition, system to digitize the PMT analogue signals when the camera's PMTs record Čerenkov radiation from the EAS.

CANGAROO uses a digital data acquisition system with both ADC and TDC electronics, for every 576 PMTs of the T1 telescope. Each PMT signal is independently converted from analogue to digital signal using the data acquisition event trigger, common to both ADCs and TDCs. This system is divided into the front-end analogue TKO data acquisition modules (for T1 only, see Figure 3.15), and the rear-end digitizing data acquisition modules. This data acquisition process is parallel processing, Ohska (1989) [131]. T2 uses VME instead of TKO for its front-end modules, see Figure 3.16. Its development was influenced by earlier high energy physics particle beam/collision experiments, such as TRISTAN, at the High Energy Accelerator Research Organization (KEK) at Tsukuba Japan, [131]. In T1 and T2, there are both digital and analogue signal discriminators incorporated into the electronics data acquisition system to enable Čerenkov photons signals to be favoured over photons generated by sky noise.

Figure 3.15: Network diagram of the overall data acquisition system electronics modules, data buses, and controlling & recording computers for T1. From Kubo *et al.* (2001), [105].

The deployment of the parallel digital processing design of both TDCs and ADCs was made in T1 and T2, because the photon arrival timing characteristics were difficult to measure using only ADC electronics. The ADC digitizes the analogue PMT pulse by "integrating over the pulse height verses time", Liu (2006) [113], whereas the TDC converts a signal of sporadic pulses into digital representation of their time indices, i.e. "the TDC outputs a time of arrival for each incoming pulse", Lampton & Raffanti (1994) [107]. Many other IACT collaborations such as HESS, Vincent *et al.* (2003) [163], MAGIC, Albert *et al.* (2008) [11], and VERITAS, Holder *et al.* (2006) [84], mainly use only ADC modules to digitize Čerenkov photon signals from individual PMTs, and TDC digitizing technology is rarely used elsewhere.

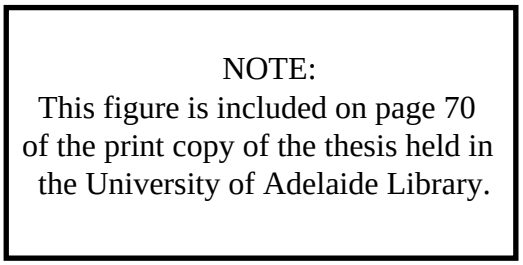

Figure 3.16: Network diagram of the overall data acquisition system electronics modules, data buses, and controlling & recording computers for T2. From Kubo *et al.* (2003) [104].

Randomly arriving (in time) night sky background (NSB) photons have to be simulated to understand the nature of the observed signals. The effect of the night sky background has been simulated for CANGAROO-II. In general, the night sky background (NSB) adds to the width of the Poisson distribution of each PMT signal channel of the IACT telescopes used by CANGAROO, for each triggered event. Data for the T1 telescope, when triggered on NSB alone (with very few or no Čerenkov photons pixels seen in the FoV), show a purely random distribution of pixels in the T1 camera, without pixels grouping or clustering. Pixel clusters are usually indicative of Čerenkov photons. An example of a purely NSB triggered event in T1 is shown in Figure 7.6 *left* (Section 7.1.4) , compared to an event triggering on Čerenkov photons in an EAS

shown in Figure 7.6 *right*.

The principal data acquisition differences between the T1 and T2 telescopes are in the speed of the data buses. Otherwise the data acquisition system used by the two telescopes is essentially the same. The read-transfer speed of the CAMAC (Computer Automated Measurement And Control), and the TKO data buses, Ohska (1989) [131], on T1 are 1 Megabyte/second, while the VME (VersaModular Eurocard) 32 type data buses read-transfer speed on T2 are 8 Megabytes/second, Kubo *et al.* (2003) [104]. Figure 3.15 shows the data acquisition network for T1 and Figure 3.16, shows the data acquisition network for T2.

Figure 3.17: This diagram shows the data bus and discriminators for the Discriminator and Summing Module, (DSM) (or TKO module), taken from the CANGAROO observation manual, Gunji (2006) [73]. The box labeled, "AC", in the diagram is the (Digital) to Analogue Converter, DAC.

For T1 the amplified signal per PMT is split into a custom made VME9U-bus ADC (*Hoshin* 2637, Nishida *et al.* (2002) [127]), 32 channel module (12 bit charge sensitive), and a custom made TKO-bus Discriminator and Summing Module (DSM) shown in Figure 3.15. For T2, the amplified signal per PMT is divided into a custom made VME9U-bus 32 channel ADC (*Hoshin* 2678, [127], 15 bit charge sensitive), and a VME9U-bus DSM, shown in Figure 3.16. Figure 3.17 (above), Figure 3.18, and 3.19 (left diagram) indicate the data stream and comparators within the TKO-bus and analogue divider, as shown in Figure 3.15. "A comparator is an operational amplifier circuit that compares two input voltages and outputs a positive or negative logic voltage

depending on the threshold level of the inputs", Smith (1987) [157]. The discriminator voltage thresholds (sometimes to be set by the observer/operator), are indicated by bold type in the following paragraphs, e.g. **tdc_disc**. The description label of the discriminator, or its signal, is put in underlined capitals, e.g. ASUM. The exception to this is CAMAC, which is an abbreviation and underlined only when it is a signal.

Figure 3.18: Left diagram: The LSUM and NHIT discriminator data bus; threshold control for **nhit_disc** discriminator. Right diagram: The ASUM data bus to the CAMAC C285 & *LeCroy* 4413 NIM crates; threshold control for the **CAMAC** and **nbox_disc** discriminators, [73].

In Figure 3.17 the signals from a camera, "carried by the 16 twisted pair cables from each camera box, are split by a signal divider. One of these signals goes to the VME ADC and the other to the TKO DSM. In the DSM, the 16 signals from each box are fed into shaping amplifiers. Three output signals are generated from the shaping amplifier, one is fed into the summing amplifier. There the 16 channel analogue sum (ASUM) is made. The second signal is input into a comparator called the **lsum_disc**, and the output is a logical sum (LSUM). The **lsum_disc** and **tdc_disc** comparators threshold level is controlled by the Digital to Analogue Converter (DAC), (shown in Figure 3.17). The logical sum, LSUM, signal is proportional to the number of pixels or PMTs with *hits*. For example, one hit is measured as -20mV and two hits are -40 mV and so on", Gunji (2006) [73]. The definition of a *hit* pixel is explained in the next paragraph. "The third signal is input into a comparator called **tdc_disc**, and by

flat data cable, it goes to the CAMAC TDC. The CAMAC comparator threshold level can be also adjusted, where the TDC start or (Čerenkov) photon arrival timing level is set. In summary, the TKO DSM module input are 16-channel signals from one box and output are three kinds of signals; LSUM, ASUM and CAMAC. One TKO DSM module operates on signals from two boxes (32 PMTs)", [73].

Figure 3.19: The left diagram is the data bus for the TKO DSM, (*Hoshin* 2548, [127]). Circuitry within the dashed line boxes are not included in T1. The right diagram shows the data bus acquisition trigger, which is an extension of the LSUM and ASUM discriminator logic gates shown in the left diagram, from Kubo (2001) [105].

"After the TKO DSM shown in Figure 3.17, the logical sum (LSUM) signal from the DSM is fed to a NIM linear fan-in module. The 16 box signals of the central camera channels are added and sent to the NIM (NHIT) discriminator", [73], (or the discriminator based on the number of pixel *hits*), shown in Figure 3.18 (left diagram). "The pulse width of this signal is 40 ns and the height is an integer multiple of -20 mV, i.e. the number of PMT channels in which the signal is greater than the **lsum_disc** level, multiplied by -20 mV. The adjustment level for the **nhit_disc** voltage threshold is ten times that of the internal circuit level for T1", [73]. For example a **nhit_disc** setting of -820 mV will become -82 mV in the internal circuit NHIT discriminator.

"From the TKO DSM, one of the two identical ASUM signals is sent to the CAMAC (C285) ADC NIM crate module via long delay cables and connector modules", [73], shown in Figure 3.18 (right). "This 32 channel ADC processes each box ASUM signal.

This particular module was circumvented after November 2000 for data acquisition. The other ASUM signal goes to the NIM divider where it is split into two. One of these two new signals is input into the TKO SUMAMP, monitored by an oscilloscope for data acquisition testing. The other split signal goes to the CAMAC (*LeCroy* 4413 discriminator), where the 16 (inner camera) boxes number of hits are transferred to analogue voltages. The pulse height of this analogue signal is an integer multiple, similar to **nhit_disc**. That is, where the number of inner camera boxes (multiplied by -50 mV) over which the signal is greater than the **CAMAC** discriminator level. This discriminator's threshold is adjusted like the **nhit_disc**, where the adjusted threshold level of the **CAMAC** discriminator, by the operator, is one-tenth the internal circuit level of the *LeCroy* 4413 module. The analogue signal from the *LeCroy* 4413 is fed to the nbox discriminator, denoted as **nbox_disc**, where again the internal circuit threshold level is one-tenth the level of the threshold setting. The (external) output signal pulse height, at or exceeding -50 mV from the *LeCroy* 4413, is the condition that one box is hit and is then put to the NBOX discriminator. In the case for T1 boxes, the **nbox_disc** threshold voltage setting of -350 mV (-35 mV internally), is the condition that more than one box is hit", [73]. The T1 box configuration can be seen in Figure 3.7, where there are 16 PMTs to a box.

To summarize the DSM and overall data acquisition processing, "the signal from each PMT is amplified with a shaping amplifier and the signals of 16 channels are summed (ASUM). The amplified signal is fed into two discriminators; one is for the measurement of the trigger time by the TDC module (CAMAC-bus 32 channel TDC; *LeCroy* 3377), with 0.5 nanosecond resolution in a time window of 256 nanoseconds (**tdc_disc**), whilst the other is for the measurement of the background counts over threshold per pixel per millisecond. The narrow 0.5 nanosecond resolution of the former channel is possible, due to the parabolic shape of the dish where the time propagation of the shower Čerenkov photons can be reproduced with an accuracy of less than 1 nanosecond, and the latter channel is used to reject bright starlight pixels in the offline analysis (Scalar in Figure 3.15 for T1). The voltage thresholds of both discriminators are adjustable via the TKO data bus where, for most Čerenkov shower events, they

are set to 2-3 photoelectrons. A third channel pulse with a voltage proportional to the number of pixels triggered, NHIT, at the same time is generated (denoted LSUM)", [104]. "One unit (or PMT box) is connected with 16 PMTs shown in Figure 3.19 (left diagram), and there are two of these units in one DSM board", [105].

The data acquisition trigger, shown in Figure 3.19 (right diagram), an extension of the LSUM and ASUM logic gates in Figure 3.19 (left diagram), is set as follows: "LSUM signals (connected to the 256 PMTs from the inner camera), from the DSM modules are summed and discriminated to determine if a sufficient number of PMTs are hit within a 20 ns width. The discriminator threshold is usually set to be 4 or 5 coincident pixels above a certain voltage level set by the operator, (**nhit_disc**). The ASUM is set to discriminate a concentrated pattern of pixels; usually a cluster of 3 adjacent pixels. Coincidence signals passing threshold levels from the ASUM and LSUM channels generate the data acquisition trigger (**CAMAC** and **nbox_disc**)", [104]. In addition in T2, a hardware pattern trigger module (selects a hit pattern whether or not hit pixels are adjacent), is set shown in Figure 3.19 (left). "The data acquisition trigger promptly opens an ADC gate between 50ns and 100ns width, which converts the amplified signal from the DSM after a 150ns delay provided by a delay-line chip aboard the ADC (for T2 only)", [104]. "The data acquisition trigger also latches the time of the Global Positioning System (GPS) clock within 1 microsecond and generates a common stop signal for the TDCs after 60 nanoseconds. It then generates an interrupt trigger to the CAMAC interrupt register after 3 microseconds. All signals shown in Figure 3.19 (right), are counted by a CAMAC scalar module, shown in Figure 3.15. The dish tracking position and the scalar data from the CAMAC DSM, collected by the VME-bus, via a VME-TKO interface shown in Figure 3.15, is updated and recorded every ten seconds. Data from the weather station (e.g. wind speed and outside air temperature), and the cloud monitor (based on thermistor temperature measurements of the sky), are also latched to the data records every minute at the VME board via computer connected by RS232C data communication lines, used in both T1 and T2", [105]. See Figures 3.15 and 3.16.

The data acquisition triggers in the CANGAROO IACTs, the various discrimi-

nators thresholds, as shown in Figure 3.17, and Figure 3.18, must be initially set before data acquisition is begun. The following flasher threshold voltage settings of the **lsum_disc**, **tdc_disc**, **nhit_disc**, **nbox_disc** and **CAMAC** discriminators, where most of these are shown in Table 5.1, are based on the CANGAROO observers manual instructions in Gunji *et al.* (2006) [73]. The **nbox_disc**, **nhit_disc** and **CAMAC** discriminators voltage thresholds are manually adjusted on the NIM crates in T1, while in T2 these discriminator thresholds are set by computer input. For both T1 and T2, the **lsum_disc** and **tdc_disc** discriminator thresholds are initiated via computer input commands under Linux.

In the discriminators of both Figure 3.19, and Figure 3.18, these particular modules usually remain at about the same threshold level, dependent on the day-to-day conditions of gamma ray source observation, or the required telescope trigger rate. As the discriminator threshold voltage is adjusted higher, the combined signals from ASUM and LSUM discriminators in particular, must reach a higher amplitude to accept a trigger. As discussed above, the LSUM signal is set by the **lsum_disc** discriminator voltage threshold, and has an effect on the **nhit_disc** voltage threshold (set manually for T1), for this discriminator as shown in Table 5.1. The NHIT module mainly controls the number of hit pixels, responding to large amplitude PMT pulses, enabling a hardware trigger event to be recorded, to favour Čerenkov events with many photon signal pixels over random sky noise with only a few random pixels, hence low summed signal. For example, the voltage level may set 3 hit pixels at random over the camera to trigger an event recording, or 4 hit pixels, and so on. Practically though in T1, NHIT is not a "pattern trigger", Bastieri (2001) [26], Bradbury (2002) [37], such as now used in all other gamma ray collaborations IACTs and in CANGAROO-III, to a certain extent.

Changes in the **nhit_disc** module threshold level are usually made to control the T1 telescope trigger rate. The number of NHIT pixels is approximately in proportion to the level of the **nhit_disc** threshold voltage. For example, "a **nhit_disc** setting of -820 mV corresponds to 5 or more hit pixels", [73]. The threshold level of this discriminator is mainly set to differing levels of sky noise or background light. The sky

noise is usually a feature of the tracking FoV location and what is in it, i.e.

- Discrete points of light, such as the numbers and brightness of stars in the FoV.
- The location of the diffuse background of the Milky Way (which has more stars and nebulosity associated with the galactic arms), compared to usually darker skies in regions outside of it.
- A cone of diffuse Ashen or Zodiacal light, which is prominent just before sunrise in the eastern sky and just after twilight in the western sky, during the winter months in particular.
- The position of the bright planets, Venus and Jupiter.
- The times of moonrise and moon-set. The HEGRA collaboration has found it possible to do gamma ray astronomy, without much loss to the quality of the data, by taking observations while the moon is above the horizon during a thin crescent phase when the moonlight intensity is low, Kranich *et al.* [100].
- The type and quantity of artificial terrestrial lights, which are in the line of sight or producing light glow beyond the horizon.

In T2, it is possible to preset the switching (off and on) of PMTs that have bright stars impinging upon them near the gamma ray source while the FoV rotates through tracking. Hence, it is possible to reduce sky noise in T2 via selective PMT switching due to bright stars. This feature is not available in T1.

A desktop 32 bit personal computer (PC) is shown for T1 in Figure 3.15, and a VME-bus CPU board is shown for T2 in Figure 3.16. These components collect and record data from the ADCs, TDCs, GPS, environment and tracking for both telescopes. The PC runs a Linux operating system and a portable data acquisition system is installed for collecting and storing all data onto a large capacity hard-disk, later to be duplicated onto *DAT* format tapes. "The total quantity of data recorded in a single event is 1.5 kilobytes for T1", [105], since the inception of this data acquisition system for T1 was made in 1999 and has remained unaltered to date. "The data

acquisition system can accept trigger data at a rate up to 80 Hz for T1 and 350 Hz for T2 with a raw trigger rate to data record rate "dead time" of 20%", [105]. Dead time occurs when data are still being processed in the bus stream and the telescope is not in a ready state to record a trigger again. For example, trigger rates (generated by random noise and EAS for instance), above the $\sim$ 80 Hz level are not all recorded for T1, and some potential telescope triggers above this rate are missed.

3.2.7 Stereoscopic data acquisition

The CANGAROO-III imaging atmospheric Čerenkov telescopes, can acquire data individually or in *stereo mode*. There is no shared common data acquisition trigger between the CANGAROO-III telescopes, unlike the HEGRA IACT array for instance, Puhlhofer *et al.* (2003) [142], and the HESS IACT array, Funk *et al.* (2004) [64], Aharonian *et al.* (2004) [6]. However, if both telescopes are pointing at the same region of the sky and trigger on the same shower event, the event can be recorded as a coincident trigger in time between two or more telescopes in the array. For example, "both the trigger pulse and the 16 bit event number of T1 are transmitted through 150m length optical fibres to the data acquisition of T2 (or between any other two or more telescopes in the array), and the differences of the arrival times of T1 and T2 triggers are measured with 1ns resolution by T2 (the measured arrival time difference of a coincident trigger is equal to the difference of the light path between telescopes)", [104]. The stereo mode Hillas parameter data cuts of a coincident event can be analyzed later offline.

The energy thresholds of T1 and T2 are different by a considerable factor due to their differences in camera design and age of construction (T1 on-line April 1999 in the 7 metre mode and April 2000 in the 10 metre mode, T2 on-line December 2002), despite having practically the same dish and mirror design. The indications are that PMTs and mirrors degrade in efficiency over time as explained by the HEGRA group [142], and in Chapter 5. Thus the overall energy threshold of an IACT gradually increases with time, excluding gain changes in the camera to offset this effect. The raw trigger rate of T2 is at least 50% larger than T1 on background (cosmic ray rate)

checks, [104]. This makes coincident shower events between T1 and T2 sparse, and at an energy above the T1 threshold after noise cleaning. The event coincidence rate is improved between the next array of CANGAROO-III telescopes included in the array; T3 and T4. They are fundamentally the same as T2 in design, but were built some time after T2's construction.

T1 ceased taking data from late 2004. The main reason for this is that T1 is incompatible with the other three telescopes, T2, T3 and T4, during a global or four-telescope trigger, making it extremely difficult to successfully incorporate T1 into the telescope array with its current design. The square geometry layout of PMTs in T1's camera design is different to the hexagonal geometry cameras of T2 to T4. Further, the $\frac{1}{2}$ inch PMTs in T1's camera, *Hamamatsu* R4124UV, are different to the $\frac{3}{4}$ inch PMTs in the T2, T3 and T4 cameras; *Hamamatsu* 3479UV. Also, the photocathode in any PMT gradually degrades with time and loses its quantum efficiency. This feature has bearing in particular to T1 compared to the other telescopes, as its camera began operation in 1999, while additionally, the electronics modules and data bus speed of T1's data acquisition is considerably slower in comparison to T2 to T4's data acquisition. Finally, since T1 has been operating for at least three years longer than T2 (and the other two telescopes), the reflectivity of T1 mirrors has degraded considerably in comparison to T2, T3 and T4. Telescope T1 could be re-incorporated into the CANGAROO-III array, provided that replacements to T1's camera and data acquisition electronics were made and upgrades to the 80 cm mirror segments were scheduled. Unfortunately, these major works incur a considerable cost, exceeding $A 3 million, and until this funding becomes available, the T1 telescope remains mothballed.

Chapter 4

The flasher calibration experiment

4.1 The custom-made flasher apparatus

4.1.1 Description of the flasher apparatus

Figure 4.1: Photograph of the flasher apparatus above (top figure), including a design sketch of Unit 1 (bottom figure), from Patterson, Swaby & Wild (2001) [136].

This chapter introduces the Flasher Calibration experiment of the T1 and T2 IACT

CANGAROO telescopes at Woomera. It specifically deals with the detailed description of the portable battery powered flasher instrument with a further description of a portable battery powered PIN diode monitor apparatus used to measure the light output from the flasher instrument.

The initial concept for the Flasher Calibration experiment was formed by observing the fine tuning of the mirror pointing by the University of Tokyo, for each individual mirror segments for T1 (see Section 3.1.1). The idea that an artificial light source could be used to check mirror alignment seeded the concept of a light flasher. This device would have blue light emission for the *Hamamatsu* R4124 UV PMTs used in T1 to more easily detect the signal with a short enough pulse width (20 and 10 nanoseconds) to be captured with the PMTs within the camera global trigger gate width of 50 nanoseconds. The flasher apparatus was sited at considerable distance from the telescope to simulate a light source at infinity. This experiment was intended to determine the telescope's changing response to a fixed strength signal over time, enabling a test of the mirror reflection efficiency and change of detector response.

Figure 4.1 shows a photograph of the flasher apparatus with a sketch of the Light Emitting Diode (LED) emitter unit below it. Apart from the achromatic eyepiece, the entire flasher apparatus was fabricated at the University of Adelaide. The light emitter is slotted into the rear of the flasher apparatus tube in the position shown in the photograph of Figure 4.1 of the black achromatic eyepiece. The flasher emitter consists of a *Nichia* NSPB 510S ultra-bright blue LED screwed into a hollow brass cylinder, 23 mm diameter at the rear and 25 mm at the front (shown in Figure 4.1 photograph, lower left). The front face of the emitter cylinder unit sits at the focal plane of a 30 mm diameter lens at the front of the optical tube (seen in Figure 4.1 photograph). To trigger the T1 and T2 telescopes in shower mode during a calibration, the LED was pulsed with a square wave pulse of either 10 nanosecond or 20 nanosecond (ns) width (see Patterson, Swaby & Wild (2001) [136], for a description of the flasher device in a developmental phase of the experiment).

The pulse width adjustment was intended to double the light output from the flasher (switching the flasher unit from 10 ns to 20 ns), if the narrower 10 ns pulse was too

dim to trigger the telescope. It was later found however, that the increase from 10 ns to 20 ns did not lead to an accurate doubling of the total signal from the flasher, see Section 4.2.2.

Light attenuating filters were used to reduce the intensity of the flasher signal. Initially aperture ring filters were used. The aperture filters consisted of aluminium discs ∼1 mm thick with various size holes in the centre. The aperture rings were held in place by a ring holder screwed to the front of the flasher; the photograph in Figure 4.1 (lower right) shows the aperture ring holder containing an aperture ring, removed from the front of the lens. The range of various aperture diameter filters used was found not to attenuate the flasher signal linearly, so an early decision was made to abandon changing the aperture diameter to attenuate the signal. However, a 9.5 mm aperture diameter filter was retained for all flasher calibrations. Neutral Density (ND) filters were then used to attenuate the flasher signal. These consisted of various transmission density polymer film inserted into a square shaped holder that was attached to the front of the ring aperture holder (see Figure 5.6). It was found that the ND filters attenuated the flasher signal more linearly than aperture rings.

The flasher device was bolted onto a 80 cm high tripod, and removed after completing the flasher calibration. The telescope dish was first brightly illuminated with a spotlight on the ground, near the telescope. To accurately point the flasher device at the centre of the telescope mirror, the flasher operator slots in the eyepiece fitted with cross hairs, into the flasher device, and views though it. Fine positioning of the pointing of the flasher apparatus is achieved through adjustment of the horizontal and vertical fine screw threads as seen in Figure 4.1. The optical tube is bolted to an upper plate which is hinged at the back with the vertical adjustment screw thread at the front. The middle plate pivots on a screw near the upper plate hinge and horizontal movement is achieved by turning the horizontal screw on the left hand side of this plate (hidden in Figure 4.1), against a spring on the other side of the plate. When pointing adjustment is complete and the flasher is pointing at the centre of the telescope dish, the operator then slots in the flasher emitter unit in place of the eyepiece and the spotlight is switched off to enable high voltage to be supplied to the telescope camera.

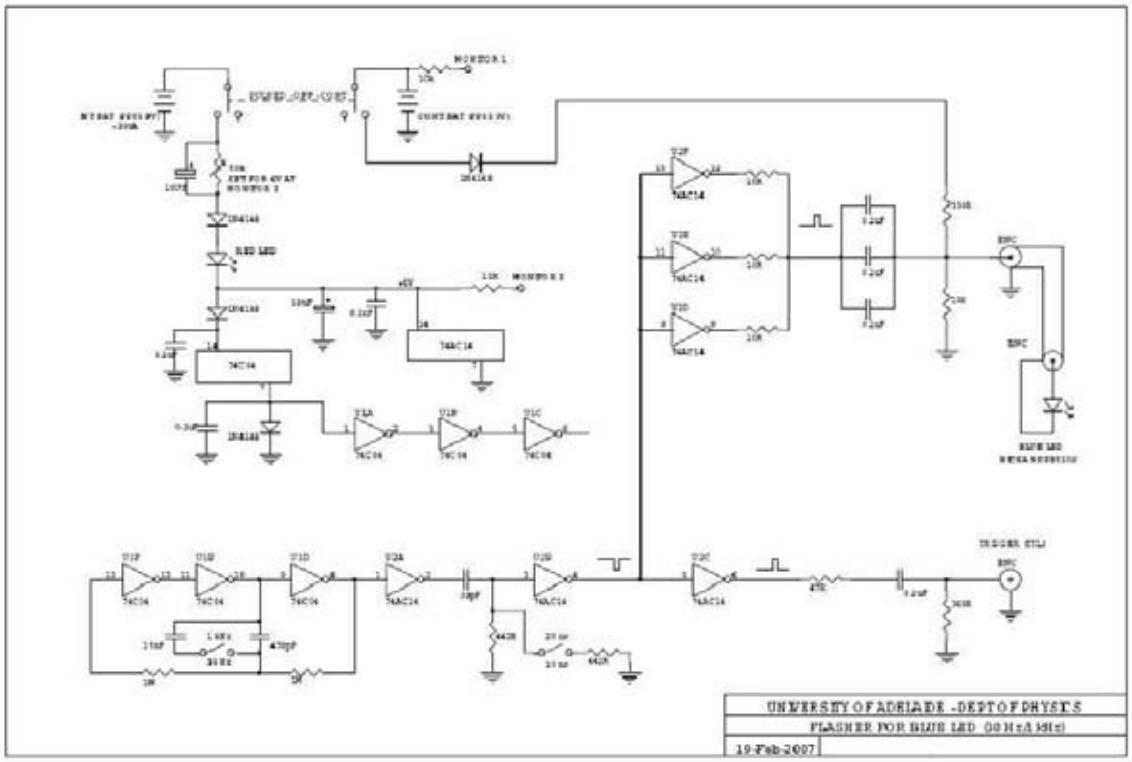

Figure 4.2: Circuit diagram of the *Nichia* blue LED flasher calibration apparatus. For clarity, this figure is shown enlarged in Appendix A, Figure A.1.

The Pulse Repetition Rate (PRR) of the flasher device can be switched between two different settings; 33 Hz or 1000 Hz (1 kHz), for either 20 ns or 10 ns pulse width. The smaller 33 Hz PRR is set if significant telescope dead time becomes a problem when using the more rapid 1 kHz PRR. However, for all flasher calibrations, the 1 kHz PRR was used as it was found that the telescope dead time did not have an effect in data loss during recording of flasher events.

The flasher apparatus operates in two switchable modes; "pulsed mode" pulsing with 10 ns or 20 ns width, and "continuous mode" where the LED brightly shines with a DC input of about -6.0 volts,. Figure 4.2 (above), depicts the flasher DC circuit controlling the 20 ns and 10 ns pulse to the *Nichia* blue LED, and the PRR which can be switched between 33 Hz and 1 kHz. The circuit is housed in an aluminium die-cast box $15 \times 9 \times 5$ cm. The voltage output from this box is sent by a metre long cable

to the LED of the flasher device. The pulsed mode circuit of Figure 4.2, "consists of a free running multi-vibrator circuit of four CMOS 74C04 gates. The repetition rate is controlled by a switchable 15 nF capacitor in the feedback, while the pulse width is set by a second switch and 442 Ω resistance pair. The output is sharpened and buffered by three 74AC14 gates in parallel to provide increased drive. Their output is AC coupled by three 0.1 μF capacitors, in a low inductance combination, to the cable and blue LED", [136]. Two flasher circuit outputs are shown to the bottom of Figure A.1 in Appendix A (i.e. Figure 4.2), via two BNC sockets. One goes to the blue *Nichia* NSPB 510S mounted at the back of the flasher optical tube and the other as a simultaneous flasher pulse (not used) intended to trigger an external circuit or connect to an oscilloscope. The internal (pulsed mode) 9V battery powers the circuit, shown on the top right of Figure A.1, while a red LED diode and 330 Ω resistor are inserted to protect against incorrect DC polarity and any possible circuit over-current.

4.1.2 Seasonal flasher calibration

Eight flasher calibrations occurred in total in the months; April 2001, July 2001, February 2002, June 2002, November 2002, January 2003, June 2003, October 2003. The successive calibrations were rather irregular, i.e. the minimum time between successive calibrations was two months (November 2002 to January 2003) and the maximum time between successive calibrations was seven months (July 2001 to February 2002). This irregularly in time between successive calibrations resulted from the availability of the telescopes for calibration. However, at least one calibration measurement was made each season (spring, summer, autumn or winter). Seasonal variation has an effect where the longer, colder nights of winter in a desert environment often leads to telescope mirror dewing, see Section 5.2.2. Dewing during summer nights (December to February) is rare.

Prior to October 2000, flasher calibrations were carried out from the Woomera airport control tower, 5.7 kilometers due south of the CANGAROO-II telescope (ascertained from maps), in the direction of the park position of the telescope. This calibration site was thereafter abandoned due to the bright white ground lights of the

Woomera detention centre, which tended to swamp the flasher calibration data with sky noise at that time (see Section 7.1.4). From October 2000, the flasher calibrations then took place with the tripod located on top of a ∼15m high rifle club mound at G-range, approximately 1 km due west of the CANGAROO-II telescope, see Figure 3.8. This location had far fewer ground lights causing interference. The telescope elevation and azimuth coordinates for pointing the telescope at the rifle club mound can be found in Table 4.1 (below). The slewing and parking of the telescope dish to point at the rifle club mound position were done via the ACU (Azimuthal Control Unit) manual controls with care, as the telescope then points below the stepper motors encoder danger limit of 10° dish elevation angle.

Azimuth	*Elevation*
5.1100°	0.0000°

Table 4.1: Azimuthal Control Unit inputs for pointing the T1 dish in the rifle club mound direction.

4.1.3 Flasher apparatus LED emitters

During the early testing stages of the flasher calibration of the T1 and T2 telescopes, the flasher was switched between two interchangeable LED emission units; unit 1 and unit 2. Unit 1, the first unit to be manufactured in June 2000, consisted of a *Nichia* NSPB 510S ultra-bright blue LED with a 1 mm diameter optical fibre coupling, of approximate length 10 mm. This was done by attaching (through a hole bored 3 mm into the front end of the LED lens) a fibre held in place with clear epoxy resin glue. The optical fibre protrudes slightly through a hole in the chamber housing the LED of this unit, see sketch in Figure 4.1, and acts as a light diffuser. Unit 2 is similar to unit 1 in that it uses the same type of *Nichia* ultra-bright blue LED enclosed in a chamber, although the light shines out of a 1 mm diameter hole in front of the LED in the chamber, with semi-opaque sticky tape film covering the hole acting as a diffuser. Unlike unit 1, unit 2 has had no modifications to the LED component, such as an

insertion of an optical fibre into a hole drilled in the LED lens.

A point emission source at the focal point of a convex lens should produce a collimated light beam with rays parallel to the optical axis. However, because the emission region of the flasher is finite (1 mm in size), the collimated beam will diverge. To test the divergence properties of the light beam from the flasher apparatus, measurements of the light spot diameter produced by the flasher beam were carried out over tens of metres in the laboratory. These results were then extrapolated to the distance of the telescope from the rifle club mound (approximately 1 kilometre). The results showed that at 1 kilometre the spot size of unit 1 is 7.4 metres in diameter and unit 2 is 14.6 metres diameter and that the angular spread of the image of unit 1 in the camera field of view is 0.4° across and unit 2 is 0.8° across.

The purpose of the optical fibre in unit 1 and the semi-opaque film in unit 2 is to diffuse the optical p-n junction image of the *Nichia* ultra-bright blue LED. This LED has two emitting p-n junctions with a small separation, viewed as two squares joined to a common vertex at a 90° angle of separation, similar to adjacent same coloured squares on a chessboard. As the light beam from the flasher is not perfectly collimated, this image is magnified giving a non-uniform light pool of significant size over the beam projection distance of about a kilometre. Tests in the laboratory, projecting the flasher beam over about 40 metres onto a screen, confirmed that both unit 1 and unit 2 diffusers successfully obscured the image of the p-n junction in the LED, and the light pool from the flasher showed no image morphology from the LED photo-diode junction.

In April 2001 we were concerned that the light output stability of the *Nichia* NSPB 510S ultra-bright blue LED of the flasher could be changing due to electrical current degradation of the photo-diode junction, so the continuous mode operation was only used when absolutely necessary and for short periods. Pulsed mode operation was in comparison much dimmer, so we considered that the pulsed mode operation would be unlikely to cause degradation of the LED p-n junction, even when operated for hundreds of hours. This was verified by the result of Figure 4.6, showing the PIN diode measurement of the flasher over many months.

4.2 Calibration of the flasher apparatus

4.2.1

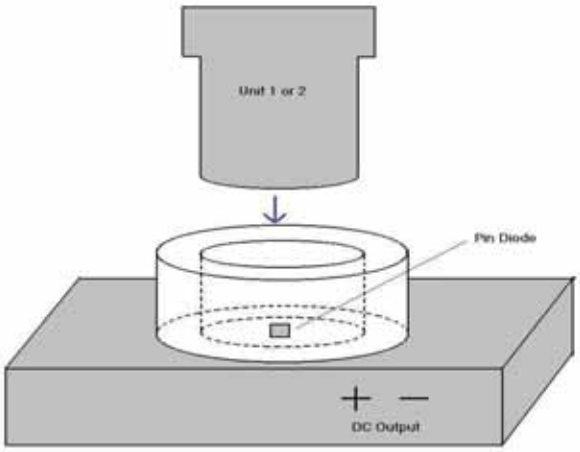

Figure 4.3: Sketch of the PIN diode flasher monitor apparatus. The circuit is held in a die cast metal box; 11.3 cm × 3 cm × 6.2 cm shown. The PIN diode monitor circuit is shown in Figure 4.4.

To test the light output of the flasher apparatus (excluding the lens), we made a PIN Diode Monitor (PDM), to measure the light output of unit 1 and unit 2. Figure 4.3 (above), shows a sketch of the apparatus. The flasher unit 1 or unit 2, fits snugly into the ring block holder shown raised above the circuit box, where the PIN diode in the bottom of the block holder registers the light output from either unit. A Digital Voltmeter (DVM) connected to the DC output terminals measures the voltage output. The light sensitive PIN diode is a blue bias filtered *Centronic* OSD15-E with maximum sensitivity at 550 nanometres. The circuit diagram for the PDM apparatus is shown in Figure 4.4. Effectively the PIN diode does not register individual flashes, as can a photomultiplier tube, but integrates the charge pulses of the flasher output. In Figure 4.4 circuit, the first 0.1 pF capacitor in series with the PIN diode screens out signal from the PIN diode if there is a constant light source impinging upon the diode. Hence the PDM has been tested in the laboratory to be relatively insensitive to outside or incandescent light.

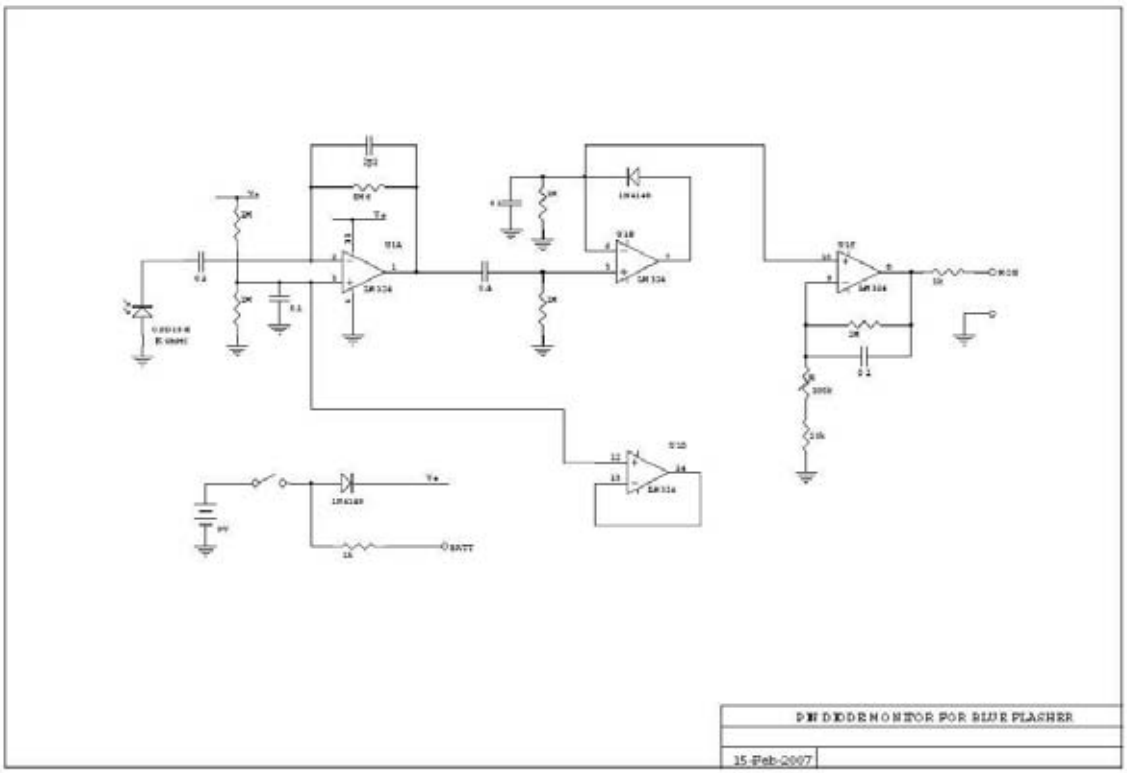

Figure 4.4: Circuit diagram of PIN diode monitor apparatus to measure the flasher output. For clarity, this figure is enlarged in Appendix A, Figure A.2.

In Figure A.2 in Appendix A (i.e. Figure 4.4) , the PIN diode is shown as the OSD15-E component on the top (left, Figure 4.4) of the circuit diagram page. When the flasher emits a light pulse, the PIN diode carries a charge pulse from the PIN diode to the first operational amplifier labeled U1A on this circuit - a *National* LM324. This is the integrating part of the circuit. The 2 pF capacitor, in parallel to the 5 MΩ resistor shown at the top right of the circuit, lengthens the time scale of the pulse decay to about 10 microseconds (fast rise time, slow fall time). The second LM324 operational amplifier labeled U1B, is the peak detector part of the circuit, it finds the positive peak voltage height from the PIN diode signal pulse and shows it as a constant voltage. This voltage is then amplified by the third series LM324 op. amp. labeled U1C, where the gain is preset by a variable 200 kΩ resistor and the DC voltage output is then measured by a DVM. The fourth LM324 op. amp. (U1D) in the chip is tied

so that it does not effect the circuit. A 9 volt battery powers the PDM circuit and is shown on the top left of the figure.

4.2.2 Measurement of the flasher output using the PIN diode monitor

Elapsed time (mins)	*20 ns volts*	*20 ns % change*	*10 ns volts*	*10 ns % change*
0	1.489	0.0	0.602	0.0
20	1.490	0.067	0.601	-0.166
40	1.482	-0.470	0.598	-0.664
60	1.479	-0.672	0.597	-0.831
75	1.481	-0.537	0.598	-0.664
90	1.488	-0.067	0.602	0.0
110	1.493	0.269	0.602	0.0
132	1.502	0.873	0.607	0.831
150	1.496	0.470	0.604	0.332
165	1.495	0.403	0.604	0.332

Table 4.2: Time elapsed fluctuation of the flasher measured by the PIN diode monitor apparatus. Changes in percentages are shown from the initial reading at zero minutes where negative percentages show a dip below the initial value. The 20 ns mean of the ten 20 ns readings is 1.490 volts, the sample standard deviation; $s = 0.0073$ volts, and standard error of the mean ≈ 0.0023 volts. Similarly, the 10 ns mean is 0.602 volts, $s = 0.0031$ volts, and the standard error of the mean is ≈ 0.0010 volts. The definition of the standard error of the mean is shown in equation, 4.1.

The flasher battery driving the pulsed mode circuit is shown at the top right of Figure A.1 in Appendix A, labeled as **NT BAT.** This battery level was adjusted to -6.0 volts just before taking flasher calibrations of the T1 and T2 telescopes. In the flasher circuit of Figure A.1 in Appendix A, a 50 kΩ variable resistor (VR), is shown in the top right hand corner of this diagram and the measurement of the flasher battery

voltage is taken at the **Monitor 1** and **Monitor 2** terminal positions indicated in this circuit diagram. Adjustment of this VR is done via a trim pot screw through the side of the flasher box housing the circuit, to set the flasher battery voltage at -6.0 volts. Measurement of the flasher battery voltage was achieved by pressing DVM probes against the small DC probe terminals **Monitor 1** and **Monitor 2** (set near to the VR screw), on the side of the flasher box. Allowing the flasher battery voltage to drift, without adjustment to -6.0 volts prior to flasher calibrations, is likely to measurably affect the intensity of the flasher LED.

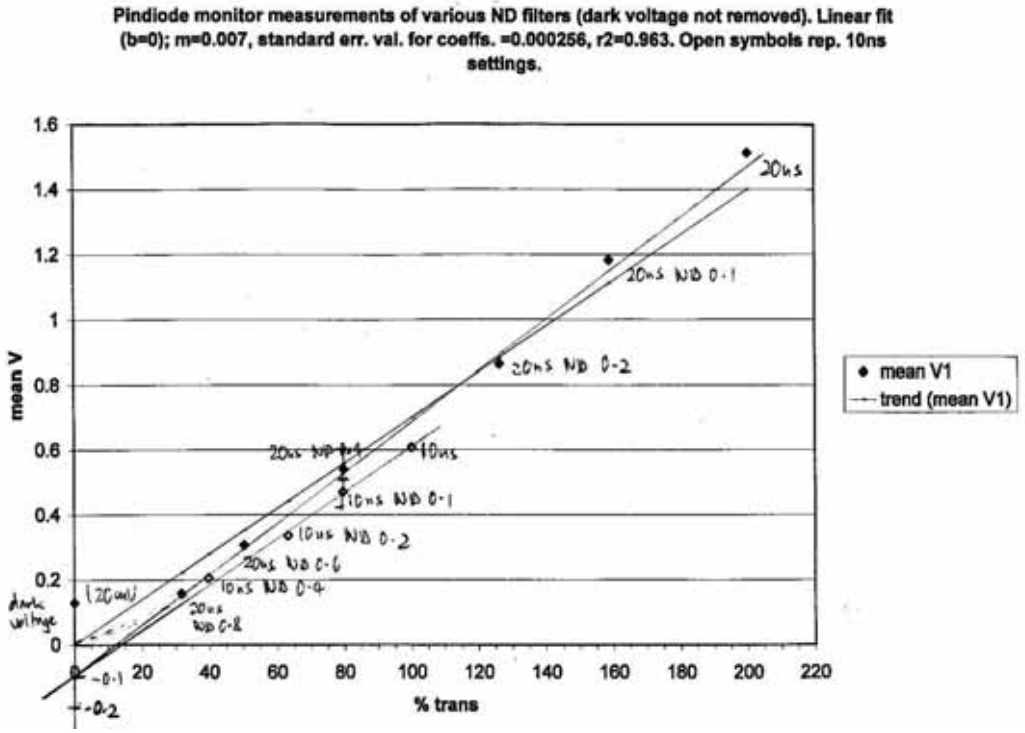

Figure 4.5: PIN diode monitor output voltages, testing the linearity of the light intensity output of the flasher using neutral density filters.

Small random voltage fluctuations of 10-100 millivolts (mV), of the pulsed mode flasher battery (Figure A.1 circuit, Appendix A), over a time period of a few minutes have also been noticed, possibly due to temperature changes or some other effect in the battery. The amplitude of the 10 ns and 20 ns pulse is affected by the battery voltage, hence the 50 kΩ VR, in the top right of Figure A.1 flasher circuit to correct it. In 2003

these small voltage fluctuations were measured with the PDM, recording the flasher output around -6.0 volts (the calibrating standard voltage of the battery), to measure the degree of systematic error introduced by the battery small voltage fluctuations over a short time period where it could affect the calibration consistency while running the flasher calibration. The maximum voltage drift range from -6.0 volts was known from repeated earlier measurements of the flasher battery. Measurements were then taken in the laboratory using the PDM to measure the light variation of the 10 ns and 20 ns flasher settings separately, while varying the VR and hence the flasher battery voltage from 5.95 volts to 6.05 volts in 10 mV increments. The following systematic errors due to the small voltage random fluctuations of the flasher battery over a few minutes are recorded; uncertainty in 20 ns = 1.50%, uncertainty in 10 ns = 1.72%. These flasher drift voltage uncertainties of the battery, were then added to the errors for all measurements of the ADC flasher signals of the telescope.

The PDM measurements of unit 2 of the flasher have been taken from April 2001 to October 2003. Table 4.2 shows the unit 2 flasher voltage as measured by the PDM for both 20 ns and 10 ns flasher settings, versus elapsed time in minutes. The VR on the flasher circuit was adjusted to -6.0 volts for consistent readings before every elapsed minute time reading of the PDM. The third and fifth columns of Table 4.2 shows the percentage change of the PDM flasher reading from the initial time reading at $t = 0$. At no time did the PDM reading of the flasher move more than $\pm 1\%$ of the initial $t = 0$ reading, over the 165 minutes of recording with the flasher continuously running in pulsed mode.

Furthermore, the caption from Table 4.2 shows the mean PDM flasher readings for the 10 time measurements for the 20 ns and 10 ns flasher settings with the standard error of the mean $\sigma_{\overline{x}}$, Kirkup (1994) [95], defined as

$$\sigma_{\overline{x}} = \frac{k\,\sigma}{\sqrt{N}} \tag{4.1}$$

where the sample size or number of data points is N, and the sample standard deviation s, is assumed to be approximately equivalent to the population standard deviation σ, which is true for large N, for a Gaussian distribution. The small sample correction factor k, corrects the difference between the sample and population standard deviations

where, $k > 1$ if the number of data points, $2 \leq N \leq 5$. Otherwise for $N > 5$, we assume $k \approx 1$. Additionally uncertainties in the readout of the 0.1 mV scale of the DVM are taken into account, with this uncertainty also contributing maximally to about $\pm 0.2\%$ for the 10 ns setting. These results confirm that on the time scale of hours with the flasher left continuously on, there is no variation of the flasher output on pulsed mode, apart from the small scale random noise effects and the flasher battery fluctuations just discussed.

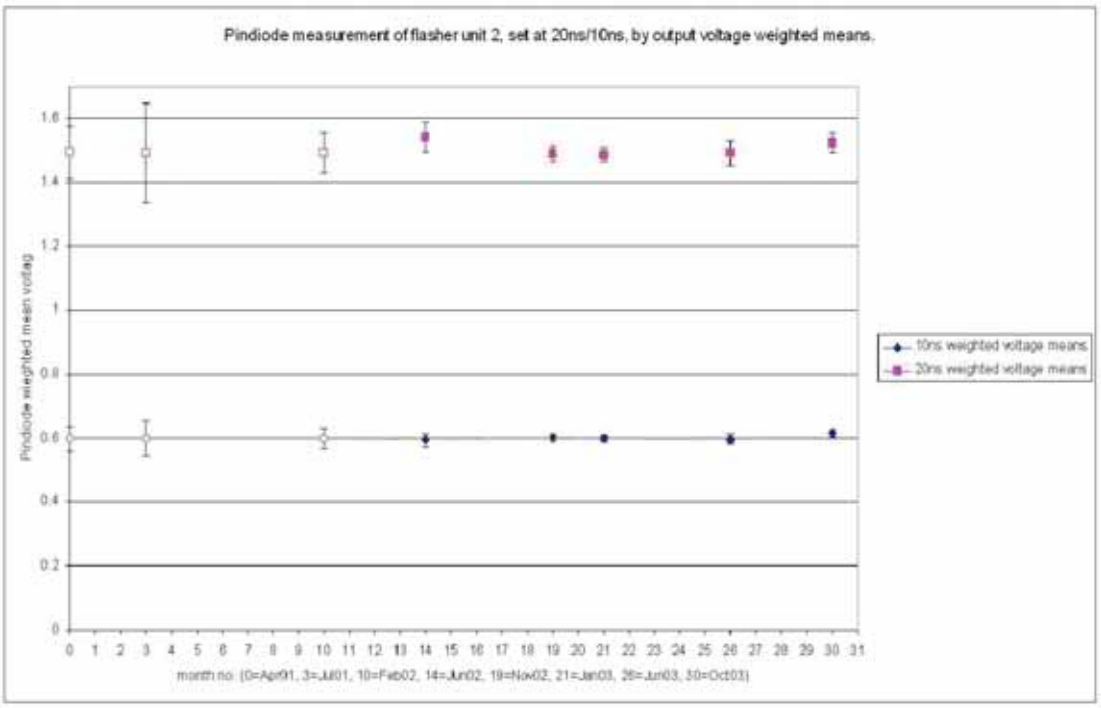

Figure 4.6: PIN Diode monitor output voltage measurements of the flasher, taken at the 10 ns & 20 ns setting, using the unit 2 emitter. Weighted means of the voltage were calculated, usually because two or more readings were taken at the time of calibration (see equation 4.2, for weighted mean definition). The open symbols indicate where the sticky tape (semi-opaque film), on unit 2 was not changed immediately before taking PIN diode readings.

Because of the very small amount of current drawn by the flasher circuit working in pulsed mode, we are confident of the consistent power supplied by the flasher battery over many months even if used on a daily basis, [136]. The continuous mode operation circuit draws power from a second 9 volt battery, labeled as **CONT. BAT.** in a

switchable circuit at the top right of Figure A.1, Appendix A. This battery is easily interchanged in a separate battery compartment in the circuit housing box.

In 2003 testing of the PDM circuit DC voltage output was done with a digital voltmeter. This was carried out to ascertain if the PIN diode monitor output was linear over a broad range of light intensities, from the flasher interchanging Neutral Density (ND) filters at room temperature. The result, Figure 4.5, shows the light "transmission" as a percentage of 10 ns and 20 ns readings by the Neutral Density (ND) filters where used. The transmission percentage is fixed at 100% for a 10 ns pulse reading without filters. Transmission values above 100% refer to 20 ns pulse readings. The linear least squares fit line includes all the 20 ns and 10 ns data points, passes through the origin, and is plotted by Excel. The 20 ns data points line-of-best-fit drawn by eye, is the steeper slope line and the lower gradient short line is the 10 ns data points line-of-best-fit drawn by eye. Both these lines-of-best fit intersect the y-axis at -0.1 volts. The difference between the slopes of the separate lines-of-best-fit for 20 ns and 10 ns readings are explained in the second paragraph (consecutive to the one below).

Figure 4.5 shows that the PDM behaves linearly with light intensity but with a DC offset of 129 mV (measured with the DVM) where there is no light to the pin diode, indicated as the "dark voltage" point on the $y-$axis in this figure. In the circuit of Figure A.2 in Appendix A, the LM324 op. amp. always has a DC input offset voltage of 2-3 mV. The input offset voltage implies that an op. amp. will produce a small non-zero voltage output even when the input pins are at exactly the same voltage. For precise DC operation, this effect should be compensated for, where some types of operational amplifiers have an offset compensation input, adjusted through a trim-pot. This is not the case for the LM324 op. amp. labeled U1B in the Figure A.2 circuit, the peak detector part previously described. Without a signal from the PIN diode, in the case where there is no light, the U1B op. amp. outputs the small DC input voltage offset of a few millivolts. The third LM324 op. amp. labeled U1C, amplifies this offset voltage with a gain of 5-100 times, depending on the setting of the 200 kΩ VR shown at the bottom of Figure A.2 in Appendix A, fixed in this circuit to +129

mV. This voltage value is always present and is added to the voltage peak height from the PIN diode whenever it responds to light pulses from the flasher. Strictly speaking, this +129 mV offset voltage should thus be subtracted from the plotted voltage points of Figure 4.5, but as the gradient of lines fitted to plotted points in this figure would remain unaffected by this procedure, it was decided to leave the results unaltered.

Scrutinizing further, Figure 4.5 shows that there is a gradient difference between the separate 10 ns and 20 ns setting line-of-best-fit. This is most likely due to the rise/fall time difference between 10 ns and 20 ns when a square wave voltage pulse width is supplied to the flasher's *Nichia* LED. The rise/fall response time of this LED is specified as 2-3 ns. This has a greater effect on the integration of the 10 ns width pulse than the 20 ns width pulse. The charge integration ratio of these two pulses have been measured, 20 : 10 ns to be 1.7 : 1.0. This was measured as the ratio between the slopes of the separate 20 ns to 10 ns PDM readings, which results in a correcting or normalizing factor of 1.18 (with 7.1% relative uncertainty), multiplied to 10 ns readings to scale it to 20 ns readings. This normalizing factor was then applied to all 10 ns flasher results, when needed with 20 ns results in the same set of data.

Figure 4.6 shows the PDM output voltage measurements of the flasher for 20 ns and 10 ns settings, over the duration of the T1 flasher calibration; (April 2001-October 2003). Weighted means of the PDM output voltages were taken if there were two or more PIN diode measurements taken within a day or two of the flasher calibration. The definition of the weighted mean, μ', for repeated results of differing uncertainties, Bevington (1992) [32], is defined as

$$\mu' = \frac{\sum (x_i/\sigma_i^2)}{\sum (1/\sigma_i^2)} \tag{4.2}$$

where each datum point, x_i, in the sum is weighted inversely by its own variance, σ_i^2. The error in the weighted mean, σ_μ^2 [32], is expressed as

$$\sigma_\mu^2 = \frac{1}{\sum (1/\sigma_i^2)} \tag{4.3}$$

There is some slight decrease in the 20 ns reading in Figure 4.6, of unit 2 over time, attributable to a minor buildup of dust and sand grains adhering to the opaque

sticky film over the hole of this unit. This dust adherence problem was rectified in June 2002, when a new clean piece of film was applied over the hole one day before flasher calibration and PIN diode monitor measurements. With all subsequent flasher calibrations, the now slightly larger reading of unit 2 was cross calibrated to the film with dust adhesion. This accounts for the larger uncertainty in the data points for April 2001, July 2001, and February 2002 compared to the other calibration months.

The results of unit 1 (not shown in Figure 4.6) on the other hand, showed quite widely changing PDM readings over time for both 20 ns and 10 ns. This large variation was caused by accidental bumping of the optical fibre which extends out of the end of the unit by 1 mm (see unit 1 sketch in Figure 4.1). The optical fibre was probably not glued adequately to the LED to make a sufficiently robust optical coupling, and thus was sensitive to jarring. This unavoidable anomaly in unit 1 led us to abandon this unit for analysis purposes, and all the flasher results used were taken by unit 2, from when this unit was first used in April 2001. Calibrations using unit 1 persisted to February 2002, although measurements using unit 2 were also taken on the same calibration nights.

calibration month	*10 ns normalized ratio*	*ratio uncertainty*
Apr. 2001	0.995	0.088
Jul. 2001	0.995	0.117
Feb. 2002	0.995	0.076
Jun. 2002	1.003	0.059
Nov. 2002	0.992	0.045
Jan. 2003	0.995	0.045
Jun. 2003	1.0	0.027
Oct. 2003	0.969	0.043

Table 4.3: Table of ratio values by month, to correct or normalize for slight variations of the flasher light output measured from the PDM, see Figure 4.6.

The varying uncertainties affecting the flasher readings of the PDM each month

are the dust adherence and battery fluctuations of the flasher, already discussed in this chapter. An additional uncertainty is in matching the rotational position of the flasher emitter unit to the block holder of the PDM (Figure 4.3) as it is coupled to the PDM at random. To find this degree of uncertainty, the variation in the PDM reading was measured by rotating the flasher emitter through 360°. The variation in the rotational position effect was estimated to be ±0.7%. From November 2002, the rotational position of the flasher emitter to the PDM was fixed by marking both parts and the insertion of the emitter unit into the PDM was then matched by these marks. Thus the sum of these three varying relative uncertainties by month, contribute to the weighted means calculation of the flasher output measured by the PDM, resulting in the 10 ns normalized ratio and ratio uncertainty shown in Table 4.3.

Based on the slight variations in the weighted mean PDM readings of the flasher, shown in Figure 4.6, Table 4.3 shows the normalized ratios of the PDM readings of the flasher. These values are normalized by taking the ratio of the weighted mean PDM flasher voltage reading from June 2003, to the weighted mean PDM voltage readings for all other calibration months. When correcting for the slight variation in the flasher light output by calibration month, the 10 ns normalized ratio value from Table 4.3 is multiplied by the flasher mean (sum) ADC value from the telescope camera, taken on the month referred in Table 4.3, with the uncertainty in this table added to the statistical uncertainty of the mean ADC value.

At each visit to Woomera, the flasher apparatus was checked to see if the point light source of either unit 1 or 2 was maintained at the focal point of the 15 mm lens in the laboratory. Also the flasher battery level was checked and adjusted to -6.0 volts. PDM readings of unit 2 were taken prior to flasher calibration of the T1 and T2 telescopes and immediately afterward.

Chapter 5

Flasher calibration: Analysis and results

5.1 Flasher field measurements and data file calibrations

5.1.1 Introduction

The aim of this chapter is to expand on the results of flasher calibrations of T1 and T2, with reference to the flasher unit explained previously in Chapter 4. This chapter is split into four overall sections: Section 5.1, that deals with the preparatory work for conversion of raw data format to calibrated data format. Section 5.2, deals with the preliminary analysis work carried out for the flasher calibration of T1 (and also applied to T2 in some cases). The third section deals with the flasher calibration of the T2 telescope (Section 5.3), where most data preparation and analysis procedures are applied in a similar fashion to T1. Chapter 6, examines a measurement of the energy detection threshold of the T1 telescope using cosmic ray showers, while the dish is pointed at the zenith.

The studies outlined in this chapter follow: Firstly, the settings of the discrimi-

nator voltage thresholds for T1 flasher calibration (Section 5.1.2), and the effect of background light on ADC data (Section 5.1.3). Secondly, the flasher settings, neutral density (ND) filters used, and data recording used for undertaking flasher calibration runs (Section 5.1.4). Also for T1, a detailed description is made of flat-fielding (Section 5.1.5), and ADC pedestal removal techniques (Section 5.1.6). Additionally, correction of camera pixels flagged as "bad channel" is examined (Section 5.1.7). Furthermore, detailed analysis of the likelihood of diffraction fringes projecting from the flasher unit or associated with the optics of the both T1 and T2 telescopes are discussed (Section 5.2.1). Finally, an analysis of the movement of the flasher image in the FoV of the T1 and T2 telescopes between calibration measurements, is explored using the two-dimensional cross-correlation technique (Section 5.2.2 and Section 5.3.2 respectively). The change in camera pixel signal as a result of the cross-correlation is concluded in Section 8.1.1 for T1 and Section 8.1.2 for T2. A summary of an attempt to measure the output of the flasher (at the telescope) by using a single photomultiplier tube apparatus is inserted (Section 5.2.4). Furthermore, a qualitative assessment of the size of the flasher image is made (Section 5.2.3) and an analysis of early procedures and results of correcting for defective pixels in T1 is included (Section 5.2.5), partnered by a similar discussion on the camera geometry and pixel correction techniques of T2 (Section 5.3.1).

The software used to carry out the raw to calibrated data file conversion was *FULL*. This software package, mainly written in *FORTRAN90* and *C* program languages was originally developed by Prof. R. Enomoto (University of Tokyo), for EAS Monte-Carlo simulations for the CANGAROO collaboration. The meaning of "raw" and "calibrated" data formats used by *FULL* are explained in Sections 5.1.4 and 5.1.5. Gradually *FULL* grew in size and complexity to include many offline analysis programs for the T1 telescope data and later for the T2 to T4 telescopes when they came on line, including stereoscopic data analysis. *FULL* continues to be developed, and now includes many additional C^{++} programs. Programs written by this author for analysis, are embedded within *FULL*'s framework.

Flasher calibrations were initially obtained on a monthly basis from April 2001 for

T1 and January 2003 for T2. Dual flasher calibrations were obtained using both unit 1 (until June 2003), and unit 2 (for all eight calibration months used in this thesis). The light outputs from units 1 and 2 were measured with the pin diode monitor, coincident with flasher calibrations. Data files of 10ns duration for unit 2 were selected from the flasher calibration of T1 and T2 and its *calib10* mean sum ADC signal (see Section 5.1.4, for an evaluation of the "mean sum ADC"), used to test the response of the T1 telescope to a signal of constant strength over the year. This data file was then normalized in mean sum ADC by the following process: A normalizing month (in our case October 2003) was selected compared to which the mean sum ADC magnitude of all the other seven flasher calibration months (for T1) was determined via the following ratio: Selected month mean sum ADC by the October 2003 mean sum ADC. The light output from the flasher was monitored by the pin diode apparatus (see Section 4.2), and the mean sum ADC was corrected from this result before the ratio was applied. The end result is referred to as the normalized mean sum ADC value (see equation 5.16).

The normalizing month (for mean sum ADC) was October 2003 for both T1 and T2. The pin diode monitor used June 2003 as a normalizing month (see Table 4.3). This choice is very unlikely to affect our results for normalizing as we are measuring the overall magnitude of the mean sum ADC, and this can be compared using any arbitrarily selected "normalizing" month for a series of independently measured results. However, in a single special case, the June 2003 mean sum ADC result was attenuated by mirror dewing (see Section 5.2.2) and so would not be a good set of data to use for mean sum ADC normalizing. The pin diode measurements, on the other hand, are unaffected by mirror dewing.

It was decided to use the 10 ns flasher duration as this pulse width would be less likely to cause saturation of the phototubes (compared to 20 ns pulse width). To further ensure that saturation would not be a problem, the flasher calibrations of T1 and T2 were carried out with a 9.5 mm diameter aperture ring inserted in front of the flasher lens (see Section 4.1.1). Unit 1 measurements were abandoned when measurements were found to be inconsistent from this unit (Section 4.2.2). Unit 2 continued to give

constant pin diode measurements over the data taking period with little fluctuation (see Figure 4.6).

From April 2001 up to October 2003, flasher calibrations of the T1 telescope were carried out on an approximately 3-6 monthly basis for a total of eight calibration periods (Section 4.1.2). From January 2003 to October 2003, three flasher calibrations of T2 were also carried out (Section 5.3.1).

5.1.2 T1 discriminator settings for flasher calibration

Module	*Level*
tdc_discri	-240 mV
lsum_discri	-380 mV
nhit	-743 mV
nbox	-351 mV
CAMAC	-1762 mV

Table 5.1: Discriminator module settings of the T1 telescope for the flasher calibration at the mound.

To trigger the T1 telescope from the flasher light pulses, the telescope discriminator module levels were set at or close to the voltage levels for T1 in Table 5.1 (above) for every calibration taken at the rifle club mound. The discriminators (levels to be set), are indicated in the following by bold text, e.g. **nhit**. The discriminator settings in Table 5.1, were used in flasher calibration data taken during "shower mode", as distinct from LED mode (or "random trigger" mode). The voltages in Table 5.1, refer to the control voltage level settings for these modules and discriminators to control trigger rate and data acquisition for the flasher calibration. Shower mode has distinct, fixed voltage levels set for most data acquisition modules for the triggering of Čerenkov events from source observation and flasher calibration, according to observation conditions (for example, by Table 5.1), whereas the LED mode has "random" voltage levels (see Section 5.1.4), for the **nhit** module in the data acquisition. The function of the discriminator modules, listed in Table 5.1; **lsum**, **tdc**, **nhit**. **nbox** and **CAMAC**, are

discussed in Section 3.2.6. Discriminator settings for the flasher calibration of the T2 telescope are discussed in Table 5.6.

The "random trigger" mode lets the voltage threshold level of the **nhit** discriminator to float, allowing much low level light background noise to actuate an event trigger. This is useful when the level of light is very low, such as when the camera lid is fastened or when the telescope is pointed at a point on the horizon where there are no ground lights and the telescope elevation is too low for most EAS Čerenkov events to trigger the telescope.

5.1.3 Background light affecting ADC count

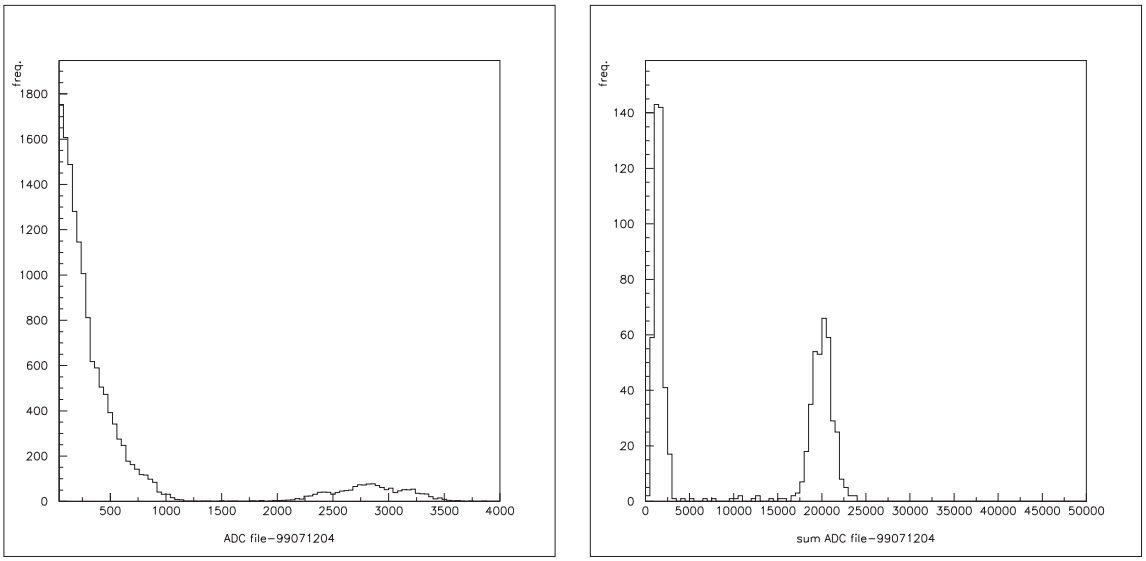

Figure 5.1: Background light peak (left peak on both histograms) with added flasher signal (right peak both histograms), taken in 1999 from the airport tower. *Left*: Histogram plot of raw ADC count values for all 256 pixels in the inner T1 camera, for all events. The number of event triggers in this run (99071204), is 5719. The flasher unit triggers at 33 Hz, interspersed with many background light event triggers without the flasher signal present. *Right*: Histogram of; $\sum_{i=1}^{256}$ (sum of raw ADC counts of the inner T1 camera pixels for each event), for all events (number of events is 5719). The data file is the same as the *left* histogram. The sum ADC (flasher signal) histogram peak at $\sim$ 20000 counts, is explained in Section 5.1.3.

The flasher ADC signal is much higher than sky noise, even when there is bright

background light, as shown in Figure 5.1 (above), when a flasher calibration was initially taken at the Woomera airport control tower (at a slow pulse repetition rate (33 Hz), at 20ns pulse width setting). In these cases, many random high level noise triggers are included in the data from bright ground lights in this vicinity. The discriminator module voltage levels thresholds indicated in Table 5.1 which are important in controlling the trigger acceptance of small Čerenkov events, such as gamma rays over sky noise, do not change the magnitude of the very bright flasher calibration signal. However, the number of background light events acceptance increases when the discriminator thresholds, shown in Table 5.1, are lowered.

The flasher ADC signal is clearly seen as a low broad peak to the right of the histogram in Figure 5.1 (*left*), ADC count histogram with a peak around 3000 ADC counts, whereas the background noise is the high peak at ADC values < 1000 counts. In this histogram, the background light event triggers considerably outnumber the flasher event triggers. In Figure 5.1 (*right*), the considerable separation between the background light signal peak at ~ 2000 sum ADC counts and the flasher signal peak at $\sim$ 20,000 sum ADC counts in this histogram, accentuates the effect in the separation of background light and noise to flasher signal. The sum ADC is the accumulation of the ADC counts, over the 256 pixels of the inner T1 camera, which accounts for its high value of mean sum ADC $\sim 20,000$ counts when all ADC count camera pixels are added together for the flasher signal event trigger. Without a flasher signal present in the event triggers, the accumulation of sum ADC values creates a histogram peak at mean sum ADC ~ 2000 counts.

In comparison to Figure 5.1 at the airport control tower, the lower background light levels result in lower noise levels at the rifle club mound. Unfortunately, at the mound, no flasher data were taken at the 33 Hz setting; all flasher data were taken at 1 kHz. An effort was made to set the discriminator voltages shown in Table 5.1, at the same level for all flasher calibration analysis in this chapter. These settings were insensitive to the recording of a constant flasher signal level with the telescopes.

The hypothesis that the recorded signal amplitude of the flasher fluctuates if the voltage levels for the discriminators are changed with all other parameters (e.g. light

filters) remaining fixed, has not been tested by experiment. However, we hypothesize that the sensitivity of the flasher signal measurement to the discriminator threshold variations may be reduced by the following points: 1. The flasher signal is present in all triggered event records (there are no background event triggers without the flasher image, present in the data file). 2. The ADC amplitude of the flasher signal is considerably higher than all but the largest cosmic ray Čerenkov shower triggers. Most of the background noise events have low summed ADC values (summed from the inner camera pixels per event), compared to the consistently high summed ADC values from the flasher, even when a low transmission ND filter considerably reduced the flasher signal amplitude. 3. The high ground light noise level produces a broader, lower amplitude signal peak for the ADC counts histogram (without background random hit pixel triggers, present in Figure 5.1.

Figure 5.2: Gaussian or Normal distribution; $f(x;\mu,\sigma) = \frac{1}{\sigma\sqrt{2\pi}} \exp\left[-\frac{(x-\mu)^2}{2\sigma^2}\right]$, where σ is the Population Standard Deviation and the mean is, μ, Bevington (1992) [32]. These three curves are based on this statistical function only and not flasher data, for illustrative purposes. Typically, while $\mu \neq 0$ for a signal, these three curves show flattening when the FWHM, Γ, widens with increasing background noise level, where Γ_1 has the lowest background noise level (smallest FWHM), to Γ_3, which has the highest (largest FHWM). All three curves have the same mean or maximum "signal amplitude", $\mu = 0$.

The effect of higher background light on ADC counts is to include more noise counts in the "wings" of the ADC histogram, hence broadening the FWHM (see equation 3.1, Chapter 3), of the flasher signal mean ADC peak. The mean ADC count for the flasher remains relatively unaffected by high sky noise, which does not change the value of the mean ADC peak, i.e. with AC coupling. Thus the position of the mean ADC flasher signal peak maximum should remain the same (if the flasher signal is constant), regardless of the levels of ground light noise at night without the moon present. Unfortunately it is not possible to provide an example of this, as the flasher signal amplitude was later found to vary between monthly calibrations as indicated later. A flasher "mean ADC count" fixed signal comparison between the high ground light noise at the airport control tower and the low ground light noise taken on a different month at the rifle club mound is also not possible because of the movement of the flasher image in the FoV of the dish, explained later in Section 5.2.2. However, Figure 5.2 indicates the general effect of Gaussian signal peak broadening in the peaks labeled Γ_2 and Γ_3, due to an inclusion of a higher level of background noise compared to the narrowest peak, Γ_1. All three peaks in this figure are of the same fixed signal amplitude or mean, μ. These overlaying peaks show the Gaussian mean as μ, and the FHWM as Γ. Note that the moon produces so much background light that it endangers the camera PMTs under high voltage (HV), hence all flasher calibrations were taken when the moon was below the horizon.

5.1.4 Flasher calibration procedure

Excluding error corrections to the ADC signal amplitude (see Sections 5.2.2 and 5.2.5 this chapter), and LED flat-fielding correction explained in the next section, the ADC signal amplitude ("mean sum ADC" for the flasher) is calculated in the following way after data acquisition: From the data file, we read the ADC value for each channel (PMT number) from the inner camera photomultiplier tubes (for T1, PMT numbers 1 to 256). We add these 256 ADC numbers together for each triggered event and produce the sum ADC. Over the number of triggered events in a data run (usually 2000 to 10,000 events as explained in the next paragraph), we produce a histogram of

sum ADC events. Using Gaussian fitting functions in the histogram graphics analysis program *PAW* (version2.11/13, Cern Institute, Geneva, Switzerland), we obtain the mean and standard deviation from the sum ADC histogram of the flasher data file, producing the "mean sum ADC" (or the "raw" ADC amplitude of the flasher signal, for that setting, without corrections).

Flasher data files were usually obtained, with the following operational steps applied at the rifle club mound (more ND filters have been added on some calibration months):

1. Unit 2 20 ns - approximately 2000 to 10000 events.
2. Unit 2 10 ns - 2000 to 10000 events.
3. Unit 2 (20 ns) with ND 0.4 filter - 2000 to 10000 events
4. Unit 2 (10 ns) with ND 0.4 filter - 2000 to 10000 events
5. Flasher is off. Night sky background run using random trigger mode - 10000 events.

For the T1 telescope, Tables B.1 and B.2 in Appendix B, indicates the flasher calibration data file run numbers, the months they were taken, the settings of the flasher and the numbers of events during each calibration run. All data files were taken using the unit 2 emitter (Section 4.1.3). Similarly, Table B.3 (Appendix B) refers to flasher settings and calibration data file runs for the T2 telescope using the unit 2 emitter. In Table B.1, there was some doubt about the flasher settings for the calibration file numbers 1071724 and 1071725, however these two data files were not used in any T1 flasher analysis.

In all three tables in Appendix B, the "background or random trigger" runs refer to the telescopes taking data when the flasher was off and trigger data was acquired from the night sky (in the field of view) only. Because of the low level of light, it was not possible to capture any more than a handful of event record triggers with (over half and hour interval or more of data acquisition) the shower mode discriminator settings set to the levels shown in Table 5.1 for T1, i.e. the flasher trigger setting. Therefore, the event trigger was set to "random trigger" where the discriminator voltage threshold

level would rapidly change up or down to maximize the number of acquired record triggers, allowed by the data acquisition rate, to record all events (see "dead time" in Section 3.2.6). Thus, the background light data could be collected in a timely fashion. The random trigger mode was also used for dish LED flat fielding by manually switching T1 between shower mode and random trigger mode (see LED flat fielding in the next Section 5.1.5).

At the end of a night's observation, the flasher data files were backed up from the telescope data acquisition computer onto DAT tape and brought back to Adelaide. The data on tape was in "raw" format, where no flat-fielding of the camera pixels was applied to the data, nor was pedestal noise removed from the ADC pixel values.

5.1.5 LED flat fielding

Flat fielding is a process where the unevenness in gain of the hundreds of PMTs across the camera can be rectified via software techniques and gain calibration. For the T1 telescope, two LED data files were taken prior to data acquisition from any gamma ray source or flasher calibration. Flat fielding was carried out on T1 using the pulse generator operating at 1 kHz, supplying power to the calibrating LED in the centre of the telescope dish. The intensity of the LED output was controlled by manually switching the pulse generator between two settings; 0 dB and 1 dB. The LED intensity ratio between 0 dB (the brighter setting) and 1 dB should be approximately 1.3 times. The expression to obtain the Decibel unit for power or intensity is, Martin (1929) [116]

$$\mathrm{dB} = 10\ log_{10}\left(\frac{X}{X_0}\right) \tag{5.1}$$

where X_0 is a specified reference unit, with the same units as X, which in our case is intensity or brightness of the LED.

Two data files at 0 dB and 1 dB settings are then used to fit a straight line through these two points and zero. An example produced by the program *calib10*, Okumura (2000) [132] (last paragraph of this section), is shown in Figure 5.3 for PMT number one. This is replicated by the same program for 1-16 PMT pixels in Figure 5.4. As seen in Figure 5.3 (and in Figure 5.4, although this is less visible), the variable on the

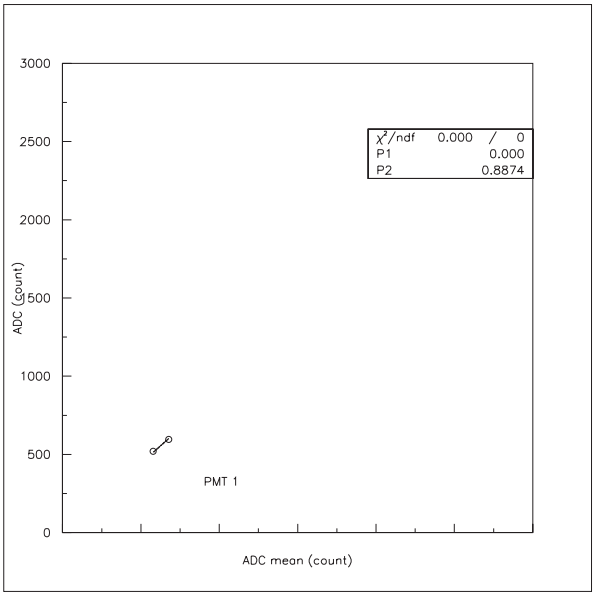

Figure 5.3: A LED calibration (or scan) plot result for a single PMT pixel (number 1), produced by *calib10*, Okumura (2000) [132]. The mean ADC (the average summed ADC counts of every camera pixel shown on the x-axis), is plotted against their individual ADC count value on the y-axis. The two circle points on each graph is a LED run; the slightly higher value pixels is a LED data file set to 0 dB, and the lower value is LED 1 dB. These points are closely spaced due to the standard output of flat-fielding calibration. The equation; $y = P2x + P1$, describes the fitted line through these two points, results shown in the upper right box.

abscissa is mean ADC count for all the pixels in the camera, and the variable on the y-axis is ADC count for each pixel. All three data points (including the axis origin) are fitted using a linear least squares fit. The slope of the fitted line is shown as the P2 parameter in the upper left right corner box in Figure 5.3, and for each pixel in Figure 5.4. The parameter P1 is the fitted y-intercept, which is required to be zero (explained in the last paragraph of this section). The equations resulting in the P1 and P2 parameters values to flat-field the T1 camera are as follows, [132]

$$Y_i = G_i^{ADC} \times X_i \tag{5.2}$$

where the relative gain value for the i^{th} pixel, G_i^{ADC}, has been obtained by fitting the following linear least squares function, (resulting in P1 and P2), by using these two

Figure 5.4: LED scan result for 16 PMTs (pixels) in Box number 1, produced by *calib10*, [132]. PMT 1 is shown larger in Figure 5.3. Each graph is a LED scan in ADC counts for the i^{th} pixel number (ADC pixel numbers 1 to 16 in this case).

points, [132];

$$(X_i, Y_i) = (Q(0 \text{ dB}), Q_i(0 \text{ dB}), (Q(1 \text{ dB}), Q_i(1 \text{ dB})) \tag{5.3}$$

where $(Q_i(0 \text{ dB}), (Q_i(1 \text{ dB}))$ is the run mean ADC value for the i^{th} pixel and $(Q(0 \text{ dB}), (Q(1 \text{ dB}))$ is the averaged mean ADC for all (run mean) ADC pixels of the camera. The definition of data file run mean ADC is described in equation 5.4 (Section 5.1.6). The i^{th} pixel gain value, G_i^{ADC}, is the slope in parameter P2 for that particular pixel, and these gain values are normalized to one by their all camera pixels averaged value. The removal of ADC pedestals from pixels is described in Section 5.1.6.

For LED flat fielding, the data acquisition was set as for the random trigger mode,

where all triggers were accepted for recording without requiring to pass most hardware discriminator threshold levels. Since the camera is uniformly brightly illuminated by the dish LED (the illumination of the camera actually falls off slightly towards the camera FoV edge in comparison to the camera centre), triggers from the dish LED dominate triggers acquired in random trigger mode.

In this section, "generic" data file formats embedded within *FULL*'s framework are highlighted in bold, e.g. **calib10b** (calibrated data for T2). "Generic" means software procedures in *FULL*, developed by CANGAROO staff, for the purposes of data retrieval and calibration and in use for analysis where a distinct data bank is produced for each calibration type. Although the data banks between T2, T3 and T4 are very similar in form, the data are unique to each telescope except for global triggers. Calibrated data file formats for T1, T3 and T4 respectively are denoted; **calib10/calib10a**, **calib10c**, and **calib10d**, although telescope data from T3 and T4 are not examined in this thesis. Telescope T1 has three names for calibrated data type, where **calib10** was generated before T2 came on line and **calib10a** after T2 became operational. In 1999 to March 2000, the T1 dish did not include all the 114 individual 0.7 metre composite mirrors out to the full 10 metre dish diameter (see Figure 3.2). Instead it had fewer composite mirrors, only out to 7 metre diameter from the dish centre, shown as the central mirrors (numbers 1 to 60) in Figure 3.2 (excluding the yellow shaded mirrors). In this period, the T1 calibrated format was named **calib7**. This format will henceforth be rarely referred to, as most calibrated data files from T1 analyzed in this thesis were taken after April 2000, hence **calib10**. Names of programs within *FULL* which produced these calibrated data file formats are indicated in italics, e.g. *calib10b*.

Conversion to *FULL* calibrated data format (**calib10** and **calib10a**) for the T1 telescope of all the flasher data files, was carried out using the LED 0 dB and 1 dB data files for flat fielding and an ADC pedestal file for ADC pedestal removal. For T1, ADC pedestal data were usually retrieved from a separate file obtained with the camera lid fastened, sometime in that month, not necessarily on the night the flasher calibration was taken. For T2, the ADC pedestal data were obtained from pedestal data files with the camera lid fastened on the night the flasher calibration was taken. Consequently,

calib10a or **calib10** data file format (henceforth denoted only as **calib10a**), was used for signal analysis for the flasher for T1. The T2 telescope used a different flat fielding and pedestal removal routine to T1, to obtain its **calib10b** calibrated data conversion.

The process of raw data conversion to **calib10a** data format was a software routine within *FULL*, written by Dr. K. Okumura, called *calib10*, [132]. The P1 parameter discussed previously in Figures 5.3 and 5.4 and in equations 5.2 and 5.3, used in calculating the gain of each pixel in T1, did not have the ADC pedestal removed before P1 was calculated for each pixel, although both the gain and pedestal factors were incorporated into the process of producing **calib10a** when making the calibrated data file. The fitted values were forced through the origin, by making the y-axis intercept zero and hence P1=0, with the inference that the zero intensity of the LED means no light signal. This would be true if the telescope camera lid were fastened, but not when background night sky photons also impinge upon the camera when the dish flat fielding LED is illuminating the camera. These two factors may be construed as being a minor systematic error in the calibration process using *FULL*, in the scale of the overall systematic errors found in T1 in the flasher calibration.

5.1.6 ADC pedestals

The ADC pedestals of T1 were checked by the author over the flasher calibration months of this telescope (Section 4.1.2), to ascertain whether there were any significant changes to the values of these pedestals in this time. The ADC pedestal files were selected from the raw to **calib10a** data format conversion by the Institute of Cosmic Ray Research at the University of Tokyo. Altogether, fifteen ADC pedestal files were selected (usually one each month), and the value of the ADC pedestal binned with that pixel from other months. Table 5.2, shows the selected ADC pedestal files. In the last column of Table 5.2, there is a reference to sky noise. The pedestal file runs were checked to see if the run was done with or without the camera lid fastened. If the camera lid was not fastened, then sky noise must be an included factor in the pedestal run.

For the data files in Table 5.2, the shell scripts to create the **calib10a** data files

No.	*Pedestal File run no.*	*Month(Year)*	*ICRR calib10a shell script*	*Sky noise included?*
1	01091104	Nov 2001	calib10-0111.sh	yes
2	01120904	Dec 2001	calib10-0112.sh	no
3	02012402	Jan 2002	calib10-0201.sh	no
4	02021301	Feb 2002	calib10-0202.sh	no
5	02031806	Mar 2002	calib10-0203.sh	no
6	02040608	Apr 2002	calib10-0204.sh	yes
7a	02051525	May 2002	calib10-0205.sh	yes
7b	02051525 (R)	Jun 2002	calib10-0206.sh	yes
8	02071403	Jul 2002	calib10-0207.sh	no
9	02080101	Aug 2002	calib10-0208.sh	no
10	02082807	Sep 2002	calib10-0209.sh	yes
11	02100902	Oct 2002	calib10-0210-part.sh	no
12	02102907	Nov 2002	calib10-0211.sh	no
13	02121224	Dec 2002	**calib10_0212_T1.sh**	yes
14	03042713	Apr 2003	**calib10_June03.sh**	yes
15	03101603	Oct 2003	**calib10_Oct03.sh**	yes

Table 5.2: Table of ADC-Pedestal Files used to test variation in ADC pedestals per month from Nov. 2001 to Oct. 2003. Shell script names in bold font have been sourced at the University of Adelaide.

were sourced from the **calib10a** archive at the ICRR institute, University of Tokyo, Japan. The shell script names in bold font have been sourced from the University of Adelaide; (R) indicates a ADC pedestal file used repetitively for two successive months.

Figures C.1 to C.16 in Appendix C, shows the mean ADC count pedestals for pixels (for the inner 1 to 16 boxes; 1 to 256 camera pixels), calculated from the raw to **calib10a** data conversion process histograms from the software package, *FULL*. The bin width for Figure C.1 (and the subsequent 15 figures in this appendix for each box), is five ADC counts.

Also in Appendix D, Figure D.1 shows the difference between the ADC pedestals and the discrete arithmetic ADC mean values (see equation 5.4, below), and the ADC mean value calculated from histograms via the program *PAW* (version2.11/13), where it is used in the **calib10a** conversion process in *FULL*, as shown in Appendix C. These histograms from Figure D.1 (box 1) are distributed about zero, and all other 15 subsequent figures in this appendix, are for boxes 2 to 16 (inclusive of all pixels 1 to 256 in this appendix). The bin-width for Figure D.1 and all other subsequent 15 figures, is one ADC count. Formula 5.4, indicates the arithmetic mean ADC ($\overline{\text{ADC}}$), or an average from discrete ADC values, rather than from binning them in a histogram and finding the mean from a Gaussian fit to the histogram, i.e.

$$\overline{\text{ADC}} = \sum^{n} \frac{\sum_{i=1}^{256} \text{ADC i}^{\text{th}} \text{ pixel value}}{n} \tag{5.4}$$

where all the $i = 1$ to 256 ADC pixels are summed over the camera for each event trigger and n is the sample size or number of flasher records or events triggers in the data file, for the mean. The sum is taken over all the 256 ADC pixel values of the inner camera (576 pixels if the outer camera boxes are included). This arithmetic mean ADC has a very similar result to finding the Gaussian mean from a histogram, as indicated for Figure D.1, Appendix D and other pixels in subsequent boxes, even for the small sample size used, because the ADC pedestal difference is closely distributed about zero.

5.1.7 Pixels corrected in the flasher image via "bad channel" correction

The flasher image in the T1 camera is no more than 1° by 1° in size near the centre of the camera, see Figure E.1, Appendix E . In Figure E.1, the pixels are not normalized to a set level, unlike Figure E.3 in Appendix E. As a consequence of retaining all the flasher signal in the inner camera boxes 1-16, it was decided to leave the outer boxes 17-36 of the T1 camera pixels out of the analysis of flasher signal, to reduce any possible systematic error introduced by the outer boxes channels.

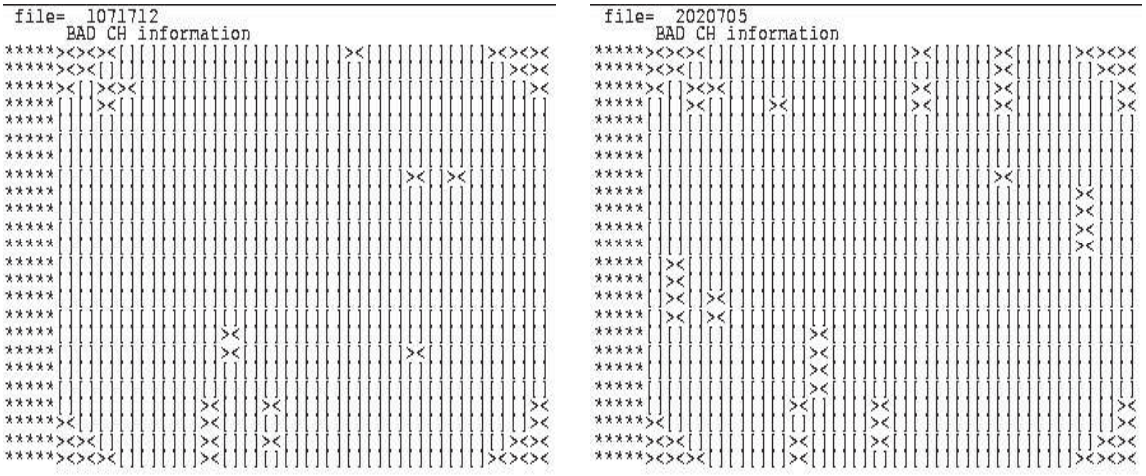

Figure 5.5: **Calib10** bad channels as represented by the T1 camera. Crossed pixels are flagged as bad channels, square ([ ]) pixels are accepted (not bad channel) pixels and the asterisks are printing padding. PMT boxes information for T1 camera is found in Figure 3.7. The left figure is from July 2001 (data file no. 1071712), and the right figure from Feb. 2002 (data file no. 2020705).

The box numbering according to the electronics channel (pixel) identities is shown in Figure 3.7. The outer boxes show mainly sky noise, but commonly have **calib10a** bad channels in at least four channels of any of the these boxes (17-28, see Figure 5.5). In the PMT array of the T1 camera, bad channel pixels are shown at the crossed pixel positions in Figure 5.5, whereas a normal pixel is not crossed. Figure 5.5, representing the T1 camera, shows seven crossed pixels at each corner. These are the corner boxes (box numbers 33 to 36) which have empty PMT sockets, and so are flagged as bad channel pixels (see Figure 3.7, where the six empty PMT sockets are shown as grey pixel numbers in boxes 33, 34, 35 and 36 respectively). These corner boxes are not used in flasher calibration analysis and are regarded as superfluous. Furthermore in Figure 5.5, a row of asterisks are displayed, however these are print character padding.

Apart from the empty sockets in the corner boxes, a bad channel data bank is flagged (or set to one) if: 1. A pixel signal is not counted (i.e. has zero counts for all triggers in that run, including a zero ADC pedestal), sometimes indicating a dead PMT, or empty PMT sockets in the camera corners. 2. The TDC hit rate or ADC count value shows a deviation more than five times larger than RMS (Root Mean

Square) from its mean or average value. 3. The ADC mean value of that pixel exceeds the value of five times the mean ADC value of all 576 pixels in the camera. If the bad channel data bank is set to zero, it is not a bad channel. Bad channel pixels record an ADC or TDC count value of zero for all trigger events in the data run.

In theory, the bad channel data bank was added to **calib10a** to remove faulty pixels from analysis. In practice, while useful to flag empty PMT sockets and grossly malfunctioning PMTs as bad channels, the bad channel feature did not flag PMTs that did not function linearly over the dynamic range designed for the particular *Hamamatsu* R4124 PMT of the T1 camera.

5.2 T1 flasher calibration analysis

5.2.1 Anomalous diffraction effects in the flasher image

In an early analysis of the flasher calibration experiment, it was noticed in the CANGAROO collaboration that an apparent "square structure" existed in a two-dimensional image of the flasher. However, note that in Figures E.1 and E.2 (Appendix E), for the two-dimensional contour images of the flasher, no indication of a "square structure" can be seen, nor in other two-dimensional images analyzed by the Adelaide group in the CANGAROO collaboration. Further hypotheses about this follow.

It was known however, that the "square structure" appeared as an apparent halo or arc around the central flasher image. From the analysis of the Adelaide group, the conclusion was that the "square structure" is either an artifact generated by the analysis software used in early analysis procedures, or is an anomalous defect of the T1 camera or data acquisition electronics modules (see Sections 3.1.2 and 3.2.6), not related to the optics of the flasher or telescope. The failure of electronics modules seems the most likely cause of the "square structure" edge or side where a vertical line of four pixels in an amplifier box fails to register any signal in the camera, which happened on occasions with T1.

Notably from repeated observations, no flaring around the central flasher image has been seen, mainly due to a internal light baffle installed in the flasher optical tube

to prevent internal reflection effects, and no shadowing from the four camera struts appears to have interfered with the flasher image. Since this last shadowing effect may only be noticeable at the very edge of the 10 metre dish, which optically transforms to the outer boxes of the camera, the flasher image is decidedly in the central boxes as discussed, and the outer boxes are not included in the flasher analysis. The "square structure" may be due to diffraction effects. This possibility is discussed in the following paragraphs in this section, and summarized at the end of this section.

For optical interference, there may be three different diffraction effects. The first effect, at the T1 telescope, may be similar to the "diffraction spike" or "spider diffraction" effect which sometimes occurs in the images of bright stars in astronomical telescopes, Illingworth (1994) [87]. Spikes are seen around the point-like star image, due to the diffraction of light according to the Huygens-Fresnel principle, Hecht (1987) [78], around the two to four supporting vanes holding the secondary mirror in place. Because of the vastly different scale of the thick camera support struts in the 10 metre dish, to the millimeter (tenths of a millimeter) thickness vanes in astronomy, for visible or near-visible light spectra, we can rule this diffraction effect out.

The second diffraction effect to take into consideration is the Airy diffraction pattern of concentric rings from a circular aperture, for Fraunhofer diffraction. The size of the central Airy disc is now due to the size of the flasher lens aperture which is the light emitter, see Figure 4.1 to view the flasher lens aperture. Far away from the aperture, the angle, θ, at which the first diffraction minimum occurs, (i.e. the edge of the Airy disc), is derived by the following formula, [78]

$$\sin\theta = 1.22\,\frac{\lambda}{D} \tag{5.5}$$

where λ is the light wavelength, which for the *Nichia* NSPB 510S LED in our case is 470 nm, and D is the diameter of the aperture. Further, to determine the displacement of the edge of the Airy disc for the T1 telescope at the rifle club mound, we use

$$\tan\theta = \frac{x}{775} \qquad x \text{ and } 775 \text{ distance in metres} \tag{5.6}$$

where x is the position of the edge of the Airy disc away from the centre of optical axis of the flasher (or centre of the flasher lens), at the distance of the T1 telescope

from the flasher on the rifle club mound. This distance has been estimated using crude theodolite measurements to be; 833±58 metres, for which we have used the lower limit of 775 metres, to minimize the size of x. The size of the aperture ring inserted in front of the flasher lens is 9.5 mm in diameter. Using this D in equation 5.5, we can estimate that the edge of the Airy disc is, $x \approx 4.7$ cm away from the centre of the the flasher optical axis at T1. If we were to use $D = 30$ mm, i.e. the full size of the flasher lens, the edge of the Airy disc is, $x \approx 1.5$ cm from T1's centre. The Airy disc is thus more likely to appear for the 9.5 mm non-refracted ring aperture, than for the 30 mm aperture holding the flasher lens. The size of the Airy disc at the telescope for the 9.5 mm diameter ring aperture inserted in front of the flasher lens ($x \approx 4.7$ cm) is not negligible, however it is very small compared to the light pool spot size of 14.6 metres diameter; calculated as the divergence of the flasher light beam in Section 4.1.3, as the properties of the finite size of the emission region (≈ 1 mm in diameter) over the flasher and telescope separation distance.

Since the Airy disc occurs for far field diffraction, we should consider whether the the near-field (or Fresnel) diffraction or the far-field (or Fraunhofer) diffraction dominates in our case by using the Fresnel number, F, [78]

$$F = \frac{a^2}{L\,\lambda} \tag{5.7}$$

where a is the size of the aperture, λ is the wavelength of the light and L is the distance between the diffraction barrier and the screen, all are in metres. In general, Fraunhofer diffraction occurs when $F \ll 1$, and Fresnel diffraction when $F \gtrsim 1$. Using the minimum distance of $L = 775$ metres from the flasher to the telescope dish, $\lambda =$ 470nm, and our two flasher aperture values of a =9.5 mm and a =30 mm, we calculate the Fresnel number for $a = 9.5$ mm to be $F = 0.25$, and for $a = 30$ mm, $F = 2.5$. Therefore according to the Frensel number in equation 5.7, it appears that we probably could approximate the smaller 9.5 mm aperture for Fraunhofer diffraction and hence calculate the size of the Airy disc, even though strictly, F is not much less than one. Fresnel diffraction effects might have to be a consideration for the larger 30 mm flasher aperture, when the flasher was positioned on the rifle club mound as $F = 2.5$.

The Fresnel number for the flasher positioned on the airport control tower, approximately 5.7 km distant from T1, has been calculated using equation 5.7 for the 9.5 mm aperture to be $F = 0.03$, and for the 30 mm aperture to be $F = 0.34$. It is uncertain whether the data file for the flasher image used to discover the "square structure" in the flasher image was taken from the airport control tower or the rifle club mound. If taken from the airport control tower, it is less likely that we need to take Fresnel diffraction into consideration and more likely that if interference fringes are present, they are caused by the Airy pattern. The size of the Airy disc from the airport tower for the 9.5 mm aperture is $x \approx 34.4$ cm and for the 30 mm aperture is $x \approx 10.9$ cm. The Airy disc sizes from the flasher sited at the airport appear more significant for off-optical-axis distances from the dish centre, compared to the results taken from the rifle club mound, especially for the 9.5 mm aperture ($x \approx 34.4$ cm). This may be responsible for the square structure seen by other colleagues. However, based on the spot size angular-spread measurement of the flasher image in the T1 camera from the mound (for unit 1 $\approx 0.4^\circ$ across and unit 2 $\approx 0.8^\circ$ (see Section 4.1.3), the flasher spot size from the airport tower is large compared to that from the rifle club mound. From the airport control tower the projected spot size of the flasher should be ≈ 40 metres across for unit 1 and ≈ 80 metres across for unit 2.

No patterns were seen when the light spot from the flasher was closely examined on a screen, by projecting the flasher beam down a 40 metre long corridor. At this distance the Fresnel number is $F = 4.5$ for the 9.5 mm aperture and $F = 47.8$ for the 30 mm aperture, negating any Fraunhofer (Airy disc) diffraction effects occurring. Since $F > 1$, indicates that Fresnel diffraction could have occurred at this short distance (40m), but interference fringes were not seen. The reason why Fresnel diffraction failed to occur is outlined in the following paragraph.

Fresnel (or near field) diffraction assumes that the propagating field is a spherical wave originating at the (circular) aperture and moving along the optical axis, where the Fresnel integral modulates the amplitude and phase of the propagating spherical wave, [78]. Fraunhofer (or far field) diffraction is through the interference of plane-parallel waves and it is much easier to calculate the position of maxima and minima fringes of

the interference pattern geometrically. In our case, the wave is refracted through the flasher biconvex lens at the aperture, whereas in the modeling for Fresnel diffraction discussed here, the circular aperture is open (a pin hole). The flasher LED emitter was positioned at the focal point of the 30 mm flasher lens and the refracted collimated beam produced from the flasher is more likely to emit plane-parallel waves from the 30 mm flasher lens, hence bolstering the case for Fraunhofer diffraction occurring.

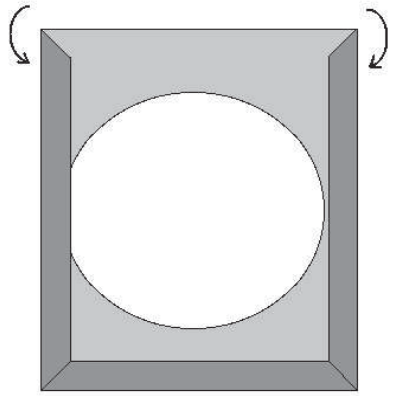

Figure 5.6: A sketch of the Neutral Density (ND) holder for the flasher. The arrows show where the aluminium sheet is folded over at the edges to enable the ND filter film to be held in place when slotted in.

The third and final diffraction effect may have unintentionally occurred, with the ND filter holder in front of the flasher lens as a light barrier. The aperture ring filter was inserted into a holder which is shown in the photograph of the flasher apparatus in Figure 4.1. This holder is positioned in front of the flasher lens and is held in place by a thumb screw. Not shown in Figure 4.1, is a later alteration of this aperture holder which now includes an additional ND filter film holder consisting of a hand made thin but rigid flat folded aluminum sheet 3.7×3.3 cm, attached to the front of the aperture ring holder, see Figure 5.6 (above). A hole was cut around the approximate centre of the ND filter, the same size as the aperture ring holder. The ND filter holder was made to enable the ND filter film to be slotted in front of the flasher lens firmly enough so that it would not blow away in the wind. Deliberately shown in the sketch of Figure

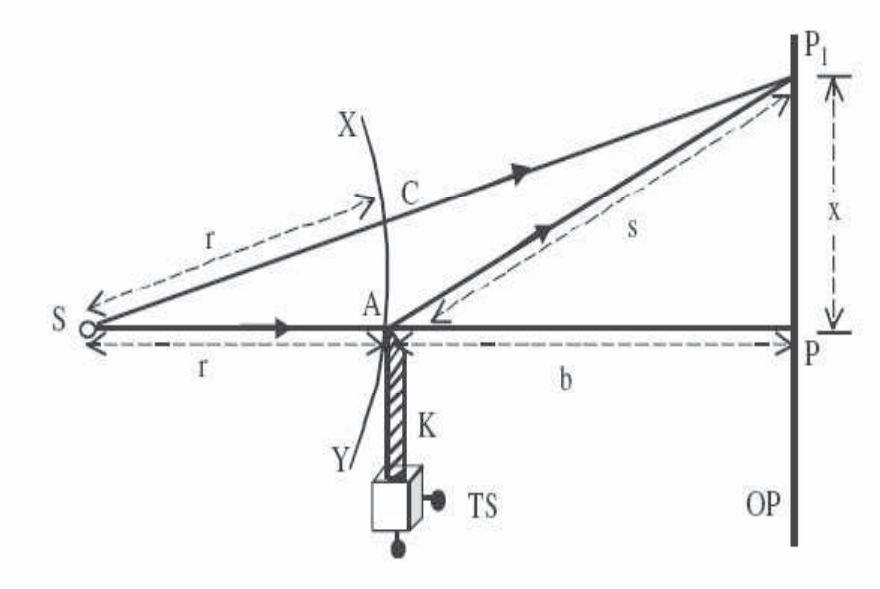

Figure 5.7: Geometry of the knife-edge diffraction, acting as an interferometer. From Kumar *et al.* (2007) [106].

5.6, is the edge of the aluminium sheet folded over on the left of this figure, so that it would partly obscure the edge of the 30 mm full-sized flasher lens (without the 9.5 mm aperture ring inserted behind it it). A thin straight barrier may cause Huygens-Fresnel interference fringes from around the edge of the barrier, [78]. The straight edge fold covering the edge of the hole may produce this effect. This was a manufacturing error, where diffraction effects from the thin straight edge were not realized until flasher calibrations were taken. Diffraction fringes caused by the edge of the ND holder appear to be a possible effect produced by a "knife-edge" interferometer, Kumar *et al.* (2007) [106].

Consider that interference of light may be produced from the knife-edge of the ND filter holder (seeing that the holder is made of thin rigid aluminium sheet) which obscures part of the lens on the left hand side, as shown in Figure 5.6, producing a "knife-edge" interferometer to produce diffraction fringes from this. Figure 5.7 (above) is a "geometrical light wave path diagram showing how two waves (one diffracting from the knife-edge at A, and the other coming direct from the source at S), can combine at point $P1$ on the projection screen where the diffraction pattern at this point is the

interference of two superimposing waves: the geometrical wave direct from the source of light and the boundary diffraction wave from the knife-edge", [106]. Shown in Figure 5.7, "the distance where the two waves meet (from the non-diffracted wave reaching point P), from $P1$ is x. The distance between the source at S and the knife-edge barrier is r (an outgoing spherical wavefront shown as XY), and the distance from the knife-edge to the projection screen OP is b", [106]. We can assume a spherical wavefront as the light beam from the flasher lens is not perfectly collimated and diverges even over relatively short distances, see Section 4.1.3. Again shown in Figure 5.7, "points on the spherical wavefront are C and A (at the knife-edge) and the optical path difference δ, between these two waves at $P1$ are", [106]

$$\delta = AP1 - CP1 = [b^2 + x^2]^{\frac{1}{2}} - [(r+b)^2 + x^2]^{\frac{1}{2}} + r \tag{5.8}$$

solving this we get, [106]

$$\delta = \frac{rx^2}{2b(r+b)} \tag{5.9}$$

where in our case b is the distance between the flasher and the telescopes (determined in the following paragraph), and r is the distance between the face of the lens and the ND holder covering it. We have measured r to be 6 ± 0.5 mm. "The bright (or constructive) diffraction fringes can be produced when $\delta = n\lambda$ [106], and the dark (or destructive) diffraction fringes can be produced when $\delta = (2n+1)\lambda/2$ [106], for positive n integer values". The wavelength of the flasher LED ($\lambda = 470$ nm) is previously stated. Additionally, "When the knife-edge gets very close to the light source S (Figure 5.7), we can approximate $r + b \approx b$", [106]. Using this assumption, solving for x at the screen OP (Figure 5.7), "for bright diffraction fringes ($\delta = n\lambda$) derived from equation 5.9, we obtain the positions of the bright diffraction fringe patterns as", [106]

$$x = \sqrt{\frac{n\lambda 2b^2}{r}} \qquad n = 1, 2, 3, \ldots \tag{5.10}$$

where ($n = 1$) is the first order bright fringe and so on. "Similarly, for dark diffraction fringes ($\delta = (2n+1)\lambda/2$) from equation 5.9, we obtain their positions as", [106]

$$x = \sqrt{\frac{(2n+1)\lambda b^2}{r}} \qquad n = 1, 2, 3, \ldots \ . \tag{5.11}$$

where ($n = 1$) is the first order dark fringe and so on. Furthermore from Kumar *et al.* (2007) [106], "the fringe-width β, for corresponding bright and dark fringes can be determined by"

$$\beta = \left[\frac{2\lambda b^2}{r}\right]^{\frac{1}{2}} [(n+1)^{\frac{1}{2}} - n^{\frac{1}{2}}] \qquad n = 1, 2, 3, \ldots \ . \tag{5.12}$$

Fringe postn., x from eqns. 5.10 and 5.11	**rifle club mound**	**airport tower**
1st Bright fringe position, n=1	10.4 ± 1.1 metres	71.3 ± 4.3 metres
1st Dark fringe position, n=1	12.8 ± 1.4 metres	87.4 ± 5.2 metres
2nd Bright fringe position, n=2	14.7 ± 1.6 metres	100.8 ± 6.1 meters
2nd Dark fringe position, n=2	16.5 ± 1.8 metres	112.8 ± 6.8 metres
Half fringe-width, $\beta/2$ from eqn. 5.12	**rifle club mound**	**airport tower**
1st Bright fringe half-width, n=1	2.2 ± 0.2 metres	14.8 ± 0.9 metres
1st Dark fringe half-width, n=2	1.7 ± 0.2 metres	11.3 ± 0.7 metres
2nd Bright fringe half-width, n=3	1.4 ± 0.2 metres	9.6 ± 0.6 metres
2nd Dark fringe half-width, n=4	1.2 ± 0.1 metres	8.4 ± 0.5 metres

Table 5.3: Projection of scales of diffraction fringes of first and second order produced by a knife-edge visible light interferometer, Kumar *et al.* (2007) [106], at T1 from the flasher projecting from the rifle club mound and the airport control tower. The knife-edge is the thin ND filter holder obscuring part of the flasher lens (Figure 5.6).

Table 5.3 (above) shows the results of calculating the distance that the knife-edge interferometer fringes are displaced from the centre, i.e. shown as x in Figure 5.7, using equation 5.10 for bright diffraction fringes and equation 5.11 for dark diffraction fringes. Calculations are made for both the rifle club mound at $b = 833 \pm 58$ metres for T1, and for the airport tower at $b = 5700 \pm 100$ metres. For the positions x, the first order bright and dark fringes at $n = 1$, and second order bright and dark fringes at $n = 2$ are evaluated. Furthermore, the fringe-width β of the first and second order bright and dark fringes is also calculated from equation 5.12, at the rifle club mound and airport control tower. Note that the fringe width β is divided by two as the position of the diffraction fringe x is the centre of the fringe band, and we wish to

determine only where the diffraction fringe may overlap the FoV of the telescope. The relative uncertainty of the fringe positions x from equations 5.10 and 5.11 (from the rifle club mound and airport tower to T1) is 11%. Similarly, the relative uncertainty of the fringe-width β from equation 5.12 (from the rifle club mound and airport tower to T1) is 6%.

From Table 5.3, it initially appears that the first order bright band from the knife-edge interferometer formed by the ND filter holder in front of the flasher lens, may project into the edge of the T1 camera's FoV. The first bright fringe appears at 10.4 metres from the center and this fringe half-width is 2.2 metres, which easily takes it into the FoV of the 10 metre diameter dish. However, since the first flasher calibration recording in April 2001 onwards, the 9.5 mm ring aperture was always inserted in front of the lens for a flasher calibration of T1 and T2. Thus the ND holder's edge (Figure 5.6) cannot act as a knife-edge interferometer when the 9.5 mm ring aperture is inserted, since this aperture size is too small to be obscured by any part of the ND holder. Incidentally, in the early testing phase of the flasher experiment, the 9.5 mm aperture ring was not always inserted in front of the flasher lens. It was possible that the 9.5 mm aperture was not inserted into the holder for the early flasher data files used for the offline analysis for the flasher calibration from the airport control tower. However, we can rule the knife-edge interferometer effect out at this distance, as the first order bright fringe is 71.3 metres away from the dish centre (with fringe band half-width of 14.8 metres), making it unlikely that diffraction fringes from the knife-edge interferometer effect contributed at all to the "square structure" seen.

To summarize, we applied calculations of Fraunhofer (Airy Disc) interference, Fresnel interference and knife-edge interferometer effects from the aperture dimensions of the flasher apparatus and the distances this instrument was placed from the (T1 and T2) telescopes during calibration. Whilst the result would be a non-uniform illumination of the mirror, it turns out that if any interference pattern would not be noticed in the image on the camera. The largest diffraction effect is the Airy disc where $\theta \sim \lambda/D = 470 \times 10^{-9}/9.5 \times 10^{-3} \approx 5 \times 10^{-5}$ radians $= 0.003$ degrees. This is much smaller than half a pixel value of the T1 camera resolution of 0.13 degrees (Section

3.1.2), where $0.13^{\circ}/2 = 0.065^{\circ}$. The pixel resolution of T2 is approximately the same as T1.

The most likely effect to produce the "square structure" were rows of pixels that were unresponsive to flasher signal. Data from logbooks taken for flasher calibration data acquired on 24th and 25th of February 2001 and the 2nd January 2001, shows an analysis of data from these nights of flasher images. Many flasher images showed dark bands mainly running horizontally though the flasher spot image, shown in Figures G.1 and G.2 in Appendix G. These dark pixel bands were semi-consistent (on the same place on the flasher spot image), probably indicating that a hardware fault had developed with the ADC data acquisition modules in the central camera boxes (see Figure 3.7). It is most likely that these dark rows were responsible for the "square structure" reported from this calibration date (February 2001), prompting the author to make an investigation (Figures G.1 and G.2) at the time. Unfortunately the flasher calibration data files from 24/2/01, 25/2/01 and 2/1/01 have gone missing, halting further analysis of these calibration results.

5.2.2 Flasher image movement in the camera field of view

It has been suggested that the flasher image tended to be positioned in a slightly different place, month by month, relative to the centre of the camera. The same Azimuth and Elevation coordinates of the flasher on the mound are entered into the tracking control of the dish each month, see Table 4.1. Thus the hypothesis is that small errors in the tracking encoders may cause a slight shift in the flasher image over the 30 months this experiment was carried out.

To test this hypothesis, we performed a cross-correlation (or cross-covariance) calculation; Bracewell, R. (1999), [36], Papoulis, A. (1962), [134], on all the inner 256 camera pixels of the flasher image. The 16×16 pixel grid of the inner T1 camera was up-scaled to a finer resolution of a 76×76 grid. This was produced by linearly interpolating the mean sum ADC of adjacent pixels in the original grid. The grid resolution of 76×76 is five times finer than the original 16×16 grid, as four more linearly interpolated mean sum ADC grid points were added between the original pixels of the

camera, in two dimensions. The same pixel-to-pixel linear interpolation process was applied to the pixel positions (from the centre) in degrees, so that finer 76×76 grid coordinates were also produced.

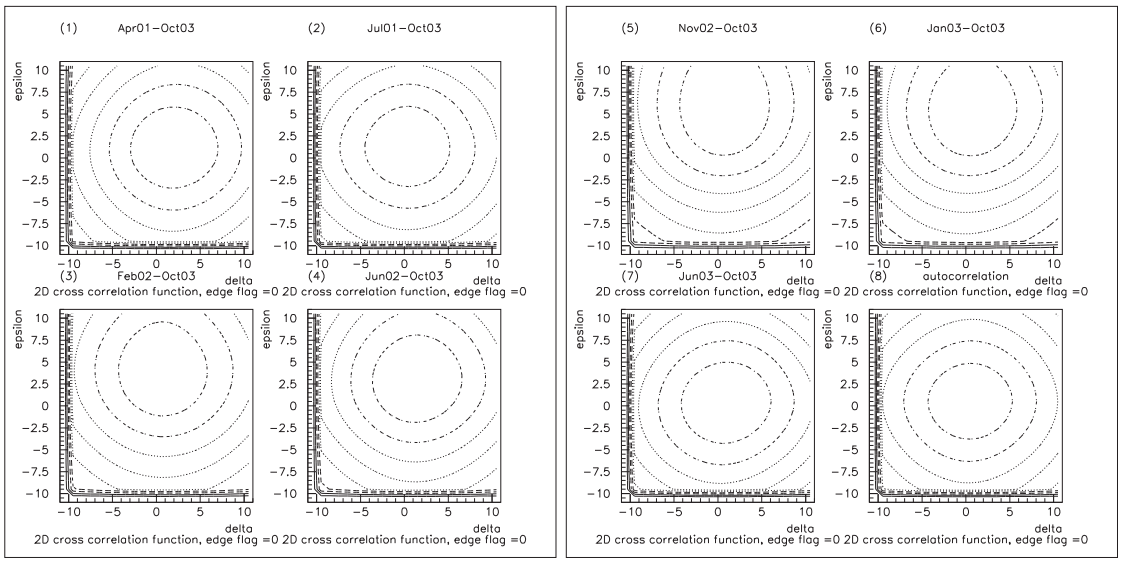

Figure 5.8: Two dimensional cross-correlation results for T1 flasher calibration by the calibration month, shown in the cross-correlation transform space of x-shift (delta, δ), y-shift (epsilon, ϵ). Flasher calibration month shown as the first month above each slide with the slide number on the top left, e.g. slide 1 is the April 2001 calibration. The concentric rings centre position in these slides (numbers 1 to 8), is the position of the cross-correlation maximum. This maximum position is shown in δ and ϵ, in Table 5.4. Slide no. 8 shows the autocorrelation function (cross-correlating October 2003 with itself). For clarity, this figure is enlarged in Figure E.4, Appendix E.

The cross-correlation is a transform function integral process, related to the Fourier Transform, [78], which is normally used in analogue signal/frequency processing. The cross-correlation transform is produced by the convolution of two functions, see equation 5.13 (below) for discrete functions. Since we are only dealing with real pixel numbers here, the complex conjugate need not be considered (although shown). The convolution is produced, in our case, by multiplying any pixel position in the fine 76×76 resolution by a shifted pixel (in two dimensions). In the x-direction, we call our shift, δ and in the y-direction we call our shift, ϵ. The shift selected in our calculations was $\delta = 10$ and $\epsilon = 10$, analogous to a shift of two adjacent pixels in the original 16×16

grid. This produces a two-dimensional cross-correlation result, see equation 5.14.

For discrete functions f_i and g_i, the one-dimensional cross-correlation function is defined as, [36], [134],

$$(f \star g)_i = \sum_j f_j^* \, g_{i+j} \tag{5.13}$$

where the sum is over the appropriate value of the integer, j, and the asterisk represents the complex conjugate.

The two-dimensional cross-correlation function, in our case, may be defined as

$$(f(\delta,\epsilon) \star g(\delta,\epsilon))_i = \sum_{\delta+j} \sum_{\epsilon+j} f^*(\delta,\epsilon)_j \, g(\delta,\epsilon)_{i+j} \tag{5.14}$$

for discrete two-dimensional functions, $f(\delta,\epsilon)$ and $g(\delta,\epsilon)$. The selection of the size of the shift in δ and ϵ, is a product of camera resolution (after processing a finer resolution if required) and image size. In a square array (as is the case for the T1 camera), δ and ϵ should be the same. In our case, the sum in j was taken over $\delta + 1 = 11$, to the grid size $76 - \delta = 66$, to avoid edge effects. Similarly for ϵ. An edge effect occurs when the image has shifted close to the edge of the (16×16) pixels of the inner camera, in our case. The summed value in each point of the 76×76 grid of the cross-correlation of our fixed flasher image from October 2003 (together with all other seven calibration months), was then plotted as a two dimensional image in δ and ϵ space, as shown in Figure 5.8 (above). As the flasher image did not shift further than two pixels (between any monthly calibration), to be positioned near the edge of the inner camera boxes frame as explained, the edge effect need not be considered nor applied. Thus the edge effect was flagged as being equal to zero (via the program producing the cross-correlation), as indicated in Figure 5.8 for each frame. The position of $\delta = 0$ and $\epsilon = 0$, for all eight frames of the two-dimensional cross-correlation contour plots shown in Figure 5.8, represent the exact centre of the T1 camera in the coordinate space of the camera. The innermost contour ring of each of the plots is the cross-correlation maximum, where the centre of this contour ring is the position of the (δ,ϵ) maximum coordinates.

The two-dimensional cross-correlation of October 2003 with itself (the auto-correlation) is also shown in frame 8 of Figure 5.8. As expected the image contour shown is in the

calibration month	*delta*	*epsilon*	*x-shift (deg.)*	*y-shift (deg.)*	*angular dist. from centre*
April 2001	1	1	0.023	0.023	0.033
July 2001	0	1	0.0	0.023	0.023
February 2002	0	3	0.0	0.069	0.069
June 2002	1	2	0.023	0.046	0.051
November 2002	0	6	0.0	0.138	0.138
January 2003	0	5	0.0	0.115	0.115
June 2003	0	0	0.0	0.0	0.0

Table 5.4: The position of the two-dimensional cross-correlation maximum point, by calibration month for T1. The last column shows the angular distance from the camera centre, calculated by $\sqrt{X\text{-shift}^2_{\text{deg.}} + Y\text{-shift}^2_{\text{deg.}}}$ (see equation 5.15, below). The *angular distance from centre* column is in units of degrees.

centre of the camera (coordinates $(0°, 0°)$), without shift. Most other cross-correlation calibrating months, except June 2003, show a shift away from the fixed October 2003 flasher image by at least half a pixel width (or 0.023°, the size of one pixel in the 76×76 grid), confirming that the dish pointing at the flasher unit on the rifle club mound was uncertain at this level, from calibration month to calibration month. The (δ, ϵ) position of the cross-correlation maximum for each flasher calibration month is shown in Table 5.4 (above), along with the angular distance of the Cross-Correlation Maximum Position (CCMP) from the auto-correlation in October 2003 (i.e. centre of the camera), where the CCMP is calculated by

$$\text{CCMP} = \sqrt{x\text{-shift}^2_{\text{deg.}} + y\text{-shift}^2_{\text{deg.}}} \tag{5.15}$$

The shift for the x- and y- coordinates are determined for T1 by multiplying the delta and epsilon value respectively (in Table 5.4) , by the width of a single pixel in the 76×76 cross-correlation grid, i.e. 0.023°.

CCMP is the scalar distance from the centre of the camera (or the auto-correlation position for T1). It is the square root of the sum of squares of the x- and y- coordinate (in camera pixel degrees) derived from the delta and epsilon shift values from the cross-

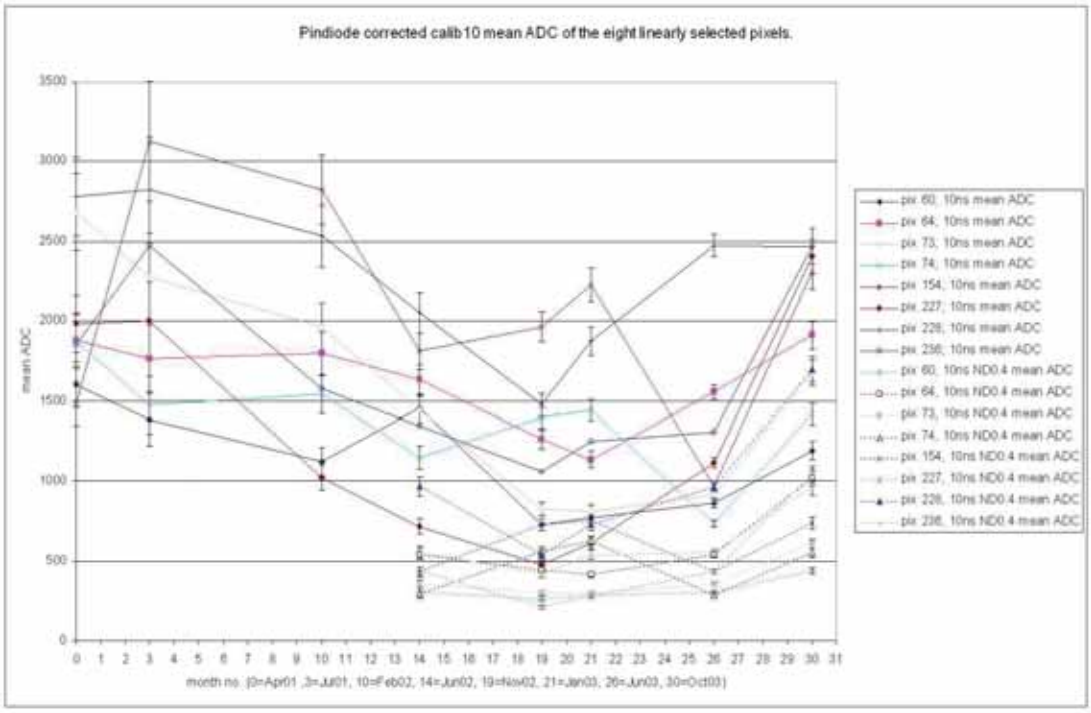

Figure 5.9: Mean ADC over all calibration months. The eight selected inner camera linear pixels used are (by ADC ID-number); 60, 64, 73, 74, 154, 227, 228, 236. Flasher settings are 10ns (solid lines), and 10ns ND 0.4 filter (dotted lines), recorded in **calib10a** data format. Each point and line, pertinent to its particular pixel, is indicated by the table on the right of the graph. Each monthly mean ADC value is corrected using the PDM derived ratio values, shown in Table 4.3. For clarity, this figure is also shown enlarged in Figure F.1, Appendix F.

correlation result (see Table 5.4). Thus the CCMP distance is scalar degree distance measurement from the camera centre (or auto-correlation position). As $x-$ (delta) and $y-$ (epsilon) values increase (in Table 5.4), this will increase the value of the CCMP scalar distance. It is not enough that the CCMP be simply measured from the centre of the camera for all eight flasher calibrations, we must find how the flasher images taken on subsequent calibrations move relative to each other. To do this we impose a "fixed flasher image position" upon all the other calibration flasher image positions which are measured relative to it. An increase in CCMP distance is an indicator that the flasher image has moved further away from the initial image upon which was based our fixed

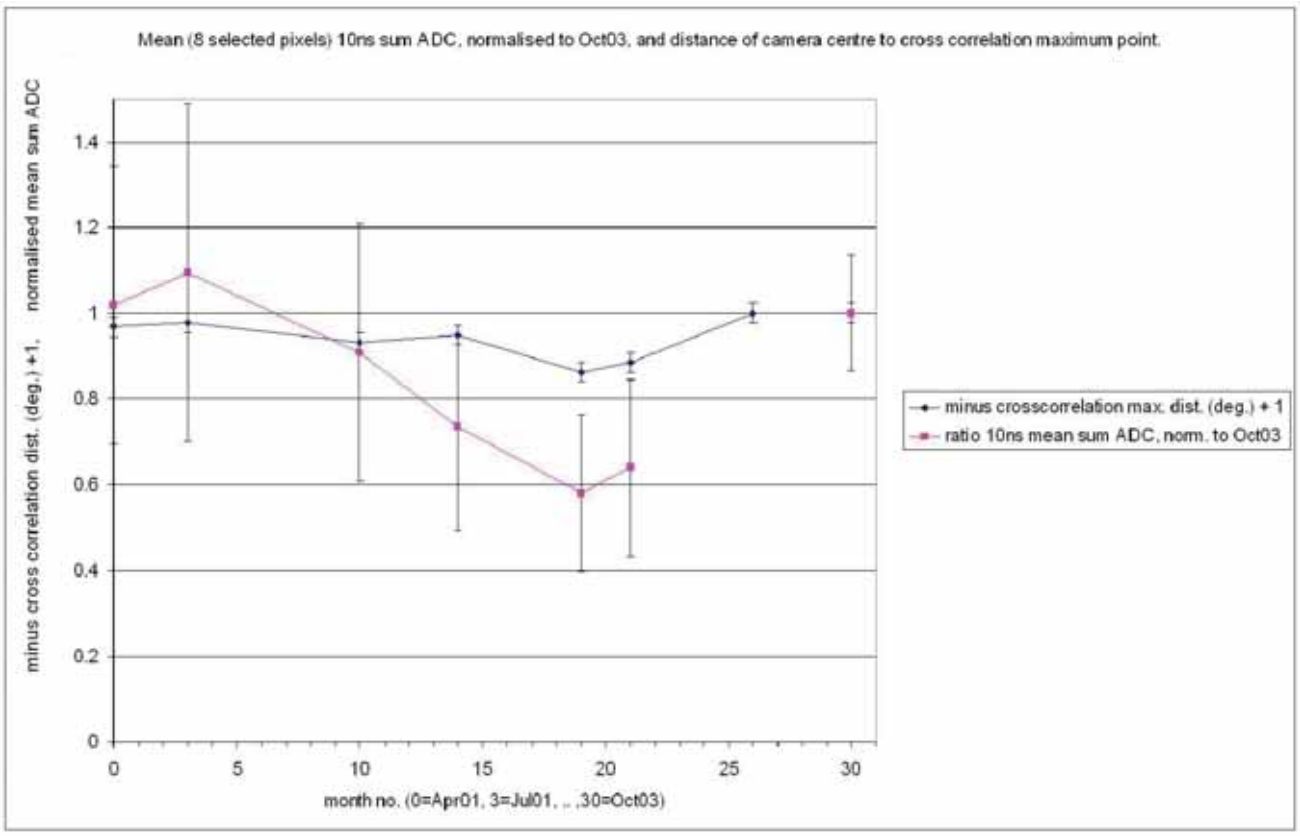

Figure 5.10: Normalized ratio of average mean ADC of the eight selected T1 camera pixels over all calibration months for the 10ns setting with T1 cross-correlation maximum position distance (where 1.0 indicates the camera centre position and a lower value, further away from it). See Table 5.5. Both these quantities plotted together are unit-less. The average mean ADC datum point from June 2003 has been left out due to mirror dewing. This figure is enlarged in Figure F.2 (Appendix F), for clarity.

position. Subsequent flasher images would measured relative to this fixed position. A test of measuring the CCMP of the fixed flasher image position with itself is called an auto-correlation. As this fixed image does not move with itself during calibration on the night, it acquires a CCMP distance of zero. Although it is not listed on Table 5.4, the fixed flasher image position was from the October 2003 position (can be observed in slide 8 of Figure 5.8). All other flasher calibration images positions are then measured relative to it in CCMP distance.

However, the increase in CCMP distance (meaning a longer shift of the flasher image from the fixed position) could be correlated with a decrease (rather than increase) of the

Calibration month	*ang. dist. from centre subtracted from 1°*	*normalized average mean ADC*
April 2001	0.967	1.019
July 2001	0.977	1.094
February 2002	0.931	0.908
June 2002	0.949	0.732
November 2002	0.862	0.579
January 2003	0.885	0.639
June 2003	1.0	dew on mirrors
October 2003	1.0	1.0

Table 5.5: Distance of the two-dimensional Cross-correlation maximum point from the T1 camera centre, versus average mean ADC of the linearly selected pixels (numbers 60, 64, 73, 74, 154, 227, 228 and 236; see Figure 5.9). The second column is in units of degrees.

overall flasher signal strength seen in Figure 5.9. Although this figure shows the eight pixels selected from the T1 camera (containing the flasher signal, see Section 5.2.5) at two different settings (10 ns and 10 ns with a ND 0.4 filter), it is illustrative of a general decrease of flasher signal amplitude in the middle of the calibration experiment followed by an increase at the end. Consequently, the CCMP distances were *inverted* when their distances increased, by the method explained in the next paragraph.

The CCMP distance is much less than 1° (see Table 5.4). Thus the CCMP is actually referenced from a circle one degree in radius from the auto-correlation position. Hence, as we increase the CCMP degree distance from the auto-correlation position, the CCMP distance from the circle of radius one degree (1-CCMP degrees) decreases in value and the average mean sum ADC will likely decrease because the shift in CCMP distance has increased. The expectation is that the telescope's optical axis was aligned slightly differently in comparison to the optical axis of the flasher image taken in the fixed or auto-correlation position (explained above). The conjecture for this phenomenon is explained in Section 8.1.1 of the conclusions chapter.

Figure 5.9 shows the variation of the normalized average mean ADC of the eight

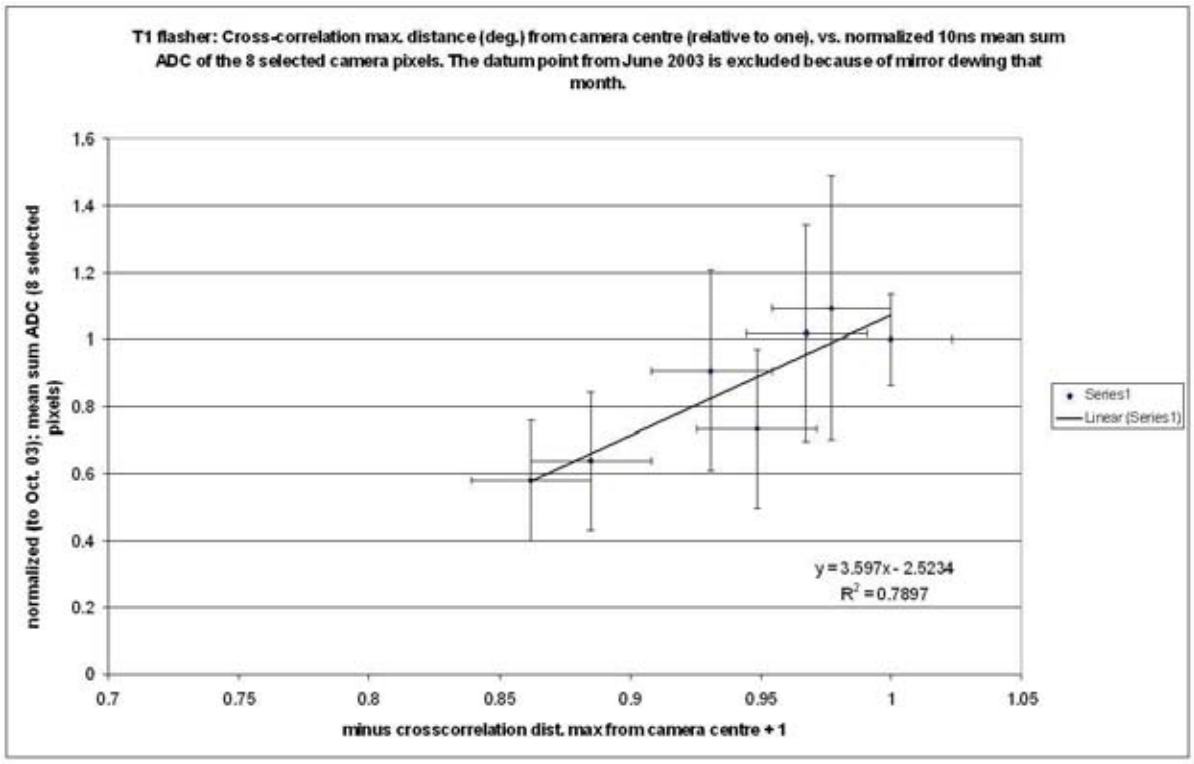

Figure 5.11: Plot of cross-correlation maximum position distance from 1.0 (see Figure 5.10), versus ratio of average mean ADC of the eight selected T1 camera pixels over all calibration months for 10ns setting to test the hypothesis, that of correlation, between these two variables. The least linear squares fit result equation is shown in the lower right of the figure.

selected pixels (selected for best linearity; see Section 5.2.5). The averages are taken over the mean ADC of the eight selected pixels (numbers 60, 64, 73, 74, 154, 227, 228 and 236). All pixels are within the four boxes nearest the centre of the camera; boxes 4, 5, 10, 15 (see Figure 3.7). The average mean ADC of the eight selected pixels can be compared with the change of CCMP distance from the 1° radius circle auto-correlation position centre (1-CCMP degrees). Figure 5.10 illustrates how these two values vary against each other over the time the flasher calibrations were taken. The 1-CCMP angular distance may be related to the average mean sum ADC. We normalized the mean sum ADC of the eight selected pixels via the following ratio

$$\frac{\overline{\text{ADC}}\,(\text{Calibrating month})}{\overline{\text{ADC}}\,(\text{October 2003})} \tag{5.16}$$

Table 5.5 (above) shows this result which is illustrated in Figure 5.10.

The values of the angular distance of the CCMP distance from the 1° radius circle with the auto-correlation position centre (1-CCMP degrees) are taken from Table 5.5. Dew on the mirrors in June 2003 was found to be highly likely after examination of the Davis Weather Station monitor Dew Point data, despite dewing having not been noticed by eye on the flasher calibration night. Figure F.4 (Appendix F), shows the variation of the calibration months with Dew Point and outside temperature (in degrees Celsius) from the Davis Weather Station at the T1 telescope. A convergence of Dew Point and outside temperature in June 2003, shows the high probability that the mirrors on T1 were dewed. The flasher signal amplitude would be diminished by this effect, and can not be considered reliable for this month. Therefore the normalized average mean ADC datum point from June 2003 is left out when testing the correlation between the average mean ADC of the selected linear pixels and the CCMP distance from one, for both T1 and T2 results. The correlation of the T1 CCMP radial distance with the 1° radius circle (auto-correlation position centre) and with the normalized mean sum ADC is shown in Figure 5.11 (repeated in Figure 8.1 of the conclusions chapter).

5.2.3 Size of the flasher image

The consistency of the size of the flasher image as calibrations are taken month by month is important. Figure 5.12 shows the contour hit map of the flasher images from July 2001 and Feb. 2002. Very little difference can be seen between the images taken in Feb. 2002 compared to July 2001. Slides A. and B. in Figure 5.12 are similar in size with both images being 1.4° in size in both the horizontal and vertical scales. For unit 1, slides C. and D. are 1.3° in size in both the horizontal and vertical scales. Unit 1 is a slightly smaller light source than unit 2, so we should expect this.

The flasher images in Figure 5.12, have not been fixed to a preset pixel amplitude. A scaling reference pixel can be applied to normalize the size of the flasher image between

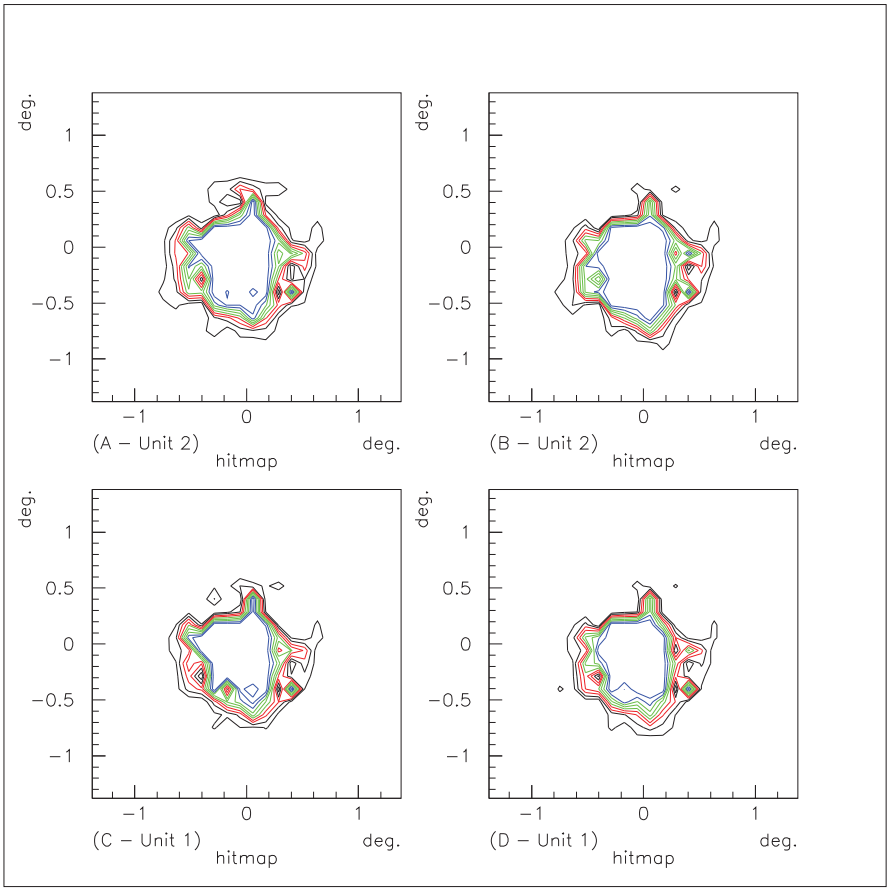

Figure 5.12: Comparison of 10ns flasher hit-map contour images with the calibration in Feb. 2002, compared to July 2001 . Slide A is July 2001 (unit 2), slide B is Feb. 2002 (unit 2), slide C is July 2001 (unit 1), slide D is Feb. 2002 (unit 1). The number of equidistant contour lines are fixed at 10. Contour colours are false and not set to any level. Contour levels are determined from the maximum pixel value to zero. This figure is enlarged in Appendix E, Figure E.2.

calibrations, i.e. this process fixes the amplitude of all the flasher image signals to a preset level. A scaling pixel was applied to the upper slides in Figure 5.13, in the lower right hand corner of both images. Figure 5.13 is the mean ADC value across the camera, where each ADC pixel mean is sampled over the number of triggered events, and an artificial scaling pixel can be easily applied *a posteriori* off the flasher image.

From previous tests, the uncertainty in pointing is about $\pm 0.5^{\circ}$ and this was from a test when the flasher was located at the airport tower, a much greater distance than from the mound. When aligning the flasher by pointing when setting up on the rifle

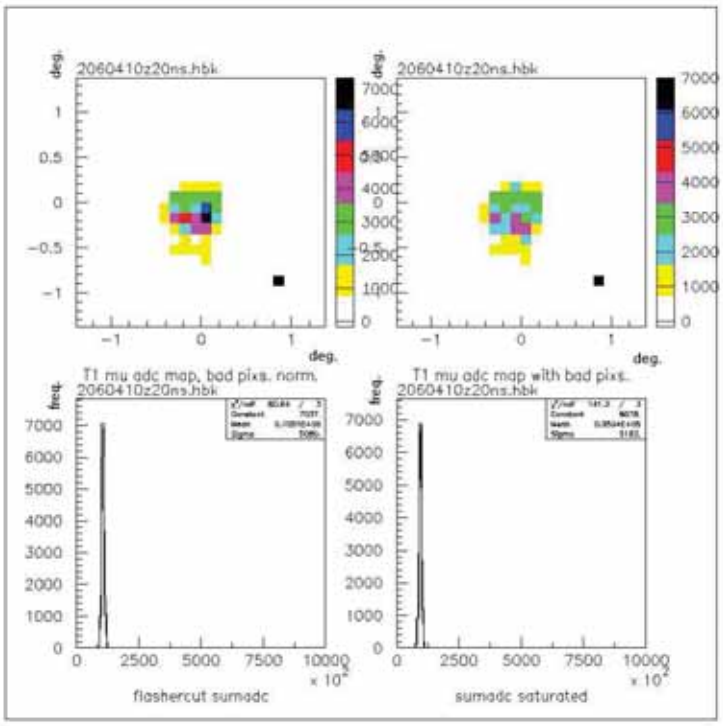

Figure 5.13: T1 flasher mean ADC two dimensional pixel map (top two slides), and mean sum ADC (bottom two histograms). The data for all four figures is 20ns (no ND filters) from T1 in June 2003. The colour scale on the right hand side of the top slides is mean ADC count where, e.g. yellow indicates a mean ADC pixel count between 1000 to 1999. The isolated bright (> 7000 mean ADC counts) pixel in the lower right hand corner of the pixel maps is a scaling reference pixel only, and is not a real data point. "Flashercut" and "saturated" were an early attempt at pixel correction, where "saturated" are uncorrected pixels, see Section 5.2.5. This figure is also shown (enlarged) in Figure E.3, Appendix E.

club mound, care was always taken to align the cross hairs in the eyepiece lens with the centre of the telescope dish (Section 4.1.1). The effect of gross error in aiming through the eyepiece cross hairs is in the simultaneous fluctuation in the signal mean value of each pixel, not in the shift of the flasher image itself. The effect of this is that the size of the flasher image may appear slightly larger or smaller on the same setting, from calibration to calibration. The alteration in the flasher image size by aiming error is similar to the effect of changing the transmission values through changing ND filters, but not to the same degree. For settings within a flasher calibration, since aiming

of the flasher at the telescope is only done at the beginning of the calibration and is not changed between flasher calibration data runs, there is no change in this aiming variable.

In comparison to possible errors in aligning the flasher calibration tube, more fluctuation in the overall signal strength in the flasher image is produced through pointing errors in the telescope tracking encoders when the telescope dish is slewed then stopped for flasher calibrations. This produces a shift in position of the flasher image relative to the auto-correlation position. This result has been demonstrated by the cross-correlation analysis of the flasher image in Section 5.2.2 and the conclusions to the cross-correlation results in Section 8.1.1. Furthermore, from Table 5.4 of T1 cross-correlation results, there appears to be systematic error in position of the telescope which is skewed more in the vertical direction (*y-shift*) than in in the horizontal direction (*x-shift*). This systematic effect is likely to be low elevation angle gravitational distortions, either in the struts holding the camera (similar to HEGRA, Sevilla *et al.* (2003) [156], see Section 3.1.1), although not to the same extent as the HEGRA telescopes, or in gravitational dish distortion. The cross-correlation analysis has proved to be sensitive to slight image movement, which could detect these low elevation angle gravitational distortions on the telescope dish.

5.2.4 Measurement of the flasher output using a single photomultiplier tube detector

Early in the flasher calibration field work, it was recognized that an attempt should be made to measure the output of the flasher device (at a distance) at the location of T1's dish. For the flasher calibration in 2000 we carried out this attempt, using a 8-inch Newtonian telescope (with a refracting lens replacing the primary mirror) to enable light to be focused onto a *Hamamatsu* R4124 UV phototube (characteristics in Section 3.1.2) positioned inside the telescope tube. The flasher "image" was crudely focused onto the PMT window: A small hole was cut into the side of the telescope

tube for the operator to view this image, so that the position of the PMT could be altered to enable the flasher image to be sharply focused onto the PMT window, with a small white piece of paper temporarily covering the PMT window for this purpose. The Newtonian telescope was initially mounted onto a custom-made mount attached to the top railing of T1's camera access tower (see photograph Figure 3.1). The PMT output signal in the telescope-PMT apparatus was detected using an oscilloscope.

Firstly, the telescope-PMT apparatus was repeatedly measuring the flasher output, with the flasher positioned at the top of the airport control tower (Section 4.1.2). Due to the brightness and number of ground lights near the flasher, there was confusion by the operator about whether he was seeing a genuine flasher image on the paper, out of other ground light contributors. Furthermore, if the flasher image was corrected identified and focused, there were concerns that the telescope-PMT apparatus would be acquiring noise from other ground lights in the FoV.

An attempt was then made to measure the flasher image when the flasher apparatus was positioned on the rifle club mound (Section 4.1.2). Despite the lack of ground lights in this location, we also failed to conclusively detect the flasher output signal (despite adding a preamplifier to the PMT signal from the telescope-PMT apparatus), and also increasing the PMT HV. Since we experienced many difficulties in using the telescope-PMT apparatus, we eventually abandoned the attempt to measure the output of the flasher device (independent of the T1 camera) over a distance.

5.2.5 Earlier abandoned attempts at pixel correction in the T1 camera

For the flasher calibration of T1 data analysis, attempts were made to correct a few pixels in the inner camera that were considered unacceptably noisy or had some obvious anomaly. Ultimately after a lengthy process, it was decided that this procedure was not effective enough in correcting the overall faults in all the 256 ADC pixels of the inner camera from which the mean sum was initially taken, and this process was abandoned. The ADC pixels (close to the centre of the camera), selected in Figure 5.9

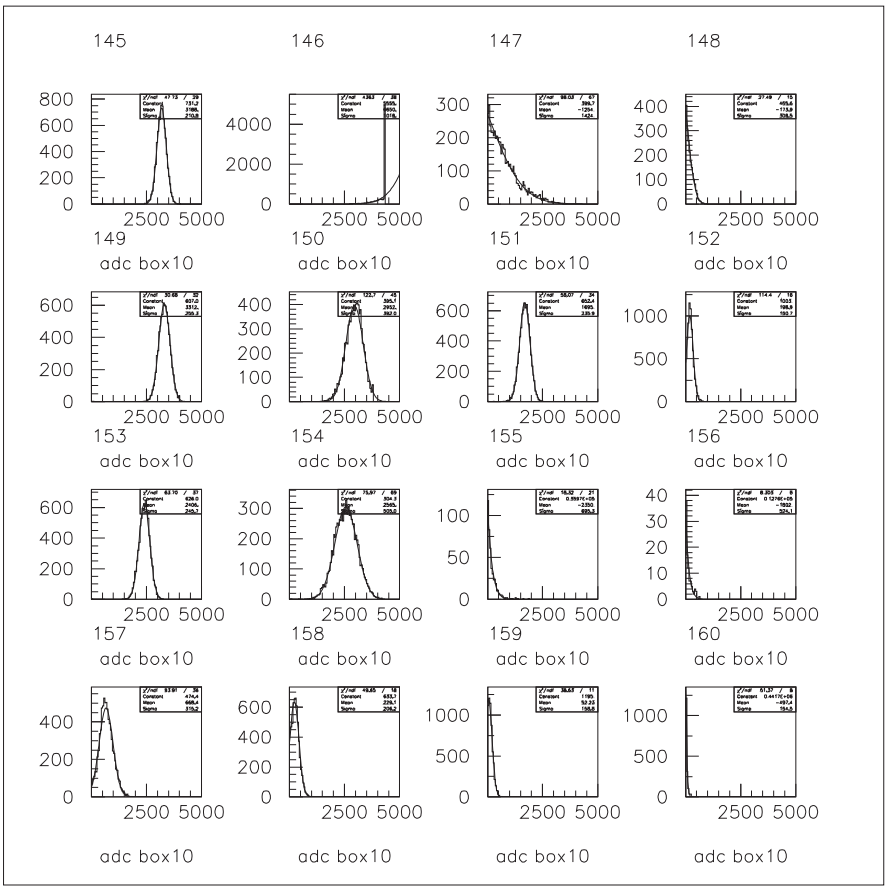

Figure 5.14: ADC count histograms per pixel (in T1) from box number 10. The ADC pixel number is shown above each histogram (i.e. 145 to 160). These histograms are used to show examples of malfunctioning PMTs.

(in Section 5.2.2), were finally judged stable enough while showing consistent linearity to a flasher calibration signal input. These "stable" pixels were selected to test the signal from the flasher.

The selection criteria for these pixels to pass "linearity" was that the linear least squares coefficient of determination (r^2), was better than 0.8 for the fit of the light intensity (normalized to 10ns), against the mean ADC for all calibration months inclusive. This was for all available flasher settings of different intensities, including 20ns without filter. The list of typical flasher settings is shown in Table 5.1, and in Section 5.1.4. Further explanation for the decision to select only a few pixels is given in Section 8.1.1. We now describe the process used in the initial attempt to correct the eight

selected pixels in Figure 5.9, while retaining most of the other 256 pixels of the inner camera for the mean ADC flasher signal calculation.

The first stage of the T1 normalizing analysis follows. Figure 5.14 shows the positive ADC pixel count distribution histograms from pixels from box number ten (T1 camera) when the flasher setting was 20 ns. Negative ADC counts, which occurred, are low amplitude (or spurious) numbers and are discounted as they slightly skew the signal in the pixel ADC count histograms. The ADC pixel number (and phototube number), is shown above each histogram. The number of events is about 10,000. The pixels in general follow a Gaussian distribution of signal as expected. However, pixels numbered 146 and 147 appear to behave non-linearly. Further examination of these pixels from different flasher settings from the same night at e.g. 10 ns and with various neutral density (ND) filters attenuating the signal, determined whether the phototubes in question were saturating, or whether the phototube was noisy over a large range of input light intensities. In this particular case it was determined that phototube number 146 was saturating and phototube 147 was flagged as "bad" (although this pixel, and other pixels showing similar behavior, may not have been flagged by *calib10*). The ADC digital counts per phototube histogram distributions for all the other boxes, were examined in a similar fashion.

It's not clear by visual examination of Figure 5.14, which anomalous phototubes are saturating and which are not. To obtain this information, a second stage T1 analysis was carried out which compared the ADC mean value for 256 pixels using separate data file runs of the same flasher setting (e.g. 10 ns), but different ND filters. Sometimes multiple neutral density filters settings were used on the night, requiring that the most attenuating filter (highest ND value), was used as a calibration setting. For example, on most flasher calibration months, there was a 10 ns setting with a ND 0.4 filter and a 10 ns setting without a filter. The neutral density (ND) filters act as an light intensity attenuator based on a logarithmic scale of base ten, where an ND value of 0.4 gives $1/(10^{-0.4}) \approx 2.51$ attenuation. Thus, the ND 0.4 transmission attenuation factor is about 2.5 times below that without a filter. If, for each pixel, we take the ratio of the mean ADC counts per pixel on 10 ns without a filter to the mean ADC counts

on 10 ns with a ND 0.4 filter, each pixel's measurement ratio should be about 2.5 (if saturation has not occurred). Pixel ratios below 1.5 were counted as saturating pixels for the ND 0.4 filter only (for 10 ns and 20 ns settings). These pixels were then flagged as "saturating" by the T1 flasher analysis algorithm.

Saturating pixels were first corrected by determining the normalization factor of the adjacent pixels to the saturating pixel in question. This saturation normalization data was provided by the most attenuated flasher calibration run (usually 10 ns, ND 0.4) From this run, the mean ADC count ratios of the eight adjacent pixels (Figure 5.15) to the saturating pixel were assessed, in comparison to brighter calibration files of the same pixel, to determine if these ratios had changed appreciably indicating that saturation had occurred. It was unlikely that the highly attenuated run (i.e. 10ns ND 0.4) would have saturating pixels. The eight adjacent pixel ratios were then used for correction (normalization). For example, a 20 ns run without ND filter attenuation would always have some saturating pixels. Where saturation had occurred, the "ratio normalized" mean ADC counts of the adjacent pixels to the saturating pixels in the run were added together and the the mean of this count was taken to be the approximate mean ADC count value of the saturating pixel. Bad pixels, if they were adjacent to the saturating pixel, would be corrected first before being multiplied by the normalization factor.

In general on any one month of flasher calibrations, there was only a small number of bad pixels (typically less than ten) due to noisy phototubes or *calib10* bad channel setting. The *calib10* bad pixels are distributed randomly over the 1 to 16 boxes of the T1 camera (Figure 5.5), but the noisy *calib10* bad channel pixels and bad pixels selected by the author's algorithm tend to be positioned towards the middle of the camera where the strongest flasher pixel signals are found. Naturally, the saturated pixels also tend to be selected close to the centre of the camera. The number of saturated pixels was small, typically less than ten.

There are eight adjacent pixels in any camera pixels shown in Figure 5.15, except pixels at the edge of the inner boxes of the T1 camera. The edge pixels were corrected using a slightly different procedure. The mean correction count was made on adjacent

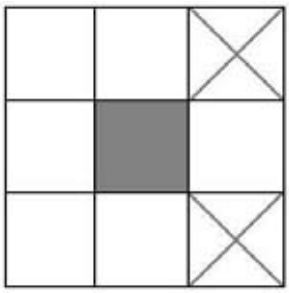

Figure 5.15: Sketch showing any T1 camera pixel (except edge pixels). The central pixel is grey shaded, with eight adjacent pixels. The two crossed pixels are "bad" pixels.

pixels to the grey central pixel in Figure 5.15 (excluding "bad" pixels shown as crosses in this example), and an allowance made for the normalization mean count correction. Adjacent pixels to the central pixel (Figure 5.15) were corrected for saturation beforehand.

After normalization correction, a two-dimensional map of the camera pixels mean ADC counts was made. Comparisons of the normalized (corrected) and non-normalized (uncorrected) maps were considered to determine where the changes occurred in the camera when normalization was applied. Figure 5.13 showed an example of changes made in a 20 ns run (without a ND filter). The two upper slides in Figure 5.13 show a saturated and bad pixel corrected T1 camera flasher image map of pixels (left upper slide) compared to a T1 camera flasher image map which has remained uncorrected or not normalized (right upper frame). A Gaussian fit to a sum ADC histogram of the normalized pixels was carried out, also shown in Figure 5.13 (left histogram). This is also compared to a histogram of non-normalized pixels in Figure 5.13 (right histogram). The mean sum ADC value of the normalized pixels on the left histogram increased as expected, compared to the non-normalized mean sum ADC value on the right histogram. When these corrections to bad and saturating pixels were made, linearity tests (or tests showing that the pixels were responding linearly to flasher signal intensity amplitudes up to a maximum of 10 nanoseconds without filter) were applied to all corrected or unmodified pixels in the T1 inner camera boxes (1 to 16).

It was found that only a handful of pixels responded linearly for all calibration

results. The change of flasher signal at 10 ns (no filter) setting was then plotted over the eight flasher calibrations totaling thirty months duration for the selected pixels (see Figure 5.9). A similar plot was made on the same figure from June 2002 onwards, for pixels at 10 ns ND 0.4 setting. The decrease in value from the initial few calibration mean ADC points for these pixels in Figure 5.9 (followed by an increase at the last calibration) is due to sensitivity to the telescope dish parking position, resulting in slight changes to the flasher image position taken monthly, located with respect to the camera centre. This effect is explained in Section 5.2.2.

5.3 T2 flasher calibration analysis

5.3.1 T2 flasher calibration introduction

Module	*Level*
tdc_discri	-220 mV
lsum_discri	-300 mV
nhit	-40 mV
nbox	-30 mV
asum	-180 mV

Table 5.6: Discriminator module settings of the T2 telescope for flasher calibration.

To trigger the T2 telescope from the flasher light pulses, the discriminator module levels were set at, or close to, the voltage levels for T2 in Table 5.6 for every T2 flasher calibration. The discriminators (levels to be set) are indicated in the following by bold text, e.g. **nhit**. The discriminator settings in Table 5.6 were used in flasher calibration data taken during "shower mode", the voltages in Table 5.6, refer to the control voltage level settings for these modules and discriminators to control trigger

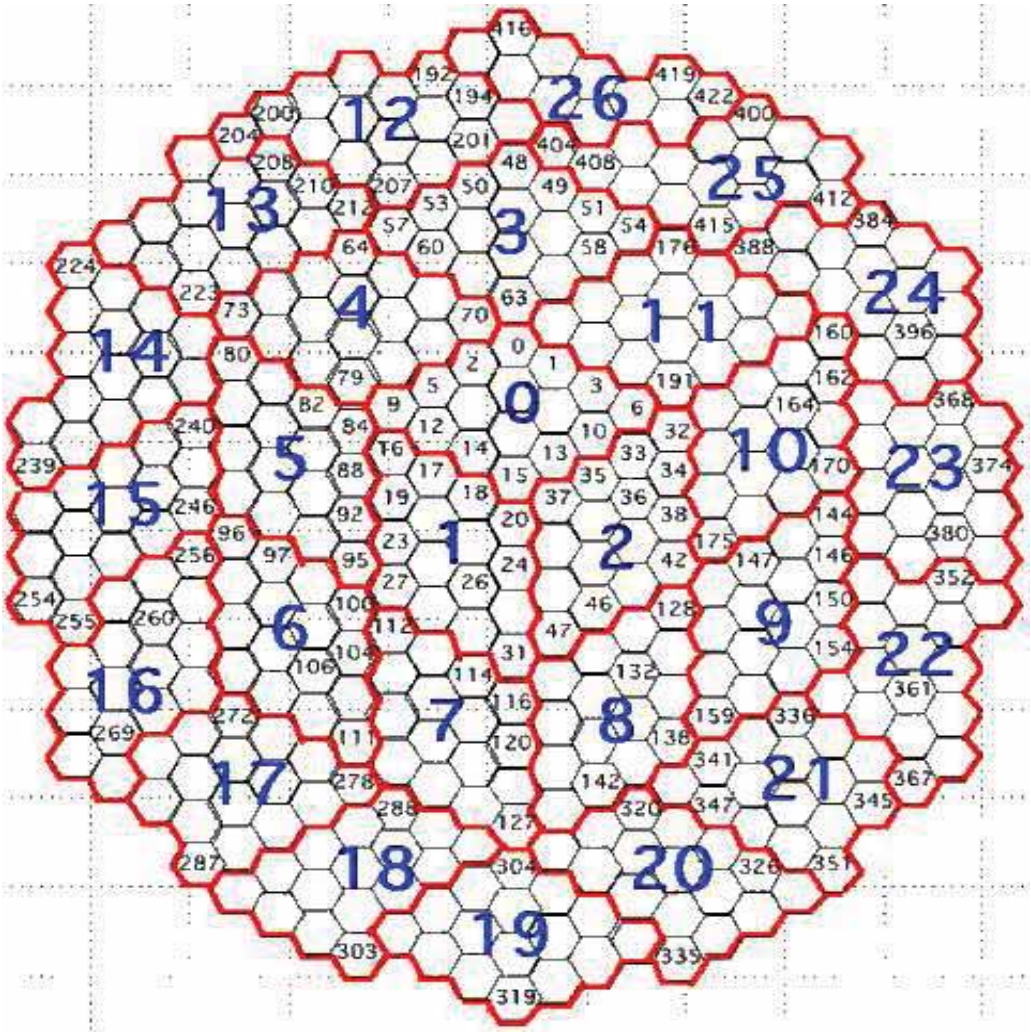

Figure 5.16: Box numbering PMT pixels in the T2 camera.

rate and data acquisition for the flasher calibration. The function of the discriminator modules, listed in Table 5.6; **lsum**, **tdc**, **nhit**. **nbox** and **asum**, are discussed in Section 3.2.6.

The T2 flasher calibration analysis procedure was similar to the T1 flasher analysis procedure, with differences between the two cameras being primarily due to geometry and gain calibration/pedestal reduction differences. Because of its hexagonal geometry the number of boxes differs for T2 compared to T1. Figure 5.16 shows the "box" separation of groups of PMTs in the T2 camera with all box numbers shown in large numbers and some PMT numbers displayed as small numbers. Box 26 is smaller than

all the other boxes in that it has 11 pixels. As with the T1 camera, the flasher signal was near the centre of the camera and the outer boxes were cut from the flasher analysis, hence boxes number 0 to 11 only were considered (PMT numbers 0-191). Boxes 0-11 have 16 PMTs each. Details of T2's camera are provided in Section 3.2.2, and the electronic data acquisition modules of T2 are discussed in Section 3.2.6.

Three calibration months of flasher data were acquired for T2 in the one year: January, June and October 2003, see Table B.3, Appendix B. In October 2003, it was decided to finish all field measurement for flasher calibrations and, as the construction and operation of T2 had only been completed just prior to January 2003, the number of months of flasher calibration data for the T2 telescope is sparse compared to T1.

Many of the optical effects already discussed from the flasher may similarly affect the results for T2, such as anomalous diffraction effects over distance (Section 5.2.1) and the size of the flasher image in the field of view (Section 5.2.3). The movement of the flasher image in the FoV of the T2 telescope is analyzed and discussed in the next section (5.3.2).

Figure 5.16 shows the pixel and box configuration of the T2 camera, where some pixel numbers are identified and all box numbers are shown (large numbers), starting from box number zero at the camera centre. Bad and saturating pixels correction was also carried out for T2, except that the number of adjacent pixels were six instead of eight. It was generally found the the quality of the ADC count distribution was considerably better for T2 compared to T1, so bad pixels were not found (according to the definition of "bad" pixels for T1 as distinct from "bad channel" pixels, see Section 5.2.5 for a description of T1 bad pixel detection). For T2, the bad pixel correction procedure relied wholly on "bad channel" flagging by the *calib10b* program. The procedure to correct T2 bad channel pixels was similar to bad channel correction in T1 (Section 5.1.7), where the **calib10b** format mean ADC values of adjacent pixels to the bad channel pixel were summed and the result averaged to produce the corrected pixel ADC value. If any adjacent pixel (to the bad channel pixel) was also flagged as a bad channel pixel, then this pixel would be skipped over the sum of mean ADC values of adjacent pixels and an allowance made in the mean count. For T2, the bad

channel pixels were corrected in the pixels of inner boxes numbers 0-11 (Figure 5.16). Bad channel pixels in the outer boxes 12-26 remained uncorrected as they were not included in the flasher calibration analysis.

Mean sum ADC values for T2 to determine the flasher signal amplitude in the T2 telescope, were also summed only over the inner 192 pixels of boxes 0-11. The flasher mean sum ADC values were subsequently corrected for measured changes in the pin diode measurement of the flasher emitter for January, June and October 2003, see Table 4.3. This mean sum ADC is compared to the cross-correlation maximum position from the camera centre in the following section.

5.3.2 T2 cross-correlation analysis of the flasher image

A two-dimensional cross-correlation analysis of the image in the FoV of T2 was made to ascertain if the flasher image shifted in the three calibration months carried out for this telescope. The cross-correlation analysis function was explained in Section 5.2.2, with Equation 5.13 and Equation 5.14, describing this function. The T2 telescope used the cross-correlation algorithm written by the author, with changes made to the coordinate grid upon which the cross-correlation analysis was made. The T2 camera has a hexagonal geometric arrangement, shown in Figure 5.16, where some of the 426 PMTs pixel numbers of this camera are shown.

In the hexagonal arrangement of the T2 camera, the six adjacent PMT pixels are 60° from any central pixel (provided the central pixel is not at the very edge of the camera), which can be seen in Figure 5.16. This geometrical arrangement of pixels in T2 is different to the T1 camera, which is based on a square grid (except for the corner boxes), see Figure 3.7.

After unsuccessfully experimenting with constructing a hexagonal grid for the two-dimensional cross-correlation analysis based on a 60° orientation from a central pixel, the author decided to graft a rectangular grid over the central section of the camera, which would be large enough to cover all the ADC pixels of the flasher image in all

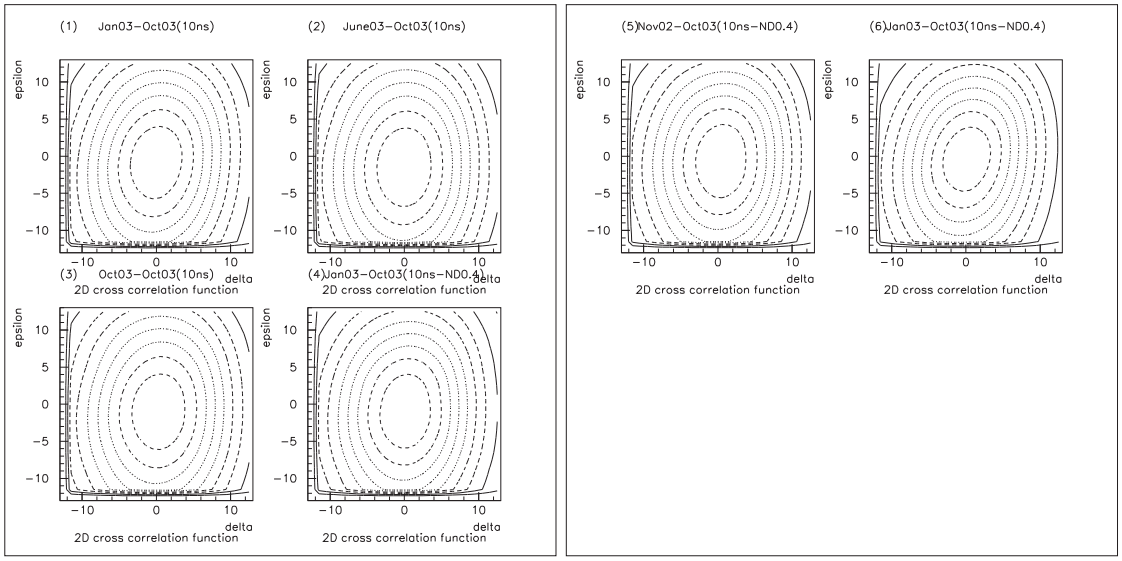

Figure 5.17: Two dimensional cross-correlation results for the T2 flasher calibration by calibration month, shown in the cross-correlation transform space of x-shift (delta, δ), y-shift (epsilon, ϵ). The centre of the concentric rings in these slides (numbers 1 to 6), is the position of the cross-correlation maximum. This maximum position is shown in δ and ϵ, in Table 5.7. Slides 1 to 3 are the 10 ns flasher setting and slides 4 to 6 are 10 ns ND 0.4 flasher setting. The cross-correlation months (shown above each slide) as January and June 2003 with slides 3 and 6 showing the auto-correlation function (cross-correlating October 2003 with itself). For clarity, this figure has been enlarged in Appendix E, Figure E.5.

calibration months. This arrangement enabled the author to proceed with a similar two-dimensional cross-correlation algorithm to the one used in T1, in order to calculate the two-dimensional cross-correlation maximum for T2. The flasher image sits comfortably within the grafted rectangular array grid pixels. The subsequent "rectangular over hexagonal" grid was nine camera pixels high and eight camera pixels wide with the central camera pixel number 20 (Figure 5.16, box 1) in the centre of the rectangular grid. The grid resolution was further subdivided by linearly interpolating the spaces between each pixel in the x-direction and y-direction separately: The difference of the mean ADC value (over the number of data file triggered events) of each adjacent pixel was divided by six on the rectangular (8×9) grid, and the section between adjacent pixels was filled by the six linearly interpolated values. This gives a total of 46 row pixel elements (not counting the end pixels twice), and 52 column pixel elements of the

rectangular array grid.

A similar procedure of linearly interpolation evaluation of adjacent pixels was carried out for the degree coordinate position of the original PMT pixel. Because there is a rectangular grid grafted over a hexagonal grid, the angular shift between the x-direction is larger than the y-direction. In our case, the difference between adjacent x-direction pixel elements on our rectangular grid is 0.050°, and the difference between adjacent y-direction pixel elements is 0.029°. This is unlike the square grid of the T1 two-dimensional cross-correlation (Section 5.2.2), where the angular difference between adjacent pixels in the x-direction and y-direction is the same.

calibration month	δ	ϵ	*x-shift (deg.)*	*y-shift (deg.)*	*angular dist. from centre*
January 2003, 10ns	-1	-2	0.050	0.029	0.057
June 2003, 10ns	0	-1	0.0	0.0	0.0
October 2003*, 10ns	0	-1	0.0	0.0	0.0
Jan. 2003, 10ns ND 0.4	0	-1	0	-0.029	0.029
Jun. 2003, 10ns ND 0.4	0	-1	0	-0.029	0.029
Oct. 2003*, 10ns ND 0.4	0	0	0.0	0.0	0.0

Table 5.7: The position of the two-dimensional cross-correlation maximum point, by calibration month for T2. The last column shows the angular distance from the camera centre, calculated by $\sqrt{X\text{-shift}^2_{\text{deg.}} + Y\text{-shift}^2_{\text{deg.}}}$ (see equation 5.15). The asterisk shows the auto-correlation month (for both 10 ns and 10 ns ND 0.4 settings) whereby the angular shift is calculated from it. In the 10 ns case, the auto-correlation result was not at the exact camera centre, i.e. $\delta = 0$, $\epsilon = -1$.

Cross-correlation analysis of T2 flasher images were carried out for the flasher set at 10 ns for the three calibration months (January, June and October 2003) and also for the flasher setting at 10 ns with the ND 0.4 filter inserted for the same months. Figure 5.17 shows the result of the cross-correlation analysis, where the contours in each slide show the value of the cross-correlation in delta and epsilon and where the centre of the central-most contour is the position of the cross-correlation maximum. The cross-correlation shift in δ and ϵ is shown in Table 5.7 with the angular shift in this movement

(from the auto-correlation result from October 2003, for both 10 ns and 10 ns ND 0.4 settings). For the 10 ns setting of the flasher, the auto-correlation result was not at the camera centre, but shifted slightly vertically from it (i.e. $\epsilon = -1$; slightly vertically downwards from the camera centre). This meant that for the previous months for this flasher setting, the value $\epsilon = -1$ is subtracted from the values of epsilon for the other months. For example, in the case of January 2003, $\epsilon = -2$ and subtracting $\epsilon = -1$ from this yields a shift result, $\epsilon = -1$ indicated in Table 5.7 in the angular shift in the y-direction. Reasons for this anomalous shift expressed in the auto-correlation result at 10 ns, are discussed in Section 8.1.2.

All the six slides in Figure 5.17 are distorted in the y-direction by the grafted rectangular grid and by the angular difference in adjacent pixels in the x- and y- directions discussed above. This shows in the "stretched" or elliptical T2 cross-correlation maximum contour lines in Figure 5.17, in comparison to the circular cross-correlation maximum contour lines for T1 in Figure 5.8.

To summarize, Table 5.7 indicates the movement of the flasher image in T2's field of view in terms of the x and y angular shifts, and the distance from the camera centre via that shift. As with the previous Section 5.2.2 for T1 in this chapter, we subtracted the CCMP (Cross-Correlation Maximum Position) distance (from Table 5.7) from 1.0° to compensate for the falling sum ADC amplitudes with increasing CCMP distance for T2. Also, as with T1, we obtained the normalized average mean ADC by taking it to a ratio for the calibrating month (see equation 5.16 in Section 5.2.2), which for T2 was the same calibrating month as T1, i.e. October 2003. Table 5.8 (below) shows this result.

Unlike T1, there are two sets of data for T2: 1. The flasher on the 10 ns setting without light attenuating ND filters and, 2. The flasher on 10 ns with the ND 0.4 neutral density filter inserted in front of the flasher lens. These two settings were available in the three calibration months for T2; January, June and October 2003, where these two settings were consistently applied. For T1, flasher calibration months April 2001 and February 2002, lacked any ND filter calibration setting.

Figure 5.18, shows the monthly variation of the CCMP distance from one and the

T2 calibration month	*1 - CCMP deg. dist.*	*normalized average mean ADC*	*flasher setting*
January 2003	0.94	1.05	10 ns
June 2003	1.0	dew on mirrors	10 ns
October 2003	1.0	1.0	10 ns
January 2003	0.97	1.02	10 ns ND 0.4
June 2003	0.97	dew on mirrors	10 ns ND 0.4
October 2003	1.0	1.0	10 ns ND 0.4

Table 5.8: Distance of the two-dimensional cross-correlation maximum point from the T2 camera centre from one (see Section 8.1.1), versus the normalized average ADC of the 192 inner camera pixels.

normalized average ADC from Table 5.8 (above). All four data points (the normalized mean ADC and CCMP distance from one for the two flasher settings discussed), in general show a dip in values in June 2003, compared to the two other calibration months. This may be attributed to mirror dewing on the T2 mirrors. Mirror dewing occurred (as discussed in the previous Section 5.2.2 for T1), during the flasher calibration on the June 2003 night. All data points in Figure 5.18, are at value one degree in October 2003 (due to normalizing the average ADC at this month and also being the auto-correlation month), and so this is shown as a single datum at this month, masking the other three data points at precisely the same value.

The normalized average ADC for T2 is shown in Figure 5.18, and in Figure 5.19. The average ADC is taken (unlike T1) to be the average value over the 192 inner camera pixels for T2, by summing their discrete mean ADC values. The uncertainty in the average ADC value (of the flasher) is larger for T2, in comparison to T1 (see Figure 8.1 (Section 8.1.1), and also Section 5.1.4 to explain T1's mean ADC value calculation), because we uncritically take all mean ADC values in the inner camera, including low ADC amplitude pixels on the edge of this area (mainly in boxes 3 to 11, see Figure 5.16) as well as high ADC amplitude pixels near the centre of the camera (mainly in boxes 0 to 2). The pixels in boxes 3 to 11, further out from the centre of the camera, are not cut from the calculation of the average ADC, because of the likelihood

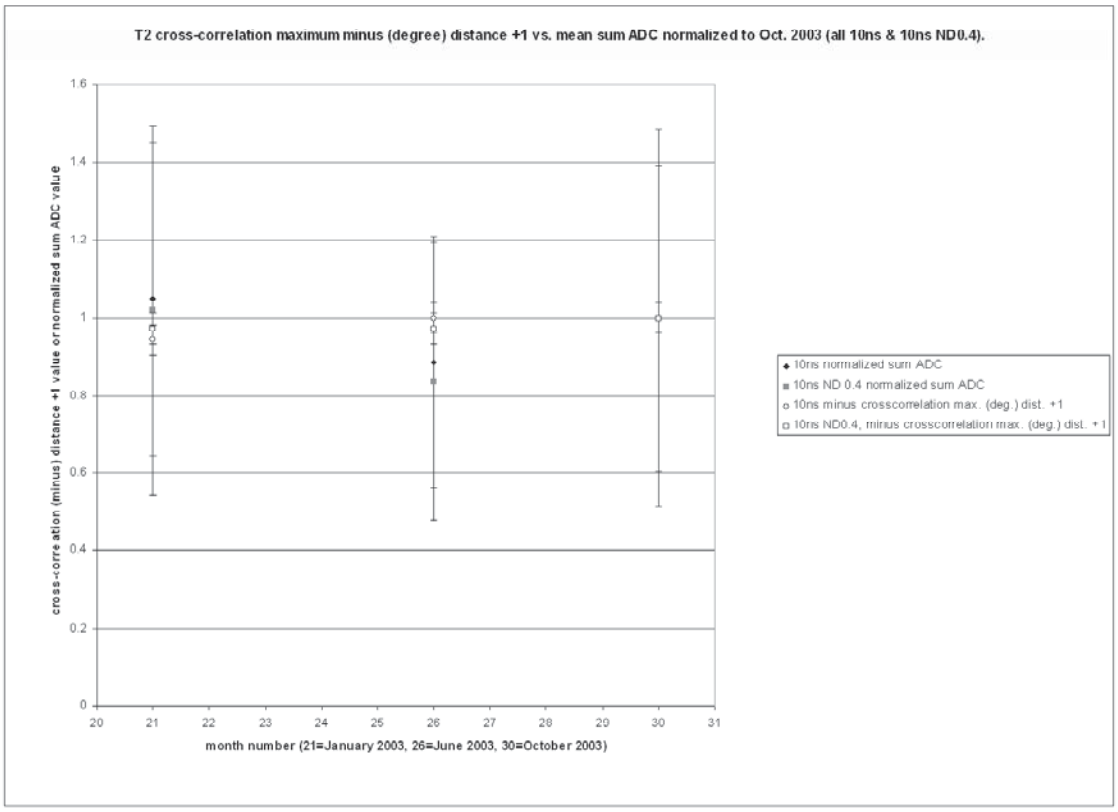

Figure 5.18: Showing: 1. Normalized ratio of average mean ADC of the 192 inner T2 camera pixels for the calibration months, January, June & October 2003, for 10 ns & 10 ns settings. 2. Normalized T2 cross-correlation maximum position distance from 1.0°, for 10 ns & 10 ns ND 0.4 settings. All results from other months are normalized to the sum ADC and cross-correlation maximum values from October 2003. Error bar size is explained in the main body of the text. This figure is enlarged in Figure F.3 (Appendix F), for clarity.

that the higher ADC amplitude pixels from the flasher image may drift into boxes 3 to 11 during a calibration month. Thus, as we can see in comparing the error bar sizes (Figure 5.18) of the normalized average ADC of T2 to the error bar sizes in Figure 5.10, and in Figure 8.1 of the normalized average ADC of T1, the error bars for T2 are somewhat larger for this quantity (at least $\sim 25\%$. larger than T1). Futhermore, because of normalization of data points in Figure 5.18 (as the ratio of a calibrating month over a fixed month), the size of the uncertainty (error bars) will approximately double.

For T2, the correlation between the CCMP angular distance from one degree and

the normalized average ADC is shown in Figure 5.19. The linear least squares line of best fit for the data points in this figure has a coefficient of determination, $r^2 = 0.9809$, indicating a very good linear fit for these three points. Additionally, the Pearson correlation coefficient for this result is, $r = -0.9904$, indicates a near perfect decrement between the CCMP angular distance, and the normalized average ADC. From the result of the Pearson correlation coefficient of T1 ($r = 0.8886$), the T2 result from Figure 5.19 is counter to the T1 result we obtained from Figure 8.1 (Section 8.1.1), as the difference of the CCMP angular distance (from the camera centre or auto-correlation position) increases, the normalized average ADC decreases. This is opposite to what had occurred (for T1 in Figure 8.1), and is counter-intuitive to our T1 hypothesis (italicized in Section 8.1.1), i.e. as CCMP angular distance increases, the normalized average ADC increases. However, given the size of the error bars, such a discrepancy is well within the range of expectations.

In comparison to the cross-correlation result for T1 showing possible gravitational distortions (Section 5.2.3), it is difficult to draw such a conclusion from T2 results, either from the cross-correlation results (Table 5.7) or from Figure 5.17. Systematic error in T2 is masked by the distortion error in converting from hexagonal grid coordinates to "square" grid coordinates (explained previously in this section). Thus, it is very difficult to test systematic error due to gravitational distortion of the T2 dish or camera struts with these results.

The conclusion to the cross-correlation maximum analysis of T2 is shown in Section 8.1.2.

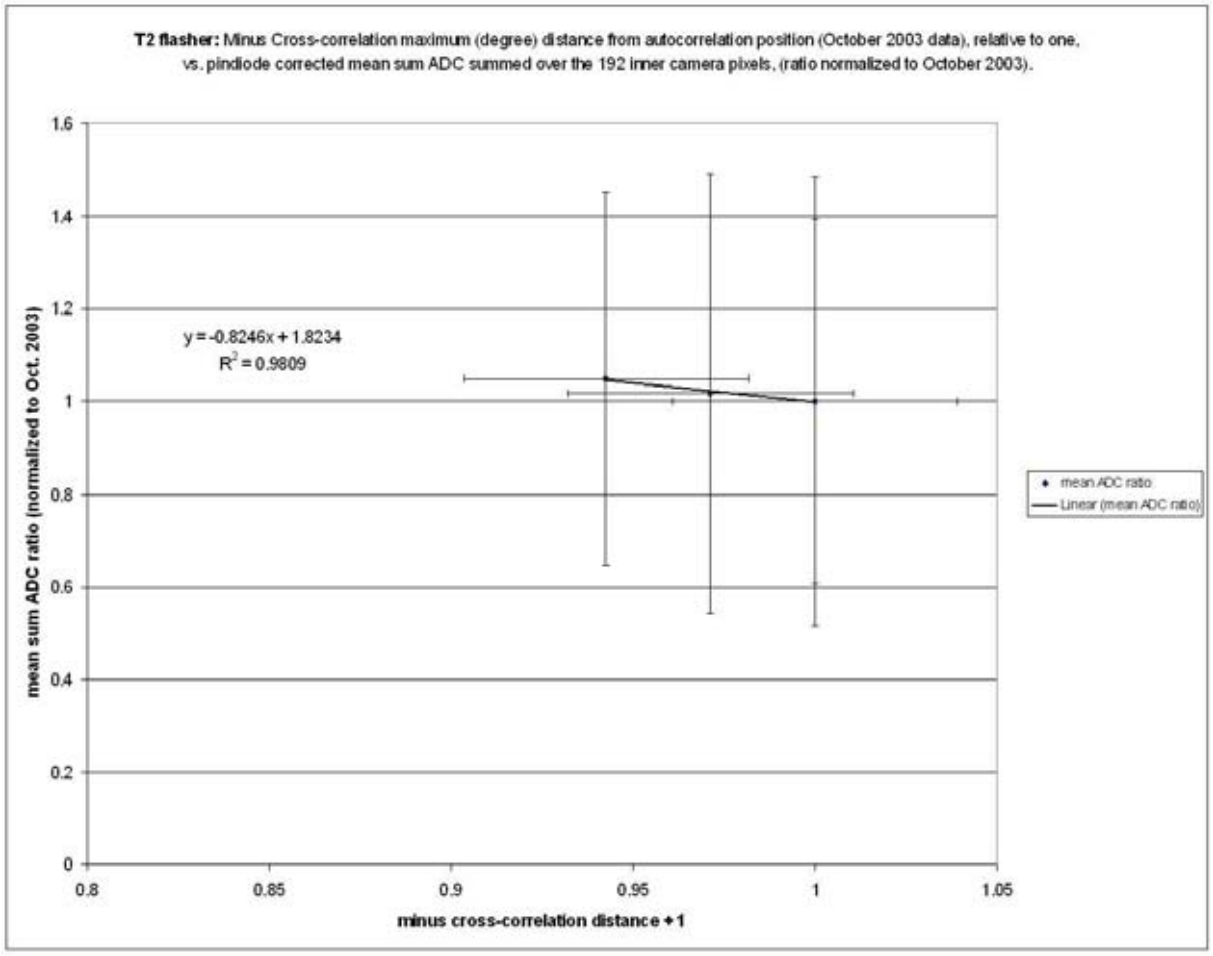

Figure 5.19: Plot of cross-correlation maximum position distance from 1.0°, versus ratio of average mean ADC of the 192 inner T2 camera pixels over January & October 2003 for 10 ns and 10 ns ND 0.4 settings, to test the hypothesis (that of correlation), between these two variables. The least linear squares fit result equation is shown in the centre left of the figure. The data from June 2003 has been left out due to mirror dewing on this month.

Chapter 6

Attempt at cosmic ray zenith angle calibration of the T1 telescope

6.1 Introduction

As a second calibration study, the author has also been determining the absolute energy threshold of the CANGAROO-II (T1) telescope by using the maximum shower rate of cosmic ray showers at the zenith (elevation 90°). The conditions for a successful cosmic-ray calibration are as follows: 1. The sky must be dark and clear. Even thin clouds will raise the energy threshold. 2. The sky at the zenith should be outside the dust lanes of the Milky Way and, if possible, no stars brighter than 4^{th} or 5^{th} magnitude should be present in the field of view. The cosmic ray data file is taken in shower mode, where the discriminator levels are set for the source which is being observed in that month whose culmination has the lowest zenith angle, i.e. which has the highest elevation upon culmination. It is desirable that the event rate for the cosmic ray showers be reasonably high ($>$ 5Hz), to improve the data statistics. Data aquisition is typically taken in the following order: 1. The cosmic ray shower run is from between 20 to 30 minutes duruation, this is so that the scheduled source observation time is not severely compromised while allowing suffcient shower event statistics. 2. A random trigger run is made to determine the level of background skynoise.

6.2 Zenith cosmic ray calibration results

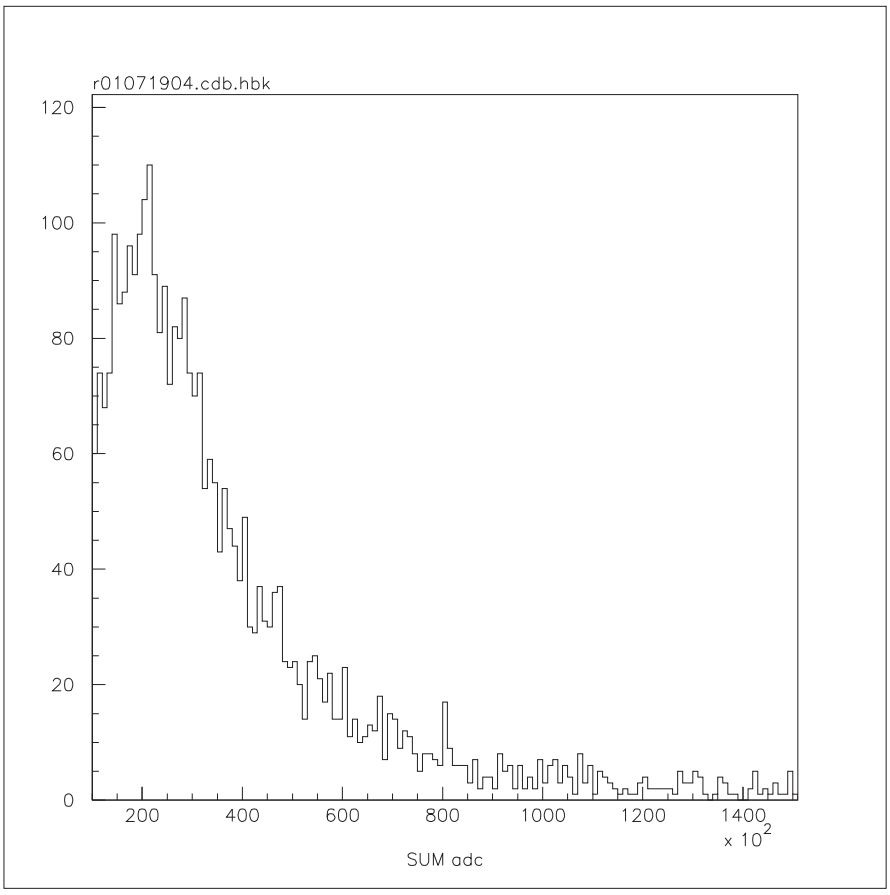

Figure 6.1: Zenith cosmic ray shower run from July 2001 from **calib10**. The abscissa range is 10000 to 150000 sum ADC counts.

The zenith cosmic ray data files are converted to **calib10** format. Histograms of the sum ADC are then made from the cosmic ray shower data. The energy distribution of cosmic ray showers should be evident as a decay from the peak turnover indicating the threshold level of CANGAROO-II (T1). Figure 6.1 (above) shows the result of a zenith cosmic ray run in July 2001. The mean sum ADC of the peak value (frequency value ~ 110) of the histogram in Figure 6.1, corresponds to the absolute energy threshold of CANGAROO-II in sum ADC. The mean sum ADC of this peak value is estimated to be $(220 \pm 20) \times 10^2$ sum ADC counts. The cosmic ray energy spectrum is clearly evident in the decay forward from the peak and falls off behind the peak as lower energy cosmic

ray showers fail to trigger the telescope.

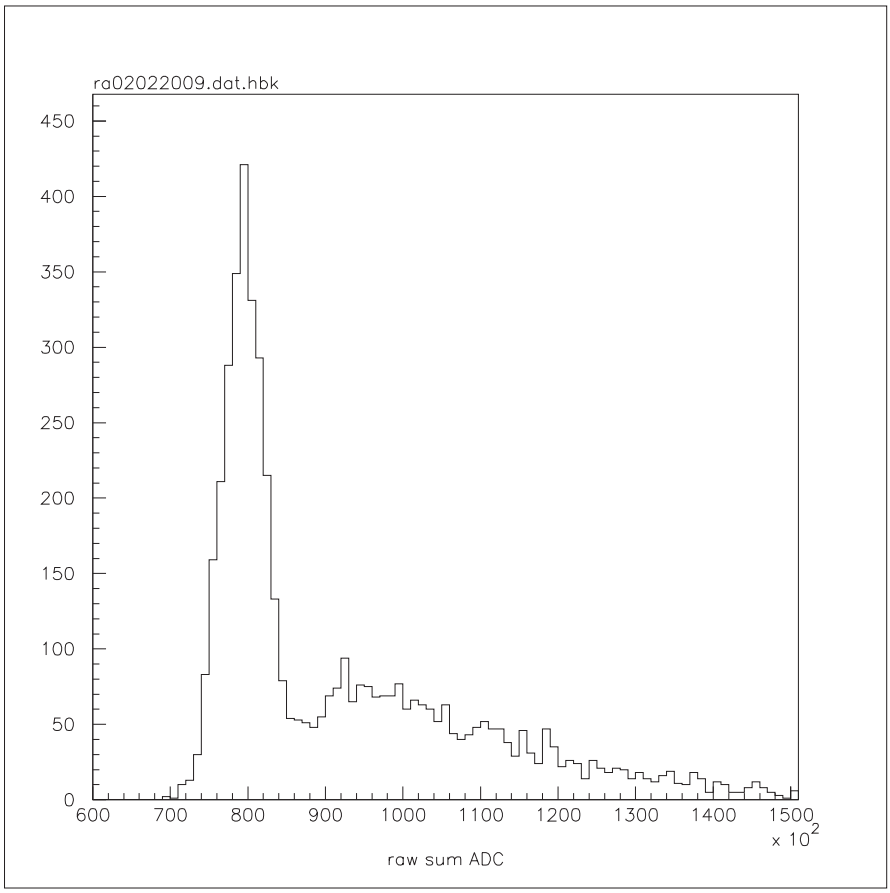

Figure 6.2: Zenith cosmic ray shower run from Feb. 2002, uncalibrated. The abscissa range is 60000 to 150000 sum ADC counts.

To convert the telescope threshold from sum ADC counts to energy, the author has used the results of Nakase (2001) [126], in his estimate of ADC counts to photo-electrons (p.e.) for CANGAROO-II. Nakase's estimate is 1 p.e. $= 99.6 \pm 0.3$ ADC counts. After conversion of sum ADC counts of the threshold to photo-electrons, the author then used a result from Hillas and Patterson (1990) [80], of simulations for a 10 metre telescope at the zenith for 320 GeV cosmic ray (proton) showers. This result assumes a single solid 10 metre diameter mirror reflector and, as CANGAROO-II is made from compound mirrors with spaces in between, the 10 metre mirror result of Hillas and Patterson (1990) [80] is multiplied by 74% to convert to the actual reflectivity

area of the CANGAROO-II 10 metre dish. The final result for the calculation of the absolute energy threshold for CANGAROO-II from the peak in Figure 6.1, assuming the above conversions, is 599 ± 29 GeV in July 2001.

A cosmic ray zenith run calibration was also carried out in Feb 2002. Figure 6.2 shows the result of this calibration. This data file is uncalibrated, as the author found that the **calib10** calibrated file did not show a threshold peak, as did the result from July 2001 (see Figure 6.1). The reason for the lack of a threshold peak in Figure 6.2 (**calib10** format) is likely to be due to *calib10* processing (see Section 5.1). The cosmic ray threshold "peak" in Figure 6.2, in any case is weak (see below). The conditions under which the data files in July 2001 and Feb. 2002 were taken were similar, i.e. the discriminators were set at similar levels and the trigger rate was about the same. Pedestal and night sky background noise removal in the conversion of the raw file to **calib10** format will remove the large night background peak at $\sim 800 \times 10^2$ sum ADC (Figure 6.2). Thus, the raw data from Figure 6.2 were not shifted to zero (as was the case for Figure 6.1) as the ADC pedestals and night sky background noise were not removed. Using the raw data in Figure 6.2, the author took the difference of the large peak at sum ADC = $(790 \pm 5) \times 10^2$ as the night sky background peak, and the threshold caused by cosmic ray showers to be the smaller peak at sum ADC = $(925 \pm 10) \times 10^2$. The difference between these two peaks is then taken to be the CANGAROO-II threshold peak position of $(135 \pm 15) \times 10^2$ sum ADC. Using the results of Nakase (2001) [126] and Hillas and Patterson (1990) [80], the threshold energy level of CANGAROO-II from cosmic ray showers in Feb. 2002 was found to be 368 ± 42 GeV.

Due to the discrepancy of these two energy threshold measurements in July 2001 and February 2002, further zenith cosmic ray measurements will be required to test the absolute energy threshold. The threshold value of 368 ± 42 GeV appears to be unlikely from February 2002, as it has a lower threshold value than the 599 ± 29 GeV in July 2001. Deterioration of the reflectivity of the telescope mirrors over the seven months (July 2001 to February 2002), would suggest that the telescope energy threshold should increase from July 2001. It should be noted here that this analysis of energy

threshold measurements using cosmic ray showers was preliminary in this investigation and resulted in unsatisfactory results, contrary to expectations that the telescope's energy threshold should rise with the passage of time (due to mirror degradation). A more successful attempt at measuring the telescope's energy threshold using this technique would require:

1. A series of measurements with the telescope pointed at the zenith (acquiring cosmic ray shower data in ADC counts) over successive nights would improve the statistical mean (energy threshold) estimate and eliminate outliers.

2. Another measurement estimate of the ADC count to photo-electron count would be required (at about the same time) when the new series of zenith cosmic ray shower data are taken. This would also take into account deterioration of the camera PMT photocathodes (loss of quantum efficiency).

3. Monte Carlo cosmic ray simulations using the dish optics and camera parameters for the CANGAROO telescopes should be run (at the zenith) to estimate energy threshold.

4. A properly calibrated reflectometer could be used to measure the reflectivity amplitude of a few telescope mirrors (on the night) when zenith cosmic ray data is acquired. A reflectometer is an instrument utilizing a blue LED emitter, measured through mirror reflection by a PIN diode.

5. Steps 1 to 4 (above) would be repeated a few months later to check response of the telescope's energy threshold over time. For good results, another two series of measurements should be taken (separated by months) after that.

Chapter 7

Gamma ray source analysis of the Markarian 421 and EXO 055625-3838.6 BL Lacertae blazars

7.1 Markarian 421 results

7.1.1 Introduction

Definitions of Active Galactic Nuclei (AGN) and blazars are found in Section 2.2. The confirmed (in TeV gamma ray) source HBL Lac. blazar, Markarian 421 (abbreviated as Mkn 421), has been studied for a comparatively long time by various well-established gamma ray astronomy IACT groups; VERITAS/Whipple (Acciari *et al.* (2009) [1], Punch *et al.* (1992) [144]), HESS (Aharonian *et al.* (2008) [2], Lemière (2004) [109]), HEGRA (Aharonian *et al.* (2002) [8], Petry *et al.* (1996) [138]), MAGIC (Aleksić *et al.* (2010) [13], Albert *et al.* (2006) [12]). This blazar source is one of the closest HBL Lac. objects to be studied (redshift; $z = 0.031$, Kohnle *et al.* (2001) [98]) in TeV gamma rays.

The results here are the first instance of a CANGAROO-II observation of this source (using the T1 telescope) at large zenith angles. Concurrent to these results, the results from Mkn 421 from T1 were independently analyzed and published by Okumura *et al.* (2002) [133]. Although the author has largely used the same raw data files from the TeV gamma ray source data from T1 for Mkn 421, the results discussed here use a different algorithm produced by the author and are not associated with the software and analysis procedure used by Okumura ([133]) in his results. Observations of Mkn 421 have been subsequently carried on by the CANGAROO collaboration using the T2 to T4 array in stereoscopic mode. However, this thesis will examine the results obtained by the T1 telescope only operating in mono (non-stereo array) mode.

Mkn 421 is discussed using the electron (positron) induced Inverse-Compton (IC) synchrotron spectrum model. The Markarian 421 gamma ray results discussed in this chapter will refer to this spectrum model (see Section 2.2). Furthermore, the attenuation of the GeV-TeV gamma ray flux by extragalactic background light from Mkn 421, is discussed in Section 2.4.

7.1.2 Markarian 421 data acquisition files

The T1 telescope's observations of Mkn 421 (examined in this thesis) were made in the period 24$^{\text{th}}$ January 2001 to the 12$^{\text{th}}$ January 2003 (see Tables H.1 and H.2 in Appendix H for a summary of these observation nights). Mkn 421 was observed in the months of January and February 2001 for six (January) and one (February) nights. Furthermore, the observations occurred over four nights in March 2001, five nights in February 2002, and four nights in January 2003, for a total of twenty nights of observation of Mkn 421 (during a flaring state in 2001). The observations taken on these nights may have interrupted *a priori* observation schedules of other gamma ray sources during these months. However, when flaring of a HBL Lac. blazar was indicated at the time (by other IACT groups) that could be observed by CANGAROO, the CANGAROO observation policy was generally to switch observation to these sources for a few nights. This procedure is known as the ToO (Target of Opportunity) observation. Since Mkn 421 is a blazar source that flares frequently, it offered some opportunity for

CANGAROO to observe this source in a flaring state (see Section 8.2.2 for a discussion of a flaring (in flux) from Mkn 421 during 2001).

The three tables of Appendix H, show the following columns of data: Observation run number, "long on" or "long off" source indicator, total number of triggered events (not exclusively gamma ray or even EAS shower events in general), exposure time in minutes (i.e. how long data was acquired for the observation run data file), weather conditions and any reported hardware or dish faults during data acquisition. The observations in any month, did not always occur on consecutive nights, due mainly to bad weather.

The data acquisition run number is set in eight digit format following; e.g. 03111204. The first two numbers indicate the year (03=2003), the second two numbers indicate the month (11=November), the third set of double digits indicate the day of the month or day stamp (12=12$^{\text{th}}$ November), the last two digits indicate the run number sequence (04=fourth data acquisition file). The two digit data file sequence number indicates that up to 99 data files may be acquired on a day. In nearly all scenarios for the CANGAROO IACT data acquisition system, this is more than enough. Individual calibration files and LED scan (LED flat fielding) files (see Section 5.1.5) are given a unique data acquisition run number, required by the data acquisition computer. At least one LED scan was typically carried out before EAS data acquisition, hence the gamma ray source files do not typically start from run number 01.

The "long on/off" indicator shows that the observations were taken with the camera centre fixed on the gamma ray source Right Ascension (RA), Declination (dec.) coordinates (on-source), with an off-source fixed at a RA-dec. coordinates offset from the source coordinates, usually for the time taken for the on-source observations, e.g. if the on-source was initially observed for 2 hours (without interruption), then the off-source is set at RA + 2 hours, so that the telescope will track though the same zenith angle in the sky. The CANGAROO collaboration exclusively used long on-off observations at the time the data (in Appendix H) was taken. Other regimes of on-off-source observation techniques for IACTs (and there are several) used by other IACT collaborations, are outside the scope of discussion in this thesis.

The "exposure time" was the data acquisition time of triggered events in seconds (rounded to minutes) of data taking for the particular run number. Because we use a "camera" of more than 500 PMT pixels to view the Čerenkov light images of EAS, the exposure time is considered to be analogous to optical light CCD camera imaging (optical CCD camera exposure is usually measured in seconds). The telescope trigger rate is dependent on various factors such as the degree of cloudiness of the sky (minimum trigger rate) to the brightness of the star field in the FoV for T1 and the ground light intensity (maximum trigger rate), where the threshold voltage settings of the hardware discriminators may affect the trigger rate (see Section 3.2.6 and Section 5.1.2). The total event triggers (number of events column in Tables, Appendix H) is the accumulation of telescope triggers over the total exposure time.

The total number of long on-source minutes for Mkn 421 (from Tables H.1 and H.2 in Appendix H) is 2313.9 minutes and the total number of long off-source minutes for Mkn 421 (from the same tables in Appendix H) is 2060.5 minutes. The ratios between the raw on-source exposure time to off-source exposure time for Mkn 421 is 1.123:1, i.e. there was 12.3% more on-source time than off-source time. After software analysis of this data, where more on-source data was rejected than off-source (e.g. cuts done due to cloudiness) then these on-to-off source exposure times come considerably closer to parity (see Section 7.1.4).

The number of triggered events are the total telescope triggers recorded during data acquisition, including Čerenkov light induced by EAS of cosmic rays and primary gamma ray showers. However, many of the events triggered will not be EAS from either gamma ray or cosmic ray events, but from noise (a few random camera pixels) depending on the voltage thresholds set in the discriminators (see Section 5.1.3 and Section 3.2.6). The nuisance value of these noise events in filling the data file with useless data is quite significant, since a data bank of relatively fixed kilobyte value (the event record) is written for every event trigger. The only way with the telescope hardware to reduce these noise triggers is to increase the discriminator thresholds accordingly. This process is relatively crude with the CANGAROO-II hardware setup and increasing the telescope discriminator thresholds to reduce the noise triggers, risks

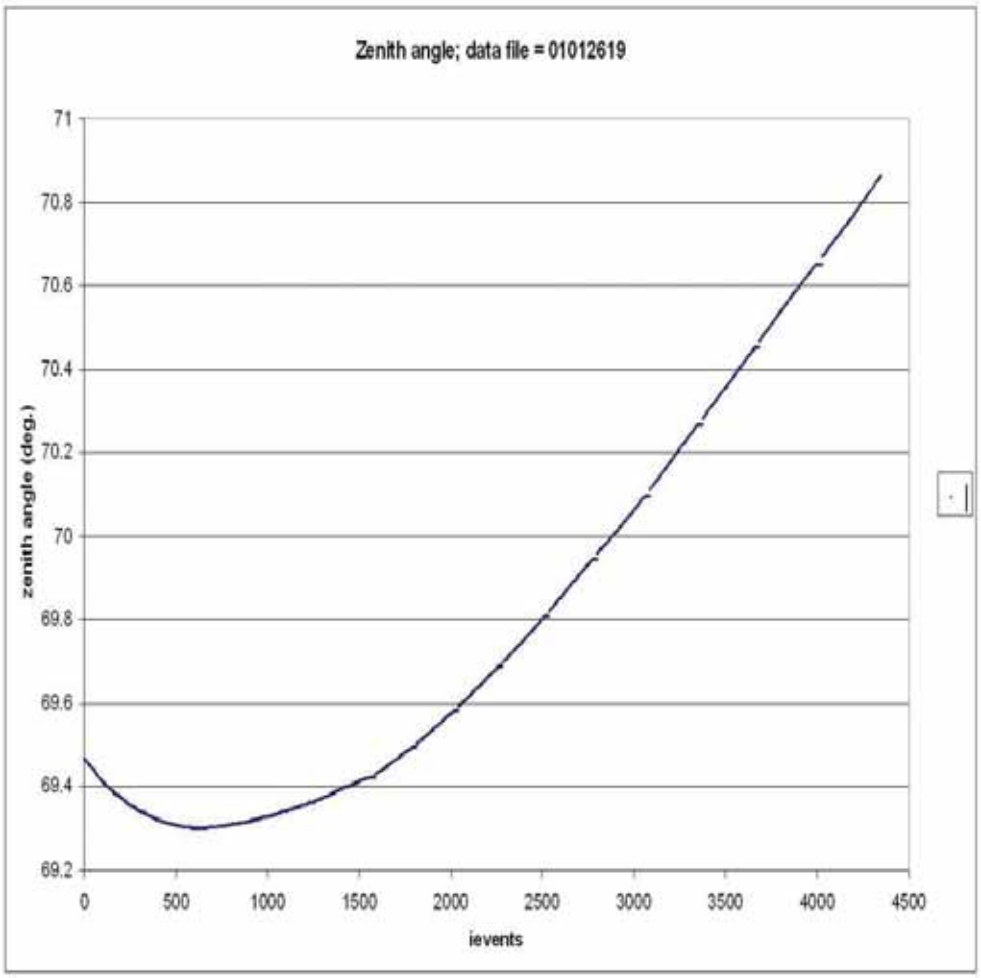

Figure 7.1: T1 dish tracking plot of the zenith angle of one Mkn 421 on-source data file (number 01012619) as an example. The zenith angle is 90° minus the dish degree elevation angle. The **ievents** number is the number of the telescope triggered events, proportional to the exposure time.

"small" (low energy or low particle) EAS from being detected. Since primary gamma ray triggered EAS fall in this category, increasing the discriminator threshold is risky. Accordingly, we need to accept many noise triggers in our raw data and to apply software "discriminator" algorithms to be able to sort EAS showers from noise, and to discriminate gamma ray EAS from cosmic ray EAS events.

The data from the tables in Appendix H, comes from the observer's summary report at the changeover in the observer's shifts at the end of the observation period. Unfortunately, the observer's report does not always contain a summary of the general

weather conditions of the night, e.g. "fine then cloudy". This omission when it occurs is puzzling and unhelpful, as the usual observer's practice was to take a weather report summary by observing the sky every twenty minutes during data acquisition.

The convention for measuring the telescope elevation of a high energy gamma ray source is the "zenith angle". From the Mkn 421 telescope data taken in 2001 to 2003, the smallest on-source zenith angle recorded (highest elevation) whilst tracking this source is 69.29° and the largest on-source zenith angle (lowest elevation) whilst tracking this source is 76.29°. An example of zenith angle changes whilst tracking the source is given in Figure 7.1.

7.1.3 Markarian 421 Monte Carlo simulation results

This section examines the results of running Monte Carlo software simulations run in the *FULL* software (Section 5.1.1) for gamma ray (on-source) and proton showers (off-source), at the zenith angle of Mkn 421 observed at Woomera (approximately 70°). The simulations were run in mono-mode (non-stereo) for the T1 10 metre diameter telescope. The results of these simulations enabled us to obtain the Hillas parameters for the ellipsoid (see Section 2.1.2, for a discussion of Hillas parameters) in order to discriminate for primary gamma ray shower events.

The Monte Carlo simulation core software code used in CANGAROO is *GEANT 3.21* (version 3.21), a subatomic particle software simulator developed by CERN in Geneva, Switzerland. Originally developed for high-energy physics experiments, *GEANT* is a framework for simulating the passage of subatomic particles through matter, for instance, particle detectors, Ravnda (1994) [145]. The simulation software algorithm involving the 552 (active) pixels of the T1 camera and dish optics geometry was added principally by Prof. R. Enomoto of the CANGAROO collaboration to complete the shower simulations through the T1 dish optics and camera. The last version of *FULL* written by him (used by the author for software simulations of primary gamma ray and proton showers), was from February 2005. The simulation software used after this date was deployed principally in stereo mode using two or more telescopes simultaneously. Since the observations of Mkn 421 were taken in mono-mode only with the T1 tele-

scope, CANGAROO simulation algorithms via camera and dish geometry developed after February 2005, deployed for *FULL*, are not useful for this thesis.

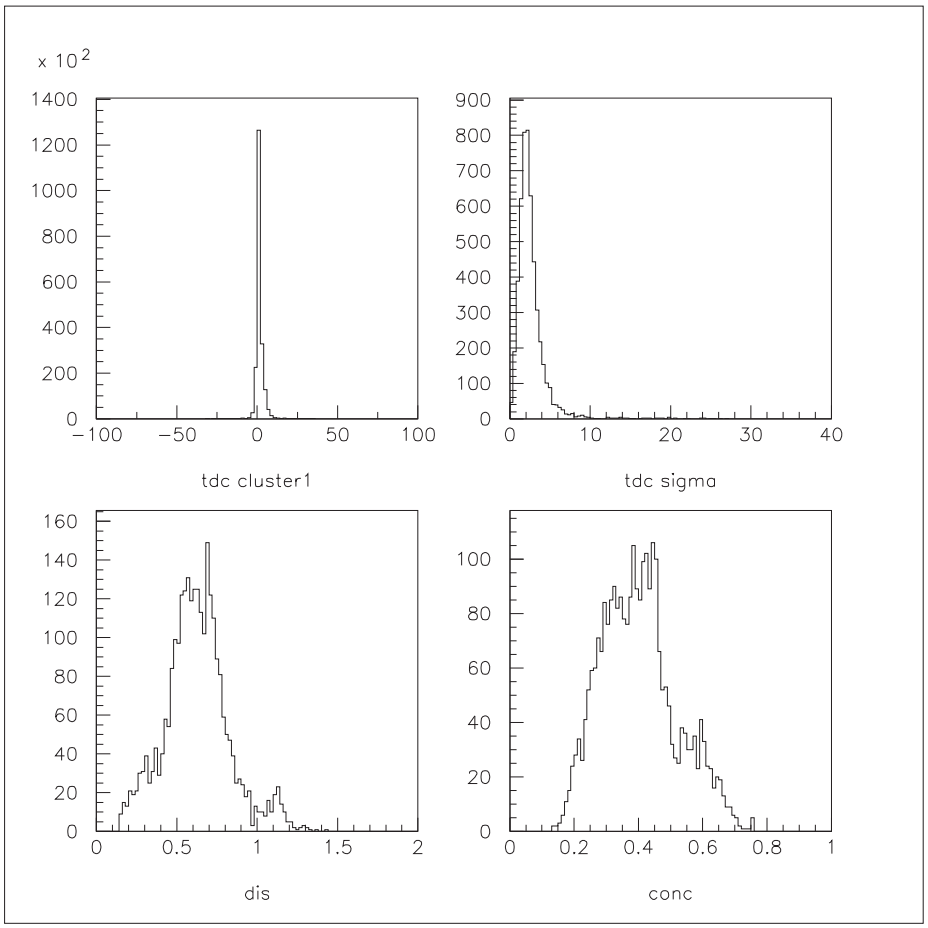

Figure 7.2: Histograms of primary gamma ray EAS Monte Carlo *GEANT 3.21* simulation results for Markarian 421: Showing the Hillas parameter *distance* (*dis*, bottom left histogram and given in units of degrees), amongst other results. The assumed spectral index for this source is 3.0, the zenith angle is 70° and the number of events simulated is 1×10^5.

We simulated primary gamma ray and cosmic ray (primary proton) showers separately for Mkn 421 using the *GEANT 3.21* EAS simulation code in *FULL* in 2005. For good statistical results, 10^5 showers were simulated in order to obtain the Hillas parameters required (Section 2.1.2). The Mkn 421 source showers were simulated at a zenith angle of 70°. This is close to average for the T1 observation data collected for Mkn 421, which is 72.8°. Since the observational mean zenith angle value is close

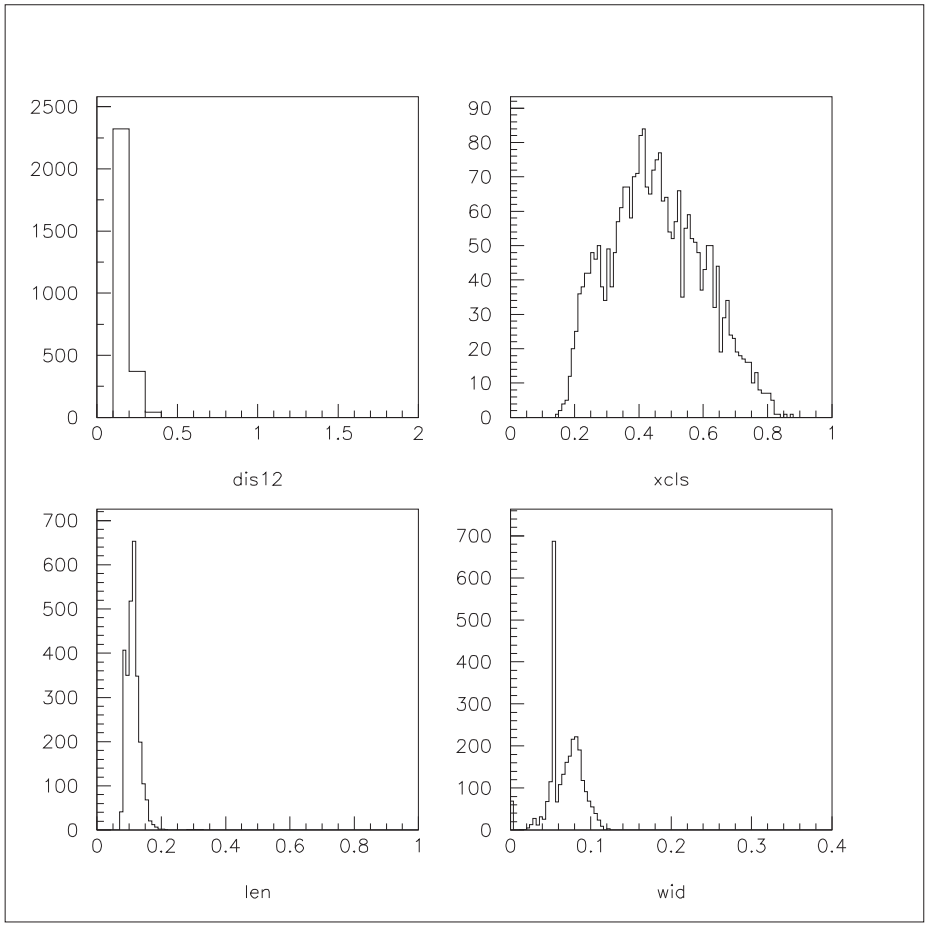

Figure 7.3: Histograms of primary gamma ray EAS Monte Carlo *GEANT 3.21* simulation results for Markarian 421: Showing the Hillas parameter *length* (*len*) and *width* (*wid*), all given in units of degrees, amongst other results. The assumed spectral index for this source is 3.0, the zenith angle is 70° and the number of events simulated is 1×10^5.

to the zenith angle used for shower simulations (70°) it should be suitable for setting the Hillas parameters for discriminating primary gamma ray showers from cosmic ray events for Mkn 421. To examine at length the effects of small changes to the simulation zenith angle (e.g. ±5°) in order to ascertain the differences in Hillas parameter results, is beyond the scope of this thesis. The Monte Carlo simulation work of Hillas & Patterson (1990) [80], has suggested that the Hillas parameter results are not sensitive to small changes in the zenith angle.

A further component of importance to Monte Carlo EAS simulations is the assumed

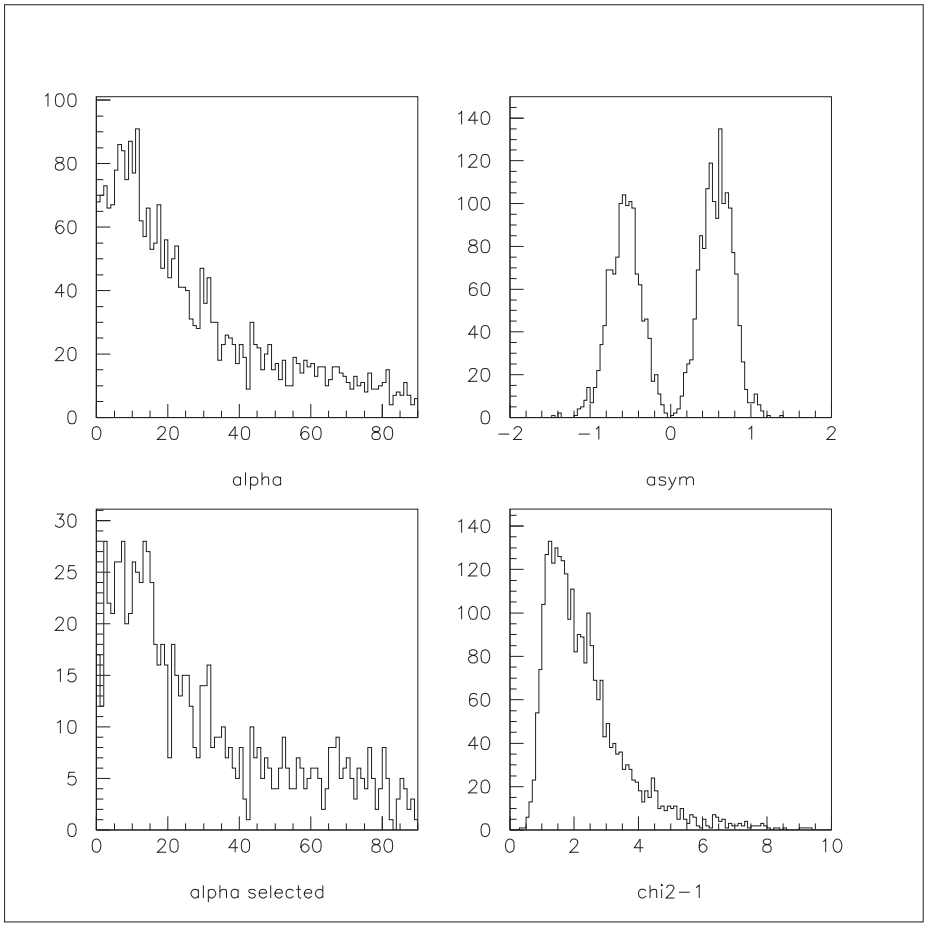

Figure 7.4: Histograms of primary gamma ray EAS Monte Carlo *GEANT 3.21* simulation results for Markarian 421: Showing the Hillas parameter *alpha* (top left histogram, given in units of degrees), amongst other results. The spectral index for this source is 3.0, the zenith angle is 70° and the number of events simulated are 1×10^5.

spectral index used. The spectral index chosen is usually based on a power law relation determining the Inverse-Compton (IC) spectrum of energy or frequency versus photon flux (for high energy particles). For instance: "The observed spectrum from a source radiating by the synchrotron process reflects primarily the distribution of energies of the radiating electrons. The energy spectrum of these electrons often has a characteristic shape or power law, and this leads to a radiated photon spectrum that is also a power law. The spectrum of radiation can thus be represented (by a power law function) as,

$$I = K\nu^{\alpha} \tag{7.1}$$

where I is the specific intensity, K is a constant and α is an exponent constant. In nature, power-law spectra usually decreases with frequency (energy), in which case α is negative. Because of this a positive spectral index ($\beta \equiv -\alpha$), is used so that (from equation 7.1 above), $I = K\nu^{-\beta}$. By convention, for high energy astrophysics, the (positive) index in equation 7.1 is used", Bradt (2004) [39]. It is understood that the power-law spectrum is decreasing with frequency (energy).

The spectral index is the index in the (GeV-TeV) synchrotron energy spectrum range for the IC gamma ray emissions of that source, usually determined by prior observation and/or simulation work, and may be extrapolated from these results. For the Mkn 421 simulation work done for this thesis, the (steep) spectral index of 3.0 was selected from Okumura (2002) [133] via the special case that the gamma rays from Mkn 421 are at a higher energy (above the cut-off energy of 3-6 TeV, [133]) due to the large zenith angle of $\sim 70°$. The detectable threshold energy of the gamma rays at this zenith angle was estimated by Okumura [133] to be 11±1 TeV. The Mkn 421 spectral index (for the simulation results presented here) determined by Okumura [133], is an extrapolation of the known Mkn 421 spectral index, derived at the time, from the observations of other IACT collaborations (HEGRA; Aharonian *et al.* (2002) [8], Whipple; Krennrich *et al.* (2002) [102]) of this source.

The primary EAS Hillas parameter "cuts" selected from our simulations were; *length* (*len*), *width* (*wid*) and *distance* (*dis*), and the secondary Hillas parameter cut *alpha* simulated in Figure 7.4 (all are given in units of degrees (Section 2.1.2)). The data analysis software (next Section 7.1.4), determines the moment of the ellipse constructed from shower pixel clusters. The discrimination selection between the elliptical gamma ray shower clusters from the source direction and the isotropically produced cosmic ray (proton) shower clusters, is analyzed by the shower events passing the cuts; *length, width*, and *distance*, after image "noise" cleaning such as pixel group clustering determination. The dimensions of these cuts were determined from simulation results shown in histograms in Figure 7.2 and Figure 7.3. The derived cuts (*distance, length* & *width*) were applied, using the following parameters, to the analysis of Mkn 421 (next Section 7.1.4), where: $0.08 \leq distance \leq 1.1$, $0.08 \leq length \leq 0.2$, and $0.02 \leq width \leq 0.13$.

The domain of these Hillas parameter cuts was determined by the range of the histogram frequencies in *distance, length* and *width* in Figures 7.2 and 7.3. The telescope EAS image event triggers passing these cut boundaries, were recorded as primary gamma ray images. The *alpha* Hillas parameter simulation, is an estimate of the shape of the *alpha* plot (Figure 7.4) with 1×10^5 shower simulations of gamma rays after event triggering losses in a high depth atmosphere (at the large zenith angle) and with assumed telescope optical parameter losses (such as mirror reflectivity).

The result for the Hillas parameter cut *alpha*, is displayed as a histogram in Figure 7.4. The *alpha* cut distribution is given in acute angle degrees. Figure 7.4 gives an indicator of how the *alpha* histogram plot should appear in terms of steepness of the slope along the top of the frequency plots from the maximum frequency value at 0°. At a small zenith angle (e.g. EXO 055625-3838.6 simulation results, Section 7.2.3), the *alpha* histogram plot slope should drop off rapidly to an approximate horizontal slope. From the EXO 055625-3838.6 *alpha* histogram plot in Figure 7.13 (Section 7.2.3), this appears to be the case where the slope of the *alpha* plot of this figure flattens out above $alpha \sim 30°$. Compare this to the *alpha* histogram plot from Mkn 421 at a much higher zenith angle in Figure 7.4, where the steepness of the *alpha* plot from the maximum (approximately 0°), is less than Figure 7.13 and the *alpha* plot curve flattens out above $alpha \sim 40°$.

Compared to a small zenith angle, in large zenith angle sources the gamma ray shower image is smaller and denser, i.e. wider at the semi-minor (elliptical) axis and shorter at the semi-major axis in comparison to large zenith angle shower images. The *alpha* cut uses the angle between the line joining the camera centre and the centroid of the ellipse, and the elliptical semi-major axis (Section 2.1.2). With smaller and denser gamma ray images at large zenith angles, the *alpha* distribution angle has greater uncertainty (in comparison to smaller zenith angles), hence the steeper slope of the *alpha* histogram plot for small zenith angles. Furthermore, the Figure 7.4 histogram appears to decrease somewhat in frequency for $alpha < 10°$. This is due to attenuation of some of the (elliptical) gamma ray images of Mkn 421, being cut off by the edge of the FoV due to the greater shower distance from the telescope (compared to EXO

055625-3838.6). This does not occur for small zenith angle *alpha* plots, as shown in Figure 7.13 (Section 7.2.3, later). As evidence of primary gamma rays, we expect a cut off from the non-horizontal to the horizontal slope of the *alpha* histogram plot for Mkn 421 to occur for $alpha > 40^\circ$ for our results in Section 7.1.4.

Different energy thresholds would be apparent at zenith angles varying as much as 60° in the MC shower simulation (comparing the zenith angle of Mkn 421 ($\sim 70^\circ$) with EXO 055625-3838.6 ($\sim 10^\circ$, Section 7.2.3)). Although not measured, we expect that (although the shower energies are higher for the greater zenith angle), more showers are acquired by the greater volume of atmosphere available to the telescope at the larger zenith angle required for Mkn 421, [133].

In addition to the on-source simulation of purely primary gamma rays (Figures 7.2, 7.3 and 7.4 this section), primary protons were also simulated at the same zenith angle ($\sim 70^\circ$), with the (proton) cosmic ray spectral index of 2.7, for the off-source analysis of Mkn 421. The simulation gives histograms for *distance, length, width* and *alpha* for the primary proton are shown in Appendix I (Figures I.1, I.2 and I.3) for the primary proton EAS simulations.

7.1.4 Mkn 421 observational data analysis results

As explained in Section 7.1.2 and indicated in Tables H.1 and H.2 in Appendix H, Mkn 421 was observed by the CANGAROO-II (T1) telescope in January, February and March 2001, February 2002 and January 2003. This source was observed for a total of 2313.9 minutes (38 hours and 33.9 minutes) on-source and 2060.5 minutes (34 hours and 20.5 minutes) off-source, including a flaring period for this source in 2001 (Section 8.2.2). The Mkn 421 data were acquired with no moon above the horizon and in generally fine (including thin cirrus cloud) weather conditions. No dewing of the mirrors were reported nor was expected to occur as the observation of Mkn 421 occurred during summer months when nights were generally warmer and the dew point was low (see Section 5.2.2 for a discussion on mirror dewing).

However, telescope observations carried out by CANGAROO during 2001 (before

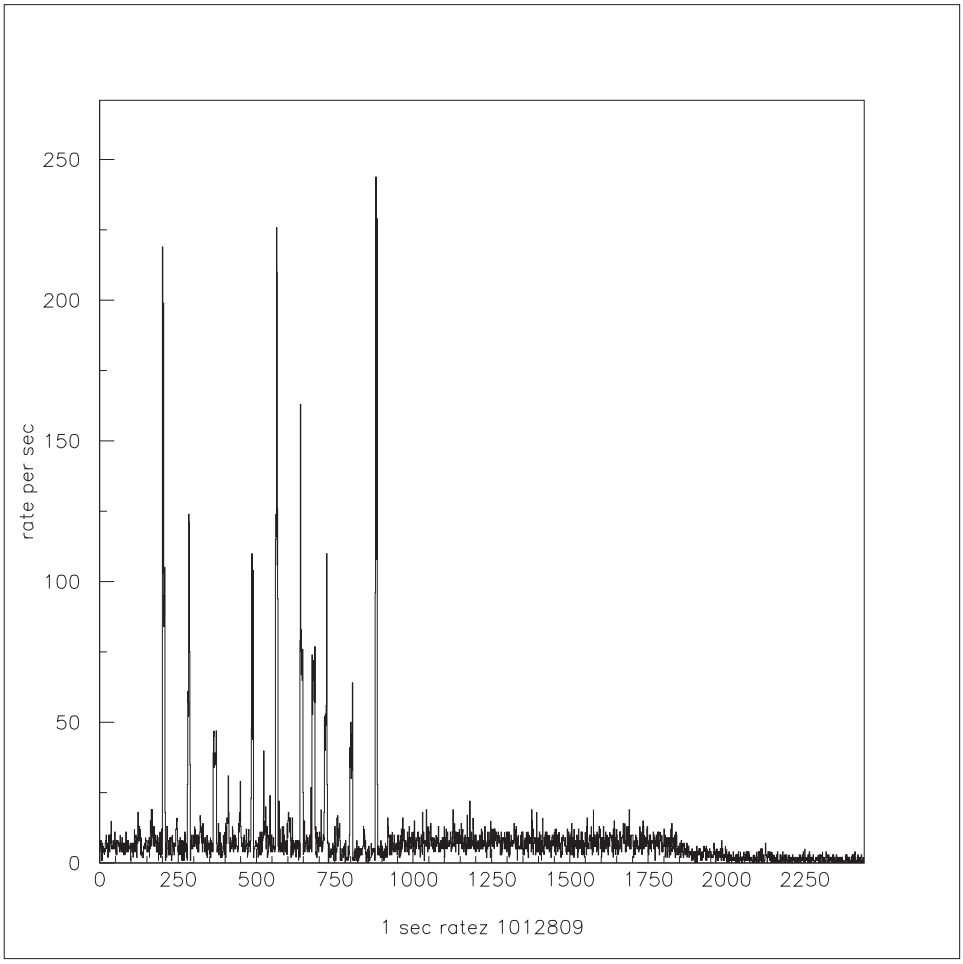

Figure 7.5: Plot of elapsed data acquisition seconds from the start, versus trigger rate for the **calib10a** data file; 01012809 (Mkn 421, see Table H.1, Appendix H). Trigger rate is the number event triggers per second (rate per sec.).

March 2002), were subject to bright unshaded white ground lights imposed from security lights mounted on stadium poles, at the Woomera detention centre (approximately eight kilometers away over uninterrupted terrain). These white lights emitted significant levels at blue wavelengths (probably emitted using high pressure Mercury vapour lamps) and caused a significant increase in background noise light level to the T1 telescope when switched on, which was usually every night. During March 2002, the security lights at the Woomera detention centre were replaced by lower, shaded, less bright lights using high pressure Sodium vapour lamps (emitting principally in less

sensitive yellow wavelengths), and from then on, the Woomera detention centre presented a less intrusive background light noise level to the telescopes. Except for the 2002 and 2003 data acquired for Mkn 421, the Mkn 421 data acquired for this thesis, suffered from high background ground light noise from the Woomera detention centre. The EXO 055625 data were collected after March 2002, for this thesis, and are not affected by high noise levels from ground lights from the detention centre.

There were difficulties experienced with data acquisition hardware during observation of Mkn 421 in 2001 as indicated in Table H.1 (Appendix H), although the fault was not specified by observers. There were difficulties experienced with the ADC electronics modules (see Section 3.2.6) during data acquisition where LED power and trigger indicators for these modules appeared to the author (as an observer) to flicker on and off for a second or two (unrelated to telescope trigger), during fine sky conditions. The author suspects that there may have been an earthing problem or under-volt problem for the ADC module cards in T1. For this reason (and for gaps in the ADC data where ADC channels were not recorded for all triggered events), the ADC channel data from EAS was sparsely used for the T1 camera pixel analysis of EAS from Mkn 421 and EXO 055625, on-source and off-source data. The source analysis algorithm used (particularly on pixel image shape), was based principally upon TDC camera pixel data for T1 (see Section 3.2.6).

Before source analysis procedures were applied to the data, the raw data format was converted to calibrated (**calib10** or **calib10a**) data format for T1 using the same conversion algorithm used in the flasher calibration, discussed extensively in Sections 5.1.5, 5.1.6 and 5.1.7.

The first analysis procedure was "cleaning", in which the events for a data acquisition file could be rejected, according to a series of conditions applied to the data. The cleaning was deployed initially in two separate programs, then further cleaning conditions were applied in tandem with the overall analysis program, before the shape of the Čerenkov images of the T1 camera pixels were discriminated, in the same running process as the cleaning.

The first cleaning process cut data from either an excess of on-source, that was not

matched to off-source zenith angles for the observation on the evening or vice-versa, e.g. if an on-source data file had observation data obtained from an on-source zenith angle that was not replicated by off-source zenith angles observations in the off-source data file (or vice-versa), then the zenith angles in the on-source file (or vice-versa) event triggers would be cut from analysis. An example in shown in Figure 7.1, (Section 7.1.2, above) where we see the on-source zenith angle data from the 26$^{\text{th}}$ January 2001. The off-source data file from that date (run number 01012609) reaches a zenith angle maximum of 71.2°. Despite the trigger rate being much higher for the on-source file; 01012619 compared to the off-source file; 01012609 (evidenced by the total events of these subsequent data files in Table H.1 (Appendix H), that may have been produced by thin cloud in the off-source observation), events that exceeded the on-source maximum of 70.9° (Figure 7.1) were discarded from the off-source data in the file; 01012609. This process tended to cut the highest zenith angle of the on-source run, which would have the least likelihood of containing shower events in that run data. The correction to the on-source and off-source zenith angle exposure after this process brought the on-source and off-source exposure times to ∼50:50.

The second cleaning process applied in a separate program, was the *noise spike & cloud rate* cut. This cut was based on average trigger rate of a data file run and events were rejected if there was an anomalous sudden data acquisition spike over a one second interval (over a preset threshold trigger rate) as the *noise spike* cut and if the trigger rate fell below a preset threshold rate (*cloud rate* cut). An example of telescope data acquisition trigger rate is given in Figure 7.5. The *noise spike & cloud rate* was assessed by the average trigger rate of the individual data files.

Firstly, the raw event trigger rate per second was assessed from the data file without any time interval skipped, and the mean of the (one second interval) trigger rate over the data run is calculated. The *noise spike* (or high rate) procedure was processed (before the *cloud rate* cut) by determining if the one-second trigger rate exceeded the threshold trigger rate value (determined by the mean plus five standard deviations) from the overall one-second mean raw event trigger rate, calculated previously. Figure 7.5 gives an example of this. Looking at this figure, we can see in excess of thirteen

one-second rate noise spikes (> 25 Hz) in the first third of this data file. The *noise spike* procedure rejects these event triggers. Note that the mean for Figure 7.5 (without these noise spikes) appears to be 5-15 Hz, which is expected for fine night sky conditions for T1. The origins of these trigger event rate noise spikes are discussed in Section 8.2.1. They were seen in many of the T1 on-source and off-source observation data files examined for Mkn 421. However, they were all cleaned.

Next, the *cloud rate* cut was performed on the observation data files cleaned of noise spikes. The mean one-second event trigger rates were re-calculated to one-minute intervals by taking the sum of one-second trigger rates over sixty second intervals, i.e. the mean one-minute interval event trigger rate was calculated. Obviously, for slow moving objects such as clouds drifting though the FoV, minute trigger rate intervals (rather than second trigger rate intervals) are much more convenient for calculating the degree of cloudiness. The cloud thickness cut was implemented if the trigger rate dropped below a third of the mean event trigger rate over one-minute intervals, and the events determined from this criteria were rejected. Difficulties with the *cloud rate* test arose if the sky was consistently cloudy (without any clear sky patches through cloud) drifting though the FoV during the data acquisition run. This could have been the case when the sky was covered by thin hazy cirrostratus cloud.

The Mkn 421 overall analysis program was deployed to the on-source and off-source observation data attenuated by the exposure time of some observation runs (on-source and off-source exposure time normalization) and then the *noise spike* and *cloud rate* attenuated the number of events of most observation runs. The resulting "cleaned" first stage observation data files were then put through further noise cleaning processes in the main program called *precuts* before the same program (but a different procedure) discriminated gamma ray from cosmic ray Čerenkov images. The *precut* procedures, were primarily event "cleaning" procedures that were applied to the raw data (primarily on the TDC channel data) prior to discrimination of Čerenkov images of the T1 camera pixels, for each telescope trigger. Similarly, as with the flasher data, the *precuts* included bad channel corrections (see Section 5.1.7). However, the main *precuts* applied in tandem with the overall analysis program were pixel clustering cuts called

the *T4a cut* (applied to each event trigger), and bright starlight cuts called *scalar cuts* made to the overall scalar data.

The EAS shower image data was typically digitally analyzed in TDC counts. The function of the TDC module in digital conversion of the analogue voltage signal from the PMT to *TDC start* (photon arrival time characteristics) and *TDC width* (TDC pulse width) is explained in Section 3.2.6, which also discussed the function of the TKO scalar module: *Scalar* measures the summed signal amplitude (background counts over a preset threshold), from 16 common PMT pixels from a box, updated every ten seconds to data acquisition.

Bright stars in the FoV, can present problems with individual PMT camera pixels receiving high light intensity from a point of light of a bright star that rotates through the FoV as the telescope is tracking. In the T2 telescope, the camera PMT pixels can be individually switched off, where the position of the bright star location in the camera can be determined *a priori*, as the bright star rotates over the camera pixels. This feature of being able to individually switch off PMT pixels in response to a bright star, was not available to the T1 telescope (as the PMT HV was supplied to clusters of 16 PMTs in a box). Consequently a bright star impinging on a PMT was determined by the *scalar cut* of the scalar data where the (software) threshold was set at more than the mean scalar value of that pixel plus five times the root mean square (RMS) value. The scalar mean (for every 576 pixels) was determined before the *precut* run and this value (and the RMS value for each pixel) was read into the *precut* procedure as a data file.

The final noise cleaning algorithm was the pixel cluster cut (or *T4a cut*). This procedure is designed to eliminate, within bounds, the random pixel event trigger generated by the telescope triggering on non-Čerenkov events, where there is no "cluster" of pixels generated by Čerenkov photons initiated by an EAS of cosmic ray or gamma ray origin. An example of both a Čerenkov induced event trigger and an event trigger generated by "noise" is in Figure 7.6. The left frame of Figure 7.6, shows what the event trigger "image" generated by noise may look like, whereas the right frame of Figure 7.6 is an image generated arguably by Čerenkov photons from an EAS, shown

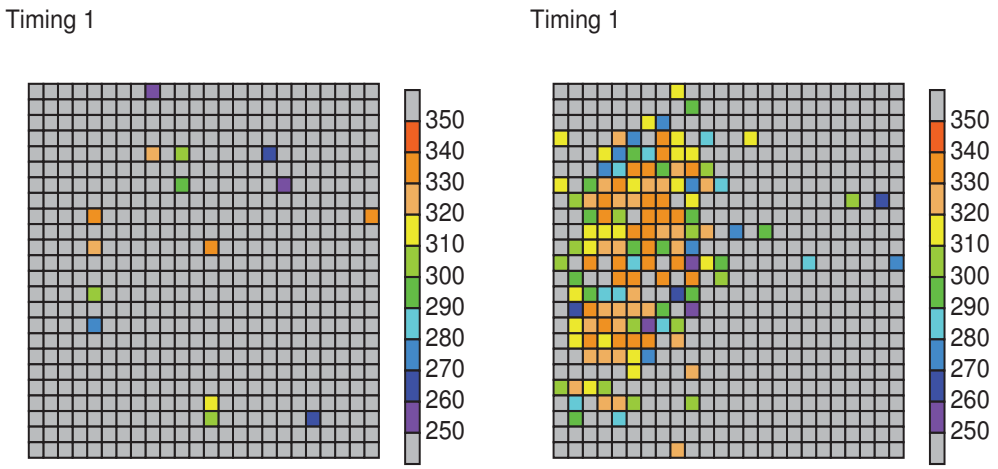

Figure 7.6: Camera image pixels as they appear for each event trigger in the the T1 telescope. The pixels are TDC data, where the light grey pixels are un-triggered low value pixels, while coloured pixels are detected EAS Čerenkov photons or random background noise photons. The relative scale of TDC pixel amplitudes is shown on the right of each camera image box. The *left* figure shows what NSB noise may typically appear like, i.e. a few randomly scattered pixels. The *right* figure is an example of an EAS shower caused by a cosmic ray EAS in this case. In EAS events, the camera pixels are usually clustered around the shower core image.

as "timing" or *TDC start* (see previous page and Section 3.2.6). The bar next to the right of each frame in Figure 7.6 is the amplitude range of the pixel, e.g. dark green coloured pixels range between a value of 290 to 300 "*TDC start* counts". Grey coloured pixels are values falling below the *TDC start* count value of 250 and also values above 350. The grey pixels fall outside the range of *TDC start* counts that may have been contributed from Čerenkov light.

The left frame of Figure 7.6 shows coloured pixels in a random (non-clustered) distribution across the camera whilst the right frame of Figure 7.6 shows coloured pixel clustering due to an EAS Čerenkov event. The *T4a* clustering cut works by determining if there are any three "coloured" pixels adjacent to any one coloured pixel across the camera in a triggered event (the "coloured" pixels are set by a preset range of *TDC start* values as previously discussed). This tends to eliminate "noise" generated event triggers, such can be seen in the left frame of Figure 7.6, where a few coloured

pixels are typically randomly distributed across the camera. Thus, the *T4a cut* tends to pass events that have Čerenkov shower images (either cosmic ray showers or gamma ray showers).

The required number of adjacent pixels in the cluster cut can be specified in the clustering algorithm. Where the clustering cut is more loosely determined by the number of adjacent pixels being two; this is known as the *T3a* cluster cut. The *T3a cut* will pass more event triggers in any given on-source or off-source data file, but will tend to pass more "noisy" non- Čerenkov event triggers. Only one coloured pixel in the camera need have two adjacent pixels to pass the *T3a cut*. Furthermore, a number of EAS Čerenkov events, sometimes generated away from the telescope's FoV by cosmic rays muons known as "muon rings", may pass the *T3a cut*. Muon rings are relatively rare triggered events, but may be accepted as gamma ray events, especially for Mkn 421 gamma ray showers ellipsoids, and muon ring arcs may resemble them. The *T4a cut* is sensitive enough to eliminate most muon ring triggered events.

The *T5a* pixel cluster cut is a harder cut than the *T4a cut* and only for a cluster of four adjacent coloured pixels to any one coloured pixel to pass this cut. This further reduces the number of event triggers passed when deployed, including eliminating a large swathe of "noise" trigger events such as seen in the left frame of Figure 7.6. However, the *T5a cut* may be too constrictive for the small gamma ray ellipsoid to pass, and so the majority of gamma ray triggered EAS events from Mkn 421 may be missed. Furthermore, the *T5a cut* rejects pixels on the edge of EAS Čerenkov images. While for large Čerenkov images (such as large cosmic ray EAS) this is not too problematic, for smaller Čerenkov images such as gamma ray showers, the overall shape of the gamma ray ellipsoid may be altered by the *T5a cut*.

Not all T1 telescope data acquired from Mkn 421 has been utilized for our analysis. The data from the 28$^{\text{th}}$ January 2001 was cut from the analysis, i.e. on-source (01012809) and off-source (01012803), see Table H.1, Appendix H. The data from this night's observation was rejected because the data were unrecoverable where a data acquisition fault was not reported by observers.

Once the Mkn 421 data analysis procedure has passed all noise "cleaning" algo-

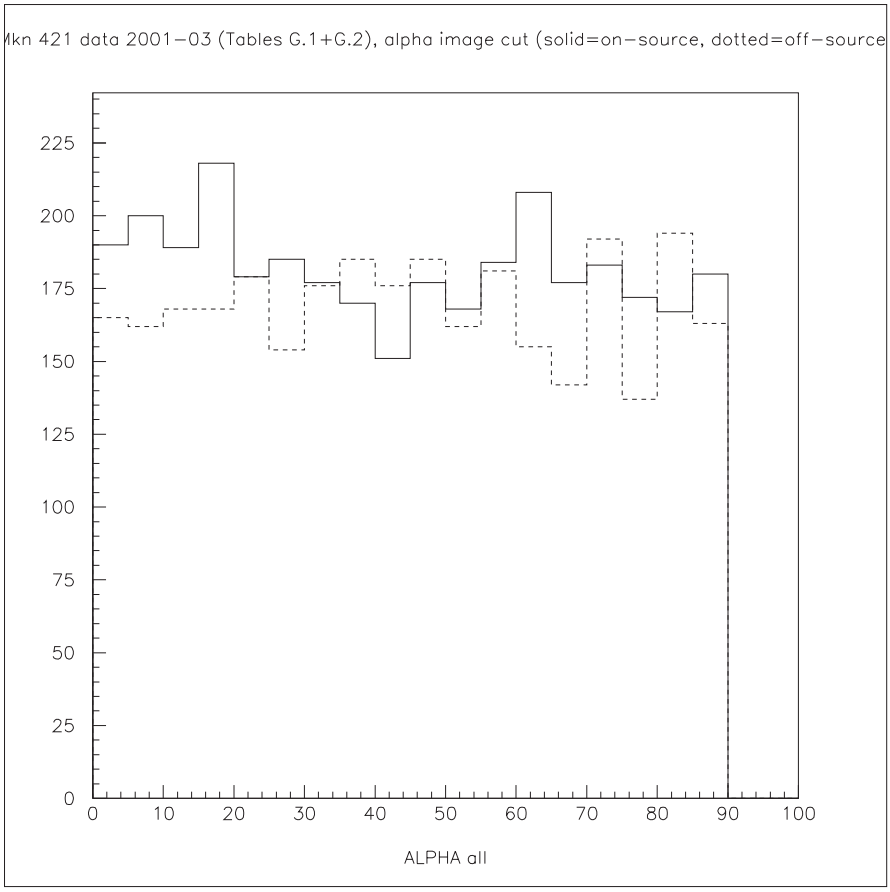

Figure 7.7: The *alpha* image plot for all Markarian 421 T1 observation data from 2001 to 2003 (data files; see Tables H.1 and H.2, Appendix H). The solid line is the *alpha* plot from on-source data and the overlaid dotted line is the *alpha* plot from off-source data. These on- and off-source *alpha* plots in the above figure, can be viewed separately in Figure J.1 (on-source) and Figure J.2 (off-source) in Appendix J.

rithms (on- and off-source exposure times normalization, *noise spike cut, cloud rate cut, bright starlight scalar cut* and *T4a* pixel cluster cut), the Čerenkov shower images observed in T1's camera from Mkn 421, were discriminated between gamma ray and cosmic ray type events. The Čerenkov shower image discrimination was based on the Hillas parameters of the moment of the ellipsoid based on the non-isotropic arrival direction of gamma ray showers (Section 2.1.2). The primary Hillas parameters used in this thesis were *length, width* and *distance*. These parameters were then used to develop the secondary Hillas parameter *alpha*, after passing these three primary cuts.

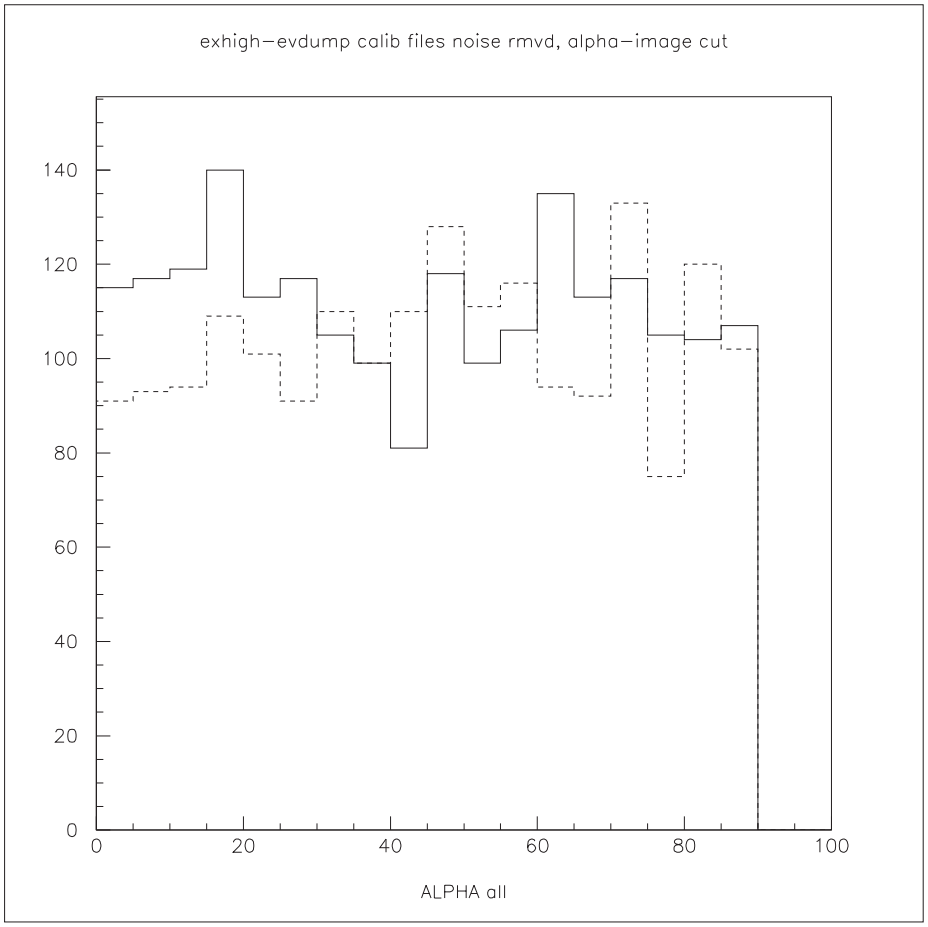

Figure 7.8: The *alpha* image plot for Markarian 421 T1 observation data from 2001 only (data files; see Table H.1, Appendix H). The solid line is the *alpha* plot from on-source data and the overlaid dotted line is the *alpha* plot from off-source data. These on- and off-source *alpha* plots in the above figure, can be viewed separately in Figure J.3 (on-source) and Figure J.4 (off-source) in Appendix J.

The cut domains for *length, width* and *distance* were determined from simulations (described in Section 7.1.3), for the zenith angle and the (extrapolated) spectral index for Mkn 421 at Woomera. The results of this work, for the observation of Mkn 421 in the observations described at the beginning of this section (2001 to 2003) and in applying the on-source and off-source data files to the analysis described in Section 7.1.2, are shown in terms of the secondary Hillas parameter *alpha* in Figure 7.7, showing both on-source and off-source *alpha* plots overlaid. For clarity, the on-source only *alpha* plot result for Mkn 421 displayed (overlaid, solid line) in Figure 7.7, is shown in Figure J.1,

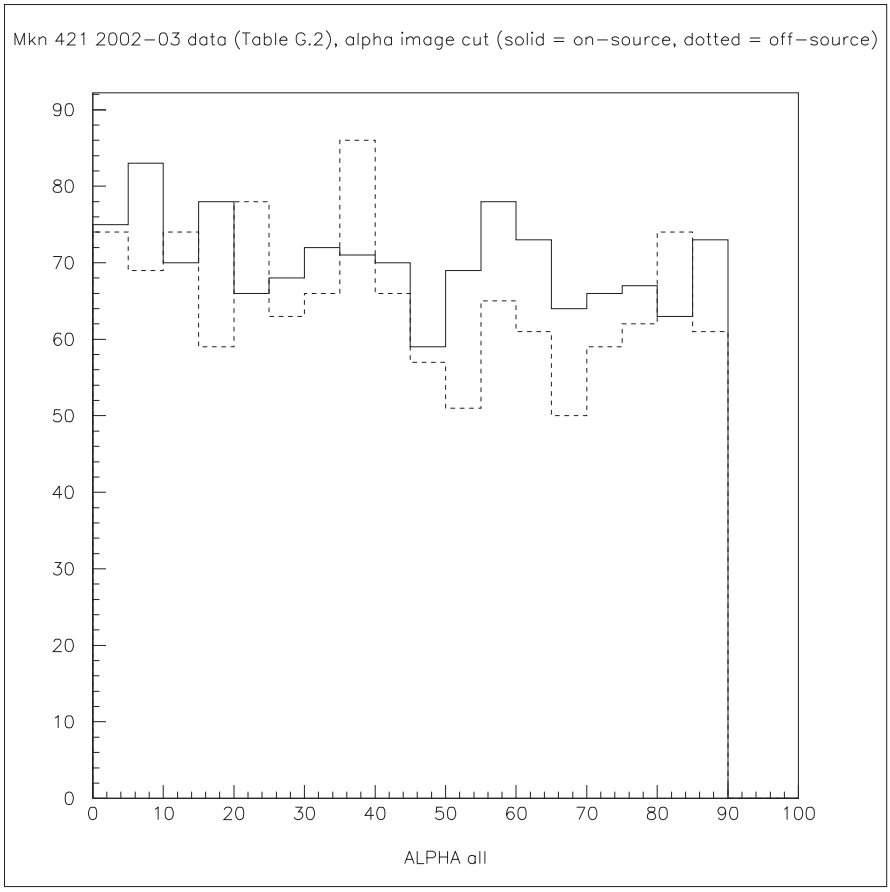

Figure 7.9: The *alpha* image plot for Markarian 421 T1 observation data from 2002 to 2003 only (data files; see Table H.2, Appendix H). The solid line is the *alpha* plot from on-source data and the overlaid dotted line is the *alpha* plot from off-source data. These on- and off-source *alpha* plots in the above figure, can be viewed separately in Figure J.5 (on-source) and Figure J.6 (off-source) in Appendix J.

Appendix J. The off-source only *alpha* plot for Mkn 421 (displayed overlaid by the dotted line in Figure 7.7 is also shown in Figure J.2 (Appendix J).

Note that ADC data was not used in the Hillas parameter cut analysis by the author (although ADC data was sometimes used for preliminary "cleaning" or *precuts* (i.e. *noise spike cut* and *cloud rate cut*). Problems were observed by the author with the T1 telescope's ADC modules during shower data acquisition. This has already been commented on, earlier in this section.

A comparison between the Mkn 421 observational data analysis *alpha* plot from T1

collected over the entire period for this thesis (2001 to 2003; Figure 7.7), was further divided between the Mkn 421 observational data *alpha* plot collected in 2001 (Figure 7.8) and the Mkn 421 data in an *alpha* plot collected in 2002 to 2003 (Figure 7.9). The purpose of this division of *alpha* plots in separate periods (Figure 7.8 and Figure 7.9), is to test the overall on-source to off-source *alpha* signal significance of different observational periods, since it was known that Mkn 421 was flaring at high flux in January to March 2001.

As with Figure 7.7 the on-source only *alpha* plot result for Mkn 421 displayed (overlaid, solid line) in both Figure 7.8 (2001), and Figure 7.9 (2002-2003), are shown consecutively in Figures J.3 (2001) and J.5 (2002-2003) in Appendix J. The off-source only *alpha* plot for Mkn 421 (displayed overlaid by the dotted line in Figure 7.8 for 2001, similarly for Figure 7.9 for 2002-2003) are also shown consecutively in Figures J.4 (2001) and J.6 (2002-2003) in Appendix J.

The overall on-source (including TeV gamma rays) signal significance for Mkn 421 (over the off-source) can be calculated from a procedure following from Li & Ma (1983) [111], using the following formula from a quasi-normal distribution, developed specifically for gamma ray astronomy:

$$S = \frac{N_s}{\hat{\sigma}(N_s)} = \frac{N_{\rm on} - \alpha N_{\rm off}}{\sqrt{\alpha(N_{\rm on} + N_{\rm off})}} \tag{7.2}$$

where the source significance- S, "S standard deviation result" of the observed number of gamma ray photons signal, N_s is estimated by the number of on-source counts, $N_{\rm on}$ and off-source counts, $N_{\rm off}$. The quantity of the ratio of on-source time over off-source time is, α where; ($\alpha = t_{\rm on}/t_{\rm off}$), and $\hat{\sigma}(N_s)$ is the standard deviation of of N_s, shown in the denominator of equation 7.2. Furthermore, because we determined the on-source and off-source exposure times to be the same before analysis (see Section 7.1.4), we can set $\alpha \approx 1$. Equation 7.2 therefore becomes:

$$S = \frac{N_{\rm on} - N_{\rm off}}{\sqrt{N_{\rm on} + N_{\rm off}}} \tag{7.3}$$

The "Li & Ma (1983) statistics" [111], described in the previous paragraph works fundamentally on the principles:

1. The on-source and off-source exposures may be of different exposure duration, hence α in equation 7.2.

2. That a detectable source of GeV-TeV gamma rays (i.e. on-source), will slightly increase signal (primary gamma ray photon) counts over the ambient cosmic ray flux level count.

3. The cosmic ray flux level is constant over the sky. This is marginally erroneous because of the slight sidereal cosmic ray flux anisotropy over the entire celestial globe, as will be discussed (below).

GeV-TeV cosmic rays (being of galactic origin), arrive at the solar system with their arrival directions made nearly completely isotropic by the galactic magnetic field. However, "the variation in the intensity of primary cosmic rays as a function of the equatorial coordinates α (right ascension) and δ (declination) is known as the *sidereal anisotropy*. Thus a detector located on the Earth observes a modulation of the cosmic ray flux with a period of one sidereal day due to Earth's rotation. The magnetic field within the heliosphere, whose structure is strongly influenced by the solar wind and the Sun's activity, plays a role in the propagation of galactic cosmic rays with energies in the order of 10 TeV and below. At these energies, the general large-scale structure of the helio-magnetic field may induce structures in the sidereal (cosmic ray) anisotropy", [160]. For this reason, the sidereal cosmic ray anisotropy may have an affect on the Li & Ma (1983) [111] statistics, because the cosmic ray flux is not constant across the celestial sphere. The East-West effect and the 6% change in flux intensity of cosmic rays between the Earth's pole and the equator, discussed in Section 1.1, are from much lower cosmic ray energies than TeV cosmic rays and do not play a part in the consideration in TeV cosmic ray flux anisotropy.

A thorough measurement of the cosmic ray sidereal anisotropy has been made by the Tibet Shower Array experiment by Amenomori *et al.* (2006) [14]. This research has concluded that the (relative) variation of the cosmic ray flux from approximately 4 to 50 TeV (see [160]), for the Tibet Shower Array experiment in 2006, is of the order $\pm 0.1\%$, [14].

While the above sidereal cosmic ray anisotropy flux variation is small (±0.1%), it is not insignificant, especially since cosmic ray showers consists of more than 99.9% of counts on-source for the Li & Ma (1983) [111] statistics (for a one-Crab gamma ray flux for example, see Section 8.2.1). Furthermore, the sidereal cosmic ray anisotropy as a factor is additionally influenced by the long-on, long-off exposure technique made by the CANGAROO collaboration for Mkn 421 (and EXO 055625). For example, a long-on exposure time of 4 hours must be matched by a similar long-off exposure made at ±4 hours in right ascension from the target coordinates. This computes to about 60° across the celestial equator, a significant change. However, compared to the Poissonian statistical variation of cosmic ray shower rate, the anisotropy variation in the sidereal cosmic ray rate is small, even for widely set on-off target positions in the sky by long-on, long-off exposure. Additionally, according to Amenomori *et al.* (2006) [14], the greatest sidereal cosmic ray flux variation occurs near the Cygnus region which is a high declination angle northern sky object, unobservable by CANGAROO.

Mkn 421 obs. year	*alpha* **distribution fig.**	**Significance,** S	S**, % relative uncert.**
2001-2003	Figure 7.7	2.821	0.121%
2001	Figure 7.8	3.31	1.519%
2002-2003	Figure 7.9	0.412	0.781%
2001-2003	Figure 7.7	3.507	0.029%
2001	Figure 7.8	3.51	0.057%
2002-2003	Figure 7.9	1.244	0.241%

Table 7.1: The gamma ray signal significance (S), of Mkn 421 *alpha* distributions, shown in this chapter as Figures 7.7, 7.8 and 7.9 in the table above. The significance of on-source gamma-ray shower signal over off-source cosmic ray showers is calculated using equation 7.3, from the *alpha* distribution for $alpha < 40°$ and $alpha < 20°$. The relative uncertainties in the above table only reflect the statistical standard deviation (from equation 7.3) in counting the height of each histogram bin (width=5°) from the *alpha* plots, and are not indicative of telescope data uncertainties, either systematic or random. The first three rows represent the signal significance for $alpha < 40°$. The next three rows (dates shown in italics) represent the signal significance for $alpha < 20°$.

Thus, accepting that the cosmic ray flux rate is constant across the celestial sphere and that the on-source and off-source exposure times are about equal, using equation 7.3, the significance for the Mkn 421 observation using T1 in 2001 to 2003 is shown in Table 7.1.

Markarian 421 (2001-2003)		
***alpha* bin angle**	**Incremental Significance (equation 7.3)**	**Uncertainty**
5°	1.33	0.05
10°	2.35	0.04
15°	2.56	0.03
20°	3.51	0.03
25°	3.14	0.02
30°	3.55	0.02
35°	3.31	0.02
40°	2.82	0.02
Markarian 421 (2001)		
5°	1.67	0.07
10°	2.35	0.05
15°	2.91	0.04
20°	3.51	0.03
25°	3.51	0.03
30°	3.94	0.03
35°	3.52	0.03
40°	3.31	0.02
Markarian 421 (2002-2003)		
5°	0.08	0.08
10°	0.86	0.06
15°	0.52	0.05
20°	1.24	0.04
25°	0.67	0.04
30°	0.79	0.03
35°	0.92	0.03
40°	0.41	0.03

Table 7.2: The gamma ray signal incremental significance (S, equation 7.3) of Mkn 421 per 5° *alpha* distribution histogram bin widths, shown in this chapter as Figures 7.7, 7.8 and 7.9. These above results are plotted in Figures K.1, K.2 and K.3 (Appendix K) respectively. The purpose of these results is to find the optimum degree cutoff from the histogram *alpha* plots to maximize signal over noise.

From Table 7.1, the gamma ray signal significance from equation 7.3, is calculated from the on- and off-source figures (indicated in this table), showing the results of the

Hillas parameter *alpha* distribution (from Figure 7.7 in 2001-2003, Figure 7.8 in 2001, and Figure 7.9 in 2002-2003). From the significance data in Table 7.1 (for $alpha < 40^\circ$), we see that a TeV gamma ray signal from Mkn 421 was weakly detected by T1 telescope in 2001 and not seen in 2002 or 2003 by the same instrument. The 2.8 σ significance result of 2001-2003 in Table 7.1, is from a concatenation of the data in 2001 ($S = 3.3\sigma$) and 2002-2003 ($S = 0.4\,\sigma$). The purpose of dividing the overall results for Mkn 421 studied in this thesis is to test the flaring episode of Mkn 421 in 2001, to episodes where Mkn 421 was possibly more quiescent (such as 2002 and 2003), see Section 8.2.2.

Additionally, we have included significance results for $alpha < 20^\circ$ for Mkn 421 (shown in Table 7.1). These results have been included because it was thought that determining the signal strength of Mkn 421 for this *alpha* angle would be more likely to maximize the signal over noise ratio for this source, rather than just maximize the signal (for $alpha < 40^\circ$ used previously). These $alpha < 20^\circ$ results show a 3.5 σ result (concatenation of data from 2001, 2002 and 2003 Mkn 421 observations). Again Mkn 421 data from 2001 on its own showed a 3.5 σ (for $alpha < 20^\circ$), evidence that a weak signal from this source was detected by T1 in 2001. From the separate Mkn 421 2002-2003 data we found a signal significance of 1.2 σ (similar to the $alpha < 40^\circ$ data) confirming that Mkn 421 was not detected by T1 in this period of observation, supporting the evidence that Mkn 421 was most likely quiescent (i.e. not flaring) in this epoch.

The decision for selecting $alpha < 20^\circ$ cut as a good basis for maximizing signal over noise, was tested by applying an incremental (Li & Ma (1986) [111]) significance calculation (equation 7.3) to each 5° bin width in *alpha* for each of the on- and off-source histograms for Mkn 421 in Figures 7.7, 7.8 and 7.9. The results of these incremental significance calculations for Mkn 421, appears in Table 7.2. The incremental significance (column two in Table 7.2) was then plotted against the *alpha* degree angle (column one, Table 7.2) to verify if using the selection ($alpha < 20^\circ$) was the best choice for maximizing signal over noise. The third column in Table 7.2 shows the uncertainty of the incremental significance and is based on $S_{\rm unc} = 1/\sqrt{\Sigma(N_{\rm on} + N_{\rm off})}$. The incremental significance versus *alpha* is plotted in Figures K.1, K.2 and K.3 in Appendix

K. From these figures we deduce that to maximize signal over noise in *alpha*, it may have been better to use $alpha < 30°$, rather than $alpha < 20°$ (indicated in Figures K.1 (2001-03) and K.2 (2001)) where the incremental significance reached its maximum value. However, the incremental significance reaches at maximum at $alpha \sim 20°$ (in Figure K.3 (2002-03)), indicating that the selection of $alpha < 20°$, was probably the best choice to maximize signal over noise for Mkn 421.

The implications for the Mkn 421 TeV source significances detected by the T1 telescope (shown in Table 7.1 above), will be discussed in Section 8.2.1. An additional discussion in this chapter will focus on the flaring status of Mkn 421 in 2001, in Section 8.2.2.

7.2 EXO 055625-3838.6 results

7.2.1 Introduction

For a discussion on AGN and BL Lac. objects, see Section 7.1.1 (above). EXO 055625-3838.6 (abbreviated as EXO 055625), is a BL Lac. blazar source (Ciliegi *et .al.* (1993) [47], George & Turner (1996) [68], Costamante & Ghisellini (2002) [51]), where the EXO prefix refers to discoverer of this source (the European X-ray Observatory satellite) and the suffixal numbers; 055625-3838.6 refer to the celestial coordinates of this source. EXO 055625 was first discovered by the European X-ray Observatory satellite in 1989 (reported in Giommi *et al.* (1989) [70]). From the discovery of EXO 055625 (and subsequent detections by the ROSAT and ACSA satellites), George & Turner [68], has identified EXO 055625 to be a hard spectral index X-ray source (spectral index $\Gamma \sim 2.5$, [68]). The redshift (distance) of EXO 055625 is $z = 0.034$ ([51], Aharonian *et al.* (2005) [4], Benbow (2005) [29]), almost the same as Mkn 421 ($z = 0.031$, Kohnle *et al.* (2001) [98]). Thus it is expected to be attenuated in TeV gamma ray flux by electron-positron pair production from the cosmic infra-red background (Section 2.4), to a similar degree as Mkn 421.

A comprehensive theoretical modeling of the most likely TeV spectrum of EXO 055625 (mainly linked to its known X-ray spectrum at the time) was carried out by Costamante & Ghisellini (2002) [51]. Principally as a result of this work, and also because EXO 055625 was at a similar redshift to Mkn 421, this source was selected by the author (in 2003) as being a reasonable candidate BL Lac. TeV gamma ray source.

However, a more recent distance estimate has been obtained for the BL Lac. EXO 055625. Sbarufatti *et al.* (2005) [154], have reported the distance of EXO 055625 (reported in [154], as the source 1RXS J055806.6-383829) to have a redshift ($z = 0.302$), derived from optical spectroscopy measurements showing spectral features by Sbarufatti *et al.* [154]. This source was previously reported as having a featureless spectrum by Giommi *et al.* (1989) [70], the distance ($z = 0.034$) which was used in Costamante & Ghisellini (2002) [51].

Details of the Inverse-Compton synchrotron GeV-TeV gamma ray source spectrum which may include the source spectrum of EXO 055625 was discussed in Section 2.2. The gamma ray results of EXO 055625 discussed in this chapter will refer to this spectrum model. Unlike the well-studied Mkn 421 source observation period that occurred during a TeV flaring of this source, the flaring status of the EXO 055625 source for the observation period in this thesis remains unknown.

7.2.2 EXO 055625-3838.6 data acquisition files

The T1 telescope's observations of EXO 055625 examined in this thesis are from the 3^{rd} to the 12^{th} of November 2002 and, in the following observation month, from the 26^{th} December 2002 to the 4^{th} January 2003 (see Table H.3, Appendix H for a summary of these observation nights). In total, EXO 055625 was observed in the months of November and December 2002, and January 2003, for nine (November), four (December), and three (January) nights. The sixteen nights of observation of EXO 055625 occurred under varying conditions of cloudiness. Table H.3, Appendix H show the following columns of data: Observation run number, "long on" or "long off" source indicator, total number of triggered events (not exclusively gamma ray or even EAS shower events in general), exposure time in minutes (i.e. how long data

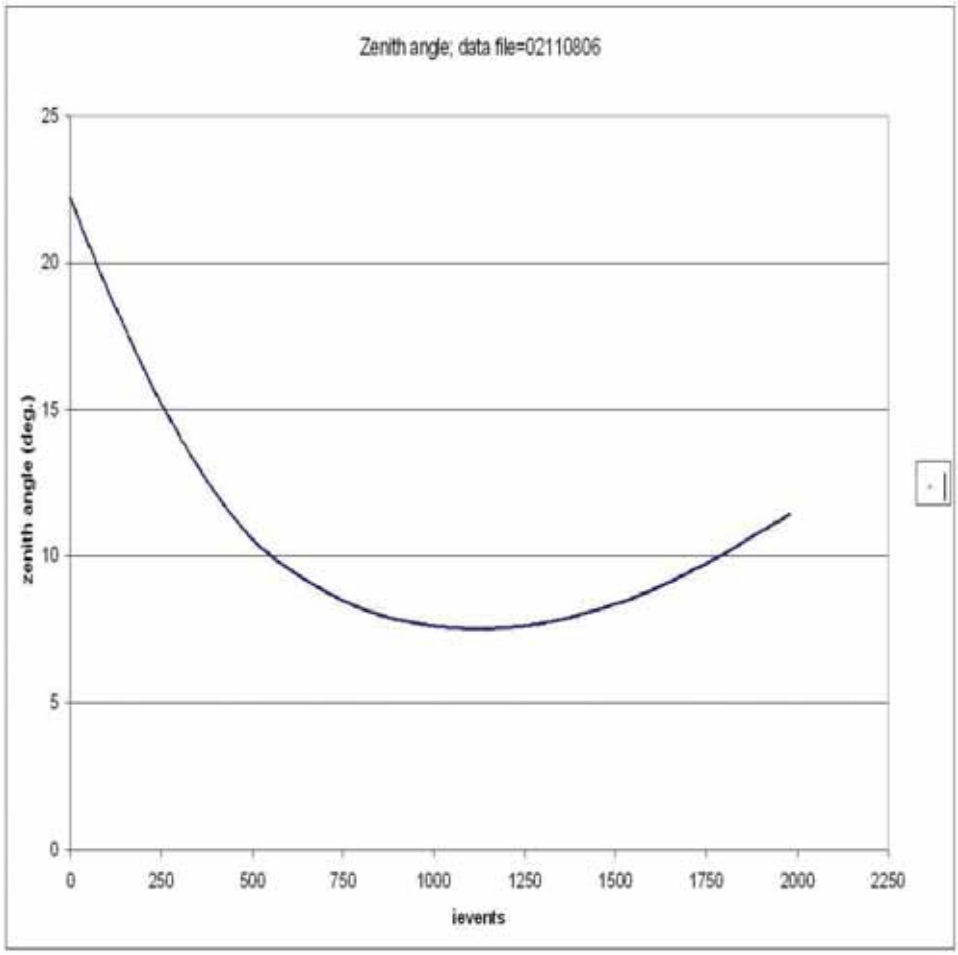

Figure 7.10: T1 dish tracking plot of the zenith angle of one EXO 055625 on-source data file (number 02110806) as an example. The zenith angle is 90° minus the dish degree elevation angle. The **ievents** number is the number of telescope triggered events, proportional to the exposure time.

were acquired for the observation run data file), weather conditions and any reported hardware or dish faults during data acquisition. See the previous Section 7.1.2, for a discussion of these data types.

The exposure time here needs some examination. The EXO 055625 source data were taken using the long-on, long-off exposure technique, similar to Mkn 421. From Table H.3 in Appendix H, a total of 962.1 minutes of on-source events and a total of 786.5 minutes of off-source events were recorded for EXO 055625. The on-source run; 02122612 was not included in the EXO 055625 source analysis because there was no

corresponding off-source run for the night's observation on the 26th December. The ratios between the raw on-source exposure time to off-source exposure time for EXO 055625 is 1.223 : 1, i.e. there was 22.3% more on-source time than off-source time. This discrepancy for 22.3% more on-source time (over off-source time) exposure for EXO 055625, could be partially or completely due to the influence of weather (i.e. increasing cloudiness and arriving thunderstorms) during data acquisition, interrupting more off-source data runs than on-source during the EXO 055625 observations using T1. This may have occurred for the Mkn 421 data of T1 as well (Tables H.1 and H.2, Appendix H). However, an examination of the data from these data acquisition files of Mkn 421 indicate that, although the weather for these observation periods in general is better than the weather conditions experienced for EXO 055625, ongoing hardware faults in T1 at the time (for Mkn 421) may have been instead responsible for a reduction of off-source exposure time compared to on-source exposure time for this source.

For the EXO 055625 telescope data taken in 2002-03, the lowest zenith angle (highest elevation) whilst tracking this source was 7.5°. The highest zenith angle (lowest elevation) whilst tracking the EXO 055625 source was 38.7°. Figure 7.10 shows an example of a zenith angle tracking curve (the EXO 055625 on-source data file; 02110806), whereby the minimum zenith angle for that night's observation could be determined.

7.2.3 EXO 055625-3838.6 Monte Carlo simulation results

A more condensed discussion of the Monte Carlo simulation results obtained for EXO 055635 will be examined here, in comparison to the Mkn 421 Monte Carlo simulation results in Section 7.1.3. See that section for a more complete discussion on shower simulations.

We simulated primary gamma ray and cosmic ray (primary proton) showers from EXO 055625 using the *GEANT 3.21* EAS simulation code in *FULL* in 2005. For good statistical results, 10^5 showers were simulated in order to obtain the Hillas parameters required (Section 2.1.2). The EXO 055625 source showers were simulated at a zenith angle of 10°.

The spectral index selected for our MC simulation data of EXO 055625 for primary

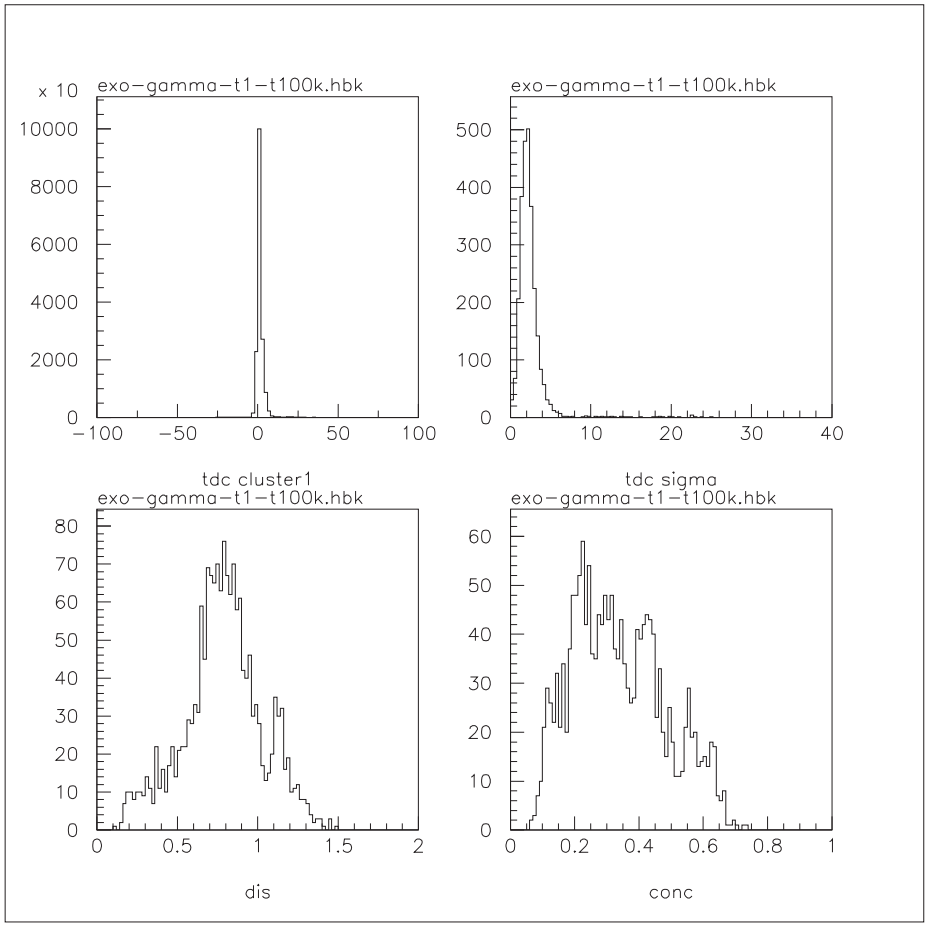

Figure 7.11: Histograms of primary gamma ray EAS Monte Carlo *GEANT 3.21* simulation results for EXO 055625-3838.6: Showing the Hillas parameter *distance* (*dis*, bottom left histogram and given in units of degrees), amongst other results. The spectral index for this source is 2.7, the zenith angle is 10° and the number of events simulated are 1×10^5.

gamma rays was 2.6. Aharonian *et al.* (2005) [4], identified that the choice of spectral indices (α) between 2.5 and 3.5, for unconfirmed AGN sources would not contribute significant systematic error in GeV-TeV gamma ray source detection. This spectral index (2.6), was selected from the TeV gamma ray spectral index of the Crab Nebula (a standard candle for TeV gamma ray astronomy), from the results of Aharonian *et al.* (2004) [7]. Since the source had not been detected prior to our observation (for GeV-TeV photon emissions), the selection of the Crab Nebula TeV spectral index was considered to be optimum for the observation of EXO 055625, until a measured GeV-

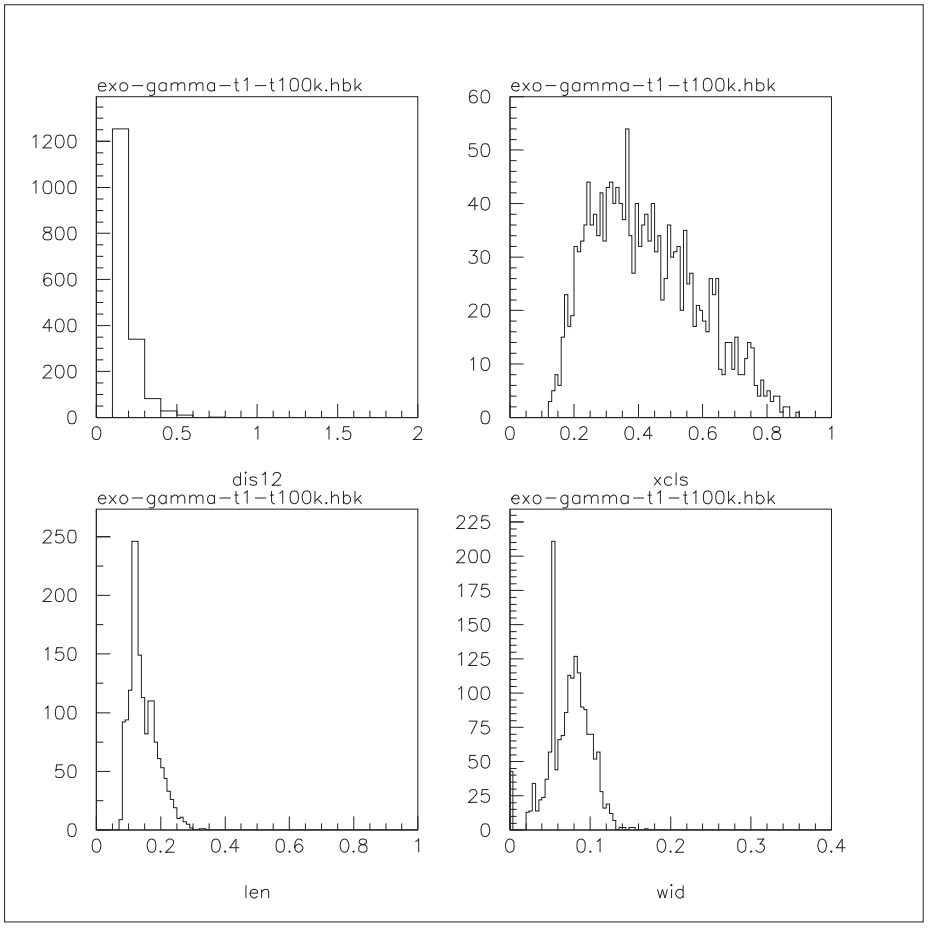

Figure 7.12: Histograms of primary gamma ray EAS Monte Carlo *GEANT 3.21* simulation results for EXO 055625-3838.6: Showing the Hillas parameter *length* (*len*) and *width* (*wid*), all given in units of degrees, amongst other results. The spectral index for this source is 2.7, the zenith angle is 10° and the number of events simulated are 1×10^5.

TeV spectrum can be obtained for this source. The cosmic ray proton MC simulation for this source (as per the MC simulation for Mkn 421 in Section 7.1.3), was simulated at the spectral index value of 2.7.

The EAS Hillas parameter "cuts" (Section 2.1.2) selected were; *length, width* and *distance* from our simulations of the moment of the elliptical gamma ray shower constructed from pixel clusters, in a similar way to the determination of these cut parameters for Mkn 421 in Section 7.1.3. The discrimination selection between the elliptical gamma ray shower clusters and the isotropically produced cosmic ray (proton) shower

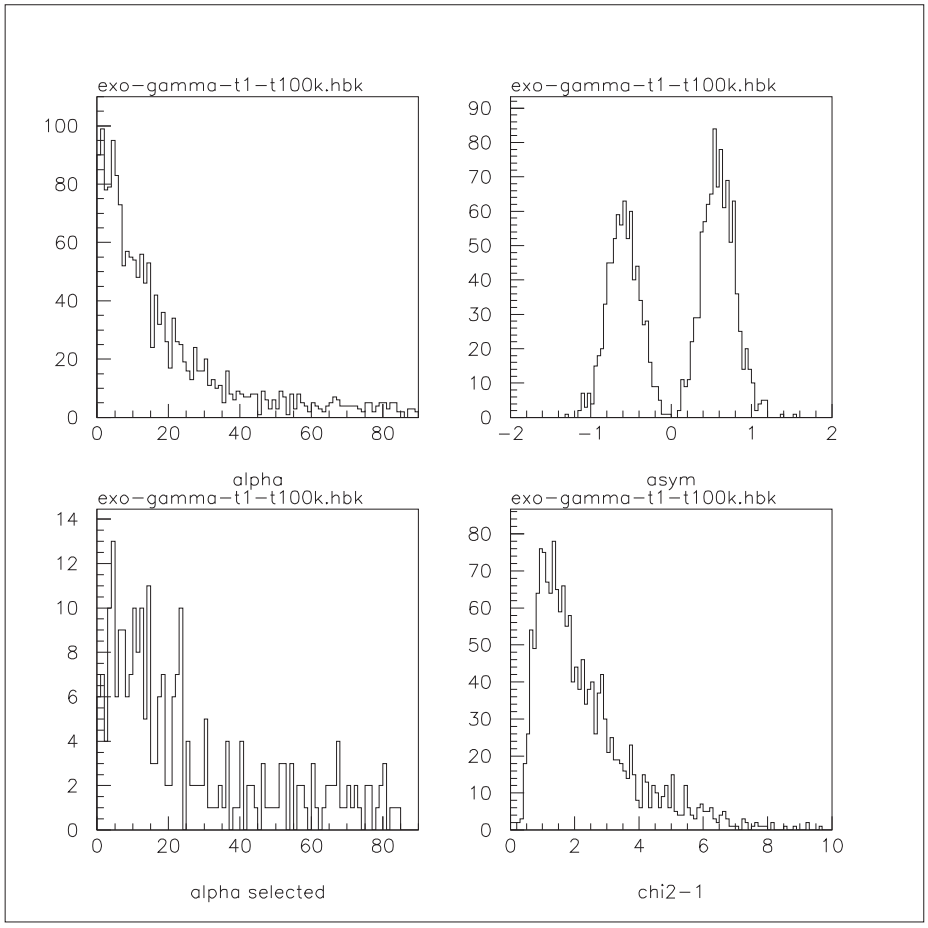

Figure 7.13: Histograms of primary gamma ray EAS Monte Carlo *GEANT 3.21* simulation results for EXO 055625-3838.6: Showing the Hillas parameter *alpha* (top left histogram, given in units of degrees), amongst other results. The spectral index for this source is 2.7, the zenith angle is 10° and the number of events simulated are 1×10^5.

clusters, was analyzed by applying (*distance, width* and *length*) after image "noise" cleaning. The dimensions of these cuts were determined from simulation results shown in histograms in Figures 7.11 and 7.12. The results of these histograms (*distance, length* & *width*) were applied, using the following cut parameters, to the analysis of EXO 055625 (next Section 7.2.4), where: $0.4 \leq distance \leq 1.2$, $0.1 \leq length \leq 0.2$ and $0.02 \leq width \leq 0.11$. The domain of these Hillas parameter cuts were determined by the range of the histogram frequencies in *distance,* (*dis*), *length* (*len*), and *width* (*wid*), in Figures 7.11 and 7.12. The telescope EAS image event triggers passing these

cut boundaries, were discriminated as primary gamma ray images.

The result for the secondary Hillas parameter cut *alpha* (see Section 2.1.2) is displayed as a histogram in Figure 7.13. This cut result has been described in Section 7.1.3, where the shape of the *alpha* cut distribution histogram for EXO 055625 is compared to the *alpha* cut distribution profile for Mkn 421 in Figure 7.4 (Section 7.1.3).

In addition to the on-source simulation of purely primary gamma rays for EXO 055625, primary protons were also simulated at the same zenith angle ($\sim 10°$), with the (proton) cosmic ray spectral index of 2.7, for the off-source analysis of EXO 055625. The simulation results histograms for *distance, length, width* and *alpha* for the primary proton are shown in Appendix I (Figures I.4, I.5 and I.6) for the primary proton EAS simulation.

7.2.4 EXO 055625-3838.6 observational data analysis results

As indicated in Table H.3 (Appendix H), and explained in the previous Section 7.2.2 of this chapter, the HBL Lac. blazar EXO 055625-3838.6 was observed by the CANGAROO-II (T1) telescope in November and December 2002, and also in January 2003. This source was observed for a total of 962.1 minutes (16 hours, 2 minutes) on-source and 786.5 minutes (13 hours, 7 minutes) off-source. The EXO 055625 data was acquired with no moon above the horizon with occasionally cloudy conditions, but usually fine. No dewing of the mirrors were reported or expected from these warm months over the observation of EXO 055625 (see Section 8.1.1).

Since the less intrusive lighting from the Woomera detention centre was installed in March 2002, before observation of EXO 055625 was carried out by T1, the imposition of the intrusive lighting from the detention centre (as had occurred for Mkn 421 observations in 2001), was of low impact on the EXO 055625 data. Additionally or perhaps coincidentally, fewer telescope data acquisition faults were reported by the T1 telescope for the period of EXO 055625 observation (Table H.3, Appendix H) than had occurred for the Mkn 421 observation period (Tables H.1 & H.2).

Identical to the analysis of Mkn 421 data, the EXO 055625 shower data were digi-

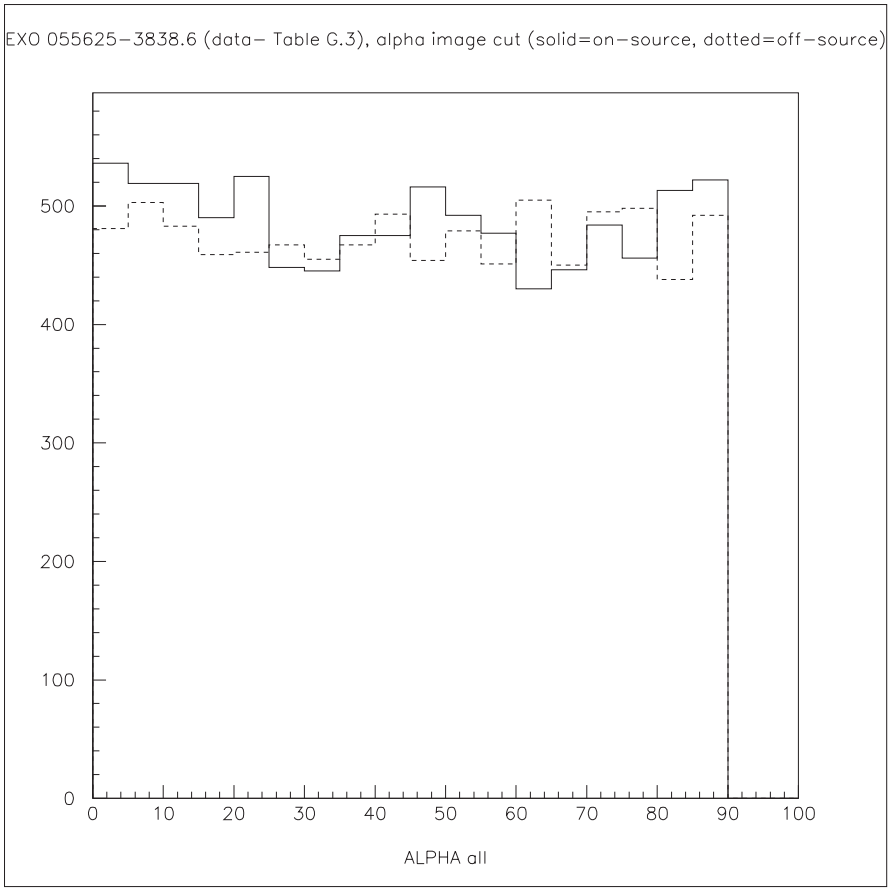

Figure 7.14: The *alpha* image plot for EXO 055625-3838.6 T1 observation data from 2002 to 2003 (data files; see Table H.3, Appendix H). The solid line is the *alpha* plot from on-source data and the overlaid dotted line is the *alpha* plot from off-source data. These on- and off-source *alpha* plots in the above figure, can be viewed separately in Figure J.7 (on-source) and Figure J.8 (off-source) in Appendix J.

tally analyzed in terms of *TDC start* and *TDC width*, Section 7.1.4. Furthermore, the "cleaning" before *precut* analysis (i.e. matching on-source to off-source exposure times, *noise spike & cloud rate* cuts), and the *precut* procedures for EXO 055625 (i.e. bright star *scalar cut* and *T4a* cluster cut) were similar. These procedures (performed on EXO 055625 observation data), were identical to that of "cleaning" and *precut* procedures performed on Mkn 421 observation data (Section 7.1.4), and outlined in detail above.

Once the EXO 055625 data analysis procedure had passed all noise "cleaning" algorithms discussed in the previous paragraph, the Čerenkov shower images observed

in T1's camera from EXO 055625, were discriminated between gamma ray and cosmic ray type events. The Čerenkov shower image discrimination was based on the Hillas parameters of the moment of the ellipsoid based on the non-isotropic arrival direction of gamma ray showers (Section 2.1.2). The primary Hillas parameters used in this thesis were *length, width* and *distance*, whose parameters for EXO 055265 were simulated using a Monte-Carlo code in Section 7.2.3. These parameters (from simulations) were then used to develop the secondary Hillas parameter *alpha*, after passing these three primary cuts. The results of this work, for the observation of EXO 055625 where the T1 observation data files are found in Table H.3 (Appendix H), applying the on-source and off-source data files to the analysis, are shown in terms of the secondary Hillas parameter *alpha* in Figure 7.14, showing both on-source and off-source *alpha* distribution plots overlaid. For clarity, the on-source only *alpha* distribution plot result for EXO 055625 displayed (overlaid, solid line) in Figure 7.14, is shown in Figure J.7, Appendix J. The off-source only *alpha* plot distribution for EXO 055625 (displayed overlaid by the dotted line in Figure 7.14) is also shown in Figure J.8, Appendix J.

The signal significance was found from Figure 7.14 (showing the results of the Hillas parameter *alpha* distribution), to be $2.247 \pm 0.006\ \sigma$ (statistical error only; not inclusive of telescope data acquisition systematic and random errors). This significance result was calculated using equation 7.3, in the previous Section 7.1.4 (since the on- and off-source exposure times for EXO 055625 were normalized to parity). Furthermore, this significance result was calculated from the *alpha* plot distribution of Figure 7.14, where *alpha* was restricted to $alpha \leq 20°$. This restriction in the *alpha* distribution significance from Figure 7.14 was made for similar reasons to the restriction of $alpha \leq 40°$ for Mkn 421, but this smaller angle ($alpha \leq 20°$) is in response to the small zenith angle of EXO 055625, where the *alpha* plot distribution peak is higher and narrower than Mkn 421 (see Figure 7.13). It is accepted that a 0.1% (maximum) variation in the sidereal cosmic ray flux, will not have an effect on the Li & Ma statistics (discussed in Section 7.1.4), particularly as the the long-on/long-off exposure technique was applied when observing EXO 055625.

Additionally, we calculated the signal significance for EXO 055625 for $alpha > 20°$,

alpha **bin angle**	**Incremental Significance (equation 7.3)**	**Uncertainty**
5°	1.76	0.03
10°	1.62	0.02
15°	1.99	0.02
20°	2.25	0.02
25°	2.93	0.01
30°	2.45	0.01
35°	2.16	0.01
40°	2.11	0.01

Table 7.3: The gamma ray signal incremental significance (S, equation 7.3) of EXO 055625 per 5° *alpha* distribution histogram bin widths, shown in this chapter as Figure 7.14. This above result is plotted in Figure K.4 (Appendix K). The purpose of this result is to find the optimum degree cutoff from the histogram *alpha* plots to maximize signal over noise.

using equation 7.3 (Section 7.1.4). This was done to confirm our hypothesis that the *alpha* distribution significance (from Figure 7.14) is TeV gamma ray signal from this source and is not due to some random fluctuation in the *alpha* plot distribution for the small angle ($alpha \leq 20°$), where the statistics is more susceptible to random fluctuations than for larger angles (e.g. $alpha \leq 40°$). Our significance result for EXO 055625 for $alpha > 20°$ for the *alpha* distribution of Figure 7.14 is $0.893 \pm 0.011\ \sigma$. This result indicates that there is no significant on-source count over off-source for $alpha > 20°$, and confirms the hypothesis that a weak $2.2\ \sigma$ TeV gamma ray signal (at $alpha \leq 20°$), has been detected by the T1 telescope for EXO 055625 for the period of observation shown in Table H.3 (Appendix H).

Similar to the incremental significance calculation for Mkn 421 in Section 7.1.4 (Table 7.2), we have calculated the incremental significance result (equation 7.3, Li & Ma (1983) [111]) for each 5° bin width of Figure 7.14, to ascertain if the selection of $alpha < 20°$ was the best choice for maximizing signal over noise for EXO 055625. These results are shown in Table 7.3. We have also plotted the incremental significance against histogram bin angle (see Figure 7.14) in Figure K.4 (Appendix K). This figure

(in Appendix K) indicates that the incremental significance reaches a maximum at $alpha \sim 25^{\circ}$. Since we have already calculated the gamma-ray signal significance for $alpha < 20^{\circ}$ (2.2 σ), an inclusion of an extra bin at $alpha \sim 25^{\circ}$ may only slightly improve our signal over noise.

Chapter 8

Conclusions

8.1 Flasher Calibration

8.1.1 T1 flasher image movement analysis

As discussed in in Section 5.2.2, Table 5.4 showed us that the flasher image in the T1 camera did move slightly from calibration month to calibration month. We performed a test in which we attempted to match the distance that the image Cross-Correlation Maximum Position (CCMP) correction, to the camera centre, correlates with the magnitude of the average mean sum ADC of the eight selected pixels. *The hypothesis is that the movement of the flasher image relative to the centre of the camera (or auto-correlation position) correlates with changes in the average amplitudes of the calibration mean sum ADC* (in the case of T1, the average of the mean sum ADC of the eight linearly selected pixels), shown in Figure 5.9.

Although discussed in Section 5.2.2, the CCMP result will be repeated here. CCMP is the scalar distance from the centre of the camera (or the auto-correlation position for T1). It is the square root of the sum of squares of the x- and y- coordinate (in camera pixel degrees, see equation 5.15, Section 5.2.2), derived from the delta and epsilon shift values from the cross-correlation result (see Table 5.4).

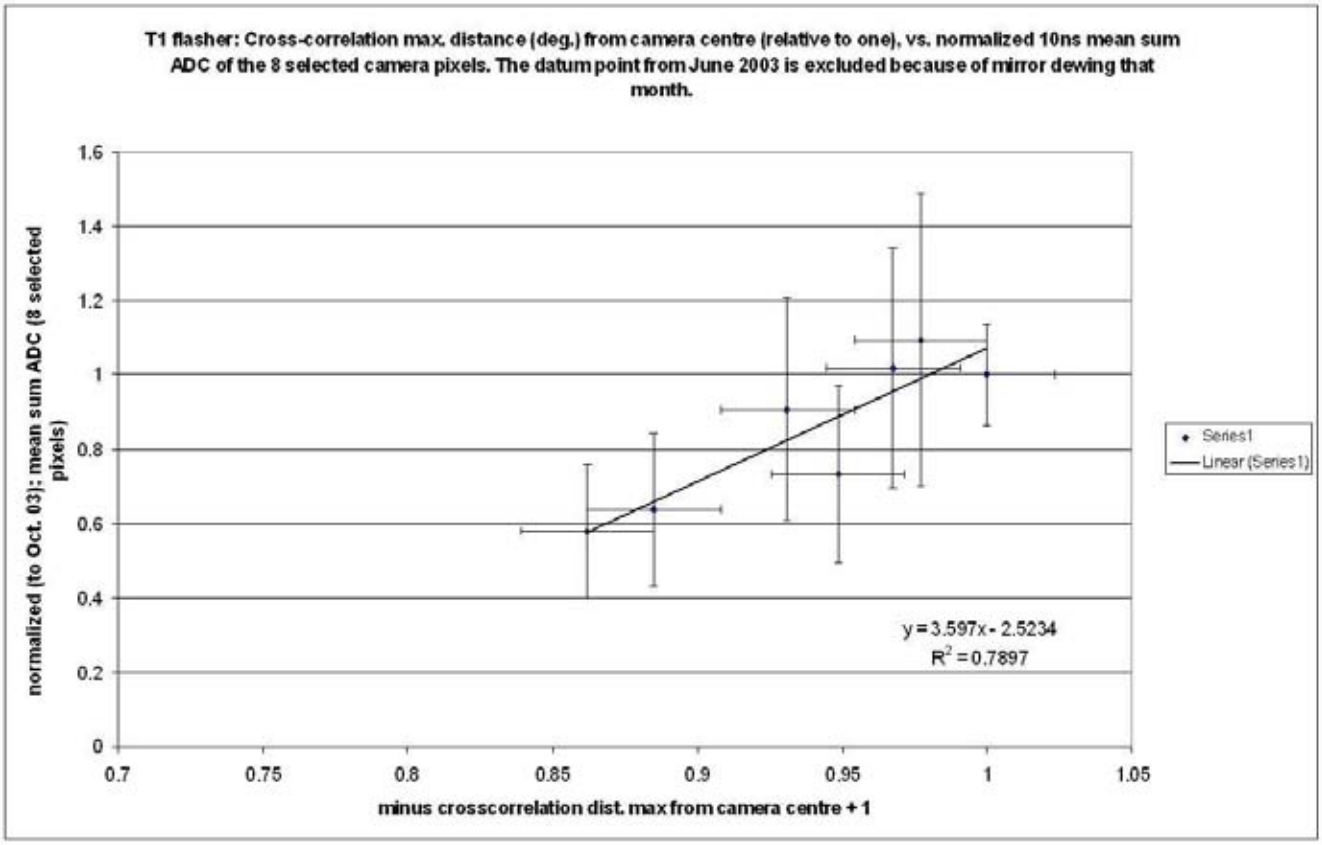

Figure 8.1: Plot of cross-correlation maximum position distance from 1.0 (see Figure 5.10), versus ratio of average mean ADC of the eight selected T1 camera pixels over all calibration months for 10ns setting to test the hypothesis, that of correlation, between these two variables. The least linear squares fit result equation is shown in the lower right of the figure.

It remains to show from Figure 5.10, if there is any correlation between the CCMP distance correction from the camera centre and the average mean ADC of the selected pixels. Figure 8.1 (above) shows this result, taken from the data in Table 5.5, with the June 2003 datum point missing as previously explained (i.e. mirror dewing) in Section 5.2.2. Despite this, we were able to show from seven flasher calibration months from Figure 8.1 that there appears to be a correlation between the increasing CCMP distance and the falling average mean ADC amplitude of the eight selected pixels (Figure 5.9). From the linear least squares result of this correlation between these two variables, the Pearson (product-moment) correlation coefficient for this result is, $r = 0.8886$ arguing

that there is a correlation between the CCMP distance from one and the average mean ADC. Similarly, the linear least squares fit coefficient of determination from the same result is, $r^2 = 0.7897$, indicating that the correlation between the CCMP distance and the average mean ADC is much better than a random distribution, verifying our hypothesis (shown in italics in the first paragraph of this section). Note that these two variables are quite independent of each other, despite the use of the extrapolated mean ADC of every inner camera pixel to calculate the cross-correlation transform. The CCMP distance from the camera centre, as shown in the movement of the contours in Figure E.4 (Appendix E), has no *a priori* connection to the average mean sum ADC amplitude of the eight selected pixels (Figure 5.9). Note also that the linear least squares fit line to the data in Figure 8.1, does not intersect near the origin. In fact, the CCMP distance movement was no further away from the normal image (October 2003), than slightly more than a pixel (see Table 5.4), making the CCMP distances small from the camera centre.

Summarizing, the changes in mean ADC values of the flasher signal appear to correlate with the changes in the position of the image in the camera's FoV and the fluctuations in the flasher mean ADC signal amplitude are sensitive to this. This shows us that small fluctuations or errors in the encoders (recording the tracking/slew and parking direction of the dish), can be responsible for significant signal amplitude uncertainties for a calibrating light source (when not mounted onto the dish or telescope mounts), when the dish is brought into a park position for calibration, because of changes to the alignment of (primarily) the optical axis of the telescope dish with the flasher light source. Similarly, when an independent light recording device, such as a CCD camera, is mounted onto the dish or telescope mounts to record the calibrating light source at infinity, we might find that errors in the telescope encoders of a parked dish could also contribute to fluctuations in the CCD signal amplitude of the recorded signal, such as from a light flashing device used in this thesis, or a bright non-variable star. However, by only using a coarse pixelated IACT camera with PMTs of variable gain to record the light source at infinity, the "errors in encoders" effect will most likely accentuate the light signal amplitude fluctuations compared to a high resolution

charge-coupled (CCD) chip, especially if it is recording a point of light.

A way to remedy this effect is to have a CCD camera device (used in Astronomy) to photograph the calibrating light source in the same slew-stop alt-azimuth position of the dish, when the telescope dish is pointed at the flasher. This CCD camera would be mounted onto the dish near the HV PMT camera. The differences in the positions of the calibrating flasher image in the two successive CCD images (in-between flasher calibrations), would precisely register the degree of error in the dish slew-stop position of the encoders and also measure the degree of light intensity fluctuation of the flasher over the calibrating distance. A discussion of gravitational effects on dish position encoder errors and in dish distortion of the telescope, is given in Section 5.2.3.

8.1.2 T2 flasher image movement analysis

Factors that mitigate the hypothesis that as the CCMP distance increases, the normalized average ADC decreases in T2 (discussed in the previous section for T1) are: Firstly, we have only collected three months of independent flasher calibration data for T2 in comparison to eight months of independent flasher calibration data for T1. Thus for T2, we have less than half the data points of T1, which is important when fitting data using linear least squares as the accuracy of the linear fit increases with more data points. Secondly, for both T1 and T2, we have removed the June 2003 data from the correlation results (Figure 8.1 for T1 and correlation of CCMP dist vs. mean ADC, Figure 5.19 for T2) as a result of mirror dewing from this month. Removing a single datum from a total of eight points (T1 data), has considerably less impact on the overall data trend in comparison to removing one datum from a total of three (T2 data). Thirdly, as discussed in Section 5.3.2, we grafted a square array over the central part of the hexagonal array geometry of the T2 camera, for the purpose of calculating the cross-correlation maximum the same way as we did for T1. However, this result was not perfect as indicated in Figure E.5, Appendix E. The contours for T2 in this figure, show that the proportional increase in the CCMP for each point in the 46×52 array in this figure are not circularly symmetric, which was not the case for T1 (shown in Figure E.4, Appendix E). Instead, the contours in Figure E.5 are ellip-

tical, which may be a result of positioning a different gap between x- (horizontal row) and y- (vertical column) pixels to fit the grafted rectangular array over the hexagonal array. To examine the construction of this grafted rectangular array, see Section 5.3.2. Because of this irregularity in the x- and y- distances, the gap between the adjacent x- (or row pixels) is 0.050°, and the gap between the adjacent y- (or column pixels) is 0.029° (Section 5.3.2). Presumably, the highest value of the CCMP position is located less accurately in the elliptical contours of Figure E.5 for T2, compared to the circular contours of Figure E.4 for T1. This is accentuated by the movement of the flasher image in the telescope being small (due to encoder errors in the dish tracking/slewing mechanism), whilst showing that the mean ADC amplitude value is highly sensitive to this, as discussed in Section 8.1.1.

To summarize, the correlation results for T2 in particular (Figure 5.19) do not have enough data points (three in total; two points after subtracting the mirror dewing month) to prove conclusively that our hypothesis (based on T1 results in Section 8.1.1), is not valid. Furthermore, the position of the CCMP for T2 is not accurately proved, since the CCMP contours are elliptical (Figure E.5, Appendix E). Hence, the correlation results given in Figure 5.19, for T2, have to be discounted as showing essentially that the increasing CCMP degree distance (from the auto-correlation position) will increase the mean ADC amplitude. Collecting more flasher calibration data for T2 would improve the chance of verifying our hypothesis (shown in italics in the first paragraph of Section 8.1.1), but the flasher calibration experiment was finalized before this could be undertaken.

8.2 HBL Lacertae blazar source analysis

8.2.1 Conclusions from the Markarian 421 source analysis

Discussions on the source analysis of Markarian 421, for this section will be firstly on the affects of anomalous noise effects (such as seen in Figure 7.5), then the on-source gamma-ray signal significance from the *alpha* distributions shown in Figures 7.7, 7.8 and 7.9, will be investigated.

The origins of the trigger event rate noise spikes in Figure 7.5, as an example, are unclear. Shown in this figure, these noise spikes appear to be clustered around the first third of the data file duration (and which appear to range as high as ∼240 Hz), argues an artificial origin. This means that the noise spikes are either produced by an unknown data acquisition hardware fault, or are produced externally by ground light interference to the telescope (considered to be less likely). As previously mentioned in Section 7.1.4, the T1 telescope laboured under continuous bright ground light conditions from the Woomera detention centre in 2001. However, this would produce only a moderate increase of (a few Hertz) in the overall trigger rate for every second and not the noise spikes seen. Furthermore, there were occasional headlights from passing vehicles (usually no closer than 5.7 kilometres distant from the airport) and on even rarer occasions, a kangaroo shooter would come within a few kilometers of the operating telescope and send around a spotlight beam. This remains an unlikely scenario because of its rarity, as trigger event rate noise spikes were seen in many of the data files produced from Mkn 421, arguing a hardware fault origin.

It is impossible that the trigger event rate spikes seen in Figure 7.5 would have been produced by any astrophysical affect, such as very high flaring from Mkn 421. The event rate spikes are many magnitudes higher than expected from any blazar source to flare, for example, at an unheard of 50 Crab units flux (integral Crab unit above 1 TeV; $(2.1 \pm 0.2 \pm 0.3) \times 10^{-7}\,\mathrm{m}^{-2}\,\mathrm{s}^{-1}$, Hillas *et al.* (1998) [79]). For an example of an extreme flaring event of Mkn 421, see Gaidos *et al.* (1996) [65].

The same 2001 T1 telescope data for Mkn 421 (in this thesis) were independently analyzed by Okumura *et al.* (2002) [133]. Okumura *et al.* claimed a overall signal significance for the near-identical data (used in this work) from the same telescope, finding a considerably stronger TeV gamma ray signal than reported by this work. Okumura *et al.* [133] wrote; "An excess of 298±52 events, with a significance of 5.7 σ (calculated using the method of Li & Ma (1983) [111]) was obtained in the region of $alpha < 20°$. For the confirmation of the detected signal, the conventional parameterization cuts of $0.2° < distance < 1.1°$, $0.06° < length < 0.18°$, and $0.03° < width < 0.14°$, were applied to the data, and a signal of 286 ±55 events was obtained

with 5.2 σ significance."

The primary Hillas parameters used by Okumura *et al.* [133] (for the observation of Mkn 421 at zenith angle $\sim 70^{\circ}$ above), are somewhat different to these primary Hillas parameters (*distance, length and width*) selected by the author (see Section 7.1.3). The primary Hillas parameterizations are determined from simulations. This work used the *GEANT 3.21* simulation code (commonly used by the CANGAROO collaboration at the time), with a spectral index of 3.0 (identical to Okumura *et al.* [133]), for primary gamma ray shower simulations through the T1 telescope. It is not clear whether the same *GEANT 3.21* simulation code was used by Okumura *et al.* [133], in deriving the primary Hillas parameters for gamma ray showers in his work. Furthermore, Okumura [133] *et al.*, has stated that cosmic ray hadron shower simulations were carried out in his work using *CORSIKA* (version 6.004).

The work of Okumura *et al.* [133], has set the *alpha* distribution to be analyzed for the limit; $alpha < 20^{\circ}$. However, the *alpha* distribution for Figure 1 in [133] indicates that the on-source gamma ray shower peak *alpha* distribution has amplitude over the off-source for $alpha < 40^{\circ}$. The on-source *alpha* distribution result from simulations in our work (Figure 7.4), confirms that setting $alpha < 40^{\circ}$, is considerably more likely at the zenith angle of Mkn 421 at Woomera ($\sim 70^{\circ}$) to include all of the on-source *alpha* distribution peak for the gamma ray shower signal, than half this value ($alpha < 20^{\circ}$). See Section 7.1.3, for a discussion on the *alpha* plot peak cutoff angle for Mkn 421 at high zenith angle. However, noting that a selection for $alpha < 40^{\circ}$ maximizes signal, rather than signal over noise, a further calculation was made for $alpha < 20^{\circ}$ (maximizing signal over noise) for the Mkn 421 *alpha* plot results (see Table 7.1).

The choice of slightly different Hillas parameters used in this work, compared to Okumura *et al.* [133], for the primary Hillas parameters; *distance, length* and *width*, is partially responsible for the different gamma ray signal significance (3.3 σ ($alpha < 40^{\circ}$) and 3.5 σ ($alpha < 20^{\circ}$) in 2001, see Table 7.1) obtained in this work compared to Okumura's (*et al.*) observations in [133]. Additionally, the *precuts* (noise, starlight and cloud reduction) procedures applied to the Mkn 421 data in this work (see Section 7.1.4), are also different from those deployed by Okumura *et al.* [133]. Furthermore,

Okumura *et al.* [133] applied Point Spread Function probabilities to the simulation data, further refining the result. These differences may also contribute to the lower signal significance in this work (3.3 σ ($alpha < 40°$), 3.5 σ ($alpha < 20°$)), compared to Okumura *et al.* [133] at 5.7 σ. There was no flux measured for Mkn 421 in this work.

8.2.2 Flaring state of Markarian 421 during 2001

Markarian 421 was in a GeV-TeV gamma ray flux flaring state in the first three months of 2001 (January to March). As well as CANGAROO (Okumura *et al.* (2002) [133], and work in this thesis), GeV-TeV flaring from Mkn 421 for this period was observed by other IACT groups; HEGRA (Kohnle *et al.* (2001) [98]), and VERITAS (Holder (2001) [85]). Additionally TeV flaring from Mkn 421 was observed in 2001 by other (non-IACT) observatories sensitive in the GeV-TeV region: The Tibet air shower array experiment (Amenomori *et al.* (2003) [15]) and the STACEE experiment, (Boone, *et al.* (2002) [35]).

Mkn 421 is known to vary rapidly in flaring episodes, cycling in days or even minutes; Gaidos *et al.* (1996) [65], reported a flaring rate from Mkn 421 $\sim$15 minutes. The Whipple telescope (Holder (2001) [85]), reported extreme flaring rates from Mkn 421, with a near doubling of the flaring flux in a time-span of $\leq$ 30 minutes. The maximum flaring flux from this data was up to 3.6 Crab from a minimum of 0.2 Crab, [85] (definition of the standard candle Crab unit in TeV energies $= 1.8 \times 10^{-11}$ photons cm^2/second above 0.7 TeV, Weekes *et al.* (1989) [166]). HEGRA (Kohnle *et al.* (2001) [98]), reported a flaring maximum for Mkn 421 of up to 7.8 Crab for February 2001. The flaring episodes in 2001 from Mkn 421 were well correlated with contemporaneous X-ray data from RXTE ([85], Horns, Kohnle & Aharonian (2001) [86]), which strengthens the TeV emission model for Mkn421 on the same population of radiating electrons (SSC model in Section 2.2.3), rather than the Hadronic emission model (Section 2.3) for this source. The modeling of X-ray and TeV gamma ray correlation from electronic SSC sources while flaring is, however, inconclusive for Mkn 421 in the quiescent state.

The observed size of an emission region, R, depends on the following factors [98],

$$R < \Delta t_{obs} \cdot c \cdot \delta \sim 3 \times 10^{14} \cdot \Delta t_{obs}[h] \cdot \delta \quad \text{cm} \tag{8.1}$$

where t_{obs} is the observed variability timescale and δ is the Doppler factor of the jet. Even with high Doppler factor and beaming of the IC electrons in the direction of the Earth, the extremely short timescales of ≤ 30 minutes indicates that the emission region for Mkn 421 must be extremely compact for an AGN source.

Energy spectra were obtained from the observation of Mkn 421 during the flaring state in the first three months of 2001, Aharonian *et al.* (2002) [8] (HEGRA), Krennrich *et al.* (2001) [103] (Whipple; VERITAS). Both these IACT collaborations described the (differential) GeV-TeV energy spectra from Mkn 421 as a (straight line) power law with an exponential cutoff. The (gamma ray photon count) differential energy spectra for Mkn 421 (in 2000-2001) were;

$$\frac{dN}{dE} \propto E^{-2.14\,\pm 0.03_{\rm stat} \pm 0.10_{\rm sys}} \cdot e^{-E/E_0}\ \text{m}^{-2}\ \text{s}^{-1}\ \text{TeV}^{-1} \quad \text{(Whipple, [103])} \tag{8.2}$$

$$\frac{dN}{dE} = 11.4 \pm 0.3_{\rm stat} \pm 0.4_{\rm sys} \left(\frac{E}{\text{TeV}}\right)^{-2.19\,\pm 0.02_{\rm stat} \pm 0.04_{\rm sys}} \cdot e^{-E/E_0}\ \text{m}^{-2}\ \text{s}^{-1}\ \text{TeV}^{-1}\ \text{(HEGRA, [8])} \tag{8.3}$$

with the exponential cutoff energy thresholds as; $E_0 = 4.3 \pm 0.3_{\rm stat}(-1.4 + 1.7)_{\rm sys}$ TeV [103] for Whipple and, $E_0 = 4.19 \pm 0.04_{\rm stat}$ TeV [8] for HEGRA (systematic uncertainty unspecified). The majority of the data to obtain the energy spectra for Whipple and HEGRA were taken during the Mkn 421 flaring state in 2001, fairly contemporaneous with work in this thesis. As one can see from the differential spectra above, the spectral index for Whipple ($\alpha = 2.14$), is slightly harder than the spectral index for HEGRA, ($\alpha = 2.19$). GeV-TeV spectral hardening with increasing flux levels (during flaring episodes) was clearly noted when Mkn421 was flaring in the first three months of 2001; (HEGRA [8]), (VERITAS [103]), compared to Mkn 421 data in a more quiescent state.

The exponential cutoff energy, $E_0 \sim 4.25$ TeV (mean value between Whipple and HEGRA) is very similar, within statistical uncertainties, for these two IACT groups. Because of this and because the data for the energy spectra comes from the same source, the exponential cutoff in energy is most likely due to either the pair-production

attenuation of TeV photons with the CIB above the E_0 energy (Section 2.4), or the change of IC scattering cross-section from the Thomson to the less efficient Klein-Nishina cross-section in the emission process [103], [8], or a combination of both these effects.

A comparison of the differential spectra from these two IACT collaborations (equations 8.2 and 8.3, above), to a power law straight-line fit differential energy spectrum determined by CANGAROO for near-contemporaneous data for Mkn 4121 in the flaring state, is shown below as determined by Okumura *et al.* (2002) [133]:

$$\frac{dN}{dE} = (3.3 \pm 0.9_{\rm stat} \pm 0.3_{\rm sys}) \times 10^{-13} \cdot \left(\frac{E}{10\,{\rm TeV}} \right)^{-4.0 \pm (-0.6+0.9)_{\rm stat} \pm 0.3_{\rm sys}} \text{ photons cm}^{-2}\text{ s}^{-1}\text{ TeV}^{-1} \tag{8.4}$$

The spectral index of the above differential energy spectrum from CANGAROO ($\alpha = 4.0$), is much softer than the spectral indices from Whipple and HEGRA ($\alpha = 2.14$ and 2.19 respectively), determined from a much steeper gradient, as is expected at the energies observed at the high zenith angle by the T1 telescope. Taking into account the exponential cutoff threshold energy of ∼4.25 TeV from Whipple and HEGRA, there is no exponential energy cutoff threshold for CANGAROO, since the lowest threshold energy photon detected by Okumura (*et al.*) was $\geq$ 11 TeV, [133]. It is expected that, at these energies ($\geq$ 11 TeV), the flux of gamma ray photons from Mkn 421 is already considerably attenuated from pair-production with the CIB and losses in IC scattering production at these higher energies at the source. Okumura *et al.* [133] surmised that there was an observable exponential cutoff in the CANGAROO energy spectrum at about 8 TeV. The addition of this (below CANGAROO threshold) cutoff factor into spectral energy results in [133] improves the goodness of fit in the CANGAROO differential energy spectrum. However, the high degree of (known) systematic and statistical uncertainties would place the (higher) exponential cutoff energy threshold at $\sim$ 8 TeV into doubt without corroborating evidence from another IACT collaboration. Figure 8.2 shows the combined differential energy spectra from CANGAROO (Okumura *et al.* (2002) [133]), Whipple and HEGRA from Mkn 421 in late 2000 to early 2001.

Diurnal or hourly flaring rates were not tested for in the Mkn 421 (2001) CANGAROO data in Okumura *et al.* (2002) [133], and work in this thesis.

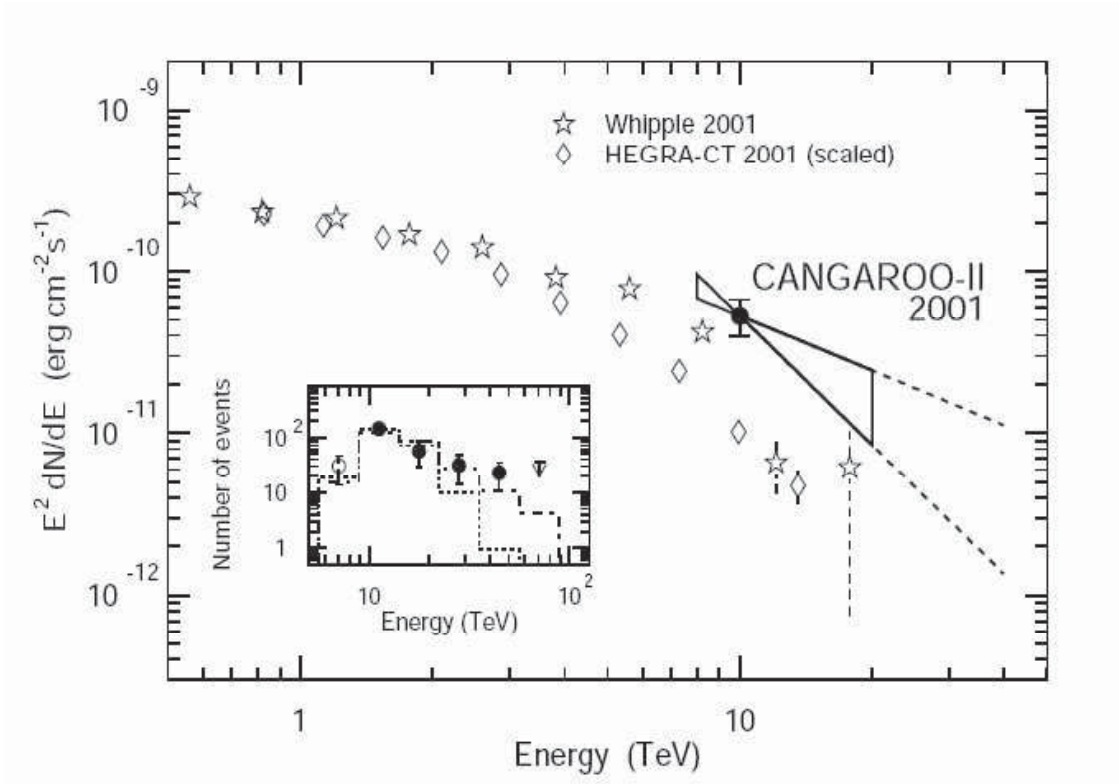

Figure 8.2: From Okumura *et al.* (2002) [133]: Differential energy spectra from CANGAROO shown from Okumura *et al.* (2002) [133], Whipple and HEGRA (shown separately) derived from the Mkn 421 TeV gamma ray observation dataset, during a flaring state in late 2000/early 2001. The differential energy spectra is described by equation 8.2 (Whipple [103]), equation 8.3 (HEGRA [8]), and equation 8.4 (CANGAROO [133]) in this section. The inset; "with the filled circles was used for the spectral shape fitting. The fluxes plotted for the HEGRA group have been scaled in order to normalize it to the Whipple flux at 1 TeV", [133].

8.2.3 Conclusions from the EXO 055625-3838.6 source analysis

This section includes a discussion on the TeV gamma ray signal significance from EXO 055625 (including any possible contemporaneous X-ray satellite observations and GeV-TeV observations from other IACT collaborations), and the implications from a probable TeV gamma ray source discovery with CANGAROO.

The BL Lac., EXO 055625, was observed in 2004-2005 by HESS as a part of a southern sky AGN survey, Aharonian *et al.* (2005) [4], Benbow (2005) [29]. It was

observed for a total of 1.2 hours with the array of all four HESS IACTs and a 1.7 σ significance signal in TeV-GeV gamma rays was found by HESS for this source, [4], [29]. HESS calculated the flux sensitivity from this source (for the exposure duration) to be 5.1% Crab units, [4], [29] (see previous Section 8.2.2, for the Crab flux definition). An upper limit has been claimed for this source, with insufficient energy/flux from EXO 055625, to claim a GeV-TeV gamma ray source discovery of this source by the HESS collaboration, [4], [29].

While this result from the more sensitive HESS telescope array may undermine our claim for EXO 055625 to be a weak TeV gamma ray source, the HESS observation time was short compared to the 16 hours on-source exposure time for EXO 055625 by CANGAROO (Section 7.2.4). Furthermore, Aharonian *et al.* (2005) [4], has acknowledged the shortcomings of the brief time exposure of HESS to EXO 055625. As shown in Table 7.1, the HBL Lac. Mkn 421, was observed by CANGAROO in 2001 when this source was found to be flaring by at least two IACT collaborations, other than CANGAROO (see previous Section 8.2.2). From the CANGAROO observation of this source in 2002-2003 (Table 7.1), Mkn 421 did not show a TeV gamma ray signal with T1 (1.2 σ for $alpha < 20^{\circ}$ upper limit), because this source was no longer flaring in 2002-2003. It may be that CANGAROO has observed EXO 055625 while this source was in a flaring state and HESS has observed it for a short time while it was in a quiescent state. There was no flux measured for EXO 055625 in this work.

Since the 2.1 σ signal was detected by the T1 telescope for EXO 055625 (on the supposition that this BL Lac. source gamma ray emission process is from electronic IC), it may have been flaring above a quiescent state in X-rays to achieve sufficient flux to be detected in TeV energies by T1. Hence, a hardening of the TeV spectrum of EXO 055625 may have also occurred as a result (similar to Mkn 421, Section 8.2.2). Aharonian *et al.* (2005) [4], has acknowledged that a source (such as EXO 055625) may be detectable in GeV-TeV when flaring in X-rays, and a hardening of the GeV-TeV spectrum may result. A search for contemporaneous X-ray satellite observation data was made for EXO 055625, for the dates in which observation of this source was carried out by CANGAROO (see Table H.3, Appendix H). A query was

conducted with the SIMBAD (the Set of Identifications, Measurements, and Bibliography for Astronomical Data) database website at; **http://heasarc.gsfc.nasa.gov/cgi-bin/W3Browse/w3browse.pl** (Astrophysical Science Division, NASA/GSFC), for contemporaneous X-ray data from RXTE, ROSAT, ASCA, *Chandra, XMM-Newton* and *BeppoSAX* on EXO 055625. The result showed that there was no finding X-ray data from these satellite experiments on the dates when EXO 055625 was observed by CANGAROO in 2002-2003.

Although the 2.2 σ signal from EXO 055625 is weak, it is not insignificant and warrants further observational investigation in stereo mode. A contemporaneous GeV-TeV observation schedule of EXO 055625 between two IACT groups would be considerably more useful, since like Mkn 421, spectral hardening of EXO 055625 might be expected if this source is flaring. George & Turner (1996) [68], reported X-ray intensity (i.e. flux) variation in EXO 055625 of up to 1.5 times between two epochs of observation. Ideally, the GeV-TeV observation of EXO 055625 by IACTs should be occurring when this source is detected flaring in X-ray, hence a contemporaneous multi-wavelength campaign involving an X-ray satellite experiment and at least one IACT should be considered as soon as X-ray flaring of this source is detected. More observational data is required on EXO 055625 in GeV-TeV energies, before a source energy spectrum can be derived.